

Time-Dependent Transport Through Quantum Dots Coupled to Normal and Superconducting Leads

Dissertation

zur Erlangung des
Doktorgrades der Naturwissenschaften (Dr. rer. nat.)
der

Naturwissenschaftlichen Fakultät II
Chemie, Physik und Mathematik

der Martin-Luther-Universität
Halle-Wittenberg

vorgelegt von

Herr **Klaus Jochen Pototzky**

geb. am 14.02.1986 in Nürnberg

Datum der Verteidigung
24. Juni 2015

Gutachter:
Prof. Dr. E. Gross (Betreuer), Prof. Dr. I. Mertig, Prof. Dr. T. Frauenheim

Contents

1	Introduction	1
1.1	Superconductivity	3
1.2	Josephson effects	4
1.3	Andreev reflection	7
1.4	Andreev bound states	8
2	Mathematical prerequisites	10
2.1	Basic definitions and notations	10
2.2	Nonequilibrium Green's functions	11
2.2.1	Keldysh contour	11
2.2.2	Definition of the nonequilibrium Green's function	14
2.2.3	Nonequilibrium Green's function in the Nambu space	15
2.3	Model Hamiltonian	16
3	Methods	21
3.1	Landauer-Büttiker formula	22
3.2	Time propagation of wave functions	23
3.2.1	Ground state calculation	23
3.2.2	Time propagation	29
3.2.3	Calculation of observables	32
3.2.4	Efficient numerical implementation	33
3.3	Large time behaviour of the nonequilibrium Green's functions	48
3.4	Comparison	51
4	Features of SQDS junctions	53
4.1	DC Josephson effect	54
4.2	AC Josephson effect	55
4.3	Subharmonic gap structure	57
4.4	Inverse AC Josephson effect	60
4.5	Insights from the spectral function	64
4.5.1	Ground state	66

4.5.2	Nonequilibrium state - constant bias	67
4.5.3	Nonequilibrium state - switching the bias	72
4.6	Conclusion	76
5	Junctions with classical vibrations	77
5.1	Model	77
5.2	Stability analysis	79
5.3	Vibrations in Josephson junctions	86
5.3.1	Ground state	86
5.3.2	Biased system in the static limit	87
5.3.3	Biased system in resonance	88
5.4	Conclusion	92
6	Controlling observables in time-dependent quantum transport	93
6.1	Optimization problem	94
6.2	Results for NQDN junctions	97
6.2.1	Controlling current and density of a NQDN junction	97
6.2.2	Controlling classical vibrations	99
6.2.3	Imposing further constraints on the bias	101
6.3	Results for SQDS junctions	102
6.4	Cooper pair splitting in a Y-shaped junction	105
6.5	Conclusion	111
7	Summary and Outlook	112
Appendix A	Time propagation method	115
A.1	Diagonal elements of the inverse of a tridiagonal matrix	115
A.2	Calculation of the embedding matrices	117
A.3	Calculation of the source term	119
Appendix B	Derivation of the NEGF method	122
B.1	Large time behaviour of the current and density	122
B.2	Evaluation for a monochromatic central Hamiltonian	127
B.3	Calculation of the matrices $\mathbf{G}_m(\omega)$	130
Appendix C	Calculation of the spectral function using NEGFs	133
C.1	Large time behaviour of the spectral function	133
C.2	Convolutd spectral function	137
	Bibliography	140
	Acknowledgements	161
	Curriculum vitae and Publications	162

Chapter 1

Introduction

Since the invention of the first computer, engineers and scientists have put a lot of effort in increasing the computational speed. It goes along with Moore's law, which states that the number of transistors on a chip doubles approximately every two years [Moo65]. Keeping the chip size constant yields an exponential decrease in the size of the transistors. Intel's current chip generation is based on the 22nm technology, the future generations will get even smaller [BM11]. The ultimate goal is to produce electronics using single molecules as its building blocks. The first work proposing a single molecule as an electric component was published by Aviram and Ratner in 1974 [AR74] and realized experimentally by Metzger *et al.* [MCH+97] several years later. Since then, lots of different aspects have been studied and an enormous amount of papers on this topic has been published. The books [CFR05, CS10] provide a very good introduction into the research field of molecular electronics.

Until today, electronics is usually based on normal-conducting materials like metals or semiconductors. Prospective devices could also make use of superconducting parts, opening new ways for further developments.

One advantage of superconducting wires is the absence of resistivity and the enormous reduction of the heating of the device. For example, the heat generation is one of the major problems when increasing clock frequencies of processors above the intended values, known as overclocking. Often, additional cooling mechanisms like water circuits or even liquid nitrogen reservoirs are attached to the processor in order to avoid damages and computational errors.

A second advantage is the existence of phenomena which do not occur in normal-conducting materials, like the Josephson effects. They open new possibilities to construct novel electronic devices and will be explained in the sections 1.2 - 1.4.

First steps into this direction have already been made, like the invention of the Josephson field effect transistor [CPG80] and the superconducting quantum interference device [JLSM64, JLMS65]. The latter are very sensitive measure-

ment instruments for magnetic fields and are used in various applications for already quite some time. Besides, they are promising candidates for the realization of a future quantum computer. It is therefore essential to have a profound knowledge of common features and differences between junctions with normal and superconducting leads. The aim of the thesis is to address novel questions and to provide insights into phenomena in junctions with normal and superconducting leads, focusing on the latter. It is structured as follows:

In the next four sections of the first chapter, we give a short introduction into superconductivity and explain three phenomena related to interfaces between normal and superconducting materials: the Josephson effects, the Andreev reflections and the Andreev bound states.

Chapter 2 lays the mathematical foundations for the simulations in the later chapters. We briefly explain the idea of the Keldysh contour and define the nonequilibrium Green's functions. We further present our model Hamiltonian.

In chapter 3, we show three different ways to calculate properties of junctions with an applied bias: (a) The Landauer-Büttiker approach, (b) the calculation of the large time behaviour of the nonequilibrium Green's functions and (c) a method for propagating single particle wave functions in time. For the latter, an efficient numerical implementation is discussed. The chapter is concluded with a short comparison of the mentioned methods.

In chapter 4, Josephson junctions are investigated in more detail. We report and explain deviations of our results from the original current-phase relation for the DC, AC and inverse AC Josephson effect, which was derived by Brian D. Josephson [Jos62] using a first order approximation. The subharmonic gap structure and the spectral function provide further insights into the charge transfer mechanisms in Josephson junctions.

In chapter 5, a quantum dot is coupled to a vibration, which is treated in the Ehrenfest approximation. We report bistabilities and instabilities for junctions with normal and superconducting leads. Conditions for stability are derived. We further demonstrate resonance phenomena in these junctions.

Chapter 6 combines time-dependent quantum transport with optimal control. We show how to tailor the bias such that an observable, like a current, a density or a vibration, follows a predefined target pattern as best as possible. This is done for junctions with normal and superconducting leads. We further demonstrate how to generate a DC current flowing through a Josephson junction in two different ways. Besides, we use the approach to maximize the Cooper pair splitting efficiency in a Y-shaped junction. This creates entangled electrons which get spatially separated.

1.1 Superconductivity

The history of superconductivity started with the discovery of the resistivity loss of mercury below 4.2K by Heike Kamerlingh Onnes in 1911 [Onn11a, Onn11b, Onn11c]. He was awarded with the Nobel prize for “his investigations on the properties of matter at low temperatures which led, inter alia, to the production of liquid helium” in 1913 [Nob14].

A theoretical explanation of superconductivity was an open problem for a long time. The London brothers invented the first phenomenological model [LL35]. It was able to describe the phenomenon that magnetic fields cannot penetrate a superconductor, which is known as the Meissner effect [MO33]. Some years later, Ginzburg and Landau developed a macroscopic theory for superconductivity including phenomenological parameters, which is known as the Ginzburg-Landau theory [GL50]. It correctly predicts the existence of two different types of superconductors, named type I and II [Abr57].

The first microscopic theoretical description was published by Bardeen, Cooper, and Schrieffer in 1957, which is known as the BCS theory [BCS57]. The authors received the Nobel prize in 1972 for their theory. It was later shown that the Ginzburg-Landau theory can be derived from the BCS theory, providing an interpretation for the phenomenological parameters [Gor59]. The BCS theory is based on the idea of Leon N. Cooper that electrons can form bound pairs in a degenerate electron gas, if there is an attractive force [Coo56]. These pairs were named Cooper pairs. The attractive force is a result of the interaction between phonons and electrons [Frö54]. The formation of electron pairs causes a gap of 2Δ in the excitation spectra of a superconductor around the Fermi level μ . The binding energy 2Δ of a Cooper pair is of the order of 1 to 10meV. Thermal energy can brake these pairs, if the temperature is too high. The maximum temperature for a solid to be superconducting is the critical temperature T_C . The BCS theory correctly predicts the temperature dependence of the superconducting gap $\Delta(T) \propto \sqrt{1 - \frac{T}{T_C}}$ for temperatures T slightly smaller than T_C . It further captures the isotope effect [RSWN50, Max50] which relates the critical temperature T_C to the mass number A of the material via $T_C \propto A^{-\frac{1}{2}}$.

But, the BCS theory relies on a weak electron-phonon coupling and does not take the properties of the superconducting material properly into account. For example, it is not possible to predict the critical temperature of a certain material accurately. Nowadays, there are further, more advanced theories available to describe superconducting materials like the Eliashberg theory [Eli60] or the superconducting density functional theory [OGK88]. Both can be used to calculate T_C for different materials.

Since the discovery of the superconductivity of mercury in 1911, lots of other phonon-driven superconducting materials have been found, for example MgB_2 . Its critical temperature is 39K [NNM⁺01], which is the current record of all known materials belonging to this group. Although MgB_2 is a phonon-driven superconductor, it cannot be described within the framework BCS theory since the electron-phonon coupling is not weak.

Besides these phonon-driven superconductors, there is the group of unconventional superconductors with even higher critical temperatures. One prominent member is the compound YBaCuO with a critical temperature of 93K [WAT⁺87]. But, the pairing mechanism in these materials is still under investigation.

1.2 Josephson effects

In 1962, Brian D. Josephson predicted the tunneling of electron pairs between two superconductors separated by a thin insulating barrier [Jos62]. The first experimental verification was published by Anderson and Rowell in 1963 [AR63]. The tunneling of electron pairs is the origin of three effects: (a) the DC Josephson effect, (b) the AC Josephson effect and (c) the inverse AC Josephson effect. Apart from the original derivation, the Josephson effects appear whenever two superconductors are weakly linked and not only for an insulating barrier. The weak link may be a normal-conducting barrier or even a short constriction. All these types of junctions are called “Josephson junctions”. Figure 1.1 shows a sketch of a Josephson junction.

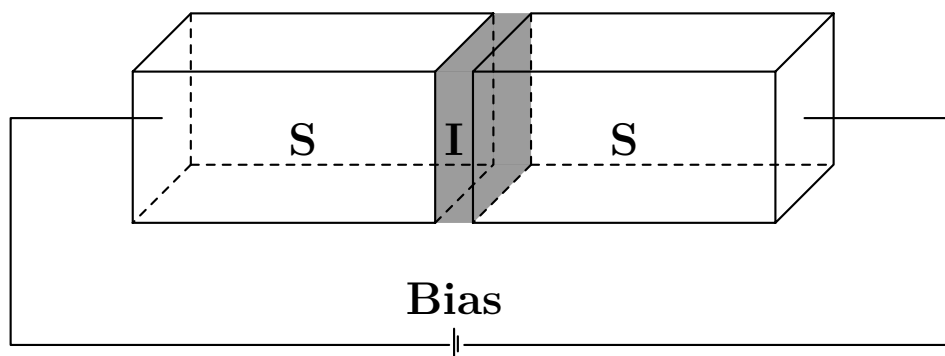


Figure 1.1: Sketch of a Josephson junction. The two superconductors (S) are separated by a thin insulating barrier (I).

In order to explain the Josephson effects, we define the Cooper pair wave function $\varphi_\alpha = \sqrt{n_\alpha} e^{i\chi_\alpha}$, where n_α represents to Cooper pair density and χ_α the phase of the Cooper pairs of lead α . The basic equations in the description of the Josephson effects in terms of χ_α are [Jos62, Wal76]:

$$U(t) = \frac{\hbar}{2e} \frac{d\chi(t)}{dt}, \quad (1.1)$$

$$\chi(0) = \chi_0 = \chi_R - \chi_L, \quad (1.2)$$

$$I(t) = I_0 + I_1 \sin(\chi(t)) + I_2 \cos(\chi(t)). \quad (1.3)$$

The equation (1.3) is the current-phase relation. The terms I_0 , I_1 and I_2 depend on the system and the bias. In the absence of a bias, the contributions I_0 and I_2 vanish and only I_1 survives [Wal76]. In this case, I_1 is called “critical current” and we use the notation I_C instead. For junctions with two identical superconductors, I_C is given by the Ambegaokar and Baratoff formula as a function of the temperature T [AB63a, AB63b]:

$$I_C = \frac{\pi \Delta(T)}{2eR_n} \tanh\left(\frac{\Delta(T)}{2k_B T}\right). \quad (1.4)$$

In the above equation, R_n denotes the resistance in the normal state.

The equations (1.1) - (1.3) were derived using the transfer Hamiltonian approach [CFP62]. The wave functions were calculated in first order of the lead coupling, hence we expect to see deviations in the current compared to the current-phase relation in equation (1.3). Nevertheless, the equations are a good starting point for further investigations. They give rise to the three Josephson effects:

1. DC Josephson effect

The junction has no applied bias. The phase difference $\chi(t)$ is constant and a constant (DC) current flows through the junction:

$$I = I_C \sin(\chi_0). \quad (1.5)$$

2. AC Josephson effect

A constant (DC) bias U is applied across the junction, yielding a linear increase in the phase difference:

$$\chi(t) = \frac{2e}{\hbar} U t + \chi_0 \quad (1.6)$$

and

$$I(t) = I_0 + I_1 \sin\left(\frac{2e}{\hbar}Ut + \chi_0\right) + I_2 \cos\left(\frac{2e}{\hbar}Ut + \chi_0\right). \quad (1.7)$$

The current oscillates with frequency $\omega = \frac{2e}{\hbar}U$.

3. Inverse AC Josephson effect

An alternating (AC) bias is applied on top of a DC bias as

$$U(t) = U_{\text{DC}} + U_{\text{AC}} \cos(\omega_{\text{AC}}t). \quad (1.8)$$

The phase difference then reads

$$\chi(t) = \chi_0 + \frac{2e}{\hbar} \left[U_{\text{DC}}t + \frac{U_{\text{AC}}}{\omega_{\text{AC}}} \sin(\omega_{\text{AC}}t) \right]. \quad (1.9)$$

We reformulate the current-phase relation of equation (1.3) into

$$I(t) = I_0 + I_{1,2} \sin\left(\chi(t) + \arctan\frac{I_2}{I_1}\right) \quad (1.10)$$

with $I_{1,2} = \sqrt{I_1^2 + I_2^2}$. We further define $\tilde{\chi}_0 = \chi_0 + \arctan\frac{I_2}{I_1}$ and insert equation (1.9) into equation (1.10):

$$I(t) = I_0 + I_{1,2} \sin\left(\chi(t) + \arctan\frac{I_2}{I_1}\right) \quad (1.11)$$

$$= I_0 + I_{1,2} \text{Im} \left\{ \exp \left[i\tilde{\chi}_0 + i\frac{2e}{\hbar}U_{\text{DC}}t + i\frac{2e}{\hbar}\frac{U_{\text{AC}}}{\omega_{\text{AC}}} \sin(\omega_{\text{AC}}t) \right] \right\} \quad (1.12)$$

$$= I_0 + I_{1,2} \text{Im} \left\{ \sum_{m \in \mathbb{Z}} J_{-m} \left(\frac{2eU_{\text{AC}}}{\hbar\omega_{\text{AC}}} \right) \right. \quad (1.13)$$

$$\left. \exp \left[i\tilde{\chi}_0 + i\frac{2e}{\hbar}U_{\text{DC}}t - im\omega_{\text{AC}}t \right] \right\} \\ = I_0 + I_{1,2} \sum_{m \in \mathbb{Z}} J_{-m} \left(\frac{2eU_{\text{AC}}}{\hbar\omega_{\text{AC}}} \right) \sin \left[\tilde{\chi}_0 + \left(\frac{2eU_{\text{DC}}}{\hbar} - m\omega_{\text{AC}} \right) t \right]. \quad (1.14)$$

In the reformulation, we have made use of the Jacobi-Anger identity [CK98]

$$e^{i\alpha \sin \theta} = \sum_{m \in \mathbb{Z}} J_{-m}(\alpha) e^{-im\theta}, \quad (1.15)$$

where $J_m(\alpha)$ are the Bessel functions of the first kind. Taking the time

average of the current yields

$$I_{\text{DC}} = I_0 + I_{1,2} \sum_{m \in \mathbb{Z}} J_{-m} \left(\frac{2eU_{\text{AC}}}{\hbar\omega_{\text{AC}}} \right) \sin(\tilde{\chi}_0) \delta_{\frac{2e}{\hbar}U_{\text{DC}}, m\omega_{\text{AC}}}. \quad (1.16)$$

The Josephson effects have been utilized in many different ways for practical applications. An applied DC bias U generates a frequency $f = \frac{2e}{\hbar}U$, hence Josephson junctions can be used as voltage-to-frequency converters. The proportionality constant is called Josephson constant $K_J = \frac{2e}{\hbar}$ and its recommended value is $K_J = 483\,597.870(11) \frac{\text{GHz}}{\text{V}}$ [MTN12]. It is independent of the device geometry and the measurement setup.

Josephson junctions are the basic parts of superconducting quantum interference devices (SQUIDs), which can be used to measure magnetic fields very accurately [JLSM64, Fag06]. They can be found in various types of measuring instruments. The underlying mechanisms are the DC Josephson effect and the magnetic flux quantization through superconducting loops. In the future, Josephson junctions might be part of novel electronic devices. An example is the quantum computer with superconducting quantum bits as its building blocks [MSS01, DWM04].

1.3 Andreev reflection

The Andreev reflection is a special type of reflection which can occur at the interface of a normal conductor with a superconductor. It was discovered by Alexander F. Andreev in 1964 [And64]. The mechanism is illustrated in figure 1.2.

An electron in the normal conductor with an energy slightly above the Fermi level μ hits the interface of a normal conductor with a superconductor. It cannot enter the superconductor since there is the gap in the density of states between $\mu - \Delta$ and $\mu + \Delta$. But, there are two other possibilities:

1. Normal reflection: The electron gets reflected back to the normal conductor. The sign of momentum and velocity changes due to the reflection.
2. Andreev reflection: The electron combines with a second electron with opposite momentum and forms a Cooper pair in the superconductor. This creates a hole in the normal conductor with almost the same momentum but opposite velocity as the incoming electron. The momentum is conserved if the incoming electron is at the Fermi energy. The relative energies to the Fermi level of the incoming electron and outgoing hole are the same.

Blonder, Tinkham and Klapwijk developed a model to describe transport through an normal-superconducting (NS) interface, taking Andreev reflections as well as transmissions and normal reflections into account [BTK82]. This opened the possibility to calculate current-voltage characteristics for junctions with one normal and one superconducting lead.

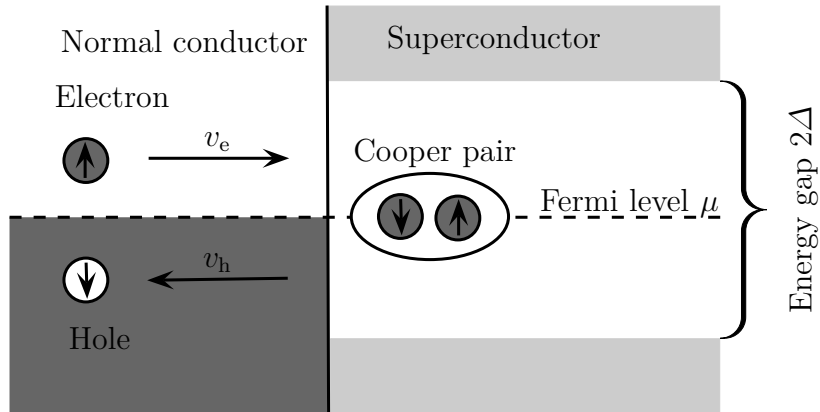


Figure 1.2: Sketch of an Andreev reflection at a normal-superconducting (NS) interface. The incoming electron creates a Cooper pair in the superconductor and leaves an outgoing hole in the normal conductor. The arrows indicate the velocity of the particles. The momentum of the electron and the hole point both to the right.

1.4 Andreev bound states

Andreev reflections also appear in sandwich structures of two superconductors and a normal conductor in between. This geometry creates bound states between the superconductors: the Andreev bound states. Figure 1.3 displays the mechanism of an Andreev bound state. The electron in the normal conductor travels to the right and finally hits the right boundary. Together with a second electron of opposite momentum, it creates a Cooper pair in the right superconductor. The resulting hole moves towards the left boundary. It annihilates a Cooper pair in the left superconductor and creates an electron, which is traveling again towards the right interface and the procedure starts over. One iteration moves a Cooper pair from the left to the right lead and thus creates a current flowing from left to right.

The opposite process, which moves Cooper pairs from the right to the left lead, also takes place and is shown in figure 1.4. The resulting currents of these

two processes only add up to zero if $\chi_R - \chi_L = k\pi, k \in \mathbb{Z}$. Otherwise, there is a non-zero current flowing through the normal conductor. Then, the Andreev bound states contribute to the DC Josephson effect, which was explained in section 1.2.

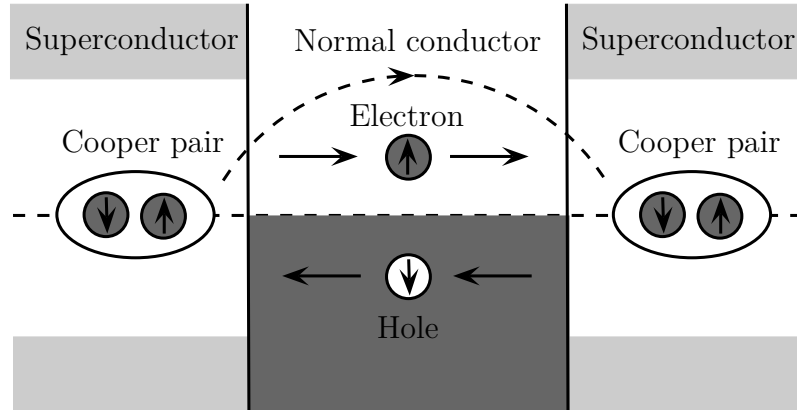


Figure 1.3: Schematic of an Andreev bound state. Cooper pairs are destroyed in the left superconductor and new ones are created in the right one. The opposite process is also possible and shown in figure 1.4.

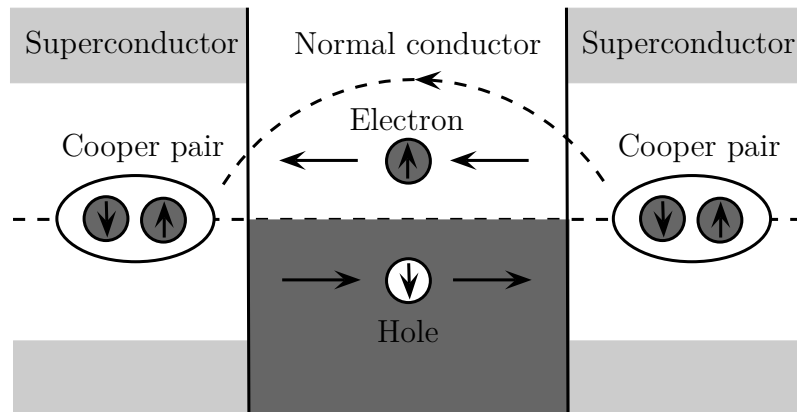


Figure 1.4: Schematic of the reversed process of figure 1.3. Cooper pairs are destroyed in the right superconductor and new ones are created in the left one.

Chapter 2

Mathematical prerequisites

2.1 Basic definitions and notations

We will make use of the second quantization. The usual definitions are:

$$\hat{c}_{k,\sigma}^\dagger \quad \text{Creates an electron at site } k \text{ with spin } \sigma, \quad (2.1)$$

$$\hat{c}_{k,\sigma} \quad \text{Annihilates an electron at site } k \text{ with spin } \sigma. \quad (2.2)$$

Alternatively, one can interpret $\hat{c}_{k,\sigma}^\dagger$ ($\hat{c}_{k,\sigma}$) as the annihilation (creation) operator for a hole at site k with spin σ . It is useful to follow the convention introduced by Yoichiro Nambu [Nam60] and group the operators in two-dimensional vectors:

$$\hat{\psi}_k^\dagger = \begin{pmatrix} \hat{c}_{k,\uparrow}^\dagger & \hat{c}_{k,\downarrow} \end{pmatrix}, \quad (2.3)$$

$$\hat{\psi}_k = \begin{pmatrix} \hat{c}_{k,\uparrow} \\ \hat{c}_{k,\downarrow}^\dagger \end{pmatrix}. \quad (2.4)$$

The resulting space is the Nambu space. The upper component represents spin up electrons, the lower component can be interpreted as spin down holes. We use hats to symbolize operators and bold face letters for matrices. Furthermore, we work with atomic units ($\hbar = e = m_e = k_B = 1$) throughout this thesis.

2.2 Nonequilibrium Green's functions

In the following chapters, we want to study the evolution of an infinite system in a nonequilibrium situation. By using nonequilibrium Green's functions, we are able to work only with a finite part of the system showing exactly the same behaviour as if it is still part of the original infinite system. The truncated infinite parts of the original system are incorporated by additional terms, which are the embedding self energies. With the resulting finite system at hand, we are able to perform numerical simulations.

But first, we need to explain the concept of the Keldysh contour and define all necessary Green's functions. An excellent comprehensive introduction for nonequilibrium Green's functions can be found in the book [SvL13]. Therefore, we restrict our explanations to a minimum. We briefly explain the concept of the Keldysh contour and define all relevant Green's functions.

2.2.1 Keldysh contour

The Keldysh contour is a valuable tool in the description of systems out of equilibrium and allows a compact and simple notation.

We define the time evolution operator $\hat{U}(t, t')$ as the solution of the equations

$$i \frac{d}{dt} \hat{U}(t, t') = \hat{H}(t) \hat{U}(t, t'), \quad (2.5)$$

$$i \frac{d}{dt'} \hat{U}(t, t') = -\hat{U}(t, t') \hat{H}(t'), \quad (2.6)$$

$$\hat{U}(t_0, t_0) = \hat{1}. \quad (2.7)$$

$\hat{U}(t, t')$ propagates the system's wave function from time t' to t and has the useful property $\hat{U}(t_1, t_2) = \hat{U}(t_1, t') \hat{U}(t', t_2)$. The expectation value of an operator is defined as

$$O(t) = \langle \hat{O}_H(t) \rangle \quad (2.8)$$

$$= \text{Tr} \{ \hat{\rho}(t_0) \hat{O}_H(t) \} \quad (2.9)$$

with the operator \hat{O} in the Heisenberg picture $\hat{O}_H(t) = \hat{U}(t_0, t) \hat{O} \hat{U}(t, t_0)$. All operators in the Heisenberg picture are labeled with a subscript H. The density

operator $\hat{\rho}(t_0)$ is defined as

$$\hat{\rho}(t_0) = \frac{e^{-\beta(\hat{H}(t_0) - \mu\hat{N})}}{\text{Tr} \left\{ e^{-\beta(\hat{H}(t_0) - \mu\hat{N})} \right\}}. \quad (2.10)$$

Further, it is useful to define the time ordering and anti-time ordering operators \hat{T} and $\hat{\bar{T}}$. They order $N + 1$ Hamilton operators \hat{H} at times $t_0 < t_1 < \dots < t_N$ chronologically or anti-chronologically and are defined as

$$\hat{T} \left\{ \hat{H}(t_{\mathcal{P}(0)}) \dots \hat{H}(t_{\mathcal{P}(N)}) \right\} = \hat{H}(t_0) \dots \hat{H}(t_N), \quad (2.11)$$

$$\hat{\bar{T}} \left\{ \hat{H}(t_{\mathcal{P}(0)}) \dots \hat{H}(t_{\mathcal{P}(N)}) \right\} = \hat{H}(t_N) \dots \hat{H}(t_0) \quad (2.12)$$

with \mathcal{P} being a permutation of the set $\{0, \dots, N\}$. Using these ordering operators allows us to write the evolution operator $\hat{U}(t, t')$ as

$$\hat{U}(t, t') = \begin{cases} \hat{T} \left\{ e^{-i \int_{t'}^t d\bar{t} \hat{H}(\bar{t})} \right\} & \text{for } t > t', \\ \hat{1} & \text{for } t = t', \\ \hat{\bar{T}} \left\{ e^{-i \int_{t'}^t d\bar{t} \hat{H}(\bar{t})} \right\} & \text{for } t < t'. \end{cases} \quad (2.13)$$

We extend the definition of the Hamilton operator to complex time arguments by

$$\hat{H}(z) = \begin{cases} \hat{H}(\text{Re}(z)) & z \text{ is real,} \\ \hat{H}(\text{Re}(z)) - \mu\hat{N} & z \text{ is complex.} \end{cases} \quad (2.14)$$

Using the extension to complex arguments, the density operator can be rewritten as

$$\hat{\rho}(t_0) = \frac{e^{-i \int_{t_0}^{t_0 - i\beta} dz' \hat{H}(z')}}{\text{Tr} \left\{ e^{-i \int_{t_0}^{t_0 - i\beta} dz' \hat{H}(z')} \right\}}. \quad (2.15)$$

Now, equation (2.8) can be reformulated as

$$O(t) = \frac{\text{Tr} \left\{ e^{-i \int_{t_0}^{t_0 - i\beta} dz' \hat{H}(z')} \hat{\bar{T}} \left\{ e^{-i \int_t^{t_0} dt' \hat{H}(t')} \right\} \hat{O} \hat{T} \left\{ e^{-i \int_{t_0}^t dt' \hat{H}(t')} \right\} \right\}}{\text{Tr} \left\{ e^{-i \int_{t_0}^{t_0 - i\beta} dz' \hat{H}(z')} \right\}}. \quad (2.16)$$

The integration path of equation (2.16) is illustrated in figure 2.1.

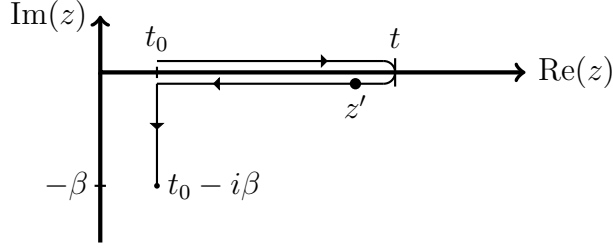


Figure 2.1: Illustration of the integration path in the complex time plane for equation (2.16) reading the integrals in the numerator from right to left. It starts at t_0 and ends at $t_0 - i\beta$. This path is called contour.

We define the contour ordering operator $\hat{\mathcal{T}}$ as the analogue ordering operator to $\hat{\mathbb{T}}$, but defined on a contour. It orders operators according to their time-arguments on the contour, later argument on the contour are shifted to the left. This allows a simpler notation of equation (2.16) as

$$O(t) = \frac{\text{Tr} \left\{ \hat{\mathcal{T}} \left\{ e^{-i \int_{t_0 \rightarrow t \rightarrow t_0 \rightarrow t_0 - i\beta} dz' \hat{H}(z')} \hat{O}(t) \right\} \right\}}{\text{Tr} \left\{ \hat{\mathcal{T}} \left\{ e^{-i \int_{t_0 \rightarrow t \rightarrow t_0 \rightarrow t_0 - i\beta} dz' \hat{H}(z')} \right\} \right\}}. \quad (2.17)$$

The operator $\hat{O}(t)$ is not the Heisenberg representation of \hat{O} , the time argument just specifies the position of the operator \hat{O} on the contour. We recall that operators in the Heisenberg picture are denoted by a subscript H. The artificial time argument of $\hat{O}(t)$ ensures that the contour ordering operator $\hat{\mathcal{T}}$ places \hat{O} correctly. The integration path in the denominator has been extended, the forward and backward branches cancel each other.

As a next step, the integration path is extended to infinity making it independent of time argument t . The operator \hat{O} can be inserted on the forward (equation (2.19)) or backward (equation (2.20)) part of the integration path:

$$O(t) = \text{Tr} \left\{ \hat{\rho}(t_0) \hat{U}(t_0, t) \hat{O} \hat{U}(t, t_0) \right\} \quad (2.18)$$

$$= \text{Tr} \left\{ \hat{\rho}(t_0) \hat{U}(t_0, t) \hat{U}(t, \infty) \hat{U}(\infty, t) \hat{O} \hat{U}(t, t_0) \right\} \quad (2.19)$$

$$= \text{Tr} \left\{ \hat{\rho}(t_0) \hat{U}(t_0, t) \hat{O} \hat{U}(t, \infty) \hat{U}(\infty, t) \hat{U}(t, t_0) \right\}. \quad (2.20)$$

The contour is therefore extended to infinity as shown in figure 2.2 and is labeled with γ . Times on the forward (upper) branch are labeled by t_- , on the backward (lower) branch by t_+ . The variable z is used for all times on the contour. The advantage of this extension is that the contour is the same for all

time arguments t of $O(t)$. This allows the following simpler notation:

$$O(t) = O(t_{\pm}), \quad (2.21)$$

$$O(z) = \frac{\text{Tr} \left\{ \hat{\mathcal{T}} \left\{ e^{-i \int_{\gamma} dz' \hat{H}(z')} \hat{O}(z) \right\} \right\}}{\text{Tr} \left\{ \hat{\mathcal{T}} \left\{ e^{-i \int_{\gamma} dz' \hat{H}(z')} \right\} \right\}}. \quad (2.22)$$

Again, the argument z of $\hat{O}(z)$ specifies the position of \hat{O} on the extended contour γ , which is the Keldysh contour. Note that $O(t_-)$ is the same as $O(t_+)$ since equations (2.19) and (2.20) are equivalent.

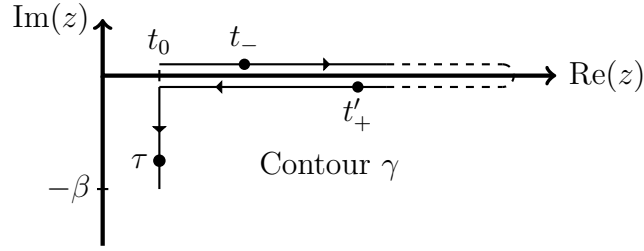


Figure 2.2: Sketch of the Keldysh contour γ in the complex time plane. Variables t_{\pm} denote times on the upper ($-$) or lower ($+$) branch of the horizontal part. The variable τ is used for times on the vertical part.

2.2.2 Definition of the nonequilibrium Green's function

We define the nonequilibrium Green's function (NEGF) as [SvL13]

$$\mathbf{G}(z, z') = -i \langle \hat{\mathcal{T}} \hat{\psi}_{\text{H}}(z) \hat{\psi}_{\text{H}}^{\dagger}(z') \rangle \quad (2.23)$$

$$= \Theta(z, z') \mathbf{G}^{>}(z, z') + \Theta(z', z) \mathbf{G}^{<}(z, z') \quad (2.24)$$

with the field operators in the Heisenberg picture: $\hat{\psi}_{\text{H}}(z) = \hat{U}(z_0, z) \hat{\psi} \hat{U}(z, z_0)$ and $\hat{\psi}_{\text{H}}^{\dagger}(z) = \hat{U}(z_0, z) \hat{\psi}^{\dagger} \hat{U}(z, z_0)$. The contour ordering operator $\hat{\mathcal{T}}$ reads for the fermionic field operators $\hat{\psi}_{\text{H}}(z)$ and $\hat{\psi}_{\text{H}}^{\dagger}(z')$ as

$$\hat{\mathcal{T}} \left\{ \hat{\psi}_{\text{H}}(z) \hat{\psi}_{\text{H}}^{\dagger}(z') \right\} = \Theta(z, z') \hat{\psi}_{\text{H}}(z) \hat{\psi}_{\text{H}}^{\dagger}(z') - \Theta(z', z) \hat{\psi}_{\text{H}}^{\dagger}(z') \hat{\psi}_{\text{H}}(z). \quad (2.25)$$

The Heaviside step function $\Theta(z, z')$ defined on the contour γ is:

$$\Theta(z, z') = \begin{cases} 1 & \text{if } z \text{ is later on the contour than } z', \\ 0 & \text{otherwise.} \end{cases} \quad (2.26)$$

The lesser and greater Green's functions for real time argument are given by

$$\mathbf{G}^<(t, t') = i \langle \hat{\psi}_H^\dagger(t') \hat{\psi}_H(t) \rangle, \quad (2.27)$$

$$\mathbf{G}^>(t, t') = -i \langle \hat{\psi}_H(t) \hat{\psi}_H^\dagger(t') \rangle. \quad (2.28)$$

The retarded and advanced Green's functions are related to $\mathbf{G}^\cong(t, t')$ via

$$\mathbf{G}^R(t, t') = \theta(t - t') [\mathbf{G}^>(t, t') - \mathbf{G}^<(t, t')], \quad (2.29)$$

$$\mathbf{G}^A(t, t') = -\theta(t' - t) [\mathbf{G}^>(t, t') - \mathbf{G}^<(t, t')]. \quad (2.30)$$

2.2.3 Nonequilibrium Green's function in the Nambu space

We will work in the Nambu space throughout the thesis. We use the creation and annihilation operators in Nambu space defined as in equations (2.3) - (2.4) and insert them into the definition of the nonequilibrium Green's function given in equation (2.23). We calculate the dyadic product of the two Nambu space vectors $\hat{\psi}_H(z)$ and $\hat{\psi}_H^\dagger(z')$ and get

$$\mathbf{G}_{kl}(z, z') = -i \begin{pmatrix} \langle \hat{\mathcal{T}} \{ \hat{c}_{k\uparrow, H}(z) \hat{c}_{l\uparrow, H}^\dagger(z') \} \rangle & \langle \hat{\mathcal{T}} \{ \hat{c}_{k\uparrow, H}(z) \hat{c}_{l\downarrow, H}(z') \} \rangle \\ \langle \hat{\mathcal{T}} \{ \hat{c}_{k\downarrow, H}^\dagger(z) \hat{c}_{l\uparrow, H}^\dagger(z') \} \rangle & \langle \hat{\mathcal{T}} \{ \hat{c}_{k\downarrow, H}^\dagger(z) \hat{c}_{l\downarrow, H}(z') \} \rangle \end{pmatrix}. \quad (2.31)$$

The contour ordering operator $\hat{\mathcal{T}}$ has been applied component-wise. The greater and lesser Green's functions are

$$\mathbf{G}_{kl}^<(t, t') = i \begin{pmatrix} \langle \hat{c}_{l\uparrow, H}^\dagger(t') \hat{c}_{k\uparrow, H}(t) \rangle & \langle \hat{c}_{l\downarrow, H}(t') \hat{c}_{k\uparrow, H}(t) \rangle \\ \langle \hat{c}_{l\uparrow, H}^\dagger(t') \hat{c}_{k\downarrow, H}(t) \rangle & \langle \hat{c}_{l\downarrow, H}(t') \hat{c}_{k\downarrow, H}(t) \rangle \end{pmatrix}, \quad (2.32)$$

$$\mathbf{G}_{kl}^>(t, t') = -i \begin{pmatrix} \langle \hat{c}_{k\uparrow, H}(t) \hat{c}_{l\uparrow, H}^\dagger(t') \rangle & \langle \hat{c}_{k\uparrow, H}(t) \hat{c}_{l\downarrow, H}(t') \rangle \\ \langle \hat{c}_{k\downarrow, H}(t) \hat{c}_{l\uparrow, H}^\dagger(t') \rangle & \langle \hat{c}_{k\downarrow, H}(t) \hat{c}_{l\downarrow, H}(t') \rangle \end{pmatrix}. \quad (2.33)$$

The retarded and advanced Green's functions for a time-independent Hamiltonian \hat{H} depend only on the time difference $t - t'$ and can be calculated as

$$\mathbf{G}_{kl}^{\text{R}}(t, t') = [\mathbf{G}_{lk}^{\text{A}}(t', t)]^\dagger \quad (2.34)$$

$$= \langle k | -i\Theta(t - t')e^{-i(t-t')\hat{\text{H}}} | l \rangle \quad (2.35)$$

$$= \int_{-\infty}^{\infty} \frac{d\omega}{2\pi} e^{-i\omega(t-t')} \mathbf{G}_{kl}^{\text{R}}(\omega), \quad (2.36)$$

$$\mathbf{G}_{kl}^{\text{R}}(\omega) = \lim_{\eta \searrow 0} \langle k | [(\omega + i\eta)\hat{\mathbf{1}} - \hat{\text{H}}]^{-1} | l \rangle. \quad (2.37)$$

This formulation is useful if one wants to calculate $\mathbf{G}^{\text{R}}(t, t')$ for systems with time-independent Hamiltonians in equilibrium. For general time-dependent Hamiltonians $\hat{\text{H}}(t)$ or for the description of relaxation processes, one can solve the Kadanoff-Baym equations [KB89] in order to obtain the nonequilibrium Green's functions. But, solving these equation is very costly since the Green's functions have two independent time arguments and one has to perform a numerical time propagation in both arguments. Nevertheless, these equations have recently been solved in various studies, for example in the works [MSSvL09, MSSvL10, UKS⁺10, TvLPS13].

2.3 Model Hamiltonian

The system is modeled using the tight-binding approach with a single orbital state for each atomic site. An introduction to the tight-binding approach can be found in the book [CS10] and in the references therein. The system is partitioned into three regions: The left lead, the central region and the right lead. Figure 2.3 explains the site numbering for the model.

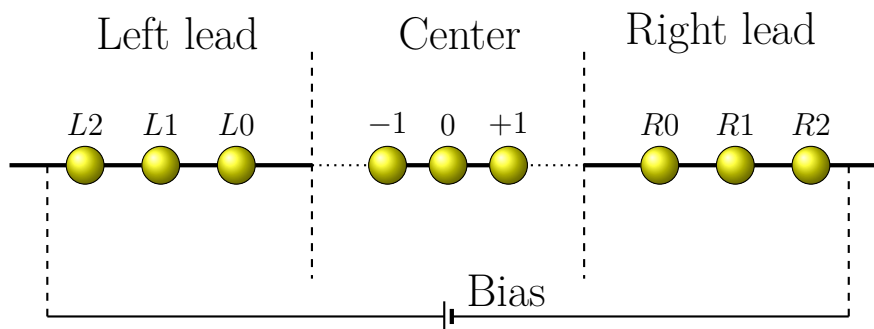


Figure 2.3: A sketch explaining the partitioning and site indices of our model with three central sites.

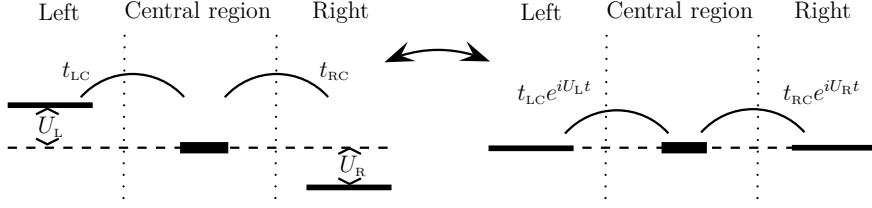


Figure 2.4: Sketch explaining the introduction of the Peierls' phases for a time-independent bias. Left: Bias is part of the lead Hamiltonians. Right: Bias is part of the hoppings. Both descriptions are equivalent.

We assume only nearest neighbor hopping in the leads and for simplicity also in the central region. The biases $U_\alpha(t)$ are chosen to be part of the hoppings and not of the lead Hamiltonians. This can be done as sketched in figure 2.4. The Coulomb interaction is neglected. We further set the temperature $T = 0$ and the Fermi level $\mu = 0$. We work in the wide-band limit throughout the thesis. In the case of normal leads, this corresponds to a constant density of states of both leads in the vicinity of the energy levels of the central region. This results in a coupling of the central region to the leads which is independent of the energy [CS10]. Such a definition is not possible for superconducting leads due to the superconducting gap, which leads to an unavoidable energy dependence of the coupling. But, we can adopt the definition for normal leads in terms of the parameters of our tight-binding model and use it for both types of leads. It is given after the introduction of the model Hamiltonian.

The Hamiltonian of the system with $2N + 1$ sites in the central region reads

$$\hat{H}(t) = \hat{H}_{\text{CC}}(t) + \hat{H}_{\text{T}}(t) + \sum_{\alpha \in \{\text{L,R}\}} \hat{H}_{\alpha\alpha} \quad (2.38)$$

with

$$\begin{aligned} \hat{H}_{\text{CC}}(t) = & \sum_{k=-N}^N \sum_{\sigma \in \{\uparrow, \downarrow\}} \varepsilon_k(t) \hat{c}_{k,\sigma}^\dagger \hat{c}_{k,\sigma} + \sum_{k=-N}^N \left(\Delta_k e^{i\chi_k} \hat{c}_{k,\uparrow}^\dagger \hat{c}_{k,\downarrow}^\dagger + H.c. \right) \\ & + \sum_{k=-N}^{N-1} \sum_{\sigma \in \{\uparrow, \downarrow\}} \left(t_{k,k+1} e^{i\gamma_{k,k+1}(t)} \hat{c}_{k,\sigma}^\dagger \hat{c}_{k+1,\sigma} + H.c. \right), \end{aligned} \quad (2.39)$$

$$\begin{aligned} \hat{H}_{\alpha\alpha} = & \sum_{k=0}^{\infty} \sum_{\sigma \in \{\uparrow, \downarrow\}} \left(t_{\alpha} \hat{c}_{\alpha k, \sigma}^{\dagger} \hat{c}_{\alpha k+1, \sigma} + H.c. \right) \\ & + \sum_{k=0}^{\infty} \left(\Delta_{\alpha} e^{i\chi_{\alpha}} \hat{c}_{\alpha k, \uparrow}^{\dagger} \hat{c}_{\alpha k, \downarrow}^{\dagger} + H.c. \right), \end{aligned} \quad (2.40)$$

$$\begin{aligned} \hat{H}_{\text{T}}(t) = & \sum_{\sigma \in \{\uparrow, \downarrow\}} \left(t_{\text{LC}} e^{i\gamma_{\text{LC}}(t)} \hat{c}_{\text{L}0, \sigma}^{\dagger} \hat{c}_{-N, \sigma} + H.c. \right) \\ & + \sum_{\sigma \in \{\uparrow, \downarrow\}} \left(t_{\text{RC}} e^{i\gamma_{\text{RC}}(t)} \hat{c}_{\text{R}0, \sigma}^{\dagger} \hat{c}_{N, \sigma} + H.c. \right). \end{aligned} \quad (2.41)$$

The Hamiltonian $\hat{H}_{\text{CC}}(t)$ allows superconductivity also on the central region, but we normally set $\Delta_k = 0$. All parameters of the model Hamiltonian are chosen real valued and non-negative. The exponents $\gamma_{k, k+1}(t)$ and $\gamma_{\alpha\text{C}}(t)$ are called Peierls' phases [SPC10] and originate from the Peierls' substitution [Pei33], which includes a vector potential into a tight-binding Hamiltonian. We assume that there is no scalar and no vector potential inside the leads, thus there are no such phases in the Hamiltonians $\hat{H}_{\alpha\alpha}$. Further, we assume that there is only an electric field between the central region and the leads, which comes from the bias $U_{\alpha}(t)$. With these assumptions, the Peierls' phases for our model are

$$\gamma_{\alpha\text{C}}(t) = \int_0^t dt' U_{\alpha}(t'), \quad (2.42)$$

$$\gamma_{k, k+1}(t) = \frac{1}{c} \int_{\vec{r}_k}^{\vec{r}_{k+1}} \vec{A}(r, t) d\vec{l}. \quad (2.43)$$

The following table lists the meaning of all parameters of the model:

Central Region	
$\varepsilon_k(t)$	on-site potential at site k
$\Delta_k e^{i\chi_k}$	pairing potential at site k
$t_{k, k+1} e^{i\gamma_{k, k+1}(t)}$	hopping elements inside C from site $k + 1$ to k
Leads	
$\Delta_{\alpha} e^{i\chi_{\alpha}}$	pairing potential, the same for all sites
t_{α}	hopping elements inside leads between nearest neighbors
Coupling	
$t_{\alpha\text{C}} e^{i\gamma_{\alpha\text{C}}(t)}$	hopping elements from C to lead α

As already stated at the beginning of the section, we will work in the wide-band limit throughout this thesis. For our model, it corresponds to $t_{\alpha} \gg$

$t_{\alpha C}, t_{k,k+1}, \varepsilon_k(t)$. In this limit, the results do not depend on t_α and $t_{\alpha C}$ separately, but on the coupling $\Gamma_\alpha = \frac{2t_{\alpha C}^2}{t_\alpha}$ [SPC10]. Hence, we will only state Γ_α in the presented results. The presence of superconductivity requires the use of the time-dependent Bogoliubov-de Gennes equation, which has the form of a Schrödinger equation in the electron-hole space. For a single particle wave function $\psi_q(k,t) = (u_q(k,t), v_q(k,t))^T$ with the site variable k , it reads

$$i \frac{d}{dt} \begin{pmatrix} u_q(k,t) \\ v_q(k,t) \end{pmatrix} = \sum_l \mathbf{H}_{kl}(t) \begin{pmatrix} u_q(l,t) \\ v_q(l,t) \end{pmatrix}, \quad (2.44)$$

$$\mathbf{H}_{kl}(t) = \begin{pmatrix} \mathbf{h}_{kl}(t) & \Delta_{kl} \\ [\Delta_{kl}]^* & [-\mathbf{h}_{kl}(t)]^* \end{pmatrix}. \quad (2.45)$$

The non-vanishing elements of $\mathbf{h}(t)$ and Δ are:

Central Region

$$\mathbf{h}_{k,k}(t) = \varepsilon_k(t), \quad (2.46)$$

$$\Delta_{k,k} = \Delta_k, \quad (2.47)$$

$$\mathbf{h}_{k,k+1}(t) = [\mathbf{h}_{k+1,k}(t)]^* = t_{k,k+1} e^{i\gamma_{k,k+1}(t)}, \quad (2.48)$$

Leads

$$\Delta_{\alpha k, \alpha k} = \Delta_\alpha e^{i\chi_\alpha}, \quad (2.49)$$

$$\mathbf{h}_{\alpha k, \alpha k+1}(t) = [\mathbf{h}_{\alpha k+1, \alpha k}(t)]^* = t_\alpha, \quad (2.50)$$

Coupling

$$\mathbf{h}_{L0, -N}(t) = [\mathbf{h}_{-N, L0}(t)]^* = t_{LC} e^{i\gamma_{LC}(t)}, \quad (2.51)$$

$$\mathbf{h}_{R0, N}(t) = [\mathbf{h}_{N, R0}(t)]^* = t_{RC} e^{i\gamma_{RC}(t)}. \quad (2.52)$$

For later use, it is convenient to define projections of $\mathbf{H}(t)$ onto the different subspaces. Using the projections, the full Hamiltonian $\mathbf{H}(t)$ as well as the nonequilibrium Green's function $\mathbf{G}(z, z')$ can be partitioned as

$$\mathbf{H}(t) = \begin{pmatrix} \mathbf{H}_{LL}(t) & \mathbf{H}_{LC}(t) & \mathbf{H}_{RL}(t) \\ \mathbf{H}_{CL}(t) & \mathbf{H}_{CC}(t) & \mathbf{H}_{CR}(t) \\ \mathbf{H}_{LR}(t) & \mathbf{H}_{RC}(t) & \mathbf{H}_{RR}(t) \end{pmatrix}, \quad (2.53)$$

$$\mathbf{G}(z, z') = \begin{pmatrix} \mathbf{G}_{LL}(z, z') & \mathbf{G}_{LC}(z, z') & \mathbf{G}_{LR}(z, z') \\ \mathbf{G}_{CL}(z, z') & \mathbf{G}_{CC}(z, z') & \mathbf{G}_{CR}(z, z') \\ \mathbf{G}_{RL}(z, z') & \mathbf{G}_{RC}(z, z') & \mathbf{G}_{RR}(z, z') \end{pmatrix}. \quad (2.54)$$

The projections $\mathbf{H}_{RL}(t)$ and $\mathbf{H}_{LR}(t)$ are zero, since there is no direct coupling between the left and the right lead. The projections $\mathbf{H}_{LL}(t)$ and $\mathbf{H}_{RR}(t)$ are time-independent. Consequently, their time argument is omitted. The hopping Hamiltonians $\mathbf{H}_{\alpha C}(t) = \mathbf{H}_{C\alpha}(t)^\dagger$ can be written as $\mathbf{H}_{\alpha C}(t) = e^{i\gamma_{\alpha C}(t)\sigma_z} \mathbf{H}_{\alpha C}$ with

σ_z being the third Pauli matrix in Nambu space. Using these properties, the partitioned Hamiltonian reads

$$\mathbf{H}(t) = \begin{pmatrix} \mathbf{H}_{LL} & e^{i\gamma_{LC}(t)\sigma_z}\mathbf{H}_{LC} & 0 \\ \mathbf{H}_{CL}e^{i\gamma_{CL}(t)\sigma_z} & \mathbf{H}_{CC}(t) & \mathbf{H}_{CR}e^{i\gamma_{CR}(t)\sigma_z} \\ 0 & e^{i\gamma_{RC}(t)\sigma_z}\mathbf{H}_{RC} & \mathbf{H}_{RR} \end{pmatrix}. \quad (2.55)$$

Most of the time, we will work with junctions containing only one central site. In these cases, we will make use of the abbreviation QD (quantum dot) instead of C. We further replace the variable $\varepsilon_0(t)$ by $\varepsilon_{\text{QD}}(t)$.

The pairing potentials for the leads can be written as $\Delta_\alpha = \xi_\alpha \Delta$. In the case of normal leads, we set $\xi_\alpha = 0$. In superconducting junctions, we always assume $\Delta_L = \Delta_R$. Consequently, we can always choose $\xi_\alpha \in \{0,1\}$. Instead of stating the values of ξ_α in our results, we will only specify the junction and introduce the following notation:

- N Normal lead,
- S Superconducting leads,
- QD Quantum dot,

and

junction type	values of ξ_α
NQDN	$\xi_L = 0, \xi_R = 0$
NQDS	$\xi_L = 0, \xi_R = 1$
SQDN	$\xi_L = 1, \xi_R = 0$
SQDS	$\xi_L = 1, \xi_R = 1$

The introduction of ξ_α allows a dimensionless representation of the problem by measuring times in units of $\hbar\Delta^{-1}$, currents in units of $\frac{e}{\hbar}\Delta$ and energies, like $U_\alpha, t_\alpha, t_{\alpha C}, \dots$, in units of Δ . Hence, all units are omitted in all simulations for any kind of junctions.

Chapter 3

Methods

There exists a large variety of approaches to quantum transport. The most popular one is the Landauer-Büttiker formula, which will be explained briefly in the next section. Since the Landauer-Büttiker formula is limited to the calculation of steady states in junctions with normal leads, it is unable to describe time-dependent phenomena or superconductivity. Another disadvantage is that it only provides access to the current and not to any other observable, like the density. Nevertheless, this approach paved the road to the theoretical description of quantum transport. Furthermore, it is a simple and valuable tool to check results in the absence of superconductivity.

The simplest method to overcome the limitations of the Landauer-Büttiker formula is to use a finite size model. Instead of dealing with infinite leads, one truncates them at some large distance to the central region. Then, one can solve the time-dependent Schrödinger equation for the finite system and calculate the observables using the propagated wave function. But, no matter how large the system was chosen, one sooner or later always sees effects of the finite size compared to an infinite system.

These effects can be avoided by working with the full infinite system. Using an embedding technique, it is possible to propagate the wave functions only in the central region. The effects of the leads are incorporated by two additional terms. This method is explained in detail in section 3.2. We will use it for most of the calculations in the thesis.

Instead of propagating wave functions, one can also obtain the observables from the nonequilibrium Green's functions. There are various ways to calculate the nonequilibrium Green's functions. We will explain one possibility to calculate their large time behaviour in section 3.3 and use it afterward. Unfortunately, it does not provide access to the transient dynamics.

3.1 Landauer-Büttiker formula

The most common approach to quantum transport with non-interacting electrons is the Landauer-Büttiker formula, which is based on works by Rolf Landauer [Lan57] and Markus Büttiker [Büt86]. It reads

$$I = \frac{2e}{h} \int_{-\infty}^{\infty} dE T(E) (f_L(E) - f_R(E)), \quad (3.1)$$

with the Fermi functions of the leads $f_\alpha(E) = \frac{1}{1+e^{\beta(E-\mu_\alpha)}}$ and the transmission probability $T(E)$ as function of energy. The bias enters via the shifted chemical potentials μ_α of the leads. The factor 2 in front of the integral accounts for the spin degeneracy. It has been extended by Meir and Wingreen to calculate the current through an interacting region [MW92]. The transmission probability $T(E)$ is typically calculated numerically, for example with density functional theory for realistic systems like molecules as it was done in the work [ZG10]. The Landauer-Büttiker formula was developed to describe transport through junctions with normal-conducting leads, but can be generalized to hybrid junctions, having one normal and one superconducting lead [BTK82].

The Landauer-Büttiker formula implicitly assumes that the systems evolves towards a steady state upon switching on the bias. This assumption is not always justified, for example in junctions with superconducting leads where the current can oscillate due to the AC Josephson effect. Nevertheless, it is often a helpful tool. For our model system, but with normal leads, it gives the correct steady state value for the current. Hence, it was used during the code development for consistency checks. Very recently, a time-dependent version of the Landauer-Büttiker formula was published [TvLPS13]. This novel formula provides access to the full transient dynamics of the system upon switching on the bias.

3.2 Time propagation of wave functions

The second approach, that we want to explain in detail, is the time propagation of wave functions. The idea of this method is to solve the time-dependent Schrödinger equation starting from initial single particle wave functions ψ_q^0 at time $t = 0$. This propagation scheme was invented by Kurth *et al.* [KSA+05] and later generalized for superconducting leads by Stefanucci *et al.* [SPC10]. The original version of the algorithm has been used in various studies of time-dependent quantum transport, like the effects of bound states [KKS08, KSK09], a time resolved picture of the Coulomb blockade [KSK+10], multistabilities for an interacting quantum dot [UKS+10, KUS+12] and classical nuclear motion [VSA06, KVS14]. To the best of our knowledge, the generalization for superconducting leads [SPC10] has not yet been used for further studies.

3.2.1 Ground state calculation

In order to carry out a time propagation of wave functions, we first need to calculate the initial wave functions. We start in the ground state and want to solve the time-independent Schrödinger equation

$$\begin{pmatrix} \mathbf{H}_{LL} & \mathbf{H}_{LC} & 0 \\ \mathbf{H}_{CL} & \mathbf{H}_{CC}(0) & \mathbf{H}_{CR} \\ 0 & \mathbf{H}_{RC} & \mathbf{H}_{RR} \end{pmatrix} \begin{pmatrix} \psi_L \\ \psi_C \\ \psi_R \end{pmatrix} = E \begin{pmatrix} \psi_L \\ \psi_C \\ \psi_R \end{pmatrix} \quad (3.2)$$

for all possible energies E . The solutions of equation (3.2) will then be used as initial values for the following time propagation.

In the literature, three different techniques for solving equation (3.2) have been proposed:

1. The work [KSA+05] suggests to diagonalize the retarded Green's functions $\mathbf{G}_{CC}^R(\omega)$. But, the normalization of the resulting wave functions has to be done separated when using this approach. Further, the calculation of $\mathbf{G}_{CC}^R(\omega)$ requires to take the limit $\lim_{\eta \searrow 0}$, which can be challenging.
2. An alternative approach is to use the Lippmann-Schwinger equation from scattering theory [Nit08]. But, it is restricted to junctions with identical leads, hence NQDS and SQDN junctions cannot be calculated in this way.
3. A method, which is superior for our application, has been suggested in the work [SPC10]. It is similar to the procedure of calculating the wave

function which is scattered at a potential step. This is our method of choice and we will explain it in the following paragraphs.

The solutions of equation (3.2) can be separated into bound and scattering states. The first decay exponentially in both leads, the latter do not. As shown in figure 3.1, there is a continuum of scattering states. We use an equidistant grid in momentum space to approximate it. In the following two paragraphs, we will explain how to calculate all three types of wave functions. We start with the scattering wave functions.

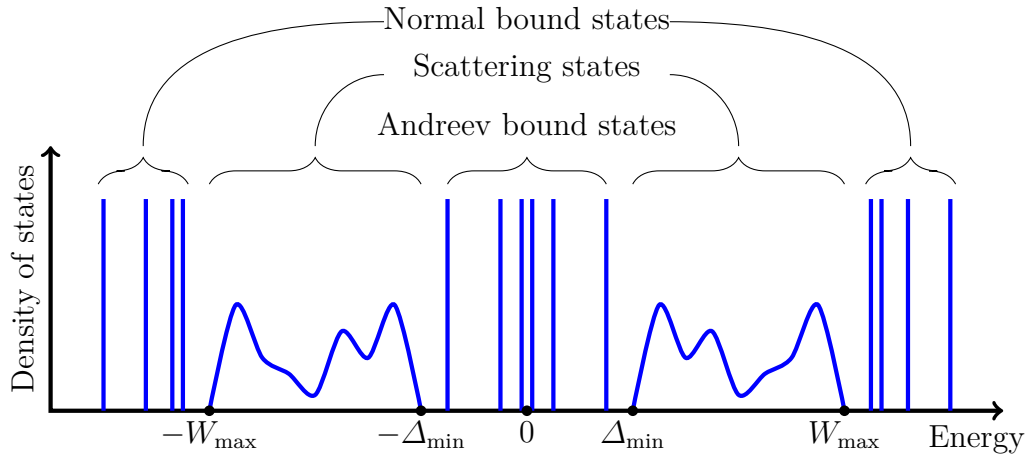


Figure 3.1: Sketch of the density of states in the central region with normal bound, Andreev bound and scattering states for a Josephson junction. $\Delta_{\min} = \min\{\Delta_L, \Delta_R\}$, $W_{\max} = \max\{\sqrt{4t_L^2 + \Delta_L^2}, \sqrt{4t_R^2 + \Delta_R^2}\}$.

Scattering states

We will use a method that is similar to the scattering of a wave functions at a potential step, which can be found in almost every book on quantum mechanics.

We first solve the stationary Schrödinger equation for the isolated leads, which are assumed to be periodic in both directions. The Bloch ansatz for the wave functions in the leads is

$$\psi_{p,L}(Lk) = \psi_{p,L}(L0)e^{-ipk}, \quad (3.3)$$

$$\psi_{p,R}(Rk) = \psi_{p,R}(R0)e^{ipk} \quad (3.4)$$

with $p \in [0, 2\pi)$, normalized such that $\|\psi_{p,\alpha}(\alpha k)\|^2 = 1$ for all sites k .

The ansatz (3.3) and (3.4) gives for the fictitious extended leads:

$$\begin{aligned} \begin{pmatrix} 0 & \Delta_\alpha e^{i\chi_\alpha} \\ \Delta_\alpha e^{-i\chi_\alpha} & 0 \end{pmatrix} \psi_{p,\alpha}(\alpha k) + \begin{pmatrix} t_\alpha & 0 \\ 0 & -t_\alpha \end{pmatrix} \psi_{p,\alpha}(\alpha k - 1) \\ + \begin{pmatrix} t_\alpha & 0 \\ 0 & -t_\alpha \end{pmatrix} \psi_{p,\alpha}(\alpha k + 1) = E \psi_{p,\alpha}(\alpha k) \end{aligned} \quad (3.5)$$

and

$$\begin{pmatrix} t_\alpha e^{ip} + t_\alpha e^{-ip} & \Delta_\alpha e^{i\chi_\alpha} \\ \Delta_\alpha e^{-i\chi_\alpha} & -t_\alpha e^{-ip} - t_\alpha e^{ip} \end{pmatrix} \psi_{p,\alpha}(\alpha k) = E_{p,\alpha} \psi_{p,\alpha}(\alpha k). \quad (3.6)$$

Note that the solutions $\psi_{p,\alpha}$ are not eigenfunctions to $\mathbf{H}_{\alpha\alpha}$, since here the leads are assumed to be infinite in both directions. The propagation direction of a wave function can be determined by the sign of its Fermi velocity $v = \partial_p E_{p,\alpha} = 2t_\alpha \cos(p) \langle \psi_{p,\alpha} | \boldsymbol{\sigma}_z | \psi_{p,\alpha} \rangle$ with $\boldsymbol{\sigma}_z$ being the third Pauli matrix in Nambu space. Wave functions in the direction towards the central region will be labeled $\psi_{p,\alpha}^{(\text{in})}$, the others by $\psi_{p,\alpha}^{(\text{out})}$.

We now select an incoming wave function $\psi_{p,\alpha}^{(\text{in})}$ and calculate all outgoing wave functions $\psi_{E_{p,\alpha},\alpha'}^{(\text{out})}$ with the same energy $E_{p,\alpha}$. One therefore reformulates equation (3.6) into an eigenvalue problem for $e^{ip'}$:

$$\begin{aligned} \left(\frac{1}{t_{\alpha'}} \begin{pmatrix} E_{p,\alpha} & -\Delta_{\alpha'} e^{i\chi_{\alpha'}} \\ \Delta_{\alpha'} e^{-i\chi_{\alpha'}} & -E_{p,\alpha} \end{pmatrix} \quad -\mathbb{1} \right) \begin{pmatrix} \psi_{E_{p,\alpha},\alpha'}(\alpha' k) \\ e^{-ip'} \psi_{E_{p,\alpha},\alpha'}(\alpha' k) \end{pmatrix} \\ = e^{ip'} \begin{pmatrix} \psi_{E_{p,\alpha},\alpha'}(\alpha' k) \\ e^{-ip'} \psi_{E_{p,\alpha},\alpha'}(\alpha' k) \end{pmatrix}. \end{aligned} \quad (3.7)$$

This gives four solutions for every lead, two propagating to the left and two to the right. In the case of real p' , outgoing solutions can be identified again using the sign of the Fermi velocity. In the case of complex p' , we consider outgoing waves as the ones which decay exponentially with increasing distance from the central region, i.e. $\text{Im}(p') > 0$ for the right and $\text{Im}(p') < 0$ for the left lead.

The wave function for the full system can then be constructed as

$$\psi_p = \begin{cases} \psi_{p,\alpha}^{(\text{in})} + \sum_m C_{\alpha,m} \psi_{E_{p,\alpha},\alpha,m}^{(\text{out})} & \text{Lead } \alpha \in \{\text{L}, \text{R}\}, \\ \psi_C & \text{Central region,} \\ \sum_m C_{\alpha',m} \psi_{E_{p,\alpha},\alpha',m}^{(\text{out})} & \text{Lead } \alpha' \neq \alpha. \end{cases} \quad (3.8)$$

We omit the index $E_{p,\alpha}$ from now on in order to simplify the notation. Inserting the ansatz (3.8) into equation (3.2) gives a set of equations with $2(2N + 3)$

unknown variables:

$$\mathcal{A}(E_{p,L/R}) \begin{pmatrix} C_{L,1} \\ C_{L,2} \\ \psi_C \\ C_{R,1} \\ C_{R,2} \end{pmatrix} = \begin{pmatrix} (E_{p,L}\mathbb{1} - \mathbf{H}_{LL})\psi_{p,L}^{(in)} \\ -\mathbf{H}_{CL}\psi_{p,L}^{(in)} \\ 0 \end{pmatrix} \text{ or } \begin{pmatrix} 0 \\ -\mathbf{H}_{CR}\psi_{p,R}^{(in)} \\ (E_{p,R}\mathbb{1} - \mathbf{H}_{RR})\psi_{p,R}^{(in)} \end{pmatrix}, \quad (3.9)$$

where

$$\mathcal{A}(E) = \begin{pmatrix} (\mathbf{H}_{LL} - E\mathbb{1})[\psi_{E,L,1}^{(out)}\psi_{E,L,2}^{(out)}] & \mathbf{H}_{LC} & \\ \mathbf{H}_{CL}[\psi_{E,L,1}^{(out)}\psi_{E,L,2}^{(out)}] & \mathbf{H}_{CC}(0) - E\mathbb{1} & \mathbf{H}_{CR}[\psi_{E,R,1}^{(out)}\psi_{E,R,2}^{(out)}] \\ & \mathbf{H}_{RC} & (\mathbf{H}_{RR} - E\mathbb{1})[\psi_{E,R,1}^{(out)}\psi_{E,R,2}^{(out)}] \end{pmatrix}. \quad (3.10)$$

Here, we used the notation $[\psi_{E,\alpha,1}^{(out)}\psi_{E,\alpha,2}^{(out)}]$ for the matrix formed of $\psi_{E,\alpha,1}^{(out)}$ and $\psi_{E,\alpha,2}^{(out)}$. We reduce the number of equations to the number of unknown variables by applying a projection operator on both sides:

$$\mathcal{B}(E_{p,L/R}) = \begin{pmatrix} \mathbf{P}_{L0} & & \\ & \mathbb{1} & \\ & & \mathbf{P}_{R0} \end{pmatrix} \mathcal{A}(E_{p,L/R}) \quad (3.11)$$

with

$$\mathcal{B}(E_{p,L/R}) \begin{pmatrix} C_{L,1} \\ C_{L,2} \\ \psi_C \\ C_{R,1} \\ C_{R,2} \end{pmatrix} = \begin{pmatrix} \mathbf{P}_{L0}(E_{p,L}\mathbb{1} - \mathbf{H}_{LL})\psi_{p,L}^{(in)} \\ -\mathbf{H}_{CL}\psi_{p,L}^{(in)} \\ 0 \end{pmatrix} \text{ or } \begin{pmatrix} 0 \\ -\mathbf{H}_{CR}\psi_{p,R}^{(in)} \\ \mathbf{P}_{R0}(E_{p,R}\mathbb{1} - \mathbf{H}_{RR})\psi_{p,R}^{(in)} \end{pmatrix} \quad (3.12)$$

where $\mathbf{P}_{\alpha k}$ is the projection operator of site αk . Inserting the solution into the ansatz in equation (3.8) gives the wave function ψ_p for the whole system which is a solution of the full stationary Schrödinger equation and solves the linear equation (3.9) with the matrix $\mathcal{A}(E)$.

Bound states

Bound states have discrete energies, which are not known a priori. But one knows at least that Andreev bound states are inside the gap with energies $|E_{\text{ABS}}| \leq \min\{\Delta_L, \Delta_R\}$ and normal bound states are typically above or below

the band continuum. Since our systems are always chosen such that they never have normal bound states, we will focus on the Andreev bound states. But, normal bound states can be treated on the same footing.

The first step is to calculate the energy of the bound states. Bound states are located at the poles of the retarded Green's functions. Taking the inverse leads to the following condition for bound states:

$$0 \stackrel{!}{=} \det \left\{ \mathbf{G}_{\text{CC}}^{\text{R}}(E)^{-1} \right\} \quad (3.13)$$

$$= \lim_{\eta \searrow 0} \det \left\{ (E + i\eta)\mathbf{1} - \mathbf{H}_{\text{CC}}(0) - \Sigma_{\text{L}}^{\text{R}}(E) - \Sigma_{\text{R}}^{\text{R}}(E) \right\}. \quad (3.14)$$

The embedding self-energies $\Sigma_{\alpha}^{\text{R/A}}(E)$ can be calculated analytically [PSC09]:

$$\Sigma_{\alpha}^{\text{R/A}}(E) = \lim_{\eta \searrow 0} \begin{pmatrix} \tilde{m}_{\alpha}(E \pm i\eta) & \tilde{d}_{\alpha}(E \pm i\eta)e^{i\chi_{\alpha}} \\ \tilde{d}_{\alpha}(E \pm i\eta)e^{-i\chi_{\alpha}} & \tilde{m}_{\alpha}(E \pm i\eta) \end{pmatrix}, \quad (3.15)$$

$$\tilde{m}_{\alpha}(z) = z \frac{t_{\alpha\text{C}}^2 \sqrt{\Delta_{\alpha}^2 - z^2} - \sqrt{\Delta_{\alpha}^2 - z^2 + 4t_{\alpha}^2}}{2t_{\alpha}^2 \sqrt{\Delta_{\alpha}^2 - z^2}}, \quad (3.16)$$

$$\tilde{d}_{\alpha}(z) = \Delta_{\alpha} \frac{t_{\alpha\text{C}}^2 \sqrt{z^2 - \Delta_{\alpha}^2} - \sqrt{z^2 - \Delta_{\alpha}^2}}{2t_{\alpha}^2 \sqrt{z^2 - \Delta_{\alpha}^2}}. \quad (3.17)$$

The energy of Andreev bound states in the case of a single normal central site coupled to two superconducting leads can be obtained by solving

$$0 \stackrel{!}{=} \det \left\{ \mathbf{G}_{\text{CC}}^{\text{R}}(E)^{-1} \right\} \quad (3.18)$$

$$= \lim_{\eta \searrow 0} \left\{ (E + i\eta - \tilde{m}_{\text{L}}(E + i\eta) - \tilde{m}_{\text{R}}(E + i\eta))^2 - \varepsilon_{\text{QD}}^2 \right. \\ \left. - \left(\tilde{d}_{\text{L}}(E + i\eta)e^{i\chi_{\text{L}}} + \tilde{d}_{\text{R}}(E + i\eta)e^{i\chi_{\text{R}}} \right) \right. \\ \left. \cdot \left(\tilde{d}_{\text{L}}(E + i\eta)e^{-i\chi_{\text{L}}} + \tilde{d}_{\text{R}}(E + i\eta)e^{-i\chi_{\text{R}}} \right) \right\}. \quad (3.19)$$

This can be done numerically using standard root-finding algorithms. The result coincides with the formula given in [SPC10] for the wide-band limit. For larger systems, one solves equation (3.14) numerically using again root-finding algorithms.

The second step is to calculate the wave function. The ansatz for the wave function of a bound state is the same as for a scattering state, but without an incoming wave function:

$$\psi_{\text{BS}} = \begin{cases} \sum_m C_{\alpha,m} \psi_{\alpha,m}^{(\text{out})} & \text{Lead } \alpha, \\ \psi_{\text{C}} & \text{Central region} \end{cases} \quad (3.20)$$

with

$$\psi_{L,m}^{(\text{out})}(Lk) = \psi_{L,m}^{(\text{out})}(L0)e^{-i\text{Re}(p_{L,m})k + \text{Im}(p_{L,m})k}, \quad (3.21)$$

$$\psi_{R,m}^{(\text{out})}(Rk) = \psi_{R,m}^{(\text{out})}(R0)e^{+i\text{Re}(p_{R,m})k - \text{Im}(p_{R,m})k}. \quad (3.22)$$

All outgoing wave functions $\psi_{\alpha,m}^{(\text{out})}$ are exponentially decaying with increasing distance from the central region and have the same energy E_{BS} . Inserting this ansatz into the stationary Schrödinger equation of the full system gives

$$\mathcal{A}(E_{\text{BS}}) \begin{pmatrix} C_{L,1} \\ C_{L,2} \\ \psi_C \\ C_{R,1} \\ C_{R,2} \end{pmatrix} = 0 \quad \text{respectively} \quad \mathcal{B}(E_{\text{BS}}) \begin{pmatrix} C_{L,1} \\ C_{L,2} \\ \psi_C \\ C_{R,1} \\ C_{R,2} \end{pmatrix} = 0 \quad (3.23)$$

with $\mathcal{A}(E_{\text{BS}})$ and $\mathcal{B}(E_{\text{BS}})$ of equations (3.10) - (3.11). The physically meaningful solutions are the non-trivial ones. They can be obtained by calculating the kernel $\ker\{\mathcal{A}(E_{\text{BS}})\}$ or $\ker\{\mathcal{B}(E_{\text{BS}})\}$. It is easier to calculate the latter since $\mathcal{B}(E_{\text{BS}})$ has a finite number of rows and columns. Applying the singular value decomposition to the matrix $\mathcal{B}(E)$ gives

$$\mathcal{B}(E_{\text{BS}}) = \mathbf{U}\mathbf{\Sigma}\mathbf{V}^\dagger \quad (3.24)$$

with unitary matrices \mathbf{U}, \mathbf{V} and a diagonal matrix $\mathbf{\Sigma}$. The kernel of $\mathcal{B}(E_{\text{BS}})$ reads

$$\ker\{\mathcal{B}(E_{\text{BS}})\} = \{\mathbf{V}(:, i) \in \mathbb{C}^{4N+6} : \mathbf{\Sigma}(i, i) = 0, \mathcal{B}(E_{\text{BS}}) = \mathbf{U}\mathbf{\Sigma}\mathbf{V}^\dagger\}. \quad (3.25)$$

The resulting wave functions have to be normalized such that $\langle \psi_{\text{BS}} | \psi_{\text{BS}} \rangle = 1$. This can be done using the explicit form of equations (3.20) - (3.22), which gives the norm as the sum of several geometric series.

Instead of searching for the roots in equation (3.14), one can also solve

$$0 \stackrel{!}{=} \det\{\mathcal{B}(E)\}. \quad (3.26)$$

This formulation has the advantage that one does not need to take the limit $\lim_{\eta \searrow 0}$. Thus, it is used in the numerical implementation. The search for roots can be done using a derivative-free root-finding algorithm. Figure 3.2 shows an example of the calculated Andreev bound states' energy depending on the phase difference χ_0 for a SQDS junction.

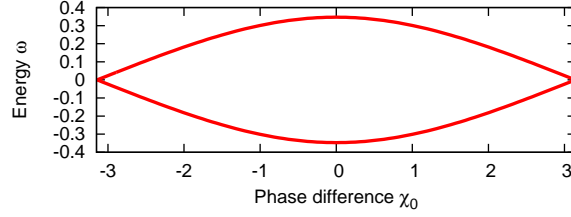


Figure 3.2: Dependence of the Andreev bound states on the phase difference $\chi_0 = \chi_R - \chi_L$ for a SQDS junction. The parameters are: $\Gamma_\alpha = 0.5$, $\varepsilon_{\text{QD}} = 0$.

3.2.2 Time propagation

Having now all single particle wave functions in the ground state at time $t = 0$ at hand, we want to propagate them in time. Since the equations are the same for all single particle wave functions, we use the generic notation ψ for all wave functions, scattering as well as bound states.

The time-dependent Schrödinger equation reads

$$i \frac{d}{dt} \begin{pmatrix} \psi_L(t) \\ \psi_C(t) \\ \psi_R(t) \end{pmatrix} = \begin{pmatrix} \mathbf{H}_{LL} & \mathbf{H}_{LC}(t) & 0 \\ \mathbf{H}_{CL}(t) & \mathbf{H}_{CC}(t) & \mathbf{H}_{CR}(t) \\ 0 & \mathbf{H}_{RC}(t) & \mathbf{H}_{RR} \end{pmatrix} \begin{pmatrix} \psi_L(t) \\ \psi_C(t) \\ \psi_R(t) \end{pmatrix}. \quad (3.27)$$

The solutions in the leads are for $t > 0$ [Ull12]

$$\psi_\alpha(t) = i \mathbf{g}_\alpha^R(t,0) \psi_\alpha(0) + \int_0^t dt' \mathbf{g}_\alpha^R(t,t') \mathbf{H}_{\alpha C}(t') \psi_C(t'), \quad (3.28)$$

where $\mathbf{g}_\alpha^R(t,t')$ is the retarded Green's function of the isolated semi-infinite lead α . This yields for the central region

$$i \partial_t \psi_C(t) = \mathbf{H}_{CC}(t) \psi_C(t) + \sum_{\alpha \in \{L,R\}} i \mathbf{H}_{C\alpha}(t) \mathbf{g}_\alpha^R(t,0) \psi_\alpha(0) + \sum_{\alpha \in \{L,R\}} \int_0^t dt' \mathbf{H}_{C\alpha}(t) \mathbf{g}_\alpha^R(t,t') \mathbf{H}_{\alpha C}(t') \psi_C(t'). \quad (3.29)$$

We want to derive and solve a discretized version of this equation on an equidistant grid with $t_m = m\Delta t$ and $\delta = 0.5\Delta t$. The derivation is based on the work [SPC10], which is the origin of the propagation algorithm. We use a second order Crank-Nicolson scheme to solve the time-dependent Schrödinger equation:

$$\left(\mathbb{1} + i\delta \mathbf{H}^{(m)} \right) \psi^{(m+1)} = \left(\mathbb{1} - i\delta \mathbf{H}^{(m)} \right) \psi^{(m)} \quad (3.30)$$

with $\psi_C^{(m)} = \psi_C(t_m)$ and $\mathbf{H}^{(m)} = \frac{1}{2} (\mathbf{H}(t_m) + \mathbf{H}(t_{m+1}))$. This gives

$$\begin{aligned} (\mathbb{1} + i\delta\mathbf{H}_{CC}^{(m)}) \psi_C^{(m+1)} &= (\mathbb{1} - i\delta\mathbf{H}_{CC}^{(m)}) \psi_C^{(m)} \\ &\quad - i\delta \sum_{\alpha \in \{L,R\}} \mathbf{H}_{C\alpha}^{(m)} (\psi_\alpha^{(m+1)} + \psi_\alpha^{(m)}), \end{aligned} \quad (3.31)$$

$$\begin{aligned} (\mathbb{1} + i\delta\mathbf{H}_{\alpha\alpha}) \psi_\alpha^{(m+1)} &= (\mathbb{1} - i\delta\mathbf{H}_{\alpha\alpha}) \psi_\alpha^{(m)} \\ &\quad - i\delta\mathbf{H}_{\alpha C}^{(m)} (\psi_C^{(m+1)} + \psi_C^{(m)}). \end{aligned} \quad (3.32)$$

If we assume that $\mathbf{H}_{\alpha\alpha}$ is bounded and δ sufficiently small, then $\mathbb{1} - i\delta\mathbf{H}_{\alpha\alpha}$ and $[\mathbb{1} + i\delta\mathbf{H}_{\alpha\alpha}]^{-1}$ commute. The fraction of both is then a well-defined object since numerator and the inverse of the denominator commute and we can reformulate the wave function in the leads as

$$\psi_\alpha^{(m+1)} = \frac{\mathbb{1} - i\delta\mathbf{H}_{\alpha\alpha}}{\mathbb{1} + i\delta\mathbf{H}_{\alpha\alpha}} \psi_\alpha^{(m)} - i\delta \frac{\mathbb{1}}{\mathbb{1} + i\delta\mathbf{H}_{\alpha\alpha}} \mathbf{H}_{\alpha C}^{(m)} (\psi_C^{(m)} + \psi_C^{(m+1)}) \quad (3.33)$$

$$\begin{aligned} &= \left(\frac{\mathbb{1} - i\delta\mathbf{H}_{\alpha\alpha}}{\mathbb{1} + i\delta\mathbf{H}_{\alpha\alpha}} \right)^{m+1} \psi_\alpha^{(0)} \\ &\quad - i\delta \sum_{k=0}^m \frac{(\mathbb{1} - i\delta\mathbf{H}_{\alpha\alpha})^k}{(\mathbb{1} + i\delta\mathbf{H}_{\alpha\alpha})^{k+1}} \mathbf{H}_{\alpha C}^{(m-k)} (\psi_C^{(m+1-k)} + \psi_C^{(m-k)}). \end{aligned} \quad (3.34)$$

Inserting this result into equation (3.31) gives the final equation [SPC10]:

$$(\mathbb{1} + i\delta\mathbf{H}_{\text{eff}}^{(m)}) \psi_C^{(m+1)} = (\mathbb{1} - i\delta\mathbf{H}_{\text{eff}}^{(m)}) \psi_C^{(m)} + \sum_{\alpha \in \{L,R\}} (S_\alpha^{(m)} + M_\alpha^{(m)}) \quad (3.35)$$

with

$$\mathbf{H}_{\text{eff}}^{(m)} = \frac{1}{2} (\mathbf{H}_{CC}(t_m) + \mathbf{H}_{CC}(t_{m+1})) - i\delta \sum_{\alpha \in \{L,R\}} \mathbf{z}_\alpha^{(m)} \mathbf{Q}_\alpha^{(0)} (\mathbf{z}_\alpha^{(m)})^\dagger, \quad (3.36)$$

$$S_\alpha^{(m)} = -2i\delta \mathbf{z}_\alpha^{(m)} \mathbf{H}_{C\alpha} \frac{(\mathbb{1} - i\delta\mathbf{H}_{\alpha\alpha})^m}{(\mathbb{1} + i\delta\mathbf{H}_{\alpha\alpha})^{m+1}} \psi_\alpha^{(0)}, \quad (3.37)$$

$$M_\alpha^{(m)} = -\delta^2 \sum_{j=0}^{m-1} \mathbf{z}_\alpha^{(m)} (\mathbf{Q}_\alpha^{(m-j)} + \mathbf{Q}_\alpha^{(m-j-1)}) (\mathbf{z}_\alpha^{(j)})^\dagger (\psi_C^{(j)} + \psi_C^{(j+1)}), \quad (3.38)$$

$$\mathbf{Q}_\alpha^{(m)} = \mathbf{H}_{C\alpha} \frac{(\mathbb{1} - i\delta\mathbf{H}_{\alpha\alpha})^m}{(\mathbb{1} + i\delta\mathbf{H}_{\alpha\alpha})^{m+1}} \mathbf{H}_{\alpha C}, \quad (3.39)$$

$$\mathbf{z}_\alpha^{(m)} = \frac{1}{2} (e^{i\gamma_{C\alpha}(t_m)\sigma_z} + e^{i\gamma_{C\alpha}(t_{m+1})\sigma_z}). \quad (3.40)$$

In the above equations, σ_z is the third Pauli matrix. The calculation of the embedding matrices $\mathbf{Q}_\alpha^{(m)}$ is explained in the appendix A.2. We mention that

only $\mathbf{Q}_\alpha^{(0)}$ has to be calculated iteratively. The equations for all other matrices $\mathbf{Q}_\alpha^{(m)}$, $m > 0$ can be transformed into a system of normal linear equation which strongly reduces the computational cost.

The additional terms $S_\alpha^{(m)}$ and $M_\alpha^{(m)}$ are called source and memory term. They incorporate the effects of the two leads. The terms can be interpreted as indicated in table 3.1.

	name	interpretation (particle movement)
$S_\alpha^{(m)}$	source term	lead $\alpha \rightarrow$ central region
$M_\alpha^{(m)}$	memory term	central region \rightarrow lead $\alpha \rightarrow$ central region

Table 3.1: Naming and interpretation of the additional terms $S_\alpha^{(m)}$ and $M_\alpha^{(m)}$ in the equation (3.35).

The source term $S_\alpha^{(m)}$ has to be reformulated for the numerical evaluation, see appendix A.3 for details. The final result is

$$S_\alpha^{(m)} = \begin{cases} -\frac{2i\delta}{1+i\delta E} \mathbf{z}_\alpha^{(0)} \left(\mathbf{H}_{C\alpha} \psi_\alpha^{(0)} + i\delta \mathbf{Q}_\alpha^{(0)} \psi_C^{(0)} \right), & m = 0, \\ \frac{1-i\delta E}{1+i\delta E} \frac{\mathbf{z}_\alpha^{(m)}}{\mathbf{z}_\alpha^{(m-1)}} S_\alpha^{(m-1)} \\ \quad + \frac{2\delta^2}{1+i\delta E} \mathbf{z}_\alpha^{(m)} \left(\mathbf{Q}_\alpha^{(m)} + \mathbf{Q}_\alpha^{(m-1)} \right) \psi_C^{(0)}, & m > 0. \end{cases} \quad (3.41)$$

In the above equation, E is the associated ground state energy of the wave function $\psi^{(0)}$.

3.2.3 Calculation of observables

The final step of the presented method is the calculation of the observables using the propagated wave functions. We denote by $\psi_p(k,t)$ all scattering states constructed out of incoming wave functions with momentum p , with ε_p being the ground state energy of $\psi_p(k,t)$. The wave functions are split up into their upper and lower components as $\psi_p(k,t) = (u_p(k,t), v_p(k,t))^T$. The integration over the momentum p is done using an equidistant grid. We enumerate the bound states with an superindex m , $\varepsilon_{\text{BS}}^{(m)}$ is again the corresponding ground state energy. We obtain the following expressions for the density and current:

$$n_k(t) = \sum_{\sigma \in \{\uparrow, \downarrow\}} \langle \hat{c}_{k\sigma, \text{H}}^\dagger(t) \hat{c}_{k\sigma, \text{H}}(t) \rangle \quad (3.42)$$

$$= \int_0^{2\pi} dp \left(f^<(\varepsilon_p) |u_p(k,t)|^2 - f^>(\varepsilon_p) |v_p(k,t)|^2 \right) \quad (3.43)$$

$$+ \sum_{m=1}^{\# \text{BS}} \left(f^<(\varepsilon_{\text{BS}}^{(m)}) |u_{\text{BS}}^{(m)}(k,t)|^2 - f^>(\varepsilon_{\text{BS}}^{(m)}) |v_{\text{BS}}^{(m)}(k,t)|^2 \right),$$

$$I_{kl}(t) = -i \sum_{\sigma \in \{\uparrow, \downarrow\}} \left(t_{kl} e^{i\gamma_{kl}(t)} \langle \hat{c}_{k\sigma, \text{H}}^\dagger(t) \hat{c}_{l\sigma, \text{H}}(t) \rangle - \text{H.c.} \right) \quad (3.44)$$

$$= 2\text{Im} \left\{ t_{kl} e^{i\gamma_{kl}(t)} \left[\int_0^{2\pi} dp \left(f^<(\varepsilon_p) u_p(k,t) [u_p(l,t)]^* \right. \right. \right. \quad (3.45)$$

$$\left. \left. \left. - f^>(\varepsilon_p) [v_p(k,t)]^* v_p(l,t) \right) \right. \right. \left. \left. + \sum_{m=1}^{\# \text{BS}} \left(f^<(\varepsilon_{\text{BS}}^{(m)}) u_{\text{BS}}^{(m)}(k,t) [u_{\text{BS}}^{(m)}(l,t)]^* \right. \right. \right. \left. \left. \left. - f^>(\varepsilon_{\text{BS}}^{(m)}) [v_{\text{BS}}^{(m)}(k,t)]^* v_{\text{BS}}^{(m)}(l,t) \right) \right] \right\}$$

with the Fermi functions $f^<(\omega) = [1 + \exp(\beta\omega)]^{-1}$ and $f^>(\omega) = f^<(\omega) - 1$. We point out that our system has a different continuity equation due to superconductivity [SPC10]:

$$\frac{d}{dt} n_k(t) = \sum_l I_{kl}(t) - 4\text{Im} \left[\Delta_k e^{-i\chi_k} \langle \hat{c}_{k\downarrow, \text{H}}(t) \hat{c}_{k\uparrow, \text{H}}(t) \rangle \right]. \quad (3.46)$$

3.2.4 Efficient numerical implementation

In the course of this thesis, we want to calculate current-voltage characteristics for junctions in various situations. Therefore, the propagation time has to be chosen large enough such that convergence for the time averaged currents and densities is achieved. The results presented later often require 10^5 up to 10^6 propagation steps. Thus, it is essential and of great importance to have an efficient numerical implementation. The code was written in C++ using the library FLENS¹ [Leh08] as the base for all numerical linear algebra.

The first step is to reduce the number of propagated wave functions. We will always work in the wide-band limit, i.e. we assume that $t_\alpha \gg t_{\alpha C}, t_{kl}$ ($k, l \in C$). This allows us to propagate only wave functions with an energy inside a certain range $[-\Lambda, \Lambda]$ since wave functions outside this windows do not contribute much to observables of the central region. The energy cut-off Λ is typically chosen an order of magnitude larger than all other parameters of the system like $\Gamma_\alpha, U_\alpha, \Delta_\alpha, \dots \ll \Lambda$. Exploiting the fact that wave functions with $\varepsilon_p \leq 0$ and those with $\varepsilon_p \geq 0$ contribute in equal parts to the density and current, reduces the required number of propagated wave functions even further.

The second step is to speed up the propagation itself. The cost can be quantified using the “Big \mathcal{O} notation” [CLRS09]. Propagating from time step t_m to t_{m+1} scales like $\mathcal{O}(m)$ since the memory term $M_\alpha^{(m)}$ requires the evaluation of m terms of the sum. The cost of all other terms is independent of the time step number. In total, the cost for propagating from time step t_0 to t_m scales like $\mathcal{O}(m^2)$. Unfortunately, it is not possible to ignore or even to truncate the sum in the calculation of the memory term $M_\alpha^{(m)}$. These attempts always produce completely useless results.

It is therefore advisable to optimize the calculation of the memory term $M_\alpha^{(m)}$ since it produces by far most of the

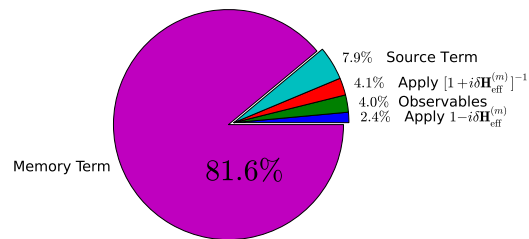


Figure 3.3: Diagram with the relative time consumptions for the propagation of 1024 wave functions and 1000 time steps, split into their main contributions, using variant 3 [page 35] to calculate the memory term.

¹ FLENS (Flexible Library for Efficient Numerical Solutions) is an open-source library for numerical linear algebra. It can be freely downloaded from <http://www.mathematik.uni-ulm.de/~lehn/FLENS/>.

computational cost. The relative time consumption of the calculation of the memory term is shown in figure 3.3 for 1000 time steps, which corresponds to a rather short propagation time. As already mentioned above, one often has to deal with way larger number of time steps. This increases the relative time for the calculation of the memory term even further. Using an efficient evaluation strategy reduces the total cost for a propagation with m time steps to $\mathcal{O}(m \log(m)^2)$. It is based on circular convolutions, which are calculated using the fast Fourier transform algorithm.

Direct method

We first show an efficient way to calculate the memory term in the way it is defined in equation (3.38). We later introduce the FFT and mixed method, which use auxiliary Fourier transforms to calculate the memory term. In contrast, the direct method calculates directly the memory term without any auxiliary transformations.

We define $\widetilde{\mathbf{Q}}_\alpha^{(m)} = \mathbf{Q}_\alpha^{(m)} + \mathbf{Q}_\alpha^{(m+1)}$ and $\widetilde{\psi}_C^{(m)} = (\mathbf{z}_\alpha^{(m)})^\dagger (\psi_C^{(m)} + \psi_C^{(m+1)})$. Then, the memory term defined in equation (3.38) can be written for each m as

$$M_\alpha^{(m)} = -\delta^2 \mathbf{z}_\alpha^{(m)} \sum_{j=0}^{m-1} \left(\mathbf{Q}_\alpha^{(m-j)} + \mathbf{Q}_\alpha^{(m-j-1)} \right) (\mathbf{z}_\alpha^{(j)})^\dagger \left(\psi_C^{(j)} + \psi_C^{(j+1)} \right) \quad (\text{variant 0})$$

$$= -\delta^2 \mathbf{z}_\alpha^{(m)} \sum_{j=0}^{m-1} \widetilde{\mathbf{Q}}_\alpha^{(m-j-1)} \widetilde{\psi}_C^{(j)}. \quad (\text{variant 1})$$

The intuitive evaluation of **variant 0** from right to left requires at least $16m + 2$ floating point operations for every wave function. However, **variant 1** only requires $8m + 2$ operations if one always saves $\widetilde{\mathbf{Q}}_\alpha^{(m)} = \mathbf{Q}_\alpha^{(m)} + \mathbf{Q}_\alpha^{(m+1)}$ and $\widetilde{\psi}_C^{(m)} = (\mathbf{z}_\alpha^{(m)})^\dagger (\psi_C^{(m)} + \psi_C^{(m+1)})$ instead of $\mathbf{Q}_\alpha^{(m)}$ and $\psi_C^{(m)}$. The additional cost for calculating the modified objects $\widetilde{\mathbf{Q}}_\alpha^{(m)}$ and $\widetilde{\psi}_C^{(m)}$ are small, since it has to be done only once.

The next step is to reformulate the expression for $M_\alpha^{(m)}$ such that its numerical evaluation is even more efficient. We will make use of BLAS¹ routines for matrix-vector and matrix-matrix products. We will measure the speed in billion floating points operations per second (GFLOPS). Matrix-vector operations are normally limited by memory bandwidth, matrix-matrix operations are limited

¹ BLAS (**B**asic **L**inear **A**lgebra **S**ubprograms) is a standard library interface for basic linear algebra operations. The documentation as well as a reference implementation is available at <http://www.netlib.org/blas/>. There exists a large variety of highly optimized implementations, commercial as well as open source ones.

by the processor frequency. Thus, the latter can typically achieve a higher peak performance.

The sum in [variant 1](#) consists of m matrix-vector products with a matrix of size 2×2 . Such operations are inefficient, especially when using BLAS. It is favorable to compute one large matrix-vector product instead of many small ones. This can be achieved by replacing the sum in [variant 1](#) by a single matrix-vector product:

$$M_{\alpha}^{(m)} = -\delta^2 \mathbf{z}_{\alpha}^{(m)} \begin{pmatrix} \widetilde{\mathbf{Q}}_{\alpha}^{(m-1)} & \widetilde{\mathbf{Q}}_{\alpha}^{(m-2)} & \dots & \widetilde{\mathbf{Q}}_{\alpha}^{(0)} \end{pmatrix} \begin{pmatrix} \widetilde{\psi}_{\mathbf{C}}^{(0)} \\ \widetilde{\psi}_{\mathbf{C}}^{(1)} \\ \vdots \\ \widetilde{\psi}_{\mathbf{C}}^{(m-1)} \end{pmatrix}. \quad (\text{variant 2})$$

The matrices in the calculation of the memory term are the same for all wave functions at a given time step m . Consequently, it is possible to replace the matrix-vector product by a matrix-matrix product, improving again the speed. The memory term for K wave functions then reads

$$\begin{pmatrix} M_{\alpha,1}^{(m)} & \dots & M_{\alpha,K}^{(m)} \end{pmatrix} = -\delta^2 \mathbf{z}_{\alpha}^{(m)} \begin{pmatrix} \widetilde{\mathbf{Q}}_{\alpha}^{(m-1)} & \dots & \widetilde{\mathbf{Q}}_{\alpha}^{(0)} \end{pmatrix} \begin{pmatrix} \widetilde{\psi}_{\mathbf{C},1}^{(0)} & \dots & \widetilde{\psi}_{\mathbf{C},K}^{(0)} \\ \widetilde{\psi}_{\mathbf{C},1}^{(1)} & \dots & \widetilde{\psi}_{\mathbf{C},K}^{(1)} \\ \vdots & & \vdots \\ \widetilde{\psi}_{\mathbf{C},1}^{(m-1)} & \dots & \widetilde{\psi}_{\mathbf{C},K}^{(m-1)} \end{pmatrix}. \quad (\text{variant 3})$$

We define for later use

$$\widetilde{\psi}_{\mathbf{C}}^{(k)} = \begin{pmatrix} \widetilde{\psi}_{\mathbf{C},1}^{(k)} & \widetilde{\psi}_{\mathbf{C},2}^{(k)} & \dots & \widetilde{\psi}_{\mathbf{C},K}^{(k)} \end{pmatrix}, \quad (3.47)$$

$$\widetilde{\mathbf{M}}_{\alpha}^{(m)} = \begin{pmatrix} \widetilde{\mathbf{Q}}_{\alpha}^{(m-1)} & \widetilde{\mathbf{Q}}_{\alpha}^{(m-2)} & \dots & \widetilde{\mathbf{Q}}_{\alpha}^{(0)} \end{pmatrix} \begin{pmatrix} \widetilde{\psi}_{\mathbf{C}}^{(0)} \\ \widetilde{\psi}_{\mathbf{C}}^{(1)} \\ \vdots \\ \widetilde{\psi}_{\mathbf{C}}^{(m-1)} \end{pmatrix}, \quad (3.48)$$

$$\mathbf{M}_{\alpha}^{(m)} = \begin{pmatrix} M_{\alpha,1}^{(m)} & M_{\alpha,2}^{(m)} & \dots & M_{\alpha,K}^{(m)} \end{pmatrix} \quad (3.49)$$

$$= -\delta^2 \mathbf{z}_{\alpha}^{(m)} \widetilde{\mathbf{M}}_{\alpha}^{(m)}. \quad (3.50)$$

In order to show the improving speed, we first benchmark the corresponding most time consuming BLAS functions. They are listed in [table 3.2](#) for the three variants. This will also reveal good choices for the block size K in the wave function domain.

Before comparing the three variants in a real simulation, one has to determine

	BLAS routine	Operation	Size	# Calls
variant 1	zgemv	$y \leftarrow \alpha \mathbf{A}x + \beta y$	$\mathbf{A} \in \mathbb{C}^{2 \times 2}$	$m \cdot K$
variant 2	zgemv	$y \leftarrow \alpha \mathbf{A}x + \beta y$	$\mathbf{A} \in \mathbb{C}^{2 \times 2m}$	K
variant 3	zgemm	$\mathbf{C} \leftarrow \alpha \mathbf{A}\mathbf{B} + \beta \mathbf{C}$	$\mathbf{A} \in \mathbb{C}^{2 \times 2m}, \mathbf{B} \in \mathbb{C}^{2m \times K}$	1

Table 3.2: Details of the most time consuming BLAS functions used for the different evaluation variants of the memory term $\mathbf{M}_\alpha^{(m)}$ for K wave functions.

a good choice of K for [variant 3](#). This is done by benchmarking the BLAS function zgemm for different values of K using the ATLAS¹ [WPD01, WP05] timing routines. ATLAS is a well established BLAS library that additionally provides benchmark functions for BLAS routines of competing BLAS implementations. These functions take care of proper processor cache flushing and are thus able to produce reliable results. We choose the BLAS implementation provided by the Intel MKL², unless otherwise stated. It outperforms ATLAS significantly on our target system, which is an Intel Xeon X5650 processor. The presented results of BLAS functions are all obtained by using the ATLAS timing routines benchmarking the Intel MKL.

We would like to emphasize that the results may be different depending on the used hardware and software. Thus a good choice for K is platform dependent. Figure 3.4 shows the results for [variant 3](#). Starting from $K = 1$, the performance increases with increasing size K and eventually saturates at around $K = 64$. Therefore one chooses $K = 64$ or even larger. In the course of the section, we will apply further optimizations and eventually see, that $K = 64$ is the optimal choice.

¹ ATLAS (Automatically Tuned Linear Algebra Software) can be downloaded from <http://math-atlas.sourceforge.net/>. It is an automatically tuned BLAS implementation, thus relying on accurate timing measurements. We use version 3.10.0.

² The Intel MKL (Math Kernel Library) is a commercial library for BLAS, LAPACK and FFT, <http://developer.intel.com/software/products/mkl>. We use version 11.0.1 and always only one thread.

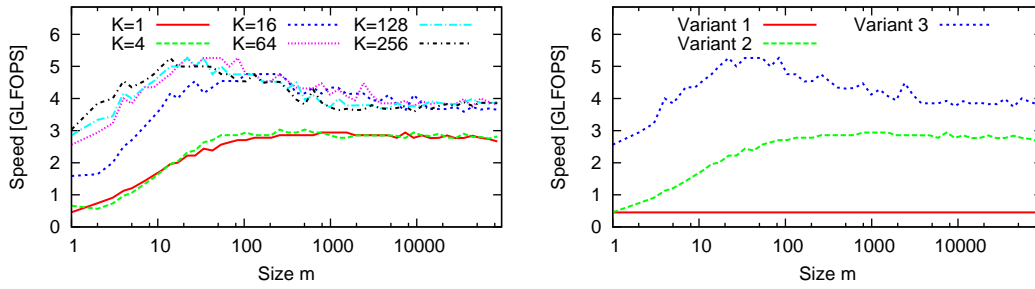


Figure 3.4: Left: Benchmark of the function `zgemv` using one thread for the variant 3, which simulates the calculation of $\mathbf{M}_\alpha^{(m)}$. We measure the speed in billion floating operations per second (GFLOPS) instead of absolute times to simplify the comparison, i.e. higher is faster. Right: Comparison of the variants 1, 2 and 3 (with $K = 64$). The peak performance for single threaded matrix-matrix multiplication for square size matrices using `zgemv` is ≈ 10.2 GFLOPS and the theoretical maximum is 10.68 GFLOPS. The reason for our low performance is that the matrices have few rows and/or columns as listed in table 3.2.

The increasing speed in a real simulation is shown in figure 3.5. For this, we used the BLAS implementation of the Intel MKL and OpenBLAS¹ [ZWZ12] and two different systems. The benchmarks predict a speedup by a factor of ≈ 9 , the simulation shows only a factor of ≈ 7.5 . The reason is the contribution of other terms in the propagation scheme which were neglected in the benchmarks in figure 3.4.

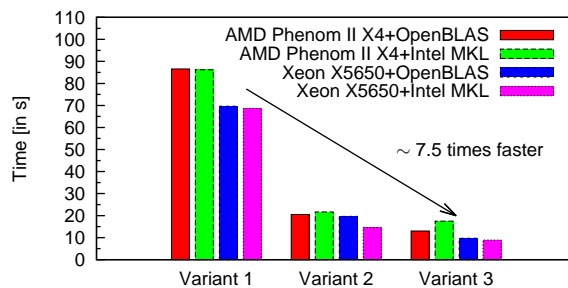


Figure 3.5: Run times for calculations with 1024 wave functions and 1000 time steps using two different BLAS implementation and two different CPUs on one core.

¹ OpenBLAS is an optimized open-source BLAS implementation. It is a successor of GotoBLAS2 [GvdG08a, GvdG08b] and can be obtained from <http://github.com/xianyi/OpenBLAS>. We use version 0.2.5.

FFT method

The benefit of the FFT method is its reduction of the required number of floating point operations by using the circular convolution theorem. This will eventually reduce the cost for m propagation steps from $\mathcal{O}(m^2)$ to $\mathcal{O}(m \log(m)^2)$, becoming very advantageous for large m . This strategy has already been used for a similar algorithm which propagates Green's functions [ZXW12]. It is based on a previous work for nonlinear Volterra convolution equations [HLS85].

Definition 3.1 (Discrete circular convolution [Mar09]) *Let x and y be two N dimensional vectors. The discrete circular convolution of x and y is defined as*

$$[x * y](k) = \sum_{l=0}^k x(l)y(k-l) + \sum_{l=k+1}^{N-1} x(l)y(N+k-l) \quad (3.51)$$

$$= \sum_{l=0}^k x(k-l)y(l) + \sum_{l=k+1}^{N-1} x(N+k-l)y(l). \quad (3.52)$$

Definition 3.2 (Discrete Fourier transform [Mar09]) *Let x be a N dimensional vector. The discrete Fourier transform of x is defined as*

$$\mathcal{F}[x](k) = \sum_{j=0}^{N-1} x(j)e^{-2\pi i \frac{kj}{N}} \quad (3.53)$$

and the inverse discrete Fourier transform as

$$\mathcal{F}^{-1}[x](k) = \frac{1}{N} \sum_{j=0}^{N-1} x(j)e^{+2\pi i \frac{kj}{N}}. \quad (3.54)$$

Note that the vector elements of x in the above definition need not to be necessarily complex numbers, but can also be complex matrices. In the latter case, x is a vector of matrices. The same is possible for the discrete circular convolution.

The fast Fourier transform algorithm reduces the cost of calculating $\mathcal{F}[x]$ and $\mathcal{F}^{-1}[x]$ from $\mathcal{O}(N^2)$ to $\mathcal{O}(N \log N)$ for N being the length of x and a power of 2 [CLRS09].

Theorem 3.3 (Discrete circular convolution theorem [Mar09]) *Let x and y be two N dimensional vectors. The discrete circular convolution of x and y can be calculated as*

$$[x * y](k) = \mathcal{F}^{-1}[(\mathcal{F}[x] \cdot \mathcal{F}[y])](k) \quad (3.55)$$

with $(\mathcal{F}[x] \cdot \mathcal{F}[y])(k) = \mathcal{F}[x](k)\mathcal{F}[y](k)$.

Proof.

$$\mathcal{F}^{-1}[(\mathcal{F}[x] \cdot \mathcal{F}[y])](k) = \frac{1}{N} \sum_{l_1=0}^{N-1} \mathcal{F}[x](l_1) \mathcal{F}[y](l_1) e^{2\pi i \frac{kl_1}{N}} \quad (3.56)$$

$$= \frac{1}{N} \sum_{l_1, l_2, l_3=0}^{N-1} x(l_2) e^{-2\pi i \frac{l_1 l_2}{N}} y(l_3) e^{-2\pi i \frac{l_1 l_3}{N}} e^{2\pi i \frac{kl_1}{N}} \quad (3.57)$$

$$= \frac{1}{N} \sum_{l_2, l_3=0}^{N-1} x(l_2) y(l_3) (\delta_{k, l_2+l_3} + \delta_{k+N, l_2+l_3}) \quad (3.58)$$

$$= \sum_{l=0}^k x(l) y(k-l) + \sum_{l=k+1}^{N-1} x(l) y(N+k-l) \quad (3.59)$$

$$= [x * y](k). \quad (3.60)$$

□

This theorem reduces the cost of calculating a circular convolution of two vectors with length N from $\mathcal{O}(N^2)$ to $\mathcal{O}(N \log N)$. We make use of this strategy to obtain the memory terms $\widetilde{\mathbf{M}}_\alpha^{(m)}$ at reduced computational cost compared to [variant 3](#).

The calculation scheme for $\widetilde{\mathbf{M}}_\alpha^{(m)}$ using [variant 3](#) is shown in [figure 3.6](#). In order to get the memory terms, one has to sum up all entries of a column. A single column is evaluated using a single matrix-matrix product as explained in previous part this section.

The idea behind the FFT method is not to evaluate every column separately, but to calculate always the vertical sum in the square sized blocks of [figure 3.6](#). The evaluation order of these blocks is indicated with numbers. If the block size is larger than 1 by 1, the computed sums have to be saved for the following time steps. We will show, that one can use the discrete convolution theorem to evaluate these block efficiently.

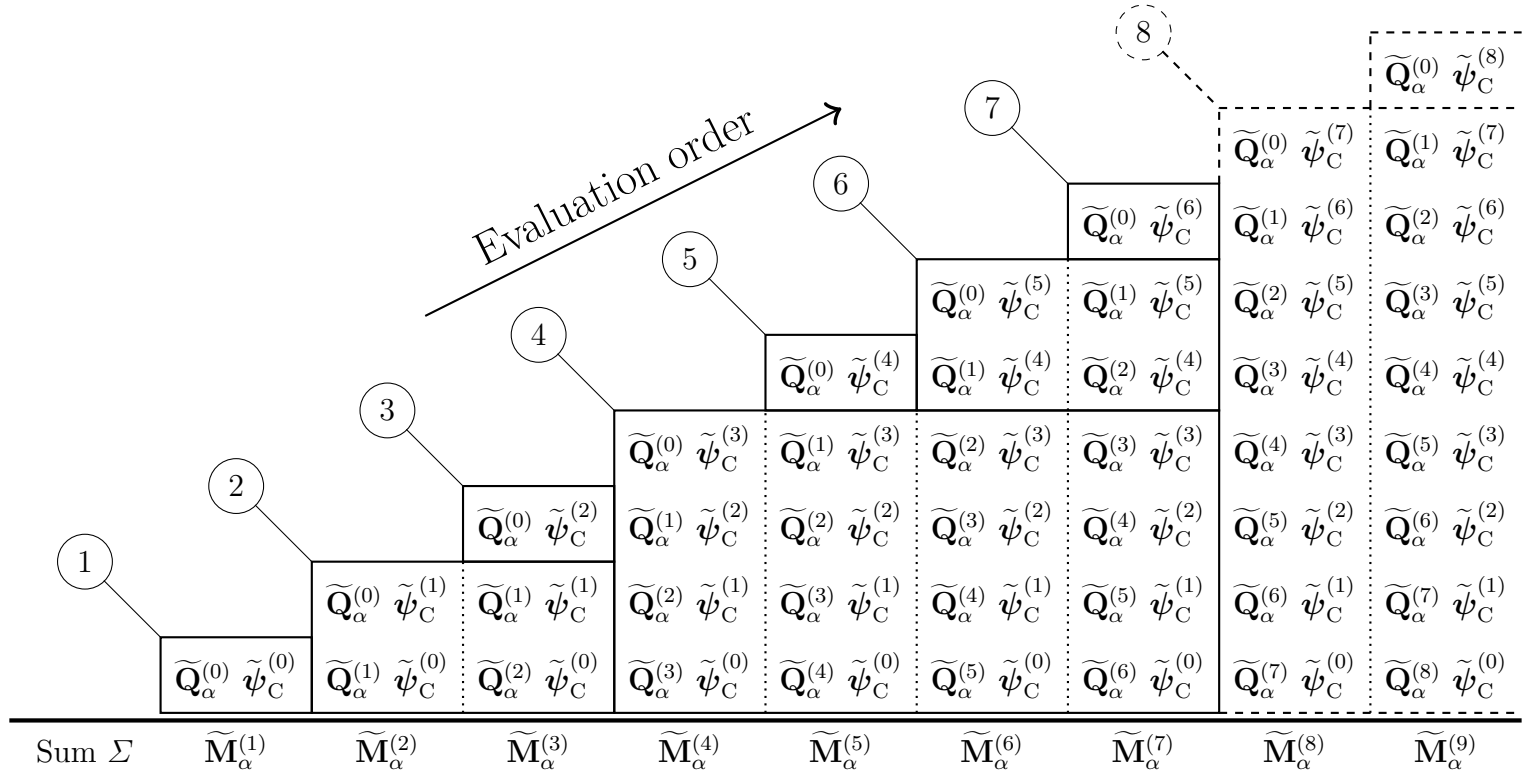


Figure 3.6: Visualization of the calculation scheme for $\widetilde{\mathbf{M}}_\alpha^{(m)}$. The terms have to be added column-wise. The evaluation is done block-wise in the indicated order. The final memory term is obtained by $\mathbf{M}_\alpha^{(m)} = -\delta^2 \mathbf{z}_\alpha^{(m)} \widetilde{\mathbf{M}}_\alpha^{(m)}$.

In the following, we present a detailed explanation of the evaluation scheme. We assume that we want to calculate the block at a time step 2^N . This simplifies the notation. Of course, the strategy can be applied at other time steps, it may only require some index shifts in order for the following formulas to be applicable.

We want to calculate $\widetilde{\mathbf{M}}_\alpha^{(2^N)}$ and parts of $\widetilde{\mathbf{M}}_\alpha^{(m)}$ with $2^N < m < 2^{N+1}$, assuming that all wave functions $\widetilde{\psi}_C^{(k)}$, $k < 2^N$ are known. Thus, we want to calculate a block of figure 3.6. An example of size 4 by 4 is shown in figure 3.7. Calculating this block gives $\widetilde{\mathbf{M}}_\alpha^{(4)}$ and parts of $\widetilde{\mathbf{M}}_\alpha^{(5)}$, $\widetilde{\mathbf{M}}_\alpha^{(6)}$ and $\widetilde{\mathbf{M}}_\alpha^{(7)}$.

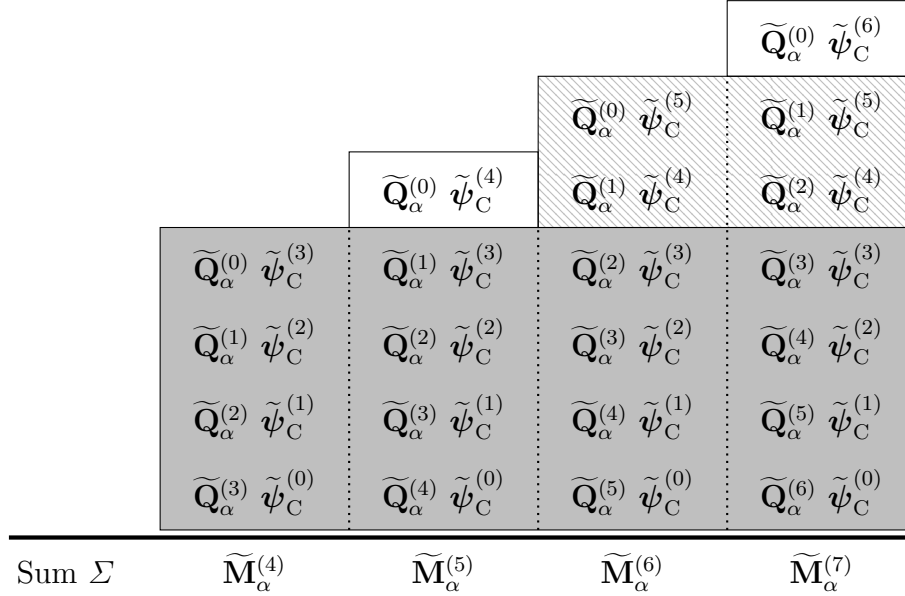


Figure 3.7: Calculation scheme for the memory terms $\widetilde{\mathbf{M}}_\alpha^{(m)}$, $m \in \{4, \dots, 7\}$ of figure 3.6. The goal is to derive an efficient scheme to evaluate the dark gray filled block. Evaluating the gray block yields $\widetilde{\mathbf{M}}_\alpha^{(4)}$ and parts of $\widetilde{\mathbf{M}}_\alpha^{(5)}$, $\widetilde{\mathbf{M}}_\alpha^{(6)}$ and $\widetilde{\mathbf{M}}_\alpha^{(7)}$. The procedure can be adapted to calculate the gray shaded block and all kinds of similar quadratic blocks of arbitrary size.

We define auxiliary wave functions

$$\phi_C^{(2^N, k)} = \begin{cases} \widetilde{\psi}_C^{(k)} & \text{if } 0 \leq k < 2^N, \\ 0 & \text{if } 2^N \leq k < 2^{N+1}. \end{cases} \quad (3.61)$$

This allows us to write the term $\widetilde{\mathbf{M}}_\alpha^{(m)}$ for $2^N \leq m < 2^{N+1}$ as follows:

$$\widetilde{\mathbf{M}}_\alpha^{(m)} = \sum_{k=0}^{m-1} \widetilde{\mathbf{Q}}_\alpha^{(m-k-1)} \widetilde{\psi}_C^{(k)} \quad (3.62)$$

$$= \sum_{k=2^N}^{m-1} \widetilde{\mathbf{Q}}_\alpha^{(m-k-1)} \widetilde{\psi}_C^{(k)} + \sum_{k=0}^{2^N-1} \widetilde{\mathbf{Q}}_\alpha^{(m-k-1)} \psi_C^{(k)} \quad (3.63)$$

$$= \sum_{k=2^N}^{m-1} \widetilde{\mathbf{Q}}_\alpha^{(m-k-1)} \widetilde{\psi}_C^{(k)} + \sum_{k=0}^{2^N-1} \widetilde{\mathbf{Q}}_\alpha^{(m-k-1)} \phi_C^{(2^N, k)} \quad (3.64)$$

$$\begin{aligned} &+ \underbrace{\sum_{k=2^N}^{m-1} \widetilde{\mathbf{Q}}_\alpha^{(m-k-1)} \phi_C^{(2^N, k)} + \sum_{k=m}^{2^{N+1}-1} \widetilde{\mathbf{Q}}_\alpha^{(2^N+m-k-1)} \phi_C^{(2^N, k)}}_{=0} \\ &= \sum_{k=2^N}^{m-1} \widetilde{\mathbf{Q}}_\alpha^{(m-k-1)} \widetilde{\psi}_C^{(k)} \quad (3.65) \end{aligned}$$

$$\begin{aligned} &+ \underbrace{\sum_{k=0}^{m-1} \widetilde{\mathbf{Q}}_\alpha^{(m-k-1)} \phi_C^{(2^N, k)} + \sum_{k=m}^{2^{N+1}-1} \widetilde{\mathbf{Q}}_\alpha^{(2^N+m-k-1)} \phi_C^{(2^N, k)}}_{= [\widetilde{\mathbf{Q}}_\alpha * \phi_C^{(2^N)}]_{(m-1)}} \\ &= \sum_{k=2^N}^{m-1} \widetilde{\mathbf{Q}}_\alpha^{(m-k-1)} \widetilde{\psi}_C^{(k)} + [\widetilde{\mathbf{Q}}_\alpha * \phi_C^{(2^N)}]_{(m-1)}. \quad (3.66) \end{aligned}$$

In the example of figure 3.7, the term $[\widetilde{\mathbf{Q}}_\alpha * \phi_C^{(2^N)}]_{(m-1)}$ corresponds to the sum of one column of the dark gray block. The sum $\sum_{k=2^N}^{m-1} \widetilde{\mathbf{Q}}_\alpha^{(m-k-1)} \widetilde{\psi}_C^{(k)}$ corresponds to the remaining parts above the dark gray block in the column of $\widetilde{\mathbf{M}}_\alpha^{(m)}$. The dark gray block is calculated via $\mathcal{F}^{-1} \left[\left(\mathcal{F}[\widetilde{\mathbf{Q}}_\alpha] \cdot \mathcal{F}[\phi_C^{(2^N)}] \right) \right]$. This immediately gives the vertical sum for every column of the dark gray block. All other blocks in figure 3.6 are evaluated in the same manner.

The extension from equation (3.63) to equation (3.64) is shown in figure 3.8 for the example of figure 3.7 with $N = 2$. This extension allows us to introduce the discrete circular convolution.

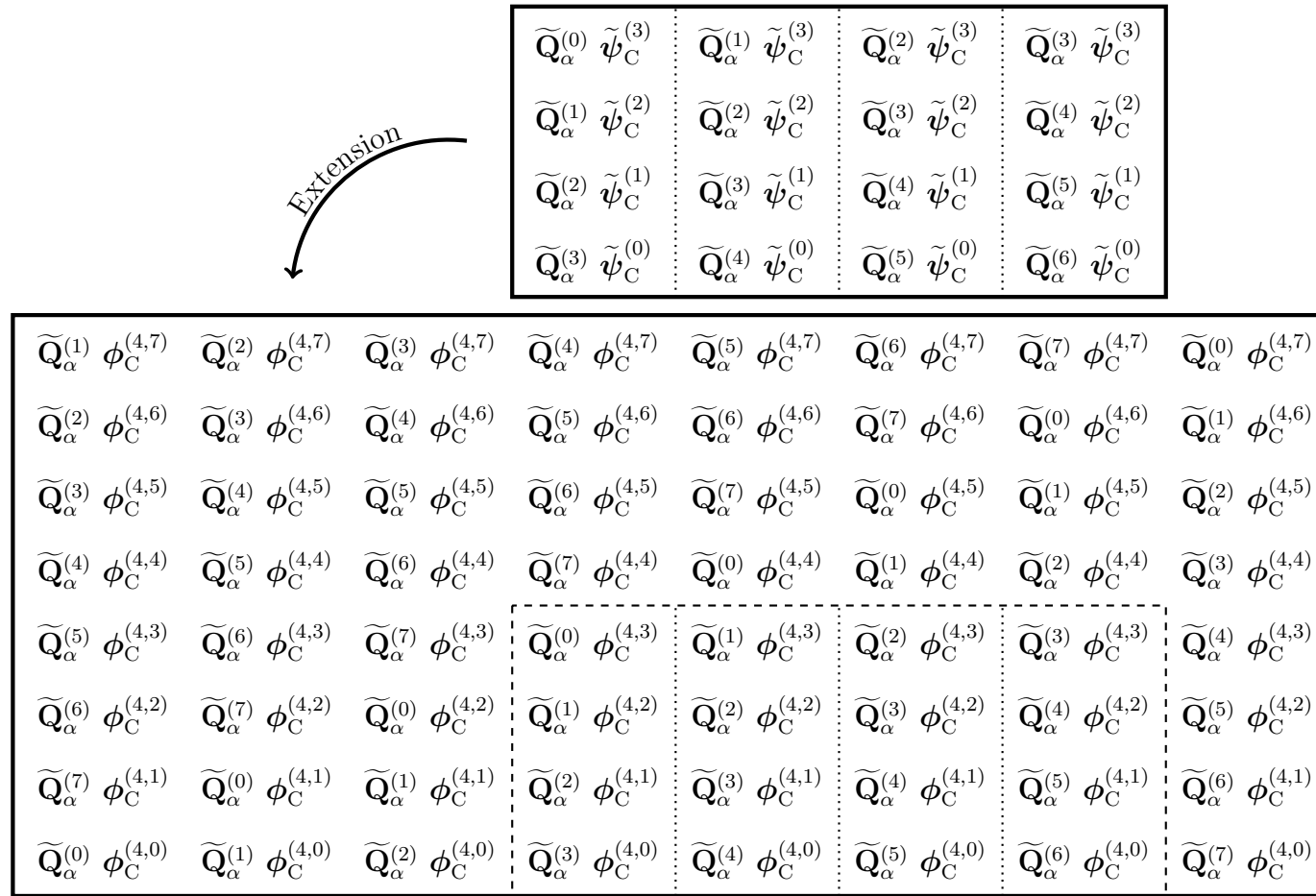


Figure 3.8: Extension of a 4 by 4 rectangle of figure 3.6 in order to make use of the discrete circular convolution theorem. The wave functions $\phi_C^{(m)}$ are defined in equation (3.61). Above, $\phi_C^{(4,m)} = \psi_C^{(m)}$ for $k < 4$ and 0 otherwise. The discrete circular convolution theorem will then be applied to $\tilde{Q}_\alpha^{(k)}$ and $\phi_C^{(4,k)}$, $k \in \{0, \dots, 7\}$. It calculates the sum of every column.

$\widetilde{\mathbf{Q}}_\alpha^{(k)}$ and $\phi_C^{(2^N, k)}$ are both matrices and their Fourier transforms are calculated for each component separately. This allows us to make use of a highly optimized library for this task, like FFTW¹ [FJ05] or the Intel MKL. The latter was used for all discrete Fourier transforms in this chapter.

The cost of calculating a discrete circular convolution using the discrete circular convolution theorem and the Fourier transform algorithm is $\mathcal{O}(N \log N)$. We define $\mathcal{C}(m)$ as the cost for a time propagation from 0 to t_m . Since the memory term is the only contribution that does not scale linearly, we can neglect all other contributions in the estimate. For simplicity, we want to calculate the cost at a time step m that is a power of 2. We use a divide & conquer scheme for the cost estimation which is visualized in figure 3.9.

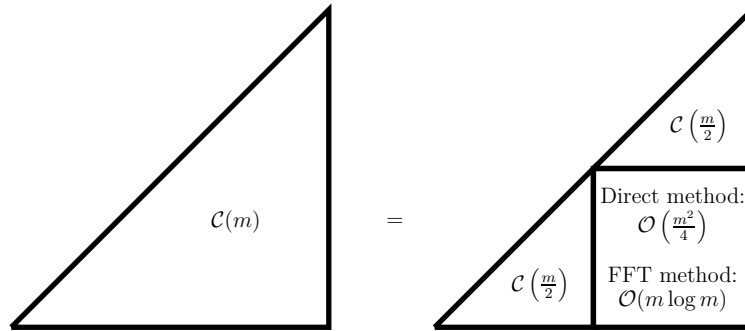


Figure 3.9: Sketch of the memory term for cost estimation. The divide & conquer scheme will be used recursively. The triangle symbolizes the summands of the memory term as shown in figure 3.6.

Using the divide & conquer scheme recursively yields for the FFT method

$$\mathcal{C}(m) = \mathcal{O}(m \log_2 m) + 2 \cdot \mathcal{C}\left(\frac{m}{2}\right) \quad (3.67)$$

$$= \mathcal{O}(m \log_2 m) + 2 \cdot \mathcal{O}\left(\frac{m}{2} \log_2 \frac{m}{2}\right) + 4\mathcal{C}\left(\frac{m}{2^2}\right) \quad (3.68)$$

$$= \mathcal{O}\left(m \sum_{k=1}^{\log_2 m} \log_2 \frac{m}{2^k}\right) \quad (3.69)$$

$$= \mathcal{O}\left(\frac{m}{2}(1 + \log_2 m) \log_2 m\right) \quad (3.70)$$

$$= \mathcal{O}(m(\log_2 m)^2). \quad (3.71)$$

¹ The library FFTW (**F**ast **F**ourier **T**ransform in the **W**est) can be downloaded from <http://www.fftw.org>.

Similarly, we get for the direct method

$$\mathcal{C}(m) = \mathcal{O}\left(\frac{m^2}{4}\right) + 2\mathcal{C}\left(\frac{m}{2}\right) \quad (3.72)$$

$$= \mathcal{O}\left(\sum_{k=1}^{\log_2 m} \frac{m^2}{2^{k+1}}\right) \quad (3.73)$$

$$= \mathcal{O}(m^2). \quad (3.74)$$

Hence, the FFT method is faster than any direct method for large m .

Mixed method

The application of the circular convolution theorem is only advantageous for large blocks of figure 3.6. For small ones, a direct calculation of the convolution is faster. We therefore combine these two methods and name it mixed method.

It works as follows: All blocks of figure 3.6 with a dimension smaller than a certain switching size L are evaluated without using the circular convolution theorem as in the direct method. For all larger blocks, we use the discrete circular convolution theorem as in the FFT method. The optimal switching size L between direct and FFT method has to be determined by benchmarks and is again system dependent. It further depends on the block size in the wave function domain K . Hence, we search the optimal values for K and L simultaneously. We use a simulation with 2048 time steps and 1024 wave functions as a test case. Similar results can be obtained for even larger test cases. The results for our target system are shown in figure 3.10. The minimum is at $K = 64$ and $L = 16$.

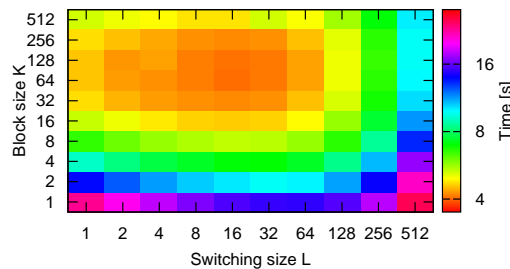


Figure 3.10: Computational time of a test calculation as a function of the block size K in the wave function domain and the switching size L between the direct and the FFT method. We used 2048 time steps and 1024 wave functions. The minimum is at $K = 64$ and $L = 16$. The calculations use one core. Very similar results can be obtained for larger numbers of time steps.

Benchmark

We finally want to demonstrate the improvement of the mixed method compared to the FFT method and an highly optimized direct method. The latter uses the same evaluation order as the FFT method, but calculates the discrete convolutions without using the discrete convolution theorem. Thus, every block of figure 3.6 is calculated using one matrix-matrix multiplication. The appearing matrices have more advantageous shapes for the BLAS matrix-matrix multiplication function compared to variant 3. This procedure outperforms variant 3 by a factor of two, but requires a large amount of memory. The comparison of the three methods is displayed in figure 3.11.

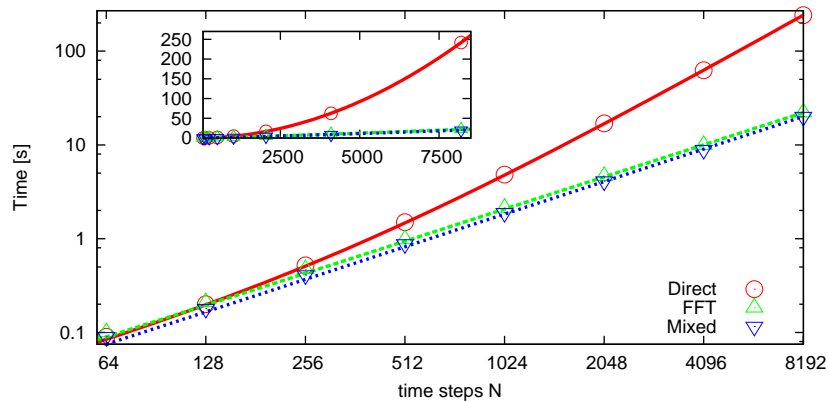


Figure 3.11: Run times for calculations with 1024 wave functions comparing the mixed method, the FFT method and an highly optimized direct method. The inset shows the same plot, but using normal instead of logarithmic axes. The block size in the wave function domain is $K = 64$, the switching of the mixed method is $L = 16$. For $8192 = 2^{13}$ time steps, the run time is reduced by a factor of ≈ 12 . The longest propagations in this work require $131072 = 2^{17}$ (or even $262144 = 2^{18}$) time steps. In these cases, the computational times of the mixed and the FFT method are almost identical. Compared to the direct method, we expect a speed increase in these cases by a factor ≈ 100 (≈ 200). The calculations use again only one core.

We inserted fits for the measured times. The direct evaluation method is outperformed by both other methods and the mixed method is only slightly ahead of the pure FFT method. Compared to a straight forward implementation using variant 0, one can expect speed improvements up to three orders of magnitude and more for the most demanding simulations carried out in this thesis.

As a closing remark to this subsection, we point out that this propagation scheme can easily be parallelized in the wave function domain using for example the Message Passing Interface (MPI) or Open Multi-Processing (OpenMP).

The propagation from time step t_m to t_{m+1} can be done for all wave functions independently, only the calculation of the observables requires some communication between the different threads. Besides, one can get access to more Random-access memory (RAM) by using several computers for a single simulation, which is especially useful for propagations with many time steps and/or wave functions, requiring often several Gigabytes of storage. Our implementation successfully used MPI with an optional further OpenMP parallelization. Further improvement could be obtained by using general-purpose graphics processing units (GPGPU) for the Fourier transforms. In order to achieve the best possible results, one would need to store $\tilde{\mathbf{Q}}_\alpha^{(m)}$ and $\tilde{\psi}_C^{(m)}$ directly in the memory of the GPGPU and thus minimize data transfers between CPU and GPGPU.

3.3 Large time behaviour of the nonequilibrium Green's functions

As a third approach, we want to explain how to calculate the large time behaviour of nonequilibrium Green's functions. This method was originally invented to describe a junction with a time-dependent monochromatic potential in the central region and normal leads [SKRG08], but without any bias. The method was originally used to calculate currents from the leads into the central region. We have modified it such that it is possible to calculate densities and currents inside the central region for superconducting junctions with an applied bias, but without the time-dependent potential in the central region.

The method is restricted to the long time behaviour, that means it gives the nonequilibrium Green's functions after all switching effects have died out. We therefore introduce the notation for the convergence in norm

$$f(t) \stackrel{t \rightarrow \infty}{\sim} g(t) \quad \Leftrightarrow \quad \lim_{t \rightarrow \infty} \|f(t) - g(t)\| = 0. \quad (3.75)$$

This describes that the function g approaches f with increasing time arguments t . This allows us to neglect all contributions of $f(t)$ which tend to zero as $t \rightarrow \infty$. The method relies on two preconditions:

1. $\mathbf{H}_{\alpha C}(t) = \mathbf{H}_{\alpha C} \Leftrightarrow \gamma_{\alpha C}(t) = 0$.

This can be achieved by extending the central region by one site in both directions since the Hamiltonians of the leads $\mathbf{H}_{\alpha\alpha}$ are time-independent. This will be assumed for this section without loss of generality.

2. $\mathbf{H}_{CC}(t) = \mathbf{H}_{CC}^0 + \mathbf{U}_+ e^{i\omega_0 t} + \mathbf{U}_- e^{-i\omega_0 t}$.

The shape of the matrices \mathbf{H}_{CC}^0 and \mathbf{U}_{\pm} can be determined by the Hamiltonian given in section 2.3. This precondition restricts the possible choices for the central Hamiltonian, especially since the central region has been extended by one site in both direction in the first step. Nevertheless it still allows the most important two cases with a constant bias: (a) The bias is only in one of the original leads ($\omega_0 = U$) and (b) the bias is in both original leads with $U_L = -U_R$ ($\omega_0 = \frac{1}{2}U$).

The density at the site k can be expressed as

$$n_k(t) = \sum_{\sigma \in \{\uparrow, \downarrow\}} \langle \hat{c}_{k\sigma, H}^\dagger(t) \hat{c}_{k\sigma, H}(t) \rangle \quad (3.76)$$

$$= -i[\mathbf{G}_{kk}^<(t, t)]_{\uparrow\uparrow} + i[\mathbf{G}_{kk}^>(t, t)]_{\downarrow\downarrow} \quad (3.77)$$

$$= -i[\mathbf{G}_{CC}^<(t, t)]_{(k\uparrow, k\uparrow)} + i[\mathbf{G}_{CC}^>(t, t)]_{(k\downarrow, k\downarrow)}. \quad (3.78)$$

The same is possible for the current between the sites k and l :

$$I_{kl}(t) = -i \sum_{\sigma \in \{\uparrow, \downarrow\}} \left(t_{kl} e^{i\gamma_{kl}(t)} \langle \hat{c}_{k\sigma, H}^\dagger(t) \hat{c}_{l\sigma, H}(t) \rangle - H.c. \right) \quad (3.79)$$

$$= 2\text{Re Tr} \{ \mathbf{G}_{lk}^<(t, t) \mathbf{H}_{kl}(t) \boldsymbol{\sigma}_z \} \quad (3.80)$$

$$= 2\text{Re Tr} \left\{ [\mathbf{G}_{CC}^<(t, t)]_{(l, k)} [\mathbf{H}_{CC}(t)]_{(k, l)} \boldsymbol{\sigma}_z \right\} \quad (3.81)$$

with site indices k, l of the central region. $\boldsymbol{\sigma}_z$ is the third Pauli matrix in Nambu space.

The task is to calculate $\mathbf{G}_{CC}^{\geq}(t, t)$, which can be expressed for large times t in terms of objects of the central region only. This is presented in detail in appendix B.1. Using the definitions $\mathbf{g}_\alpha(z, z')$ for the nonequilibrium Green's function of the isolated lead α , the embedding self-energies read $\boldsymbol{\Sigma}_\alpha(z, z') = \mathbf{H}_{C\alpha} \mathbf{g}_\alpha(z, z') \mathbf{H}_{\alpha C}$ and $\boldsymbol{\Sigma} = \boldsymbol{\Sigma}_L + \boldsymbol{\Sigma}_R$. Then, the large time behaviour of $\mathbf{G}_{CC}^{\geq}(t, t)$ is

$$\mathbf{G}_{CC}^{\geq}(t, t) \stackrel{t \rightarrow \infty}{\sim} \left[\mathbf{G}_{CC}^R \cdot \boldsymbol{\Sigma}^{\geq} \cdot \mathbf{G}_{CC}^A \right] (t, t), \quad (3.82)$$

with $[\mathbf{A} \cdot \mathbf{B} \cdot \mathbf{C}](t, t') = \iint_{-\infty}^{\infty} d\bar{t}_1 d\bar{t}_2 \mathbf{A}(t, \bar{t}_1) \mathbf{B}(\bar{t}_1, \bar{t}_2) \mathbf{C}(\bar{t}_2, t')$. The Hamiltonian $\mathbf{H}_{CC}(t)$ contains only the frequencies $\pm\omega_0$, hence we can expand $\mathbf{G}_{CC}^{R, A}$ as

$$\begin{aligned} \mathbf{G}_{CC}^{R, A}(t, t') &= \sum_{m \in \mathbb{Z}_{-\infty}} \int \frac{d\omega}{2\pi} \tilde{\mathbf{G}}_m^{R, A}(\omega) e^{-i\omega(t-t') + im\omega_0 \frac{t+t'}{2}} \\ &= \sum_{m \in \mathbb{Z}_{-\infty}} \int \frac{d\omega}{2\pi} \mathbf{G}_m^{R, A}(\omega) e^{-i\omega(t-t') + im\omega_0 t'}. \end{aligned} \quad (3.83)$$

The equivalence of the two expansions can be easily checked by a variable substitution in the integral. We use the latter representation for convenience reasons. This expansion is only possible if there is no initial state dependence and if the system does not have any bound states. We will always choose systems without normal or Andreev bound states in the biased system. Hence both conditions are fulfilled.

We define $\mathbb{Z}^2 = \mathbb{Z} \times \mathbb{Z}$, $\mathbf{m} = (m_1, m_2) \in \mathbb{Z}^2$, and insert the expansion (3.83) into the equation (3.82). This is executed in detail in appendix B.2. The final equations for the density and the current are

$$\begin{aligned} n_k(t) \stackrel{t \rightarrow \infty}{\sim} \int_{-\infty}^{\infty} \frac{d\omega}{2\pi} \sum_{\mathbf{m} \in \mathbb{Z}^2} e^{i(m_1 - m_2)\omega_0 t} \left[f^<(\omega) [\mathbf{G}_{m_1}(\omega) \boldsymbol{\Gamma}(\omega) \mathbf{G}_{m_2}^\dagger(\omega)]_{(k\uparrow, k\uparrow)} \right. \\ \left. + f^>(\omega) [\mathbf{G}_{m_1}(\omega) \boldsymbol{\Gamma}(\omega) \mathbf{G}_{m_2}^\dagger(\omega)]_{(k\downarrow, k\downarrow)} \right], \end{aligned} \quad (3.84)$$

$$I_{k,l}(t) \stackrel{t \rightarrow \infty}{\sim} 2\text{Re Tr} \left\{ \int_{-\infty}^{\infty} \frac{d\omega}{2\pi} \sum_{\mathbf{m} \in \mathbb{Z}^2} e^{i(m_1 - m_2)\omega_0 t} f^<(\omega) \right. \\ \left. \left[\mathbf{G}_{m_1}(\omega) \mathbf{\Gamma}(\omega) \mathbf{G}_{m_2}^\dagger(\omega) \right]_{(l,k)} [\mathbf{H}_{\text{CC}}(t)]_{(k,l)} \boldsymbol{\sigma}_z \right\} \quad (3.85)$$

with the Fermi functions $f^<(\omega) = [1 + \exp(\beta\omega)]^{-1}$ and $f^>(\omega) = f^<(\omega) - 1$. We further introduced $\mathbf{G}_m(\omega) \equiv \mathbf{G}_m^{\text{R}}(\omega - m\omega_0) = [\mathbf{G}_{-m}^{\text{A}}(\omega)]^\dagger$, $\mathbf{\Gamma}_\alpha(\omega) = i [\boldsymbol{\Sigma}_\alpha^{\text{R}}(\omega) - \boldsymbol{\Sigma}_\alpha^{\text{A}}(\omega)]$ and $\mathbf{\Gamma}(\omega) = \mathbf{\Gamma}_L(\omega) + \mathbf{\Gamma}_R(\omega)$. The observables are periodic with frequency $\omega_0 = \frac{2\pi}{T_0}$. The time average of the density $n_k(t)$ and the current $I_{k,l}(t)$ read

$$n_{k,\text{DC}} = \lim_{t \rightarrow \infty} \frac{1}{T_0} \int_t^{t+T_0} dt' n_k(t') \quad (3.86)$$

$$= \int_{-\infty}^{\infty} \frac{d\omega}{2\pi} \sum_{\mathbf{m} \in \mathbb{Z}} \left[f^<(\omega) [\mathbf{G}_m(\omega) \mathbf{\Gamma}(\omega) \mathbf{G}_m^\dagger(\omega)]_{(k\uparrow, k\uparrow)} \right. \\ \left. + f^>(\omega) [\mathbf{G}_m(\omega) \mathbf{\Gamma}(\omega) \mathbf{G}_m^\dagger(\omega)]_{(k\downarrow, k\downarrow)} \right] \quad (3.87)$$

and

$$I_{k,l,\text{DC}} = \lim_{t \rightarrow \infty} \frac{1}{T_0} \int_t^{t+T_0} dt' I_{k,l}(t') \quad (3.88)$$

$$= 2\text{Re Tr} \left\{ \int_{-\infty}^{\infty} \frac{d\omega}{2\pi} \sum_{\mathbf{m} \in \mathbb{Z}^2} f^<(\omega) \left[\mathbf{G}_{m_1}(\omega) \mathbf{\Gamma}(\omega) \mathbf{G}_{m_2}^\dagger(\omega) \right]_{(l,k)} \right. \\ \left. \left[\mathbf{H}_{\text{CC}}^0 \delta_{m_1, m_2} + \mathbf{U}_+ \delta_{m_1+1, m_2} + \mathbf{U}_- \delta_{m_1-1, m_2} \right]_{(k,l)} \boldsymbol{\sigma}_z \right\}. \quad (3.89)$$

The matrices $\mathbf{G}_m(\omega)$ can be calculated using the scheme explained in the appendix B.3. The retarded and advanced embedding self-energy were defined in equation (3.15).

We point out that the calculated DC current may depend on the site indices k and l , i.e. even for a linear chain $I_{k-1,k,\text{DC}}$ is not necessarily equal to $I_{k,k+1,\text{DC}}$ if $\Delta_k \neq 0$ due to the modified continuity equation for superconductors [SPC10].

All quantities can now be calculated numerically. For a practical calculation, the infinite sums in equations (3.84), (3.85), (3.87) and (3.89) have to be truncated, i.e. we replace

$$\sum_{\mathbf{m} \in \mathbb{Z}} \rightarrow \sum_{m=-\mathcal{M}}^{\mathcal{M}} \quad \text{and} \quad \sum_{\mathbf{m} \in \mathbb{Z}^2} \rightarrow \sum_{m_1=-\mathcal{M}}^{\mathcal{M}} \sum_{m_2=-\mathcal{M}}^{\mathcal{M}}. \quad (3.90)$$

The number \mathcal{M} has to be chosen large enough such that one achieves convergence. The choice $\mathcal{M} = 10$ turned out to be a good initial guess. \mathcal{M} has to be increased for small biases as well as for weak couplings.

The integrands of the frequency integrals in equations (3.84), (3.85), (3.87) and (3.89) can vary over several orders of magnitude as shown in figure 3.12. Thus, it is highly recommended to use an adaptive quadrature method for an efficient numerical integration. We chose the Gauss-Kronrod quadrature formula [Kro64, Kro65], which uses 7 points for the quadrature and 15 points for the error estimate.

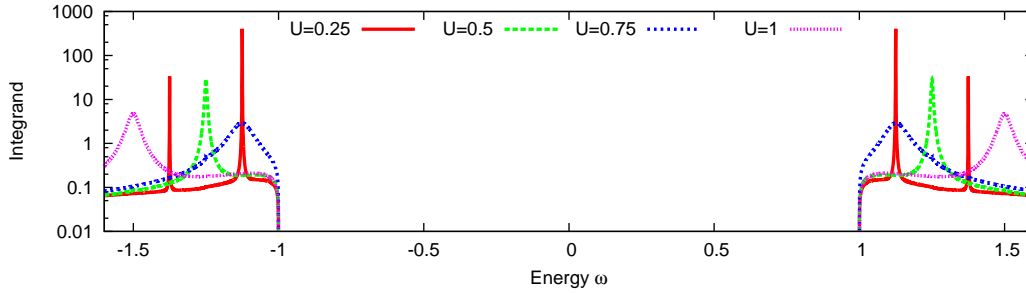


Figure 3.12: Plot of the integrand of equation (3.87) for a SQDS junction with different biases. The energy gap is clearly visible. Note that the vertical axis uses a logarithmic scale. The parameters are: $\Gamma_\alpha = 0.5, U_L = -U_R, \varepsilon_{\text{QD}} = 0$.

3.4 Comparison

We presented three methods to calculate observables of junctions with an applied bias. We now want to briefly compare these three methods:

1. Landauer+Büttiker formula, section 3.1

It only allows to calculate the steady state current. For junctions with superconducting leads, it is not applicable, since there is no steady state due to the AC Josephson effect. But, it can be used for normal and hybrid junctions.

2. Propagation of wave functions, section 3.2

This method propagates single particle wave functions in time and allows for an arbitrary time-dependence of the central Hamiltonian and the biases. It enables us to calculate the density and the current as a function of time. But, the time propagation can be expensive, depending on the

number of time steps. This is typically the case for calculations of the long time limit of the DC current, since one has to ensure that switching effects have died out.

3. Calculation of nonequilibrium Green's functions, section 3.3

We showed how to calculate the large time behaviour of the nonequilibrium Green's functions. The calculation scheme has some limitations for the junction's setup and gives the density and current after the transient, i.e. it does not provide access to switching effects. But, the method is typically computationally cheaper than a long time simulation using the time propagation algorithm. Hence, this method is used whenever possible. It further provides a reference to check the convergence of the "Time propagation method" when performing DC current calculations.

All results obtained by the NEGF method can also be calculated using the time propagation method. The results are identical as one can see in figure 3.13. In this example, we introduced an offset \tilde{t} such that the switching effects have died out at $t - \tilde{t} = 0$.

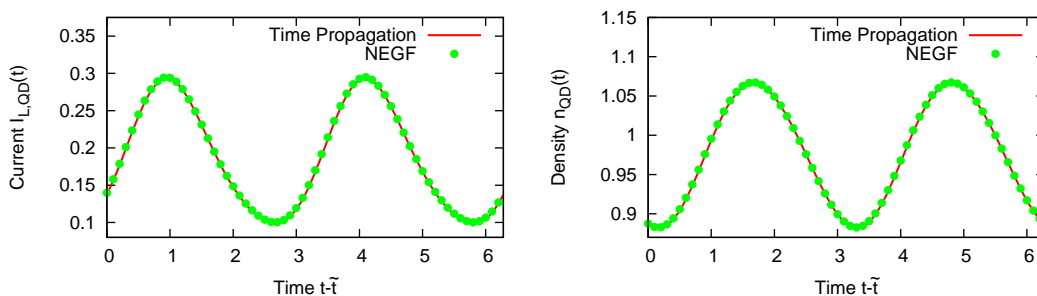


Figure 3.13: Comparison of results obtained by the "Time propagation method" and the "NEGF method" for a SQDS junction. The offset \tilde{t} is chosen such that switching effects have died out at $t - \tilde{t} = 0$. The parameters are: $\Gamma_\alpha = 1, U_L = 1, U_R = 0$ and $\varepsilon_{\text{QD}} = 0$. Times are measured in units of $\hbar\Delta$, energies in units of Δ and the current in units of $\frac{e}{h}\Delta$.

Chapter 4

Features of SQDS junctions

In this chapter, we analyse features of SQDS junctions. In particular, we look at the Josephson effects in SQDS junctions. We recall the basic equations from section 1.2 for the description of the Josephson effects. They are:

$$U(t) = \frac{\hbar}{2e} \frac{d\chi(t)}{dt}, \quad (4.1)$$

$$\chi(0) = \chi_0, \quad (4.2)$$

$$I(t) = I_0 + I_1 \sin(\chi(t)) + I_2 \cos(\chi(t)). \quad (4.3)$$

Originally, $\chi(t)$ represents the phase difference of the Cooper pair wave functions between the right and left lead. In our model, it is equivalent to the phase difference of the pairing potentials, hence $\chi_0 = \chi_R - \chi_L$. The equations were derived using approximations and we will see deviations from these relations. Recall from section 2.3 that we measure energies in units of Δ , currents in units of $\frac{e}{\hbar}\Delta$ and times in units of $\hbar\Delta^{-1}$. We will work with almost identical superconducting leads throughout this chapter, only the phases χ_α may differ between left and right.

4.1 DC Josephson effect

We start this chapter with the demonstration of the DC Josephson effect in SQDS junctions. It is a phenomenon of the ground state, hence $U(t) = 0$. Following the equations (4.1) - (4.3), we expect to see a DC current

$$I = I_1 \sin(\chi_R - \chi_L) \quad (4.4)$$

since I_0 and I_2 vanish in the absence of a bias. Figure 4.1 shows calculated currents in a SQDS junction. There are deviations from the predicted sinusoidal behaviour, being more pronounced for small gate voltages. It further shows that the Andreev bound states produce the main contribution to the current, compensating the opposite current of the scattering states. Deviations from the current-phase relation have already been reported for different types of junctions in various previous works [Gun94, Cue99, PSC09].

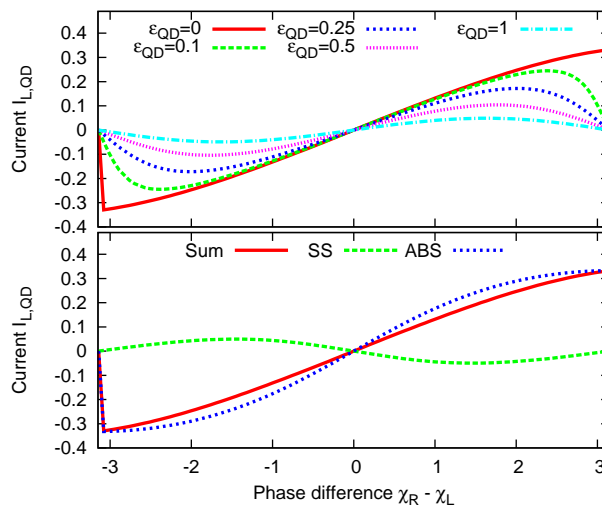


Figure 4.1: Top: DC Josephson effect in a SQDS junction for different values of ε_{QD} . Bottom: Decomposition of the current into contributions of Andreev bound states (ABS) and scattering states (SS). The parameters are: $\Gamma_\alpha = 0.5$ (both) and $\varepsilon_{\text{QD}} = 0$ (only bottom).

The current-phase relation for the ground state has been calculated analytically for a symmetric SQDS junction in the limit $\frac{\Delta}{\Gamma_\alpha} \rightarrow 0$ [Cue99, MRLY11]. It

reads

$$I = \frac{e\Delta}{2\hbar} \frac{\tau \sin \chi_0}{\sqrt{1 - \tau \sin^2 \left(\frac{\chi_0}{2}\right)}}, \quad (4.5)$$

$$\tau = \frac{1}{1 + \frac{\varepsilon_{\text{QD}}^2}{I_\alpha^2}}. \quad (4.6)$$

A comparison of the analytical with the numerical results is shown in figure 4.2.

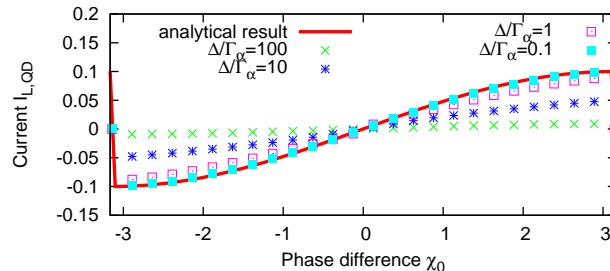


Figure 4.2: Comparison of the analytical results of equation (4.5) with the calculated ones for $\varepsilon_{\text{QD}} = 0$. In this case, the current-phase relation is independent of I_α since $\tau = 1$. The analytical formula describes the limit $\frac{\Delta}{I_\alpha} \rightarrow 0$.

4.2 AC Josephson effect

The AC Josephson effect describes the phenomenon of creating an AC current with frequency $\omega = \frac{2e}{\hbar}U$, if one applies a DC bias U across the junctions. The current-phase relation gives

$$I(t) = I_0 + I_1 \sin\left(\frac{2e}{\hbar}Ut + \chi_0\right) + I_2 \cos\left(\frac{2e}{\hbar}Ut + \chi_0\right). \quad (4.7)$$

Figure 4.3 shows two simulations of a SQDS junction with different applied biases. The bias is switched on step-like at $t = 0$. After the transient, the current is perfectly periodic. The frequency of the oscillations can be analysed by a discrete Fourier transform of the current starting after the transient. This is shown in figure 4.4 for the simulation of figure 4.3 with $U = 1$ (bottom). Besides the peaks at $\omega = \pm 2$ corresponding to the Josephson frequency $\omega_J = \frac{2e}{\hbar}U$, one observes further peaks at $\omega = 0$ and $\omega = \pm 4$. The first one originates from the DC component of the current. The latter is the second harmonic of the Josephson frequency ω_J . In principle, the observation of even higher harmonics

is possible, but their contributions are very small. The higher harmonics of the Josephson frequency are not incorporated in the current-phase relation, but have already been reported in superconducting quantum point contacts [Cue99]. Including the higher harmonics modifies the current-phase relation as follows:

$$I(t) = I_0 + \sum_{m \in \mathbb{N}} I_{1,m} \sin(m\chi(t)) + I_{2,m} \cos(m\chi(t)). \quad (4.8)$$

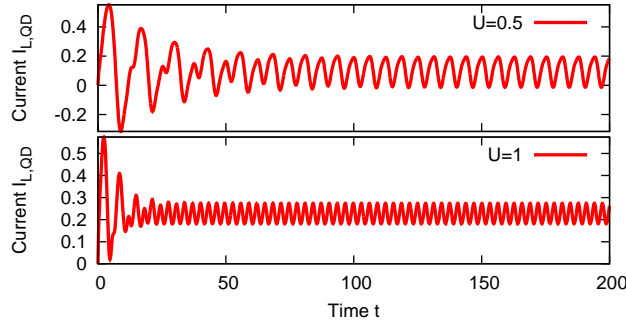


Figure 4.3: AC Josephson effect in a SQDS junction for two different biases: $U = 0.5$ (top) and $U = 1$ (bottom). The parameters are: $\Gamma_\alpha = 1$, $\chi_\alpha = 0$, $\varepsilon_{\text{QD}} = 0$ and $U_L(t) = -U_R(t) = \frac{1}{2}U\Theta(t)$.

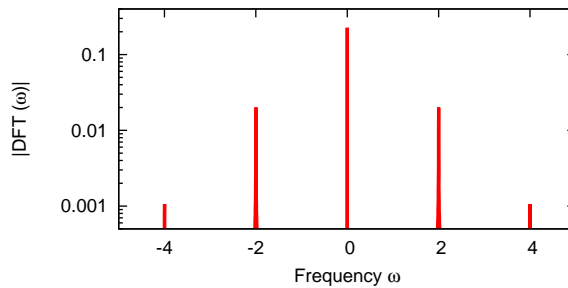


Figure 4.4: Discrete Fourier transform of figure 4.3 (bottom) with $U = 1$, but with an increased simulation time. The peaks are located at $\omega = n\omega_J$, $n \in \mathbb{Z}$ with $\omega_J = \frac{2e}{\hbar}U = 2$. The peaks at $\omega = \pm 2$ correspond to the Josephson frequency ω_J . The central peak at $\omega = 0$ originates from the DC current and the outer two at $\omega = \pm 4$ are the second harmonics of the Josephson frequency ω_J .

4.3 Subharmonic gap structure

We now look at the DC component of the current $I(t)$. We start the simulation in the ground state and switch on the bias U at $t = 0$. The DC component of the current is calculated as

$$I_{L,QD,DC} = \lim_{t \rightarrow \infty} \frac{1}{T_J} \int_t^{t+T_J} dt' I_{L,QD}(t'), \quad T_J = \frac{2\pi}{\omega_J} = \frac{\hbar\pi}{eU}. \quad (4.9)$$

In general, its value is not independent of the position due to the different continuity equation for superconductors [SPC10], i.e. calculating the average of the current inside the leads gives a different result since $\Delta_\alpha \neq 0$. But, $I_{L,QD,DC} = I_{QD,R,DC}$ since $\Delta_{QD} = 0$. Furthermore, the DC current I_{DC} is in general not equivalent to I_0 as it can be seen in the derivation of the inverse AC Josephson effect. Figure 4.5 shows the DC current for SQDS junctions with different couplings Γ_α . There are clearly visible steps at voltages $U = \frac{2\Delta}{n+1}$ with even n . The steps with odd n are suppressed, the one being best visible lies at $U = 1$. The suppression has already been observed and explained in previous works [LYCLDMR97, JBSW99]. It is absent for directly coupled superconductors, i.e. in superconducting quantum point contacts [CMRY96]. The origin of the suppression will be explained later. This structure of the DC current-voltage characteristics is called subharmonic gap structure.

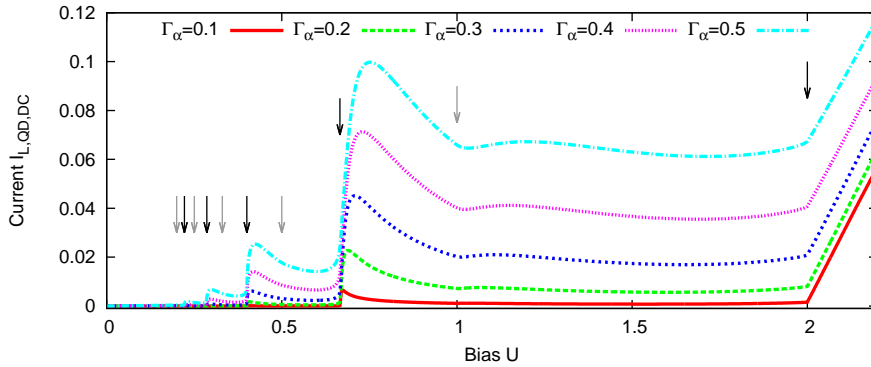


Figure 4.5: Subharmonic gap structure for different coupling strengths Γ_α . The arrows mark the positions of steps. Grey arrows indicate suppressed steps. The parameters are: $\varepsilon_{QD} = 0$ and $U_L = -U_R = \frac{1}{2}U$.

The origins of the subharmonic gap structure are the different possible charge transfer mechanisms in Josephson junctions. A direct transmission is only possible for $U > 2\Delta$ due to the superconducting gap. For a smaller bias, the only

possible charge transfer mechanism is the Andreev reflection. Figure 4.6 shows the four charge transfer mechanisms with the lowest number of Andreev reflections. The onsets of the steps in figure 4.5 are related to the opening of new transmissions channels. For example, the cusp at $U = 2\Delta$ originates from the direct transmissions process and the step at $U = \frac{2}{3}\Delta$ corresponds to the process with two Andreev reflections. In the sketch, the central region is represented by a single resonant level at $\omega = 0$. Processes with an odd number of Andreev reflections are off-resonance and thus suppressed. Unlike in the case of normal or hybrid junctions, the energy of the resonance is not the same as the gate voltage energy ε_{QD} , but additionally depends on the parameters Γ_α and U_α . In the case of a symmetric junction with $\varepsilon_{\text{QD}} = 0$ and $U_L = -U_R$, the resonance is located at $\omega = 0$. In all other cases, it is not known in advance. The deviation of the effective resonance from ε_{QD} has already been reported [LYCLDMR97], but the authors did not go into any details. The steps would be at $\frac{2(\Delta \pm \varepsilon_{\text{QD}})}{n+1}$ with even n , if there is no deviation.

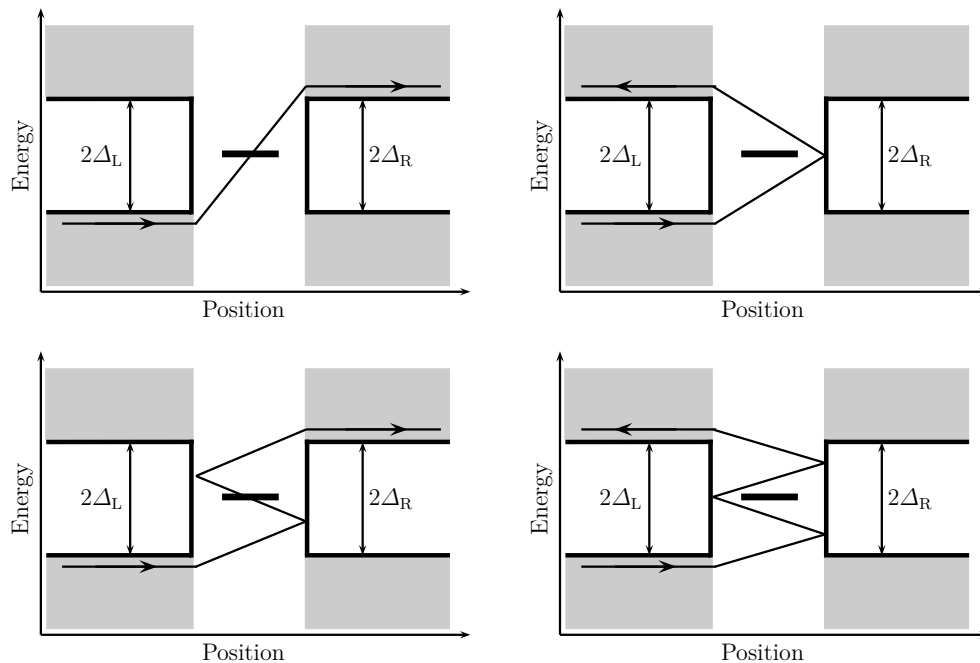


Figure 4.6: Sketch of four charge transfer processes. The energy is the excitation energy of the particles, hence the scattered hole of an Andreev reflection is at the same energy as the incident electron. Recall that a bias in the leads can be gauged into an electric field in the central region. In this way, the leads remain unchanged, simplifying the plots. The horizontal bar represents the resonant level in the central region. Processes with an odd number of Andreev reflections do not cross the resonance and are suppressed.

The dependence of the effective resonance on the gate voltage and the bias can be seen in figure 4.7. It shows the DC current $I_{L,QD,DC}$ as a function of the applied bias and the gate voltage for two different junctions. Figure 4.5

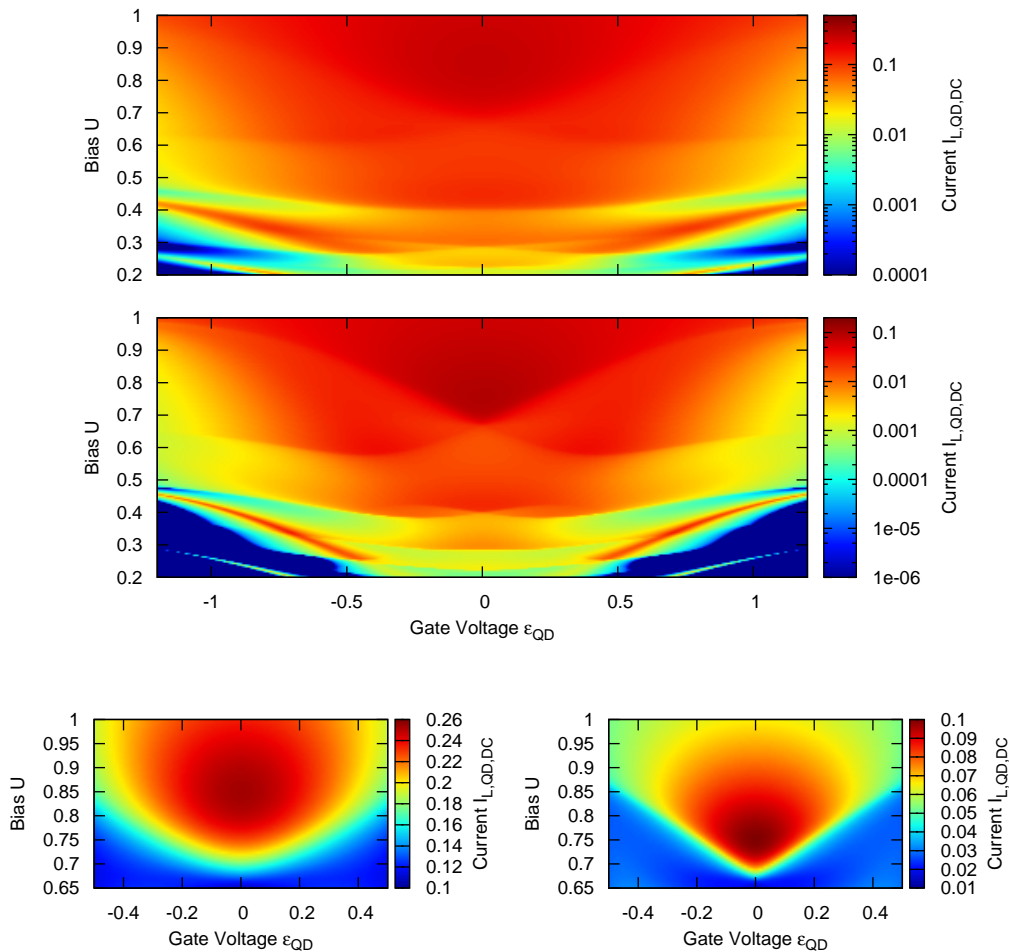


Figure 4.7: Time averaged current as a function of the bias U and the gate voltage ϵ_{QD} for $\Gamma_\alpha = 1$ (top) and $\Gamma_\alpha = 0.5$ (middle). The figures at the bottom are magnifications: The bottom left one of $\Gamma_\alpha = 1$ (top) and the bottom right one of $\Gamma_\alpha = 0.5$ (middle). Note that the color scales differ amongst all plots.

corresponds to a cut along $\epsilon_{QD} = 0$. There are numerous valleys, peaks and edges visible. Comparing the top and the middle plot of the figure shows, that the structure depends on the coupling. Minima and maxima are not always at the same position in the two plots. The edges in the plotted landscape, which correspond to steps in the current-voltage characteristics, show a non-linear behaviour as a function of the gate voltage. This indicates, that in the simple picture of a single resonance, the energy changes non-linearly with the gate voltage. Nevertheless, these edges can be associated with new resonant

transmissions processes.

The dependence of the DC current-voltage characteristics on the coupling Γ_α is demonstrated in figure 4.8, where the connection is better visible compared to figure 4.7. The positions of the edges change with Γ_α . In the chosen parameters regime, there seems to be an exponential dependence of the edges on the coupling Γ_α .

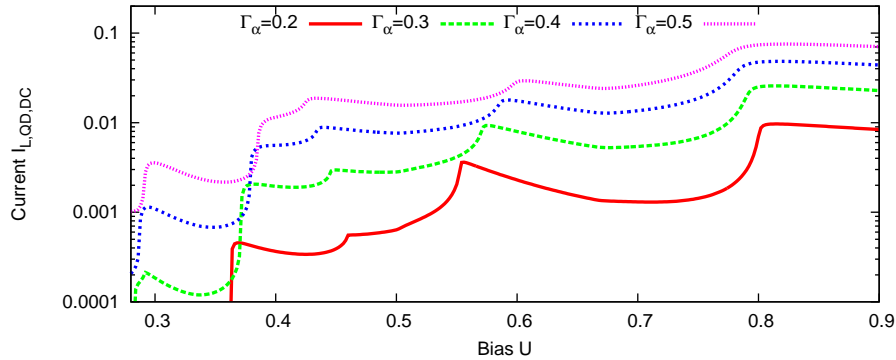


Figure 4.8: Dependence of the subharmonic gap structure on the coupling strength Γ_α . The parameters are $\varepsilon_{\text{QD}} = 0.25$, $U_L = -U_R = \frac{1}{2}U$.

4.4 Inverse AC Josephson effect

We apply an AC bias starting at $t = 0$

$$U(t) = U_{\text{DC}} + U_{\text{AC}} \cos(\omega_{\text{AC}} t). \quad (4.10)$$

The expression for the DC current using the Josephson equations is derived in section 1.2 and reads

$$I_{\text{DC}} = I_0 + \sum_{m \in \mathbb{Z}} \sqrt{I_1^2 + I_2^2} J_{-m} \left(\frac{2eU_{\text{AC}}}{\hbar\omega_{\text{AC}}} \right) \sin \left(\chi_0 + \arctan \frac{I_2}{I_1} \right) \delta_{\frac{2e}{\hbar}U_{\text{DC}}, m\omega_{\text{AC}}}. \quad (4.11)$$

Taking higher harmonics into account changes the formula for the current to

$$I(t) = I_0 + \sum_{m \in \mathbb{N}} \left(I_{1,m} \sin(m\chi(t)) + I_{2,m} \cos(m\chi(t)) \right). \quad (4.12)$$

The DC component of the current is expressed as

$$I_{\text{DC}} = I_0 + \sum_{m_1 \in \mathbb{N}} \sum_{m_2 \in \mathbb{Z}} I_{1,2,m_1} J_{-m_2} \left(\frac{2em_1 U_{\text{AC}}}{\hbar \omega_{\text{AC}}} \right) \sin(m_1 \chi_0 + \chi_{m_1}) \delta_{\frac{2e}{\hbar} m_1 U_{\text{DC}}, m_2 \omega_{\text{AC}}} \quad (4.13)$$

with $I_{1,2,m_1} = \sqrt{I_{1,m_1}^2 + I_{2,m_1}^2}$ and $\chi_{m_1} = \arctan \frac{I_{2,m_1}}{I_{1,m_1}}$. Figure 4.9 shows results of a DC current-voltage characteristic calculation. The phase difference χ_0 is

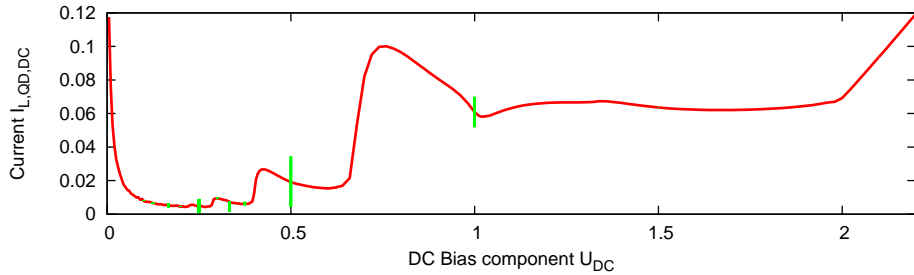


Figure 4.9: DC current-voltage characteristics showing the inverse AC Josephson effect with χ_0 being varied between $-\pi$ and π . The green spikes show that the DC current depends on the initial value χ_0 at the discrete energies $\frac{\hbar}{2e} \frac{m_2}{m_1} \omega_{\text{AC}}$. We plotted all spikes with $m_1, m_2 \leq 4$, but only the ones with $U_{\text{DC}} = \frac{m_2}{m_1} = \frac{1}{2}, \frac{2}{3}, 1$ and 2 are clearly visible. The others are very small. The parameters are: $\Gamma_\alpha = 0.5, \varepsilon_{\text{QD}} = 0, U_{\text{AC}} = 0.2, \omega_{\text{AC}} = 1$ and $U_{\text{L}}(t) = -U_{\text{R}}(t) = \frac{1}{2} U_{\text{DC}} + \frac{1}{2} U_{\text{AC}} \cos(\omega_{\text{AC}} t)$.

varied between $-\pi$ and π . The spikes are located at $U_{\text{DC}} = \frac{\hbar}{2e} \frac{m_2}{m_1} \omega_{\text{AC}}$, but only the ones with $\frac{m_2}{m_1} = \frac{1}{2}, \frac{2}{3}, 1$ and 2 are clearly visible.

The current I_{DC} at a spike depends on the chosen initial phase difference χ_0 . We plotted the DC current for different values of $\frac{m_2}{m_1}$ in figure 4.10. The dominating frequency of the oscillation is determined by the minimal possible value of m_1 . This demonstrates again the existence of higher harmonics of the Josephson frequency in the current. The ratio $\frac{I_{2,m_1}}{I_{1,m_1}}$ depends on the geometry of the junction. Figure 4.11 shows the calculated current $I_{\text{L,QD,DC}}(\chi_0)$ for $U_{\text{DC}} = 0.5$ and different gate voltages ε_{QD} .

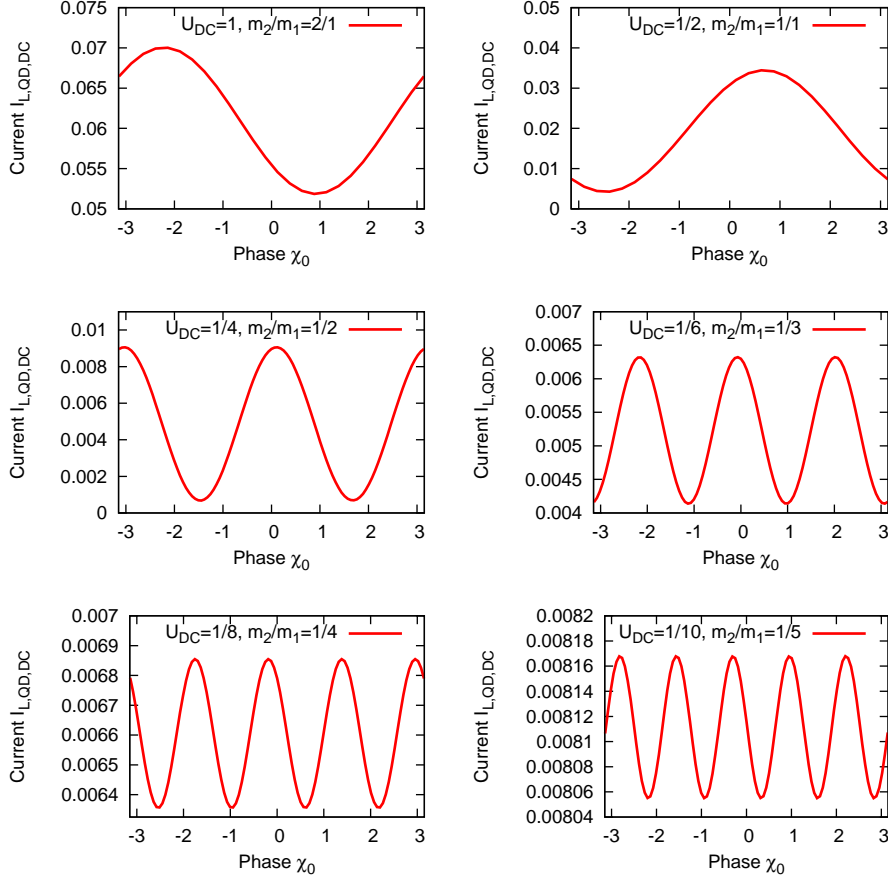


Figure 4.10: Dependence of the current $I_{L,QD,DC}$ on the initial phase difference χ_0 for different values of $\frac{m_2}{m_1}$. The frequency is dominated by the minimum value of m_1 . The parameters are: $\Gamma_\alpha = 0.5$, $\xi_\alpha = 1$, $U_{AC} = 0.2$, $\omega_{AC} = 1$, $U_{DC} = 0.5$ and $U_L(t) = -U_R(t) = \frac{1}{2}U_{DC} + \frac{1}{2}U_{AC} \cos(\omega_{AC})$.

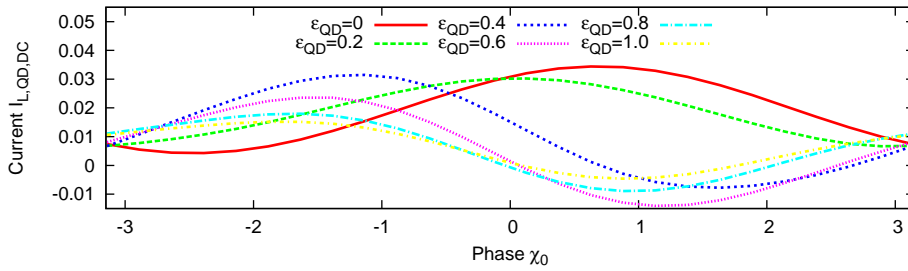


Figure 4.11: Dependence of the current $I_{L,QD,DC}$ on the initial phase difference χ_0 and gate voltage ϵ_{QD} . The parameters are: $\Gamma_\alpha = 0.5$, $U_{AC} = 0.2$, $\omega_{AC} = 1$, $U_{DC} = 0.5$ and $U_L(t) = -U_R(t) = \frac{1}{2}U_{DC} + \frac{1}{2}U_{AC} \cos(\omega_{AC})$.

The second effect of the AC bias on the DC current-voltage characteristics are the Shapiro steps [Sha63]. They modify the subharmonic gap structure by splitting the large steps up into several small equidistant steps. They can be explained by the absorption and emission of one or more quanta ω_{AC} by particles in the central region. An example is shown in figure 4.12. The steps of the subharmonic gap structure for $\varepsilon_{QD} = 0$ are at $U_{DC} = \frac{2\Delta}{n+1}$. Taking the absorption and emission of multiple quanta ω_{AC} into account yields the steps at $U_{DC} = \frac{2\Delta \pm k\omega_{AC}}{n+1}$. Recall that the steps with even n are suppressed since they are off resonance. The same argument can be applied to the emission and absorption of quanta ω_{AC} , suppressing processes with an odd number k of emitted or absorbed quanta ω_{AC} .

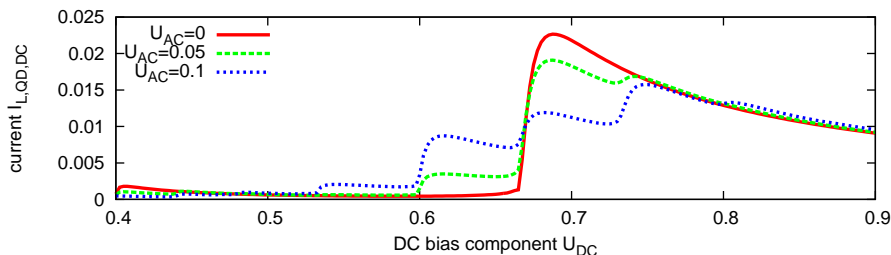


Figure 4.12: Current-voltage characteristics for a SQDS junctions with an AC bias $U_L(t) = -U_R(t) = \frac{1}{2}U_{DC} + \frac{1}{2}U_{AC} \cos(\omega_{AC}t)$. The parameters are: $\Gamma_\alpha = 0.2, \varepsilon_{QD} = 0, \omega_{AC} = 0.1$.

A very similar situation occurs in the presence of an oscillating gate voltage $\varepsilon_{QD}(t) = V_0 \cos(\omega_{AC}t)$ but without the AC bias. The oscillation can be gauged away from the central region into the bias substituting $U_\alpha(t)$ by $U_\alpha(t) - V_0 \cos(\omega_{AC}t)$. This also enables assisted charge transfers and produces a similar additional step structure. Comparing the figures 4.12 and 4.13 shows this close relationship.

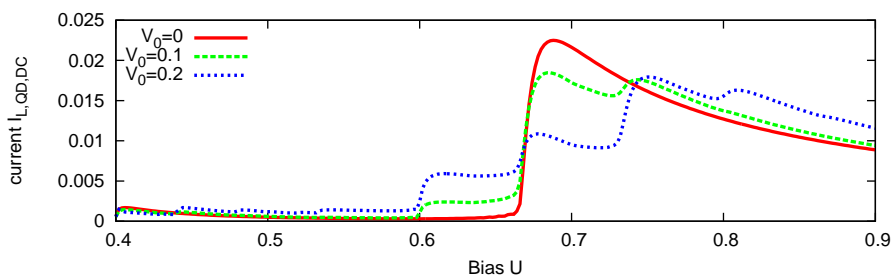


Figure 4.13: Current-voltage characteristics for a SQDS junctions with an oscillating gate voltage $\varepsilon_{QD}(t) = V_0 \cos(\omega_{AC}t)$. The parameters are: $\Gamma_\alpha = 0.2, U_L = -U_R = \frac{1}{2}U$ and $\omega_{AC} = 0.1$.

4.5 Insights from the spectral function

In this section we study the spectral function $\mathbf{A}(t, t')$ of the Keldysh nonequilibrium Green's function. It is a useful tool to understand the internal changes of molecular junctions. It provided valuable insights in the dynamics of molecular junctions [MSSvL09, MSSvL10, UKS⁺10, UKS⁺11, KUS⁺12]. The definition of the spectral functions [SvL13] is

$$\mathbf{A}(t, t') = i [\mathbf{G}^>(t, t') - \mathbf{G}^<(t, t')] \quad (4.14)$$

$$= i [\mathbf{G}^R(t, t') - \mathbf{G}^A(t, t')] \quad (4.15)$$

where $\mathbf{G}^{\gtrless}(t, t')$ are the standard greater (lesser) nonequilibrium Green's functions defined in section 2.2.2. Introducing the average time $T = \frac{t+t'}{2}$, we can define the Fourier transform of $\mathbf{A}(t, t')$ with respect to the relative time $\tau = t - t'$ as

$$\mathbf{A}(\omega, T) = \frac{1}{2\pi} \int_{-\infty}^{\infty} d\tau e^{i\omega\tau} \mathbf{A}\left(T + \frac{\tau}{2}, T - \frac{\tau}{2}\right). \quad (4.16)$$

$\mathbf{A}(\omega, T)$ is a matrix with respect to some representation referring, e.g. to space and spin coordinates $\mathbf{A}_{r\sigma, r'\sigma'}(\omega, T)$ or to localized orbitals $\mathbf{A}_{i,j}(\omega, T)$. The objective of this section is to give a clear-cut physical interpretation of the diagonal of this matrix. In particular we shall investigate whether and to which extent it can be viewed as a time-dependent density of states.

We present two approaches to calculate the spectral function $\mathbf{A}(\omega, T)$ in situations with an applied bias. The first one uses single particle wave functions which are obtained by the method explained in section 3.2. The greater and lesser Green's functions can then be calculated as [SPC10]:

$$[\mathbf{G}^{\gtrless}(t, t')]_{kl} = i \sum_q \mathcal{F}_q^{\gtrless}(\varepsilon_q) \begin{pmatrix} u_{k,q}(t) [u_{l,q}(t')]^* & u_{k,q}(t) [v_{l,q}(t')]^* \\ v_{k,q}(t) [u_{l,q}(t')]^* & v_{k,q}(t) [v_{l,q}(t')]^* \end{pmatrix}. \quad (4.17)$$

The Fermi functions $f^{\gtrless}(\omega)$ were defined in subsection 3.2.3 and fulfill $f^<(\omega) - f^>(\omega) = 1$. The symbol \mathcal{F}_q stands for the integration over scattering states and the summation over bound states. Thus, the spectral function $\mathbf{A}(t, t')$ is

$$[\mathbf{A}(t, t')]_{kl} = \sum_q \begin{pmatrix} u_{k,q}(t) [u_{l,q}(t')]^* & u_{k,q}(t) [v_{l,q}(t')]^* \\ v_{k,q}(t) [u_{l,q}(t')]^* & v_{k,q}(t) [v_{l,q}(t')]^* \end{pmatrix}. \quad (4.18)$$

The Fourier transform in equation (4.16) is done on a grid using the fast

Fourier transform algorithm. Since the grid is finite, one implicitly assumes that $\mathbf{A}(t, t') \rightarrow 0$ if $|t - t'| \rightarrow \infty$, which is a reasonable assumption if there are no bound states.

The second approach calculates the large time behaviour of $\mathbf{A}(\omega, T)$ with respect to T . It adapts the ideas of section 3.3 and uses the NEGF functions. The Fourier transform of equation (4.16) is calculated analytically and the method also relies on $\mathbf{A}(t, t') \rightarrow 0$ as $|t - t'| \rightarrow \infty$. Furthermore, it has the same two preconditions as the NEGF method presented in section 3.3:

1. The hopping matrices $\mathbf{H}_{\alpha C}(t)$ are time-independent, i.e. $\mathbf{H}_{\alpha C}(t) = \mathbf{H}_{\alpha C}$.
2. The central Hamiltonian can be written as

$$\mathbf{H}_{CC}(t) = \mathbf{H}_{CC}^0 + \mathbf{U}_+ e^{i\omega_0 t} + \mathbf{U}_- e^{-i\omega_0 t}. \quad (4.19)$$

One therefore extends the central region again by one site in both directions and works only with $U_L = -U_R$, $U_L = 0$ or $U_R = 0$. The derivation is carried out in the appendix C.1 and the final equations for $\mathbf{G}_{CC}^{\gtrless}(\omega, T)$ and $\mathbf{A}_{CC}(\omega, T)$ are:

$$\begin{aligned} \mathbf{G}_{CC}^{\gtrless}(\omega, T) \stackrel{T \rightarrow \infty}{\sim} \frac{i}{2\pi} \sum_{\mathbf{m} \in \mathbb{Z}^2} e^{i(m_1+m_2)\omega_0 T} f^{\gtrless} \left(\omega + \frac{\omega_0}{2}(m_1 - m_2) \right) \\ \mathbf{G}_{m_1} \left(\omega + \frac{\omega_0}{2}(m_1 - m_2) \right) \mathbf{\Gamma} \left(\omega + \frac{\omega_0}{2}(m_1 - m_2) \right) \\ \mathbf{G}_{-m_2}^\dagger \left(\omega + \frac{\omega_0}{2}(m_1 - m_2) \right), \end{aligned} \quad (4.20)$$

$$\begin{aligned} \mathbf{A}_{CC}(\omega, T) \stackrel{T \rightarrow \infty}{\sim} \frac{1}{2\pi} \sum_{\mathbf{m} \in \mathbb{Z}^2} e^{i(m_1+m_2)\omega_0 T} \mathbf{G}_{m_1} \left(\omega + \frac{\omega_0}{2}(m_1 - m_2) \right) \\ \mathbf{\Gamma} \left(\omega + \frac{\omega_0}{2}(m_1 - m_2) \right) \mathbf{G}_{-m_2}^\dagger \left(\omega + \frac{\omega_0}{2}(m_1 - m_2) \right). \end{aligned} \quad (4.21)$$

The matrices $\mathbf{G}_m(\omega)$, $\mathbf{\Gamma}(\omega)$ and the Fermi functions $f^{\gtrless}(\omega)$ are defined in section 3.3. The time-averaged spectral function reads

$$\mathbf{A}_{CC,DC}(\omega) = \lim_{\tilde{t} \rightarrow \infty} \frac{\omega_0}{2\pi} \int_{\tilde{t}}^{\tilde{t} + \frac{2\pi}{\omega_0}} dT \mathbf{A}_{CC}(\omega, T) \quad (4.22)$$

$$= \frac{1}{2\pi} \sum_{m \in \mathbb{Z}} \mathbf{G}_m(\omega + m\omega_0) \mathbf{\Gamma}(\omega + m\omega_0) \mathbf{G}_m^\dagger(\omega + m\omega_0). \quad (4.23)$$

In the ground state, the spectral function $\mathbf{A}(\omega, T)$ is independent of T and has peaks at the removal and addition energies. The same holds for a steady

state [MSSvL10]. Furthermore, [HJ96] relates $\mathbf{A}(\omega, T)$ to a time-dependent density of states. Until now, the time-dependent spectral function $\mathbf{A}(\omega, T)$ has only been analysed for normal conducting systems [Arr02, MSSvL09, MSSvL10, UKS+10, UKS+11, KUS+12].

Depending on the situation, we calculate $\mathbf{G}_{\text{CC}}^{\geq}(\omega, T)$ and $\mathbf{A}_{\text{CC}}(\omega, T)$ from the propagated single particle wave functions or by using the NEGF approach. The latter gives a better resolutions at lower computational cost and it used whenever possible.

4.5.1 Ground state

In the ground state, the Green's functions $\mathbf{G}^{\geq}(t, t')$ depend only on the time difference $\tau = t - t'$. We denote the Fourier transforms with respect to $t - t'$ of the Green's functions by $\mathbf{G}^{\geq}(\omega)$. The ground state density on the quantum dot at an arbitrary time t reads

$$n_{\text{QD}}(t) = \sum_{\sigma \in \{\uparrow, \downarrow\}} \langle \hat{c}_{\text{QD}\sigma, \text{H}}^{\dagger}(t) \hat{c}_{\text{QD}\sigma, \text{H}}(t) \rangle \quad (4.24)$$

$$= -i \left[\mathbf{G}_{\text{QD}}^{<}(t, t) \right]_{\uparrow\uparrow} + i \left[\mathbf{G}_{\text{QD}}^{>}(t, t) \right]_{\downarrow\downarrow} \quad (4.25)$$

$$= -i \int_{-\infty}^{\infty} dt' \int_{-\infty}^{\infty} d\omega e^{-i\omega(t-t')} \left[\mathbf{G}_{\text{QD}}^{<} \left(\omega, \frac{t+t'}{2} \right) \right]_{\uparrow\uparrow} \delta(t-t') \quad (4.26)$$

$$+ i \int_{-\infty}^{\infty} dt' \int_{-\infty}^{\infty} d\omega e^{-i\omega(t-t')} \left[\mathbf{G}_{\text{QD}}^{>} \left(\omega, \frac{t+t'}{2} \right) \right]_{\downarrow\downarrow} \delta(t-t')$$

$$= -i \int_{-\infty}^{\infty} d\omega \left[\mathbf{G}_{\text{QD}}^{<}(\omega, t) \right]_{\uparrow\uparrow} + i \int_{-\infty}^{\infty} d\omega \left[\mathbf{G}_{\text{QD}}^{>}(\omega, t) \right]_{\downarrow\downarrow} \quad (4.27)$$

$$= -i \int_{-\infty}^{\infty} d\omega \left[\mathbf{G}_{\text{QD}}^{<}(\omega) \right]_{\uparrow\uparrow} + i \int_{-\infty}^{\infty} d\omega \left[\mathbf{G}_{\text{QD}}^{>}(\omega) \right]_{\downarrow\downarrow}. \quad (4.28)$$

We use the fluctuation-dissipation theorem [HJ96, SvL13]

$$\mathbf{G}^{<}(\omega) = i f^{<}(\omega) \mathbf{A}(\omega), \quad (4.29)$$

$$\mathbf{G}^{>}(\omega) = i f^{>}(\omega) \mathbf{A}(\omega) \quad (4.30)$$

with $f^{<}(\omega) = [1 + \exp(\beta\omega)]^{-1}$, $f^{>}(\omega) = f^{<}(\omega) - 1$ and finally arrive at

$$n_{\text{QD}}(t) = \int_{-\infty}^{\infty} d\omega f^{<}(\omega) \left[\mathbf{A}_{\text{QD}}(\omega) \right]_{\uparrow\uparrow} - \int_{-\infty}^{\infty} d\omega f^{>}(\omega) \left[\mathbf{A}_{\text{QD}}(\omega) \right]_{\downarrow\downarrow}. \quad (4.31)$$

Thus, $[\mathbf{A}_{\text{QD}}(\omega)]_{\sigma\sigma}$ corresponds to the density of states for spin up electrons ($\sigma = \uparrow$) or spin down holes ($\sigma = \downarrow$). The spectral function $\mathbf{A}_{\text{QD}}(\omega)$ can be obtained using equations (4.15) - (4.16) and

$$\mathbf{G}_{\text{QD}}^{\text{R/A}}(\omega) = \lim_{\eta \searrow 0} [(\omega \pm i\eta)\mathbf{1} - \mathbf{H}_{\text{QD}}(0) - \Sigma_{\text{L}}^{\text{R/A}}(\omega) - \Sigma_{\text{R}}^{\text{R/A}}(\omega)]^{-1}. \quad (4.32)$$

Figure 4.14 shows the density of states of a SQDS junction obtained from the spectral function.

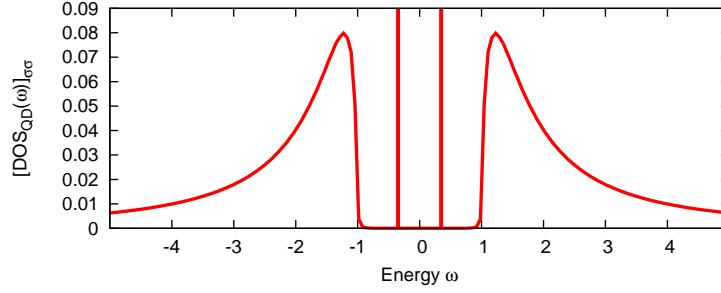


Figure 4.14: Density of states on the quantum dot (spin up and down components are identical). The gap ranges from -1 to 1 , inside there are only the two Andreev bound states. The parameters are: $\Gamma_{\alpha} = 0.5$, $\chi_{\alpha} = 0$ and $\varepsilon_{\text{QD}} = 0$.

4.5.2 Nonequilibrium state - constant bias

In nonequilibrium situations, the Green's functions $\mathbf{G}^{\geq}(t, t')$ depend explicitly on both times t and t' . We use the average time coordinate $T = \frac{t+t'}{2}$ and the relative time $\tau = t - t'$ for the Fourier transforms with respect to τ . They are written as $\mathbf{G}^{\geq}(\omega, T)$ and $\mathbf{A}(\omega, T)$. The time-dependent density can be reformulated as

$$n_{\text{QD}}(t) = -i [\mathbf{G}_{\text{QD}}^{\leq}(t, t)]_{\uparrow\uparrow} + i [\mathbf{G}_{\text{QD}}^{\geq}(t, t)]_{\downarrow\downarrow} \quad (4.33)$$

$$= -i \int_{-\infty}^{\infty} d\omega [\mathbf{G}_{\text{QD}}^{\leq}(\omega, \frac{t+t}{2})]_{\uparrow\uparrow} + i \int_{-\infty}^{\infty} d\omega [\mathbf{G}_{\text{QD}}^{\geq}(\omega, \frac{t+t}{2})]_{\downarrow\downarrow}. \quad (4.34)$$

Hence, $[\mathbf{G}_{\text{QD}}^{\leq}(\omega, T)]_{\uparrow\uparrow}$ and $[\mathbf{G}_{\text{QD}}^{\geq}(\omega, T)]_{\downarrow\downarrow}$ contain information about electrons at time T . In contrast, $[\mathbf{G}_{\text{QD}}^{\leq}(\omega, T)]_{\downarrow\downarrow}$ and $[\mathbf{G}_{\text{QD}}^{\geq}(\omega, T)]_{\uparrow\uparrow}$ are determined by holes at time T . Thus, the spectral function $\mathbf{A}_{\text{QD}}(\omega, T)$ contains information of electrons and holes. For normal and hybrid junctions in the steady state, $\mathbf{A}_{\text{QD}}(\omega, T)$ is again independent of T and has peaks at the removal and addition energies.

For Josephson junctions, $\mathbf{A}_{\text{QD}}(\omega, T)$ is not independent of T due to the AC Josephson effect. This can be seen in figure 4.15, which shows a calculation of $[\mathbf{A}_{\text{QD}}(\omega, T)]_{\sigma\sigma}$ and $[\mathbf{A}_{\text{QD,DC}}(\omega)]_{\sigma\sigma}$ using the NEGF method for a SQDS junction.

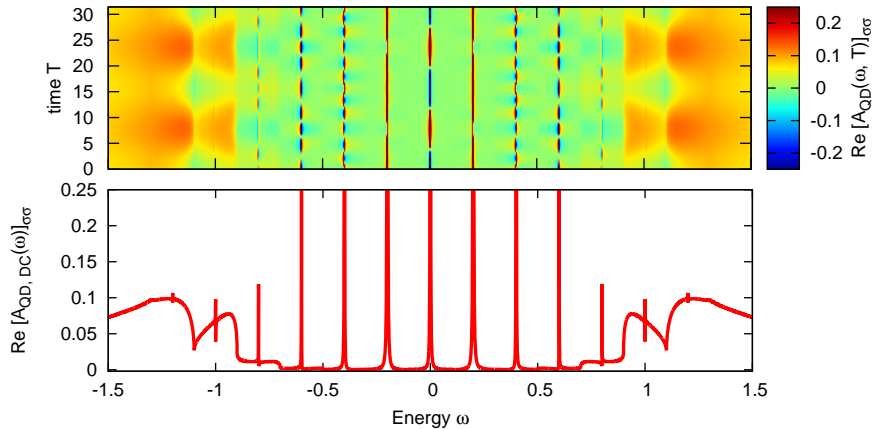


Figure 4.15: Top: Spectral function $[\mathbf{A}_{\text{QD}}(\omega, T)]_{\sigma\sigma}$. Bottom: Time averaged the spectral function $[\mathbf{A}_{\text{QD,DC}}(\omega)]_{\sigma\sigma}$. The bias has been switched on in the past. The imaginary part of the spectral function vanishes. The peaks have a finite width and height. The parameters are: $\Gamma_\alpha = 0.5$, $\varepsilon_{\text{QD}} = 0$ and $U_L = -U_R = 0.1$, $\eta = 10^{-9}$, $m_{\text{max}} = 20$.

The bias has been applied in the past. The whole structure is periodic in time according to the Josephson effect with frequency $\omega_J = \frac{2eU}{\hbar}$. Both edges of the gap structure are split up. The new ones are located at $\Delta \pm \frac{U}{2}$ and $-\Delta \pm \frac{U}{2}$. Inside the gap, there is peak structure with a spacing between the peaks of the bias U .

In the plot of the time resolved spectral function $\mathbf{A}_{\text{QD}}(\omega, T)$, we further observe small areas with negative values, mostly inside the gap. These findings contradict the interpretation of the diagonal of the spectral function $\mathbf{A}(\omega, T)$ as a time-dependent density of states, which has to be non-negative. The effect is absent in the time-averaged spectral function $\mathbf{A}_{\text{QD,DC}}(\omega)$: It is non-negative for all energies ω . This phenomenon has already been found in a study on metallic rings [Arr02], but was not further investigated. To the best of our knowledge, negative values of $\mathbf{A}(\omega, T)$ did not occur in all other studies of this quantity.

We investigate this issue and provide a reasonable explanation incorporating these negative areas. The diagonal of the spectral function $\mathbf{A}(\omega, T)$ is an

analogue of the Wigner function. The latter is defined as [Wig32]

$$P(x,p) = \frac{1}{2\pi\hbar} \int_{-\infty}^{\infty} dy e^{-ipy/\hbar} \psi\left(x + \frac{y}{2}\right) \left[\psi\left(x - \frac{y}{2}\right)\right]^* \quad (4.35)$$

$$= \frac{1}{2\pi\hbar} \int_{-\infty}^{\infty} dq e^{iqx/\hbar} \psi\left(p + \frac{q}{2}\right) \left[\psi\left(p - \frac{q}{2}\right)\right]^*. \quad (4.36)$$

It links the quantum mechanical wave functions $\psi(x)$ and $\psi(p)$ to a phase space distribution $P(x,p)$. But, $P(x,p)$ can have small negative areas [Sch01]. Hence, the simple probability interpretation of the Wigner function $P(x,p)$ is not possible. In fact, it is not unusual that $P(x,p)$ has negative areas. This issue has been solved [Ste80] by taking into account the uncertainty principle:

$$\sigma_x \sigma_p \geq \frac{\hbar}{2}, \quad (4.37)$$

$$\sigma_x = \sqrt{\langle \hat{x}^2 \rangle - \langle \hat{x} \rangle^2}, \quad (4.38)$$

$$\sigma_p = \sqrt{\langle \hat{p}^2 \rangle - \langle \hat{p} \rangle^2}. \quad (4.39)$$

This means that one cannot determine momentum and position with arbitrary precision at the same time and hence, a phase space distribution $P(x,p)$ with arbitrary sharp values of x and p does not make sense in the quantum world. In order to achieve a measurable quantity one should take a weighted average of $P(x,p)$ in some region, i.e. one should for instance investigate

$$\tilde{P}(x,p) = \iint_{-\infty}^{\infty} dx' dp' P(x',p') M_{\sigma_x, \sigma_p}(x - x', p - p'), \quad (4.40)$$

$$M_{\sigma_x, \sigma_p}(x, p) = \frac{\hbar}{2\pi\sigma_x\sigma_p} e^{-\frac{x^2}{2\sigma_x^2} - \frac{p^2}{2\sigma_p^2}} \quad (4.41)$$

rather than $P(x,p)$. It has been proven that $\tilde{P}(x,p)$ is non-negative provided that $\sigma_x, \sigma_p > 0$ and $\sigma_x\sigma_p \geq \frac{\hbar}{2}$ [Car75]. This allows a probability interpretation of $\tilde{P}(x,p)$ including the momentum and position uncertainties.

The formulation of the spectral function $\mathbf{A}(\omega, T)$ stated in equation (4.18) is very similar to the Wigner function $P(x,p)$. The time T is the analogue of the momentum p and the frequency ω corresponds to the position x . Hence it is not surprising to see that the spectral function $\mathbf{A}(\omega, T)$ can have small negative areas. The time-energy uncertainty relation plays the same role for $\mathbf{A}(\omega, T)$ as does the x - p uncertainty relation for $P(x,p)$. Like for the Wigner function, we

can verify the non-negativity of the convoluted spectral function:

$$0 \leq \left[\widetilde{\mathbf{A}}_{\text{QD}}(\omega, T) \right]_{\sigma\sigma} \quad (4.42)$$

$$= \iint_{-\infty}^{\infty} d\omega' dT' [\mathbf{A}_{\text{QD}}(\omega', T')]_{\sigma\sigma} M_{\sigma\omega, \sigma T}(\omega - \omega', T - T'), \quad (4.43)$$

with

$$M_{\sigma\omega, \sigma T}(\omega, T) = \frac{1}{2\pi\sigma\omega\sigma T} e^{-\frac{\omega^2}{2\sigma\omega^2} - \frac{T^2}{2\sigma T^2}}, \quad (4.44)$$

provided that $\sigma\omega, \sigma T > 0$ and $\sigma\omega\sigma T \geq \frac{1}{2}$. The proof is carried out in the appendix C.2. We further point out that $\mathbf{A}_{\text{QD}}(\omega, T)$ and $\widetilde{\mathbf{A}}_{\text{QD}}(\omega, T)$ are normalized such that

$$1 = \int_{-\infty}^{\infty} d\omega [\mathbf{A}_{\text{QD}}(\omega, T)]_{\sigma\sigma} = \int_{-\infty}^{\infty} d\omega \left[\widetilde{\mathbf{A}}_{\text{QD}}(\omega, T) \right]_{\sigma\sigma} \quad (4.45)$$

for $\sigma \in \{\uparrow, \downarrow\}$ and all times T . Hence we conclude that $\widetilde{\mathbf{A}}_{\text{QD}}(\omega, T)$ is a probability density function with respect to ω and allows a direct interpretation as a T -dependent density of states. We note in passing that a probability interpretation referring to the variable T is generally not possible because there is no normalization condition with respect to T .

Two different convolutions of the example in figure 4.15 are shown in figure 4.16. There are no more negative areas as expected. Hence, the spectral function $\mathbf{A}(\omega, T)$ has to be viewed as a quasiprobability density function and only the convoluted spectral function $\widetilde{\mathbf{A}}_{\text{QD}}(\omega, T)$ should be used for direct comparisons with experiments. Furthermore, the two examples show that it is impossible to resolve the peak structure inside the gap and observe the periodicity due to the Josephson effect simultaneously. The spacing of the peak structure is U and time periodicity is $\frac{\hbar}{e} \frac{\pi}{U}$. Hence, one can not resolve both features simultaneously without violating the time-energy uncertainty relation.

Having this interpretation at hand, we are able to explain the structure inside the gap. It is created by particles that cross the gap with the help of Andreev reflections (see figure 4.6). This charge transfer mechanism has been used to explain the subharmonic gap structure in several works [LYCLDMR97, JBSW99]. The negative areas can be viewed as interference effects and reveal the quantum nature of the involved particles.

It is also worth looking at the decomposition of the spectral function $\mathbf{A}_{\text{QD}}(\omega, T)$ into $\mathbf{G}_{\text{QD}}^<(\omega, T)$ and $\mathbf{G}_{\text{QD}}^>(\omega, T)$. This is shown in figure 4.17. Both show a very similar substructure inside the gap compared to the spectral function.

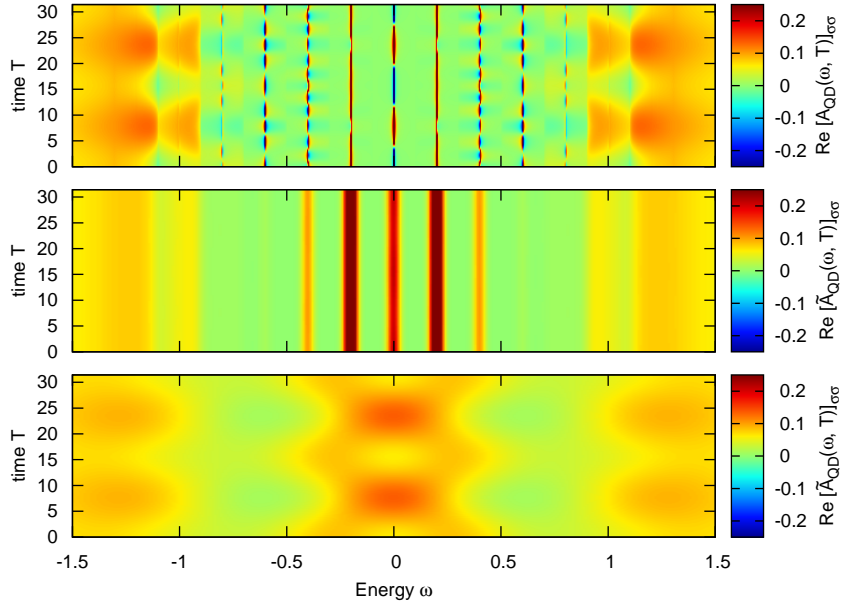


Figure 4.16: Comparison of the convoluted spectral function $[\tilde{\mathbf{A}}_{\text{QD}}(\omega, T)]_{\sigma\sigma}$ (middle and bottom) with the original one $[\mathbf{A}_{\text{QD}}(\omega, T)]_{\sigma\sigma}$ (top). The standard deviations are: $\sigma_\omega = \frac{1}{50}, \sigma_T = 25$ (middle) and $\sigma_\omega = \frac{1}{5}, \sigma_T = 2.5$ (bottom). Both cases fulfill $\sigma_\omega \sigma_T = \frac{1}{2}$. All other parameters are identical to figure 4.15.

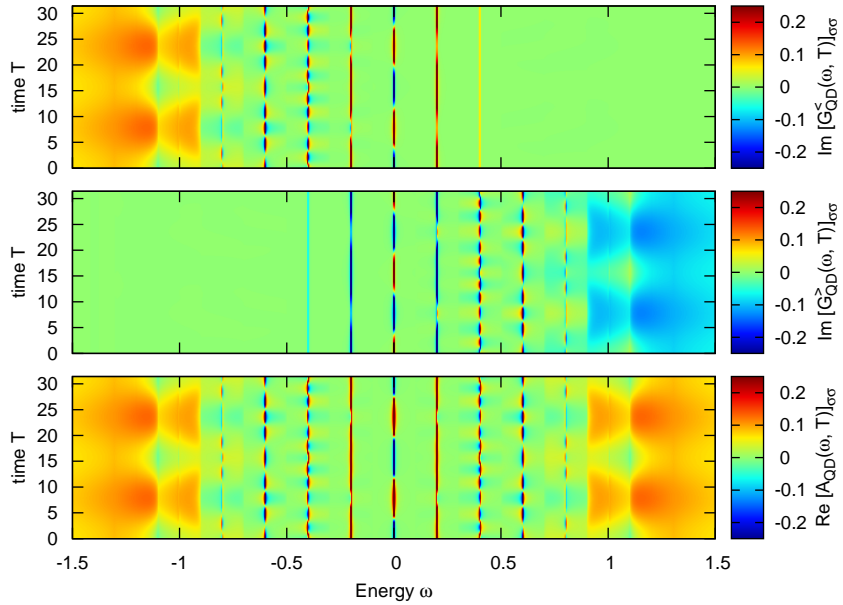


Figure 4.17: Decomposition of the spectral function $[\mathbf{A}_{\text{QD}}(\omega, T)]_{\sigma\sigma}$ into $[\mathbf{G}_{\text{QD}}^<(\omega, T)]_{\sigma\sigma}$ and $[\mathbf{G}_{\text{QD}}^>(\omega, T)]_{\sigma\sigma}$. Recall the definition $\mathbf{A}(\omega, T) = i[\mathbf{G}^>(\omega, T) - \mathbf{G}^<(\omega, T)]$. The bias has been switched on in the past. All parameters are identical to figure 4.15.

4.5.3 Nonequilibrium state - switching the bias

We can also visualize switching effects with the help of the spectral function. We prepare the system in the ground state for $t < 0$ and switch on the bias at $t = 0$. The spectral function is split up into contributions of Andreev bound states (labeled $\mathbf{A}_{\text{QD}}^{(\text{ABS})}(\omega, T)$) and scattering states (labeled $\mathbf{A}_{\text{QD}}^{(\text{SS})}(\omega, T)$). All results of this subsection are calculated using the formulation of equation (4.18) for the spectral function. The Fourier transform with respect to $t - t'$ is done on a grid. We therefore demand for $\mathbf{A}(t, t') \rightarrow 0$ as $|t - t'| \rightarrow \infty$.

In contrast to the previous results, we now have to take Andreev bound states into account. These underline the importance of the previously discussed convolutions in a second way.

Consider a system with a single bound state (BS) whose energy $\varepsilon_{\text{BS}}(t)$ changes adiabatically. Its spectral function $\mathbf{A}^{(\text{BS})}(t, t')$ is then proportional to

$$\mathbf{A}^{(\text{BS})}(t, t') = \psi^{(\text{BS})}(t) \left[\psi^{(\text{BS})}(t') \right]^* \quad (4.46)$$

$$\sim e^{+i\varepsilon_{\text{BS}}(t)t} e^{-i\varepsilon_{\text{BS}}(t')t'}. \quad (4.47)$$

Hence we can conclude $\mathbf{A}^{(\text{BS})}(t, t') \not\rightarrow 0$ as $|t - t'| \rightarrow \infty$. If we then calculate the Fourier transform of $\mathbf{A}^{(\text{BS})}(t, t')$ with respect to $\tau = t - t'$, the full past and future relative to the time $T = \frac{t+t'}{2}$ influences the value of $\mathbf{A}^{(\text{BS})}(\omega, T)$. The spectral function $\mathbf{A}^{(\text{BS})}(\omega, T)$ is not just a single peak at $\varepsilon_{\text{BS}}(T)$ as one would expect since everything changes adiabatically.

This is in contrast to the most common situation where $\mathbf{A}(t, t') \rightarrow 0$ as $|t - t'| \rightarrow \infty$. In this case, only the wave functions at times in a neighborhood of $T = \frac{t+t'}{2}$ have an influence on the value of $\mathbf{A}(\omega, T)$. Besides, this allows us to calculate the Fourier transform numerically on a grid.

The most natural way to recover the desired behaviour even in the presence of bound states is to enforce the decay $\mathbf{A}(t, t') \rightarrow 0$ as $|t - t'| \rightarrow \infty$ by hand. In this way, one mimics a finite lifetime of the bound states. We now show that this is automatically done by the convolution in frequency space presented above.

Using the convolution theorem, the convolution in frequency space can be reformulated as:

$$\frac{1}{\sqrt{2\pi}\sigma_\omega} \int_{-\infty}^{\infty} d\omega' \mathbf{A}(\omega', T) e^{-\frac{(\omega-\omega')^2}{2\sigma_\omega}} = \int_{-\infty}^{\infty} d\tau e^{i\omega\tau} e^{-\frac{\sigma_\omega^2}{2}\tau^2} \mathbf{A}\left(T + \frac{\tau}{2}, T - \frac{\tau}{2}\right). \quad (4.48)$$

Hence, the convolution of the spectral function adds the desired decay

$$e^{-\frac{\sigma_\omega}{2}(t-t')^2} \mathbf{A}(t, t') \rightarrow 0 \quad \text{as } |t - t'| \rightarrow \infty \quad (4.49)$$

even for bound states. Simultaneously, it broadens all sharp frequency peaks of $\mathbf{A}(\omega, T)$.

Since the convolutions smoothen the plots, we only apply it in frequency space to all calculations covering Andreev bound states. The time convolution is not performed in any of the following plots in order to obtain sharper structures. The value of σ_ω is set to $\sqrt{2} \cdot 0.025$ for all plots covering bound states in this section.

Figure 4.18 shows an example of a switching process. The top part shows the contribution of the Andreev bound states $\mathbf{A}_{\text{QD}}^{(\text{ABS})}(\omega, T)$ to the spectral function, the lower part the one of the scattering states $\mathbf{A}_{\text{QD}}^{(\text{SS})}(\omega, T)$. The bias is turned on at $t = 0$.

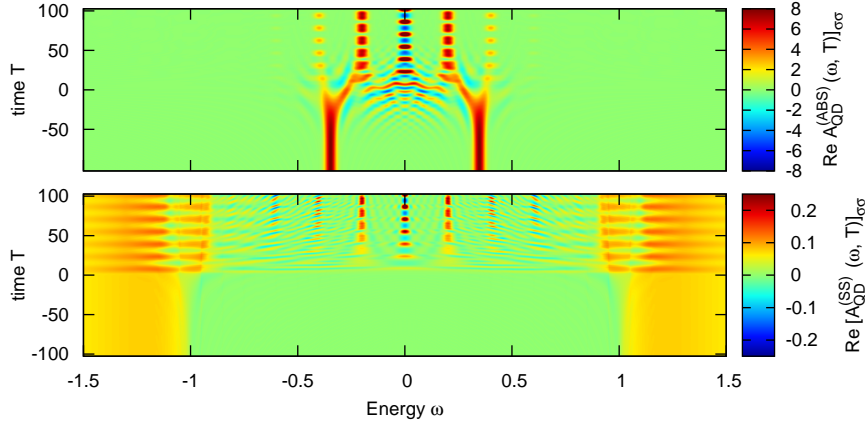


Figure 4.18: Decomposition of the full spectral function $\mathbf{A}_{\text{QD}}(\omega, T)$ into contributions of the Andreev bound states $\mathbf{A}_{\text{QD}}^{(\text{ABS})}(\omega, T)$ (top) and the scattering states $\mathbf{A}_{\text{QD}}^{(\text{SS})}(\omega, T)$ (bottom). The bias is switched on at $t = 0$. The parameters are: $\Gamma_\alpha = 0.5$, $\chi_\alpha = 0$, $\varepsilon_{\text{QD}} = 0$, $U_L(t) = -U_R(t) = 0.1\Theta(t)$.

In the lower part of figure 4.18, the structure already observed in figure 4.15 (top) starts to develop after the bias is switched on at $t = 0$. Simultaneously, the Andreev bound states move gradually into the leads. This can hardly be seen in the top figure since the decay rate in the chosen example is too slow compared to the plotted time range. This phenomenon is displayed in figure 4.19 using different parameters. Initially, the Andreev bound states are localized on the quantum dot. After applying the bias, they move gradually into the leads.

Their contribution to the spectral function will eventually be gone.

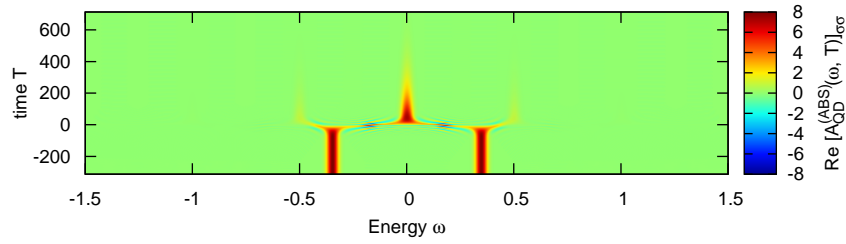


Figure 4.19: Decay of the Andreev bound states in the presence of an applied bias. The parameters are: $\Gamma_\alpha = 0.5$, $\chi_\alpha = 0$, $\varepsilon_{\text{QD}} = 0$ and $U_L(t) = -U_R(t) = 0.25\Theta(t)$

We observe effects of the bias already at times $t < 0$ which hints at a violation of causality of the spectral function. But, in order to compare the results with an experiment, one has to apply convolutions as explained above. This resolves the issue for the examples investigated here. Whether this is generally true is currently unknown.

The reformation of the Andreev bound states after a bias pulse is shown in figure 4.20. Their energy after the bias depends on the accumulated phase $\chi(t) = \chi_0 + \frac{2e}{\hbar} \int_0^t dt' U(t')$. In the situation of a symmetric junction, the location of the Andreev bound states as a function of the phase difference χ can be calculated by solving [SPC10]

$$0 = x^2 \left(1 + \frac{\gamma}{\sqrt{1-x^2}} \right) - e^2 - \frac{\gamma^2}{1-x^2} \frac{1 + \cos \chi}{2} \quad (4.50)$$

with $x = \frac{\omega}{\Delta}$, $e = \frac{\varepsilon_{\text{QD}}}{\Delta}$ and $\gamma = \frac{\Gamma}{\Delta}$.

After the pulse, the system does not evolve towards the ground state again, but shows non-decaying oscillations. The frequency is the energy difference of the newly formed Andreev bound states [SPC10].

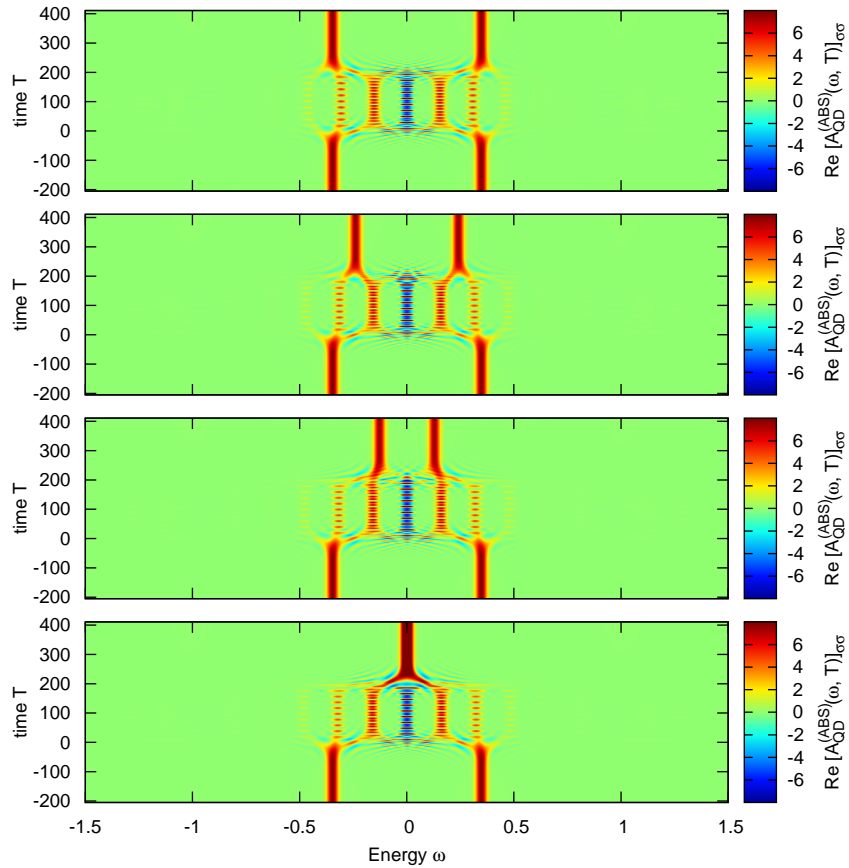


Figure 4.20: Spectral function of the Andreev bound states under the influence of a bias pulse from t_0 to t_1 . The pulse is chosen such that the accumulated phase is $\Delta\chi = \frac{2e}{\hbar} \int_{t_0}^{t_1} U(t') dt' = (20 + x)\pi$, $x \in \{0, 0.5, 0.75, 1\}$ (from top to bottom), $t_0 = 0, t_1 = 204.8$. The parameters are: $\Gamma_\alpha = 0.5, \chi_\alpha = 0, \varepsilon_{\text{QD}} = 0$. The plots show results convoluted in frequency space with $\sigma_\omega = \sqrt{2} \cdot 0.025$.

4.6 Conclusion

In this chapter, we have analysed features of SQDS junctions. We report deviations from the original current-phase relation. Our calculations for the DC Josephson effect agreed with the analytical results for the limit $\frac{\Delta}{F_\alpha} \rightarrow 0$. We observe higher harmonics of the Josephson frequency in the AC and inverse AC Josephson effect. The DC current-voltage characteristics were explained using a simple model. We see that the energy of the resonance is not known a priori and leads to a complicated structure for DC current in the bias-gate voltage landscape. This shows again the complexity of the system compared to junctions with normal-conducting leads.

The spectral function provides a time and energy resolved picture of the quantum dot. We observe negative values of the spectral function implying that the interpretation as a time-dependent density of states is problematic. Viewing it as the time-energy analogue of the Wigner function $P(x,p)$ provides a way out. The latter is well known to have negative values. This issue is solved by looking at averages which then are strictly non-negative. The same can be done for the spectral function, which then allows a physically meaningful interpretation as a time-dependent density of states. It provides useful insights into the internal changes of the quantum dot, which were illustrated by several examples.

The presented framework is not limited to a single quantum dot in the central region, it is possible to work with more complicated structures like e.g. atomic rings. But, it is very likely that the analysis and the interpretation get even more complicated.

Chapter 5

Junctions with classical vibrations

In this chapter, we study junctions with a quantum dot coupled to a vibrational degree of freedom using a mixed quantum classical propagation scheme. The vibration is treated within the Ehrenfest approximation and can be viewed as a classical version of a polaron model [GRN04, VSA06]. We will investigate the vibrational effects in junctions with normal as well as superconducting leads. The review of Galperin *et al.* [GRN07] provides a very good summary of vibrational effects in molecular junctions with normal leads. Several theoretical studies on the topic have appeared [HBT09, HT11a, HT11b, KvOA06, KSvON06, ZFM06, RHC06, LMD07, RC07, RDCR08, RS09, WPHT11, JA13] along with experimental ones [WNC⁺04, LLKD04, PPC⁺05, BES07, dLLGP08, HWL⁺09, BHS⁺10, TKLvR08, FP12]. Most of them deal with normal leads. A few studies working with superconducting leads have been published [ZEMM06, MDD⁺07, FZB08, ZE10, SPAS⁺10, TM10]. The interplay of molecular vibrations with superconductivity has not yet been studied systematically.

5.1 Model

We use the Ehrenfest approximation of a polaron model to describe the vibrations and combine it with the propagation scheme of section 3.2. It is a generalization of an existing scheme for junctions with normal leads [VSA06], replacing the electronic propagation scheme to incorporate superconducting leads.

The validity of the underlying polaron model has been discussed for the normal conducting case [GNR08], revealing that it is not a mean field approximation but exact in the static limit $\frac{\omega_{\text{vib}}}{T} \ll 1$. The limit corresponds to a slow vibrational motion compared to the electronic timescale. The same holds for our model in the static limit with large masses and slow changes in the bias [GNR08]. When expressing the electron-phonon interaction in the static limit

in term of diagrams, only the Hartree term and similiar terms with boson lines terminated in a closed loop are relevant.

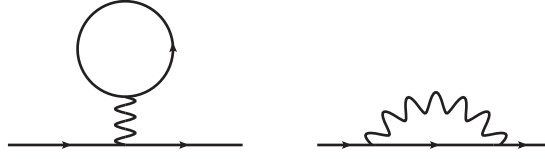


Figure 5.1: Hartree (left) and Fock (right) diagram. The straight line represents the electron propagator, the wavy line the phonon propagator. In the static limit $\frac{\omega}{T} \ll 1$ of our model, only the contribution of the Hartree diagram is relevant.

Recently, a comparative study of Ehrenfest dynamics and exact results for the polaron model in a finite system showed quantitatively similar behaviour, but time scales can be different [LMNR13]. This suggests quantitatively good results even away from the static limit.

The vibration is incorporated into the Hamiltonian as

$$\hat{H}_{\text{QD}}(t) = (\varepsilon_{\text{QD}} + \lambda x(t)) \sum_{\sigma \in \{\uparrow, \downarrow\}} \hat{c}_{\text{QD}, \sigma}^\dagger \hat{c}_{\text{QD}, \sigma} + \frac{1}{2} m \dot{x}(t)^2 + \frac{1}{2} m \omega_{\text{vib}}^2 x(t)^2. \quad (5.1)$$

The equation of motion for the vibrational coordinate $x(t)$ has the shape of a driven harmonic oscillator and reads

$$m \ddot{x}(t) = - \left\langle \frac{\partial \hat{H}_{\text{QD}}}{\partial x} \right\rangle \quad (5.2)$$

$$= -m \omega_{\text{vib}}^2 x(t) - \lambda n_{\text{QD}}(t). \quad (5.3)$$

The coupling parameter λ is chosen positive and the mass m will be set to $m = 0.5 \omega_{\text{vib}}^{-1}$ for all calculations. The equation (5.2) has to be solved simultaneously with the time-dependent Bogoliubov-de Gennes equation (2.44).

We carry out a time propagation starting from an initial position x^0 and initial single particle wave functions ψ_q^0 . The initial state is the ground state of the system, which is calculated using a self-consistency cycle. In the ground state, the vibrational coordinate $x(t)$ is at rest, i.e. $\dot{x}(t) = \ddot{x}(t) = 0$. Hence

$$x^0 = - \frac{\lambda}{m \omega_{\text{vib}}^2} n_{\text{QD}}^0. \quad (5.4)$$

This can be used to set up the self-consistency cycle shown in figure 5.2.

The propagation of the coordinate and the wave functions from t_m to t_{m+1} is

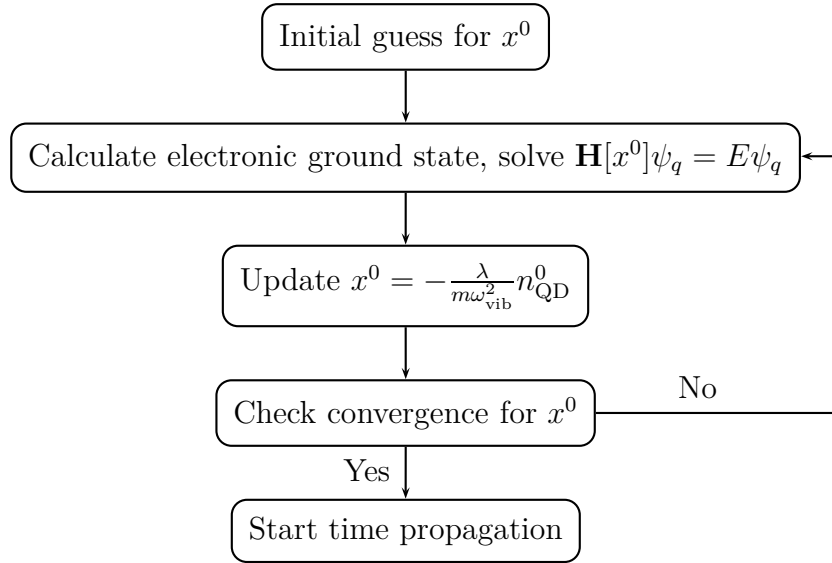


Figure 5.2: Iterative procedure to calculate the ground state

done successively via

$$\left\{ \begin{array}{l} x(t_m) \xrightarrow{n_{\text{QD}}(t_m)} x(t_{m+1}) \\ \psi_q(t_m) \xrightarrow{x(t_m), x(t_{m+1})} \psi_q(t_{m+1}) \end{array} \right\}. \quad (5.5)$$

The propagation of the wave functions $\psi_q(t_m)$ works as described in section 3.2. The vibrational coordinate is updated using a second order finite difference. The time step reads

$$x(t_{m+1}) = (2 - \omega_{\text{vib}}^2 \Delta t^2)x(t_m) - x(t_{m-1}) - \frac{\lambda}{m} \Delta t^2 n_{\text{QD}}(t_m). \quad (5.6)$$

5.2 Stability analysis

In this section, we analyse the stability of the system against small perturbations of the coordinate x in the static limit $\frac{\omega_{\text{vib}}}{\Gamma} \ll 1$, corresponding to vibrations being much slower than the electrons. This also reveals a way to drive the vibration.

We define time-independent states as the states of the system with time-independent observables, like n_{QD} , $I_{\alpha\text{C}}$ as well as x . This can either be a ground

state without any bias or a steady state with a constant bias after the transient.

The following analysis requires systems without any initial state or history dependence. Systems which do not reach a steady state in the non-vibrational case, systems with bound states [KKS08, KSK09] as well as normal junctions in the Coulomb blockade regime [KSK+10, UKS+10, KUS+12] are not included in the following analysis. Since we neglect the Coulomb interaction, this leaves normal and hybrid junctions without bound states. Josephson junctions (SQDS) with an applied bias can be included in the following analysis, provided that the Josephson frequency is much larger than the vibrational frequency. In this limit, the vibration does not react to the fast changes in the density $n_{\text{QD}}(t)$ due to the Josephson effect, but rather to its average over a time period $T_{\text{J}} = \frac{2\pi}{\omega_{\text{J}}} = \frac{\hbar}{eU}$.

We intend to work with adiabatic approximations and therefore define $n_{\text{QD}}^{(\text{ad})}(x)$ as the time-independent electronic density for a fixed position x . This is $n_{\text{QD}}^{(\text{ad})}(x) = n_{\text{QD}}(x)$ for the ground state. For junctions with a constant bias applied at $t = 0$, it is $n_{\text{QD}}^{(\text{ad})}(x) = n_{\text{QD}}(T, x)$ (NQDN, NQDS or SQDN junctions) with T chosen large enough to ensure that switching effects have died out. In the case of Josephson junctions, the AC Josephson effect lets the current and density oscillate. But since the Josephson frequency ω_{J} is chosen much larger than the vibrational frequency ω_{vib} , we can work with the time-average $n_{\text{QD}}^{(\text{ad})}(x) = \frac{1}{T_{\text{J}}} \int_T^{T+T_{\text{J}}} n_{\text{QD}}(t', x) dt'$ with $T_{\text{J}} = \frac{\pi}{\omega_{\text{J}}}$. T is again chosen sufficiently large.

For the following analysis, we work in the static limit, i.e. the time period $T_{\text{vib}} = \frac{2\pi}{\omega_{\text{vib}}}$ of the vibration is much larger than the equilibration time of the density, which is proportional to Γ^{-1} . This allows us to make the adiabatic approximation $n_{\text{QD}}(t) = n_{\text{QD}}^{(\text{ad})}(x(t))$. In order to improve the approximation, we introduce a small time shift τ and work with the approximation $n_{\text{QD}}(t) = n_{\text{QD}}^{(\text{ad})}(x(t - \tau))$. The time τ is considered to be small and describes the phase shift between the density and the position. We assume it to be constant in time, although it depends on various parameters, for example on $\dot{x}(t)$.

Figure 5.3 shows two examples of this approximation with τ set to zero. The optimal choice of τ can be either positive or negative, the first case being observed most of the times. The latter case is counter intuitive in the first place, since one would expect that the density follows the slow motion of $x(t)$ with a short time delay. In a way, it looks like the reaction can be observed prior to the perturbation.

The phenomenon originates from a temporary ‘‘overreaction’’ of the density to changes in $x(t)$. The lower part of Figure 5.4 shows an example with an externally controlled abrupt change in $x(t)$. The density increases rapidly, passes its new steady state value and then finally converges to the new value for the long time limit. Thus, too much density is temporarily accumulated. Next, we force $x(t)$ to perform a sinusoidal motion starting at $t = 200$. The density

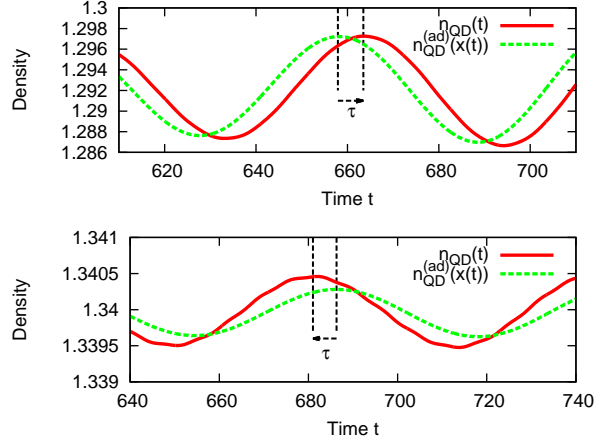


Figure 5.3: Comparison of $n_{\text{QD}}(t)$ with $n_{\text{QD}}^{(\text{ad})}(x(t))$ (i.e. $\tau = 0$) for two NQDS junctions with vibrations. The best agreement is achieved for $\tau = 5.6$ (top) and $\tau = -5.29$ (bottom). The parameters are: $\Gamma_\alpha = 0.5$, $\lambda = 0.1$, $\omega_{\text{vib}} = 0.1$, $U_L = -U_R = 0.45$ (both), $\varepsilon_{\text{QD}} = 0$ (top) and $\varepsilon_{\text{QD}} = 0.275$ (bottom). $x(t)$ is kept fixed to -2.55 (top) and -2.7 (bottom) until $t = 50$.

reaches its maximum value before the adiabatic approximation without a phase shift $n_{\text{QD}}^{(\text{ad})}(x(t))$. The same holds for the following minima. It thus looks like the density is ahead of the motion of $x(t)$. So far, this effect was only observed in junctions with at least one superconducting lead and an applied bias.

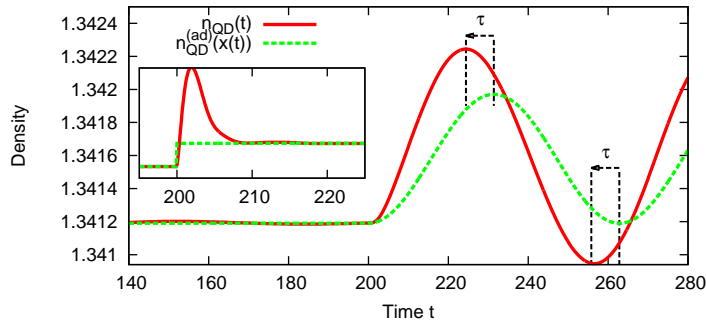


Figure 5.4: Reaction of the density to an externally controlled sinusoidal motion of $x(t)$. The inset shows the effects of a step-like change in $x(t)$. The parameters are the same as in figure 5.3 (bottom) with $x(t) = -2.75 - 0.05\Theta(t - 200)(1 - \cos(0.1t))$ and $x(t) = -2.75 - 0.1\Theta(t - 200)$ (inset).

Within this approximation the equation of motion for $x(t)$ takes the form:

$$m\ddot{x}(t) = -m\omega_{\text{vib}}^2 x(t) - \lambda n_{\text{QD}}^{(\text{ad})}(x(t - \tau)). \quad (5.7)$$

We approximate $n_{\text{QD}}^{(\text{ad})}(x(t - \tau))$ by making a Taylor expansion

$$n_{\text{QD}}^{(\text{ad})}(x(t - \tau)) = n_{\text{QD}}^{(\text{ad})}(x(t)) - \tau \dot{x}(t) \partial_x n_{\text{QD}}^{(\text{ad})}(x(t)) \quad (5.8)$$

and obtain

$$m\ddot{x}(t) = -m\omega_{\text{vib}}^2 x(t) - \lambda n_{\text{QD}}^{(\text{ad})}(x(t)) + \lambda \tau \dot{x}(t) \partial_x n_{\text{QD}}^{(\text{ad})}(x(t)) \quad (5.9)$$

$$= -\frac{d}{dx} V(x) + \lambda \tau \dot{x}(t) \partial_x n_{\text{QD}}^{(\text{ad})}(x(t)). \quad (5.10)$$

The potential $V(x)$ is implicitly defined by the equations above up to a constant, which can be chosen freely. The stationary points \bar{x} of the potential $V(x)$ define time-independent positions of the vibration. But not all of them are stable against small perturbations δx , like for example maxima or saddle points of $V(x)$. But also minima are not always stable as we will see later. The correct way to check the stability is to solve equations (5.2) and (2.44) for an initial value $x^0 = \bar{x} + \delta x^0$ with a small perturbation δx^0 . Maxima and saddle points are never stable, we therefore can assume \bar{x} to be a minimum of $V(x)$, for simplicity with $\partial_x^2 V(\bar{x}) > 0$. The equation of motion for $x(t)$ reads

$$m\ddot{x}(t) = -m\omega_{\text{vib}}^2 \bar{x} - \lambda n_{\text{QD}}^{(\text{ad})}(\bar{x}) - \left(m\omega_{\text{vib}}^2 + \lambda \left(\partial_x n_{\text{QD}}^{(\text{ad})}(\bar{x}) \right) \right) \delta x(t) + \lambda \tau \dot{\delta x}(t) \left(\partial_x n_{\text{QD}}^{(\text{ad})}(x(t)) \right). \quad (5.11)$$

The first two terms on the right hand side cancel each other since \bar{x} is a minimum of $V(x)$. We define the damping coefficient

$$\gamma(x(t)) = -\frac{1}{2} \lambda \tau \left(\partial_x n_{\text{QD}}^{(\text{ad})}(x(t)) \right) \quad (5.12)$$

and its approximation

$$\gamma = -\frac{1}{2} \lambda \tau \left(\partial_x n_{\text{QD}}^{(\text{ad})}(\bar{x}) \right). \quad (5.13)$$

Having this approximation at hand, we can solve the equation of motion for $x(t)$ by

$$x(t) = \bar{x} + \left(C_0^+ \cos(\Omega t) + C_0^- \sin(\Omega t) \right) e^{-\frac{\gamma}{m} t} \quad (5.14)$$

with

$$\Omega = \sqrt{\omega_{\text{eff}}^2 - \frac{\gamma^2}{m^2}}, \quad (5.15)$$

$$\omega_{\text{eff}} = \sqrt{\omega_{\text{vib}}^2 + \frac{\lambda}{m} \left(\partial_x n_{\text{QD}}^{(\text{ad})}(\bar{x}) \right)}. \quad (5.16)$$

Hence, minima of $V(x)$ are stable against small perturbations δx if $\gamma > 0$. Thus, a stationary point \bar{x} of the potential $V(x)$ fulfilling the following two conditions is stable:

$$\bar{x} \text{ is a local minimum of } V(x), \quad (5.17)$$

$$\gamma = -\frac{1}{2}\lambda\tau \left(\partial_x n_{\text{QD}}^{(\text{ad})}(\bar{x}) \right) > 0. \quad (5.18)$$

The density $n_{\text{QD}}^{(\text{ad})}(x)$ for NQDN junctions can be calculated analytically [GNR08]. Its derivative reads

$$\partial_x n_{\text{QD}}^{(\text{ad})}(x) = -\frac{\lambda}{\pi} \sum_{\alpha \in \{\text{L,R}\}} \frac{\Gamma_\alpha}{\Gamma} \frac{1}{1 + \left(\frac{U_\alpha - \varepsilon_{\text{QD}} - \lambda x}{0.5\Gamma} \right)^2}, \quad (5.19)$$

being always negative. We observe only positive values for τ for NQDN junctions, thus local minima of $V(x)$ are always stable against small perturbations. This leaves equation (5.17) as the relevant condition. This confirms the findings of the work by Galperin *et al.* [GRN04] using a quantum mechanical description of the vibration in a NQDN junction. A recent analysis of a very similar model of a stretching vibrational mode showed that persistent oscillations can occur due to negative damping coefficients even in junctions with normal leads [KVS14]. Similar effects have been observed in junctions with multiple vibrational degrees of freedom [LBH10].

The derivative $\partial_x n_{\text{QD}}^{(\text{ad})}(\bar{x})$ can take positive and negative values in NQDS and SQDN junctions with an applied bias. We show two examples for this phenomenon in figure 5.5.

The plot in figure 5.5 reveals the existence of junctions with multiple solutions of equations (5.17) and (5.18), as it has already been discovered in the case of two normal leads [GRN04]. This finding extends the list of bistability in junctions with vibrations [GK02, GRN04, DRCR08, RS09, DK11, AWM⁺12]. The validity of approximations made in some of these works has been intensively discussed [AB06, GNR06, AB07, GNR08, AB09].

The case in Figure 5.5 (top) has two stable solutions. In contrast, the same junction with an applied bias (middle plot) has only one stable minimum. It is even possible to have no stable solution as in the example in Figure 5.5 (bottom).

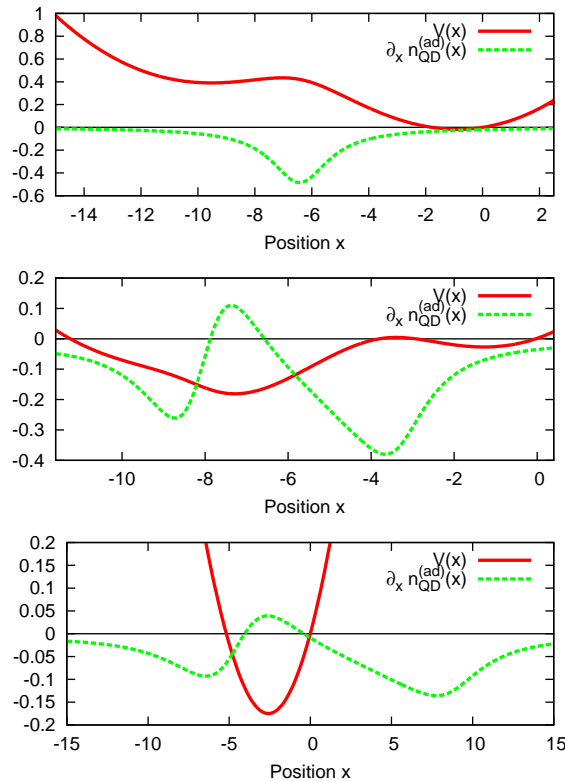


Figure 5.5: Potential $V(x)$ and derivative $\partial_x n_{\text{QD}}^{(\text{ad})}(x)$ for three different NQDS junctions with $\Gamma_\alpha = 0.5$ and $\omega_{\text{vib}} = 0.1$. The time τ is positive for all minima. Top: Ground state (no bias) with two stable local minima of $V(x)$ ($\lambda = 0.28, \varepsilon_{\text{QD}} = 1.8$). Middle: Same junction as the top one, but with a bias $U_L = -U_R = 0.45$. The minimum of $V(x)$ on the right is stable, the left one is unstable. Bottom: Biased junction ($U_L = -U_R = 0.45$) with no stable minimum ($\lambda = 0.1, \varepsilon_{\text{QD}} = 0$).

We test the quality of the approximations by comparing the predicted motion of $x(t)$ with the calculated one for $x^0 = \bar{x} + \delta x^0$. The quantities $\bar{x}, V(\bar{x})$ and $\partial_x n_{\text{QD}}^{(\text{ad})}(\bar{x})$ can all be obtained using a series of further time propagations. τ is determined by measuring the time shift of minima and maxima between $n_{\text{QD}}(t)$ and $x(t)$ of a full calculation with vibration. We show three test cases in figure 5.6, a stable NQDS and two unstable NQDS junctions, all of them having an applied bias. We carry out a full time propagation, switch on the bias at $t = 0$ and enforce $x(t \leq 50) = x^0$. The equation of motion of $x(t)$ is solved starting from $t = 50$. We compare the prediction of equation (5.14) with the results obtained by the time propagation. The free parameters C_0^\pm are determined by the initial conditions $x(t \leq 50) = x^0, \dot{x}(t \leq 50) = 0$ yielding $C_0^+ = x^0 - \bar{x}$ and $C_0^- = 0$. The agreement is good in the sense that the frequency as well as the

damping are well reproduced, showing small deviation with increasing times.

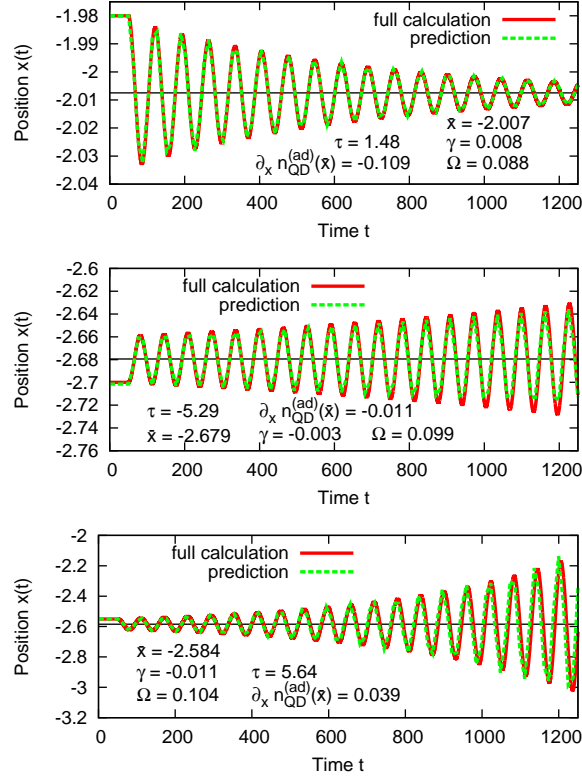


Figure 5.6: Example of a stable (top) and two unstable (middle and bottom) states. Instability can occur if $\tau < 0$ (middle) or $\partial_x n_{\text{QD}}^{(\text{ad})}(\bar{x}) > 0$ (bottom). $x(t)$ is kept fix until $t = 50$. The solid black line represents the stationary point \bar{x} . The parameters are: $\Gamma_\alpha = 0.5$, $\lambda = 0.1$, $\omega_{\text{vib}} = 0.1$, $U_L = -U_R = 0.45$ (all), $\varepsilon_{\text{QD}} = 0.75$ (top), $\varepsilon_{\text{QD}} = 0.275$ (middle) and $\varepsilon_{\text{QD}} = 0$ (bottom).

In the case of the unstable examples of Figure 5.6, the amplitude of the oscillation is slowly but exponentially increasing as predicted. Figure 5.7 shows the long time behaviour of one of such a junction.

The amplitude of the oscillation converges to a constant value in the long time limit. This originates from the fact, that the coordinate x leaves the interval with an effective damping coefficient $\gamma < 0$, thus γ is negative only around the stationary point \bar{x} of $V(x)$ and positive at both other ends. This leads to an acceleration in the middle and a slowdown otherwise. In the long time limit, the system reaches a state with a balance of acceleration and slowdown, resulting in permanent oscillations with a constant amplitude.

The experimental search for unstable solutions can be done by varying the gate voltage ε_{QD} . The time averaged current-gate voltage characteristics has steps revealing changes from stable to unstable solutions and vice versa, as

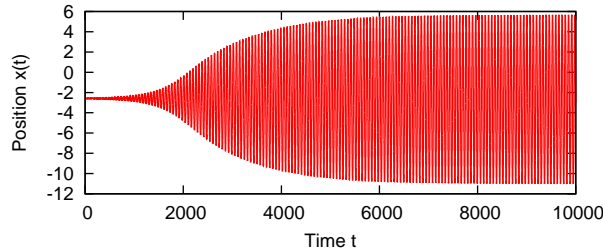


Figure 5.7: Long time behaviour of the example in figure 5.6 (bottom).

shown in figure 5.8. The region of instability can be separated into two parts with different origin for $\gamma < 0$. We observe one part with $\partial_x n_{\text{QD}}^{(\text{ad})}(\bar{x}) > 0$, $\tau > 0$ and a second one with $\partial_x n_{\text{QD}}^{(\text{ad})}(\bar{x}) < 0$, $\tau < 0$. They are next to each other with the cross-over at a gate voltage corresponding to $\partial_x n_{\text{QD}}^{(\text{ad})}(\bar{x}) = 0$. The stable intervals have $\partial_x n_{\text{QD}}^{(\text{ad})}(\bar{x}) < 0$ and $\tau > 0$. This presented instability can be used to drive the vibration.

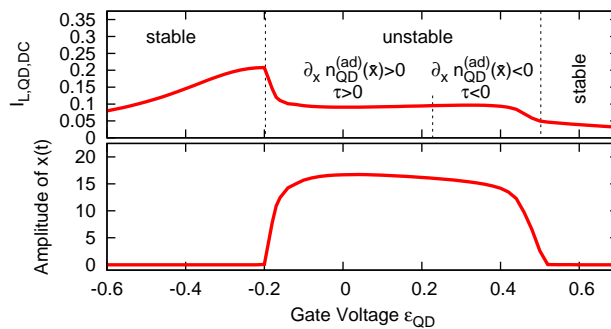


Figure 5.8: Time averaged current-gate voltage characteristics for NQDS junction. The parameters are the same as in figure 5.5 (bottom).

5.3 Vibrations in Josephson junctions

5.3.1 Ground state

We demonstrate the possibility of bistability in the ground state for Josephson junctions. The bistability can depend on the chosen phase difference $\chi_0 =$

$\chi_L - \chi_R$. Such an example is shown in figure 5.9. Note, that the analysis of stability as it was done in section 5.2 is not applicable. Starting from the ground state at $t = 0$ and disturbing the system only for a short time does not guarantee that it will return to its initial state. This has been shown for an applied bias pulse resulting in persistent oscillations in the current and density [SPC10].

The correct way to answer the question of stability is to carry out a full time propagation. The criterium “*minimum of $V(x)$* ” turned out to be reliable for SQDS systems in the ground state studied here.

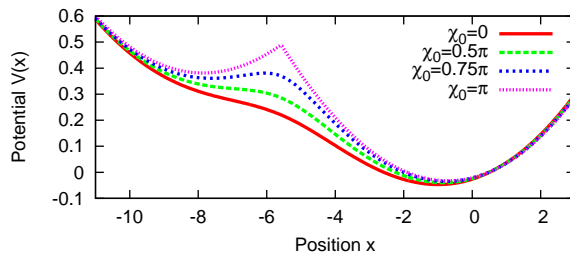


Figure 5.9: Potential $V(x)$ for a Josephson junction in the ground state for different phase differences $\chi_0 = \chi_R - \chi_L$. All minima turned out to be stable. The parameters are: $\Gamma_\alpha = 0.5$, $\varepsilon_{\text{QD}} = 1.25$, $\lambda = 0.225$ and $\omega_{\text{vib}} = 0.1$.

5.3.2 Biased system in the static limit

We now turn to Josephson junctions with vibrations in the static limit, i.e. $\omega_J, \Gamma \gg \omega_{\text{vib}}$ with $\omega_J = \frac{2e}{\hbar}(U_L - U_R)$. In this limit, the harmonic oscillator does not react to the fast changes in the density $n_{\text{QD}}(t)$ due to the Josephson effect, but rather to its average over a time period $T_0 = \frac{\pi}{U}$. The system does not reach a time-independent state as it is described in section 5.2. In this limit, it is reasonable to replace the condition of constant observables by the demand for constant time averaged observables over a period $T_0 = \frac{\pi}{U}$ in the long time limit. Thus, the analysis of stability from section 5.2 can be applied if we replace $n_{\text{QD}}^{(\text{ad})}(x)$ by $\langle n_{\text{QD}}^{(\text{ad})} \rangle(x) = \frac{1}{T_0} \int_T^{T+T_0} n_{\text{QD}}(t', x) dt'$ with x being fixed and T chosen large enough such that switching effects have died out. We again encounter two possible states: stable and unstable ones. Figure 5.10 shows a Josephson junction with two stable and two unstable minima. The oscillations due to the instability can have a notable influence on the current-voltage characteristics. In figure 5.11, we compare it to a junction with a vibration which is coupled to a bath of secondary phonons. The bath is modeled by introducing a small damping parameter γ_{art} to equation (5.2) which is chosen large enough

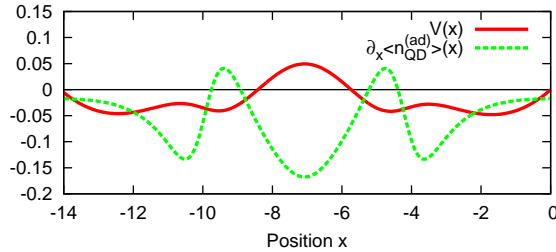


Figure 5.10: Potential $V(x)$ and derivative $\partial_x \langle n_{\text{QD}}^{(\text{ad})} \rangle(x)$ for a Josephson junction with an applied bias $U_L = -U_R = 1$. The outer two minima are stable, the inner ones are unstable against small perturbations in x (τ is positive). The parameters are: $\Gamma = 1$, $\varepsilon_{\text{QD}} = 2.5$, $\lambda = \sqrt{0.125}$ and $\omega_{\text{vib}} = 0.1$.

to overcome any instability, but small enough not to change the results more than necessary. The amplitude of the oscillation of $x(t)$ in the long time limit is shown in the lower part of figure 5.11. There are regions with vanishing amplitude, corresponding to stable time-independent states, and others with non-zero amplitudes, coming from unstable ones. The currents of damped and undamped calculations deviate from each other, if the amplitude of the oscillation is non-zero, and match otherwise. Again, one can use the bias to drive the vibration.

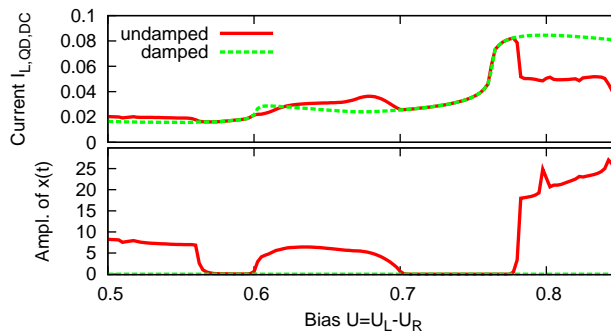


Figure 5.11: Top: Time averaged current-voltage characteristics for a Josephson junction with a bias dependent stability. Bottom: Amplitude of the oscillation. The parameters are: $\Gamma_\alpha = 0.5$, $\varepsilon_{\text{QD}} = 0$, $\lambda = 0.1$, $\omega_{\text{vib}} = 0.1$ and $\gamma_{\text{art}} = 0.01$.

5.3.3 Biased system in resonance

We finally want to analyse resonances in Josephson junctions. There can be up to three frequencies involved: The vibrational frequency ω_{vib} , the Josephson

frequency ω_J and the frequency of an AC bias ω_{AC} . In a real experiment, only the latter two ones can be varied easily. Hence, we keep ω_{vib} fix and vary one of the others.

Resonance of the vibration with the Josephson frequency

We start with the demonstration of the interplay between ω_J and ω_{vib} , first in the absence of an AC bias. We tune the DC bias such that the Josephson frequency is in resonance with the vibrational degree of freedom. This is shown in figure 5.12 We make the following observations:

(a) As a function of the applied bias $U = U_L - U_R$ (and hence as a function of the Josephson frequency $\omega_J = \frac{2e}{\hbar}U$), the amplitude of the Josephson effect-driven vibration has the expected shape a driven harmonic oscillator (see Figure 5.12 second to top panel).

(b) The peak of the amplitude is shifted compared to the frequency of the pure vibration as expected for a damped driven harmonic oscillator.

(c) The absolute value $|\langle x \rangle|$ of the time average of the classical coordinate, i.e. the average distance between the vibrating nuclei, becomes slightly larger at the resonance and has two different values above and below the resonance. Note that this effect is by 2 – 3 orders of magnitude smaller than the enhancement of the amplitude.

(d) The current as a function of the bias shows a resonance effect as well: The DC part shows a down-up variation near the resonance within the otherwise linear behaviour.

(e) The amplitude of the oscillatory part has a relatively sharp maximum at the resonance and has different values above and below the resonance. The peak is again slightly shifted towards smaller biases.

A second example is presented in figure 5.13, but with a different vibrational frequency. The observations are very similar except that there is a break down of the vibrational oscillation near the resonance at slightly larger values. The reason currently still unknown.

Since the amplitude of the current can easily be measured in experiments, the above effects provide a way of accurately determining the vibrational frequency of the molecule in the junction. The signatures in the current-voltage characteristics are much sharper compared to those produced by photon assisted tunneling, which can also used to determine the vibrational frequency experimentally.

We now add an AC bias on top, giving

$$U(t) = U_{DC} + U_{AC} \cos(\omega_{AC}t). \quad (5.20)$$

We show results for three choices of ω_{AC} in figure 5.14: (i) slightly smaller than ω_{vib} , (ii) the same as ω_{vib} , and (iii) slightly larger than ω_{vib} . The influence of the

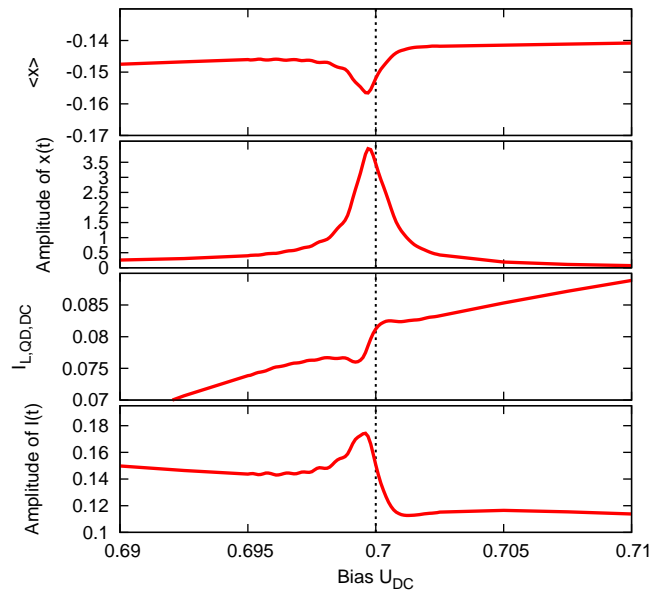


Figure 5.12: Resonance of the Josephson frequency $\omega_J = \frac{2e}{\hbar}U$ with the vibrational frequency ω_{vib} . The parameters are: $\Gamma_\alpha = 0.5, \varepsilon_{\text{QD}} = 0, \lambda = 0.1, \omega_{\text{vib}} = 1.4$) and $U_L = -U_R$.

additional AC bias is rather small for the off-resonance choices of ω_{AC} . The case of $\omega_{\text{vib}} = \omega_{\text{AC}}$ shows a more complicated structure with several additional dips. There, one further observes the inverse AC Josephson effect at the resonance, which is drawn using the color green. It is absent in the other two plots since the frequencies ω_J and ω_{AC} do not match in the plotted range.

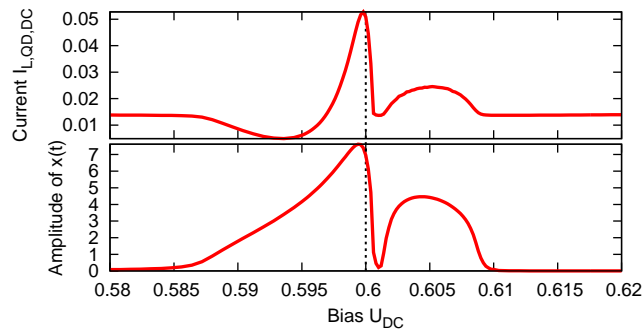


Figure 5.13: Resonance of the Josephson frequency $\omega_J = \frac{2e}{\hbar}U$ with the vibrational frequency ω_{vib} . The parameters are: $\Gamma_\alpha = 0.5, \varepsilon_{\text{QD}} = 0, \lambda = 0.1, \omega_{\text{vib}} = 1.2$) and $U_L = -U_R$.

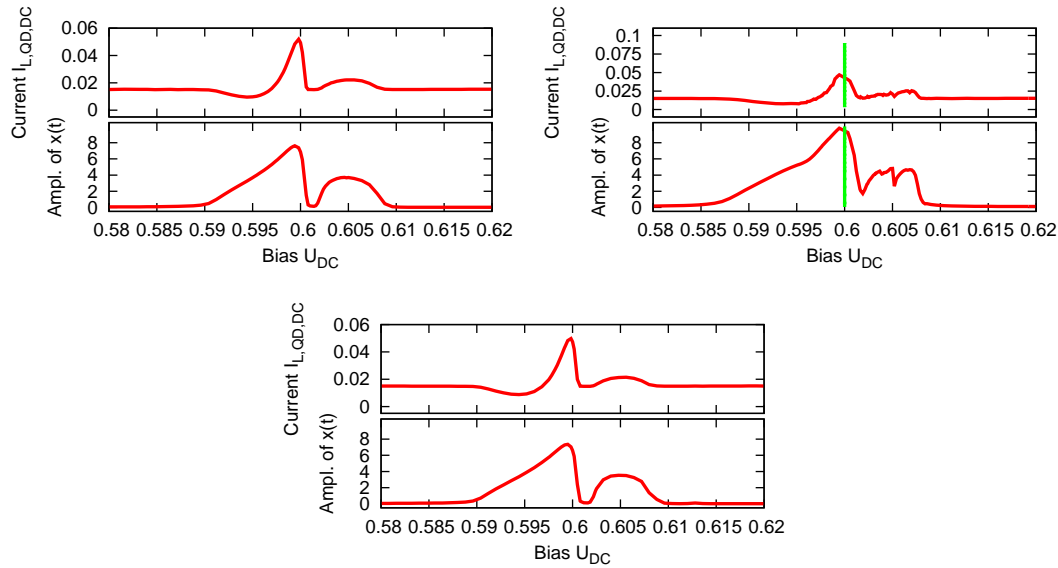


Figure 5.14: Resonance of the Josephson frequency with the vibrational frequency. The green vertical line represents results depending on the initial phase difference χ_0 due to the inverse AC Josephson effect. The parameters are: $\Gamma_\alpha = 0.5$, $\varepsilon_{\text{QD}} = 0$, $\lambda = 0.1$, $\omega_{\text{vib}} = 1.2$, $U_{\text{AC}} = 0.2$, $\omega_{\text{AC}} = 1.15$ (top left), 1.2 (top right) and 1.25 (bottom) and $U_{\text{L}}(t) = -U_{\text{R}}(t)$.

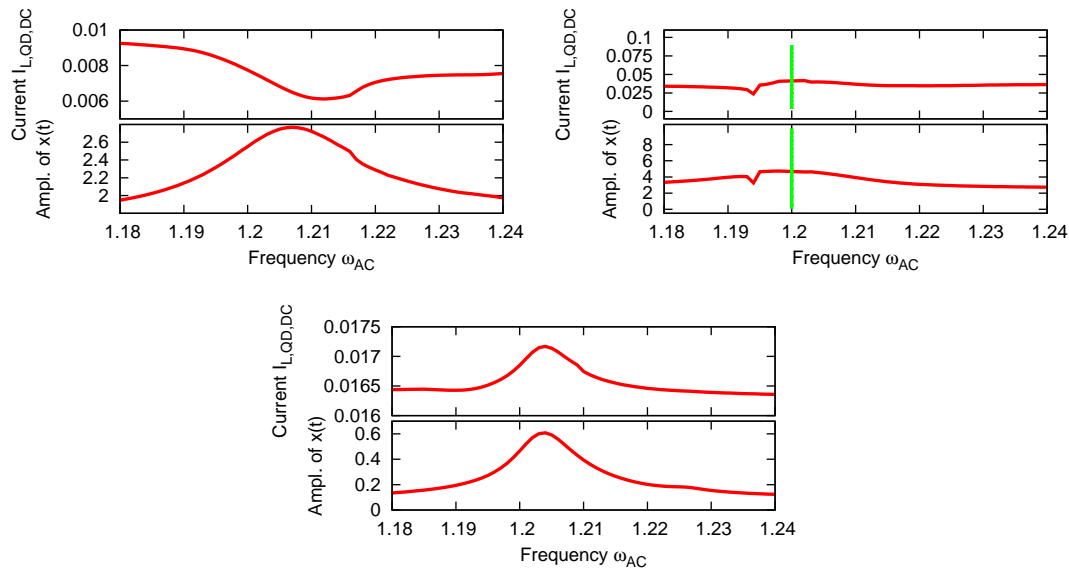


Figure 5.15: Resonance of the AC bias with the vibrational frequency. The green vertical line represents results depending on the initial phase difference χ_0 due to the inverse AC Josephson effect. The parameters are: $\Gamma_\alpha = 0.5$, $\varepsilon_{\text{QD}} = 0$, $\lambda = 0.1$, $\omega_{\text{vib}} = 1.2$, $U_{\text{AC}} = 0.2$, $U_{\text{DC}} = 0.575$ (top left), 0.6 (top right), 0.625 (bottom) and $U_{\text{L}}(t) = -U_{\text{R}}(t)$.

Resonance of the vibration with the AC bias

Next, we fix U_{DC} such that the Josephson frequency ω_{J} is close to the vibrational frequency ω_{vib} and vary the frequency ω_{AC} of the AC bias. Again, we show three examples in figure 5.15: (i) $\omega_{\text{J}} < \omega_{\text{vib}}$, (ii) $\omega_{\text{J}} = \omega_{\text{vib}}$, and (iii) $\omega_{\text{J}} > \omega_{\text{vib}}$.

The amplitude of $x(t)$ shows a broadened resonance peak in all cases. The current changes depending on the value of ω_{J} . If ω_{J} is smaller than ω_{vib} , the current gets enhanced and otherwise reduced. The inverse AC Josephson effect is again present in the case of $\omega_{\text{J}} = \omega_{\text{vib}}$. In contrast to resonances of vibration and Josephson frequency, the overall structures for all three cases look much more like a driven harmonic oscillator in resonance.

5.4 Conclusion

Hybrid and Josephson junctions with a vibration in the Ehrenfest approximation are studied in this chapter. We rigorously discuss the stability of the vibration against small perturbations and finally obtain a criterium for stability. It helps us to understand why the vibration sometimes shows persistent oscillations and is damped in other cases. Besides, we discover the possibility of bistabilities in the course of the stability analysis. We suggest to test our findings in experiment by creating a molecular junction with a vibrational degree of freedom. Variations of the bias and gate voltage hopefully lead to the predicted significant changes in the current.

Furthermore, we demonstrate the possibility to drive the vibration with the bias and observe that this works only in certain parameter regimes. Besides, the resonance of the Josephson frequency, the vibration and the AC bias in Josephson junctions is discussed. We show that resonance produces a peak in the amplitude of the current's oscillation. It is particularly sharp in the case of a resonance between Josephson frequency and the vibration. In experiments, a measurement of the latter can be used to accurately determine the vibrational frequency of the molecule. The vibrational signatures in the current-voltage characteristics are much sharper than those produced by photon assisted tunneling, which can alternatively be used to determine the vibrational frequency.

Chapter 6

Controlling observables in time-dependent quantum transport

The theory of time-dependent quantum transport addresses the question: How do electrons flow through a junction under the influence of an external perturbation as time goes by? In this chapter, we invert this question and search for a time-dependent bias such that the system behaves in a desired way. This can, for example, be an observable that is forced to follow a certain pattern or the minimization of an objective function which depends on the observables. Our system of choice consists of quantum dots coupled to normal or superconducting leads. We present results for junctions with normal leads where the current, the density or a molecular vibration is optimized to follow a given target pattern. For junctions with two superconducting leads, where the Josephson effect triggers the current to oscillate, we show how to suppress the Josephson oscillations by suitably tailoring the bias. In a second example involving superconductivity, we consider a Y shaped junction with two quantum dots coupled to one superconducting and two normal leads. This device is used as a Cooper pair splitter to create entangled electrons on the two quantum dots. We maximize the splitting efficiency with the help of an optimized bias.

The research field of optimal control was pioneered by the work of Pontryagin [PBG62] and Bellman [Bel57] who paved the way for numerous applications. Initially, optimal control theory was mainly used to solve problems of classical mechanics. Later, it found applications in many other research fields including quantum mechanics [PDR88, SWR88, KRG+89].

A particularly interesting field goes under the heading of “femto-chemistry” where chemical reactions are influenced with femto-second laser pulses such that a specific reaction gets suppressed or enhanced [ABB+98, HMM89, EKMO03, EG04]. A successful experimental application is the selective bond dissociation of molecules [LMR01]. Other applications of optimal control theory in the quantum world include the control of the electron flow in a quantum ring

[RCW⁺07], the accelerated cooling of molecular vibrations [RK13], the control of the entanglement of electrons in quantum wells [RBBH12], the optimization of quantum revival [RH13], the control of ionization [CRRG09, RM12] or the selection of transitions between molecular states [JMS90].

Kleinekathöfer and coworkers combined optimal control theory with the master equation approach for quantum transport and demonstrated the control of various observables in junctions with normal leads [LSK07, ALPK09, LK10]. We take a different approach to the same problem by propagating wave functions using the scheme described in section 3.2. This allows us to treat not only normal but also superconducting leads. We further use a direct instead of a variational optimization method, which is closer to optimizations in experiments.

6.1 Optimization problem

We start at $t = 0$ in the ground state of the junction with $U_\alpha(t \leq 0) = 0$. The goal is to tailor the bias $U_\alpha(t)$ such that the observable of choice $O(t)$ follows a predefined target pattern as best as possible. The corresponding optimization problem reads

$$\begin{aligned} & \min_{U_L(t), U_R(t)} \|O[\Psi](t) - O^{(\text{target})}(t)\|_{2,[0,T]}^2 & (6.1) \\ \text{s.t.} \quad & i\partial_t \psi_q(t) = \mathbf{H}[U_L, U_R](t) \psi_q(t), \quad t \in [0, T], \\ & \psi_q(0) = \psi_q^0. \end{aligned}$$

Here, $\|\cdot\|_{2,[0,T]}$ denotes the L^2 -norm on the time interval $[0, T]$, i.e. the objective function is the following integral:

$$\int_0^T dt |O[\Psi](t) - O^{(\text{target})}(t)|^2. \quad (6.2)$$

The integral is well-defined since T and the integrand are finite in all examples studied in this work.

Most common is a variational approach to this problem, like the Rabitz approach [ZBR98] or Krotov's method [ST02, PK03]. Such an approach incorporates the constraints into the objective function using Lagrange multipliers and searches for the roots of the variation of the new objective function. An alternative approach, which we shall adopt in this chapter, is the direct minimization of the objective function using derivative-free minimization algorithms. This strategy was successfully used in several works [CRRG09, KCG11, HRG13, RPM13].

In this way, we avoid various difficulties arising from the time propagation algorithm. This approach can be viewed as the computational analogue to the closed-loop learning algorithms employed in experimental optimization [JR92].

The basic idea of our numerical approach is to approximate $U_\alpha(t)$ by cubic splines with $N + 1$ equidistant nodes at $\tau_k = \frac{k}{N}T, k \in \{0, \dots, N\}$. We choose $\frac{d}{dt}U_\alpha(\tau_0) = \frac{d}{dt}U_\alpha(\tau_N) = 0$ as the boundary conditions for the splines. The dependence of the problem (6.1) on the bias $U_\alpha(t)$ is replaced by

$$U_\alpha(t) \rightarrow [U_\alpha(\tau_0), \dots, U_\alpha(\tau_N)] \equiv \vec{u}_\alpha. \quad (6.3)$$

In this way, the spline-interpolated bias $U_\alpha(\vec{u}_\alpha, t)$ becomes a function of \vec{u}_α . This then yields a normal non-linear optimization problem with the unknown variables $U_\alpha(\tau_k)$. We further impose the condition $U_\alpha(\tau_0) = 0$ since the bias has to be continuous and we assume $U_\alpha(t < 0) = 0$. Figure 6.1 demonstrates this approach.

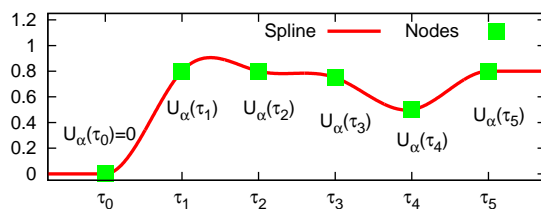


Figure 6.1: Cubic spline interpolation using six nodes τ_k . The optimization algorithm changes the values $U_\alpha(\tau_k), k \in \{1, \dots, 5\}$. The value $U_\alpha(\tau_0)$ is fixed to zero. The derivatives at both ends are set to zero. The spline does not necessarily take the maximum or minimum value at one of the nodes. In this example, the maximum lies between τ_1 and τ_2 .

Additionally, we add the constraint $U_L(t) = -U_R(t)$ unless otherwise stated, since it reduces the dimensionality of the optimization problem in the numerical implementation by a factor of two. This implies the constraint $\vec{u}_L = -\vec{u}_R$. The resulting non-linear optimization problem is

$$\begin{aligned} \min_{\vec{u}_L, \vec{u}_R \in \mathbb{R}^{N+1}} & \|O[\Psi](t) - O^{(\text{target})}(t)\|_{2, [0, T]}^2 & (6.4) \\ \text{s.t.} & \quad i\partial_t \psi_q(t) = \mathbf{H}(\vec{u}_L, \vec{u}_R, t) \psi_q(t), \quad t \in [0, T], \\ & \quad \psi_q(0) = \psi_q^0, \\ & \quad \vec{u}_L = -\vec{u}_R, \\ & \quad U_\alpha(\vec{u}_\alpha, \tau_0) = 0, \quad \alpha \in \{L, R\}. \end{aligned}$$

The single particle wave functions $\psi_q(t)$ in the problem (6.4) are only auxiliary variables. Hence, the time-dependent Bogoliubov-de Gennes equation can be removed from the constraint equations for the numerical implementation. The

objective function is then written as $\|O[\psi_q^0, \mathbf{H}(\vec{u}_L, \vec{u}_R, t)](t) - O^{(\text{target})}(t)\|_{2,[0,T]}^2$, whose evaluation requires us to solve the time-dependent Bogoliubov-de Gennes equation in order to calculate the observable $O(t)$.

The problem (6.4) can be solved using standard derivative-free algorithms for non-linear optimization problems. The library NLopt¹ provides a common interface to numerous non-linear optimization algorithms. Some of them can be used for our problem. The proposed method relies on a fast optimization algorithm for the search of the optimal bias $U_\alpha(t)$. We tested the following algorithms: Sbxpl [Row90], COBYLA [Pow94, Pow98], Nelder-Mead Simplex [NM65], PRAXIS [Bre73], NEWUOA [Pow06] and BOBYQA [Pow09]. Figure 6.2 shows benchmarks of these algorithms for a system with $N = 12$. Qualitatively similar results are obtained for larger values of N . The algorithm

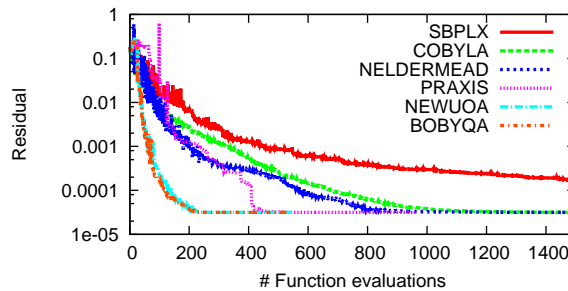


Figure 6.2: Benchmark of six different derivative free-minimization optimization algorithms for a system with $N = 12$.

BOBYQA outperforms all others. Thus, we choose it for optimizations without additional non-linear constraints. It is based on a quadratic approximation of the objective function. The only algorithm of the above listed which supports non-linear constraints is COBYLA. It approximates the objective function in linear order and is used whenever non-linear constraints are needed.

We point out that the quality of the results depends on the number of nodes τ_k for the splines. A larger number of nodes is typically favorable for better results, i.e. yields a better match of the observable $O[\Psi](t)$ with its target pattern $O^{(\text{target})}(t)$. But, the computational cost increases with the number of nodes. Besides, it is not guaranteed that the obtained minimum is the global minimum since the used algorithms are local optimization algorithms. Thus, the results may depend on the initial choice for $U_\alpha(\tau_k)$.

¹ NLopt is a library for non-linear optimization. It can be freely downloaded from <http://ab-initio.mit.edu/nlopt>. We use version 2.3.

6.2 Results for NQDN junctions

6.2.1 Controlling current and density of a NQDN junction

As a first example, we show the optimization of the current $I_{L,QD}(t)$ from the left lead onto the quantum dot. This is done for two different numbers of spline nodes N . The case $N = 4$ shows strong deviations while $N = 20$ already yields an excellent agreement of the calculated current $I_{L,QD}(t)$ with its target pattern.

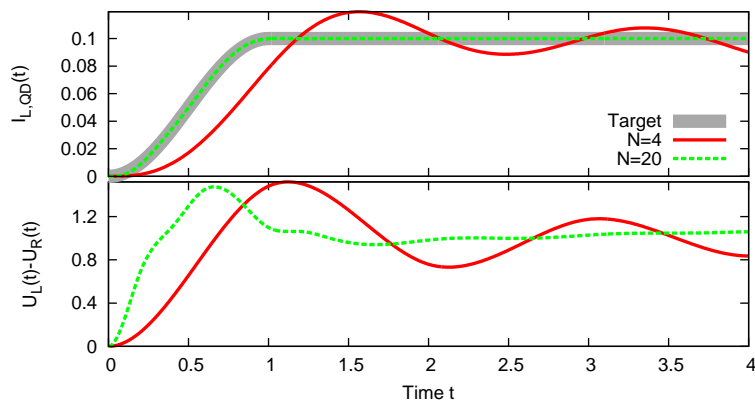


Figure 6.3: NQDN junction with an optimized current for two different number of spline nodes N . The parameters are: $\Gamma_\alpha = 0.2$, $\varepsilon_{QD} = 0.5$.

The evolution from the initial guess $U_\alpha(t) = 0$ towards to final solution is displayed in figure 6.4. The first evaluations are used to construct the initial quadratic model of the objective function and the algorithm tries to determine the reaction of the system to bias pulses at different times. After the first $2N+1$ evaluations, the algorithm starts the real optimization and eventually converges towards the target.

The optimization of the density $n_{QD}(t)$ is very similar to the optimization of a current, one simply exchanges the observable in the objective function. An example is shown in figure 6.5. The density follows perfectly the target pattern.

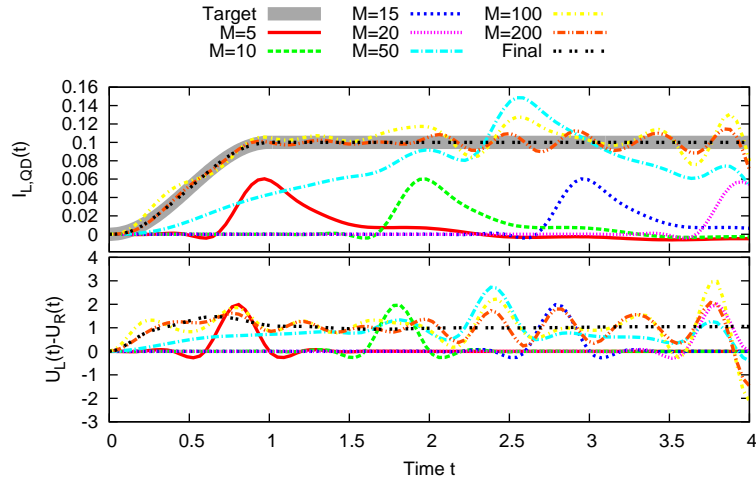


Figure 6.4: Visualization of the convergence using the BOBYQA algorithm, M denotes the number of objective function evaluations. The parameters are: $\Gamma_\alpha = 0.2$, $\varepsilon_{\text{QD}} = 0.5$, $U_{\text{L}}(t) = -U_{\text{R}}(t)$, $N = 20$.

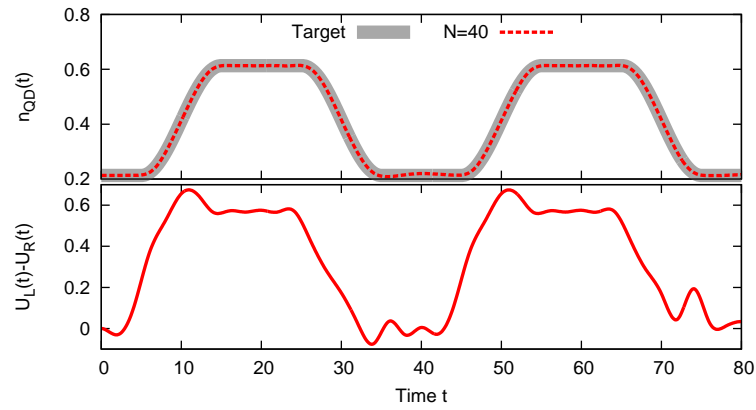


Figure 6.5: NQDN junction with an optimized density. The parameters are: $\Gamma_\alpha = 0.2$, $\varepsilon_{\text{QD}} = 0.5$.

6.2.2 Controlling classical vibrations

In this paragraph, we extend the model to incorporate a vibrational degree of freedom in the central region. In the past, most theoretical work focused on the electronic system and neglected the nuclear motion. In experiments, the nuclei are, of course, not fixed to a position and their motion can have a significant influence on the measured properties, for example on the current-voltage characteristics [GRN07, KvO05, RHC06, HBT09].

The goal of this section is to control the nuclear motion using the bias as before. Although the bias couples only to the electronic part of the system, it induces changes in the density which in turn influences the nuclear motion. Hence, the electrons mediate between the bias and the vibration. The feasibility of controlling the nuclear motion in a quantum-classical system has already been demonstrated [CG14].

The vibrational degree of freedom is described within the Ehrenfest approximation following Verdozzi *et al.* [VSA06] as it was already done in chapter 5. The modified central part of the electronic Hamiltonian reads

$$\hat{H}_{\text{QD}}(t) = (\varepsilon_{\text{QD}} + \lambda x(t)) \sum_{\sigma \in \{\uparrow, \downarrow\}} \hat{c}_{\text{QD}, \sigma}^\dagger \hat{c}_{\text{QD}, \sigma}. \quad (6.5)$$

The parameter λ determines the interaction strength between the electronic and the nuclear system. The equation of motion for the vibrational coordinate $x(t)$ is

$$m\ddot{x}(t) = -\frac{d}{dx} \left(\frac{1}{2} m \omega^2 x^2 + \langle \Psi | \hat{H}_{\text{QD}}(t) | \Psi \rangle \right) \quad (6.6)$$

$$= -m\omega^2 x(t) - \lambda n_{\text{QD}}(t), \quad (6.7)$$

$$x(0) = x^0.$$

The initial value x^0 is calculated self-consistently and the classical equation of motion for the vibrational degree of freedom is solved simultaneously with the time-dependent Schrödinger equation. The optimization problem for controlling

the vibrational coordinate $x(t)$ then reads

$$\begin{aligned}
 & \min_{\vec{u}_L, \vec{u}_R \in \mathbb{R}^{N+1}} \|x(t) - x^{(\text{target})}(t)\|_{2,[0,T]}^2 & (6.8) \\
 \text{s.t.} \quad & i\partial_t \psi_q(t) = \mathbf{H}(\vec{u}_L, \vec{u}_R, x(t), t) \psi_q(t), t \in [0, T], \\
 & m\partial_t^2 x(t) = -m\omega^2 x(t) - \lambda n_{\text{QD}}(t), t \in [0, T], \\
 & \psi_q(0) = \psi_q^0, \\
 & x(0) = x^0, \\
 & \vec{u}_L = -\vec{u}_R, \\
 & U_\alpha(\vec{u}_\alpha, \tau_0) = 0, \quad \alpha \in \{\text{L}, \text{R}\}.
 \end{aligned}$$

Figure 6.6 shows the results of such a calculation.

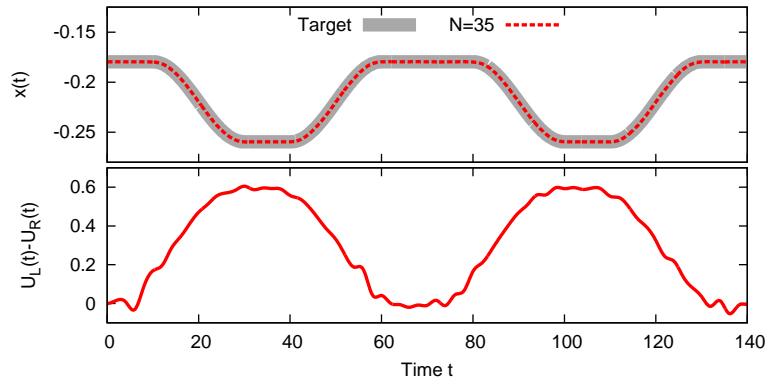


Figure 6.6: NQDN junction with an optimized coordinate $x(t)$ of a vibration coupled to the quantum dot. The parameters are: $\Gamma_\alpha = 0.2$, $\varepsilon_{\text{QD}} = 0.5$, $\lambda = 0.1$, $\omega = 0.5$, $m = 1$.

6.2.3 Imposing further constraints on the bias

In real-world control experiments, an arbitrary time-dependence of $U_\alpha(t)$ is difficult to achieve. In this section, we therefore impose further constraints to restrict the bias $U_\alpha(t)$ or the derivative $\partial_t U_\alpha(t)$. The optimization problem including such additional constraints then reads

$$\begin{aligned}
& \min_{\vec{u}_L, \vec{u}_R \in \mathbb{R}^{N+1}} \|O[\Psi](t) - O^{(\text{target})}(t)\|_{2,[0,T]}^2 & (6.9) \\
& \text{s.t.} \quad i\partial_t \psi_q(t) = \mathbf{H}(\vec{u}_L, \vec{u}_R, t)\psi_q(t), \quad t \in [0, T], \\
& \quad \psi_q(0) = \psi_q^0, \\
& \quad \vec{u}_L = -\vec{u}_R, \\
& \quad U_\alpha(\vec{u}_\alpha, \tau_0) = 0, \\
& \quad U_\alpha^{(\min)} \leq U_\alpha(\vec{u}_\alpha, t) \leq U_\alpha^{(\max)}, \\
& \quad \tilde{U}_\alpha^{(\min)} \leq \frac{d}{dt}U_\alpha(\vec{u}_\alpha, t) \leq \tilde{U}_\alpha^{(\max)}.
\end{aligned}$$

The conditions $U_\alpha^{(\min)} \leq U_\alpha(\vec{u}_\alpha, t) \leq U_\alpha^{(\max)}$ are in general not equivalent to $U_\alpha^{(\min)} \leq \vec{u}_\alpha \leq U_\alpha^{(\max)}$, unless one uses a monotonic cubic spline. This can be seen in figure 6.1, where the maximum value of the spline lies between τ_1 and τ_2 . The constraint for the time derivative is not accessible in this way.

The cubic spline is a third degree polynomial between two nodes τ_j and τ_{j+1} . Thus, the minimum and maximum values can be calculated analytically in every interval $[\tau_j, \tau_{j+1}]$. The constraints are replaced by

$$\max_{t \in [\tau_j, \tau_{j+1}]} U_\alpha(\vec{u}_\alpha, t) \leq U_\alpha^{(\max)}, \quad (6.10)$$

$$\min_{t \in [\tau_j, \tau_{j+1}]} U_\alpha(\vec{u}_\alpha, t) \geq U_\alpha^{(\min)}, \quad (6.11)$$

$$\max_{t \in [\tau_j, \tau_{j+1}]} \frac{d}{dt}U_\alpha(\vec{u}_\alpha, t) \leq \tilde{U}_\alpha^{(\max)}, \quad (6.12)$$

$$\min_{t \in [\tau_j, \tau_{j+1}]} \frac{d}{dt}U_\alpha(\vec{u}_\alpha, t) \geq \tilde{U}_\alpha^{(\min)} \quad (6.13)$$

for $j \in \{0, \dots, N-1\}$. Figure 6.7 shows the influence of the additional constraints. They are chosen such that the steady state value can still be reached, but the transient time is lengthened.

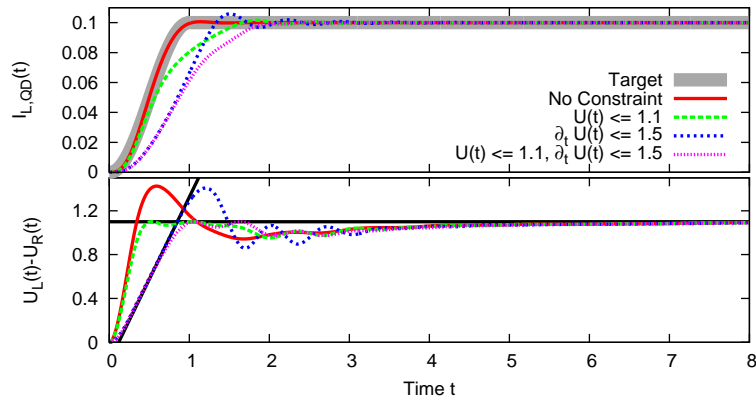


Figure 6.7: NQDN junction with an optimized current $I_{L, \text{QD}}(t)$. The black lines represent the additional constraints $U(t) \leq 1.1$ and $\partial_t U(t) \leq 1.5$. The parameters are: $\Gamma_\alpha = 0.2$, $\varepsilon_{\text{QD}} = 0.5$, $N = 25$.

6.3 Results for SQDS junctions

When making the leads superconducting, a junction with an applied DC bias does not reach a steady state anymore, but ends up in a time-periodic state. A DC current, on the other hand, can flow through the junction even without applying a bias. These phenomena are known as the AC and DC Josephson effects [Jos62]. The underlying relation is

$$U(t) = \frac{\hbar}{2e} \frac{d\chi}{dt}, \quad (6.14)$$

$$\chi(0) = \chi_R - \chi_L, \quad (6.15)$$

$$I(t) = I_0 + I_1 \sin(\chi(t)) + I_2 \cos(\chi(t)), \quad (6.16)$$

where the variables χ_α describe the phase of the superconducting wave function in lead α . Thus, the current oscillates with the frequency $\omega = \frac{2e}{\hbar}U$ when applying a constant bias U across the junction. The values of I_0 , I_1 and I_2 depend on the bias and only I_1 is non-zero for zero bias. Following these equations, the only solution for a DC current flowing through the junction would be $\chi(t) \equiv \text{const}$ and hence $U(t) = 0$. But these equations do not take switching effects into account and only approximate the current after the transients as it is discussed in chapter 4. In order to force the current to follow a predefined pattern, one can make use of the reaction of the current to time-dependent changes in the bias. These can be used, for example, to compensate the Josephson oscillations.

We start again with optimizing the current $I_{L,QD}(t)$ from the left lead onto the quantum dot such that it follows the target pattern. In this way, we generate a DC current $I_{L,QD}(t)$. But the current $I_{QD,R}(t)$ still shows the typical oscillation as it is shown in figure 6.8.

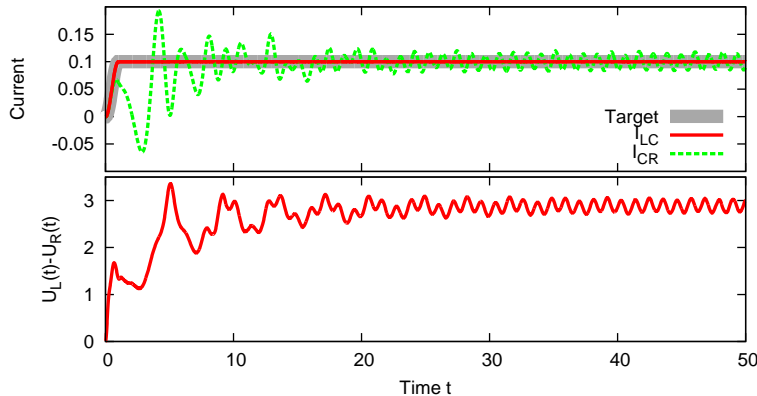


Figure 6.8: SQDS junction with an optimized current for two different number of spline nodes N . The parameters are: $\Gamma_\alpha = 0.2$, $\varepsilon_{QD} = 0.5$, $\chi_\alpha = 0$.

In order to obtain a real DC current flowing through the Josephson junction, one has to modify the objective function. The idea is to optimize $I_{L,QD}(t)$ and $I_{QD,R}(t)$ simultaneously such that each of them follows a target pattern. The targets have to be chosen carefully, since one might end up in situations where the targets cannot be reached simultaneously.

Suppose that the currents $I_{L,QD}(t)$ and $I_{QD,R}(t)$ follow the predefined patterns perfectly. The density on the quantum dot can then be obtained by integrating the continuity equation at the quantum dot:

$$n_{QD}(t) = n_{QD}(0) + \int_0^t dt' \sum_{\alpha \in \{L,R\}} I_{\alpha,QD}^{(\text{target})}(t'). \quad (6.17)$$

As we see, this can easily lead to contradictions like $n_{QD}(t) < 0$ or $n_{QD}(t) > 2$, if the targets are not chosen carefully. Even situations with $I_{L,QD}(t) = -I_{R,QD}(t) \neq 0$ for all times t are in general not possible, since the density in such cases would be constant, but switching on a bias normally changes the density. The density and currents are much more linked than one might think in the first place.

We avoid these difficulties by using the norm $L^2([t_0, t_1])$, $0 \leq t_0 < t_1 \leq T$ in the objective function, which is denoted by $\|\cdot\|_{2,[t_0,t_1]}$. Furthermore, we remove the constraint $U_L(t) = -U_R(t)$ in order to make the targets reachable. The

modified optimization problem reads

$$\begin{aligned}
& \min_{\vec{u}_L, \vec{u}_R \in \mathbb{R}^{N+1}} \left(\|I_{L, \text{QD}}[\Psi](t) - I_{L, \text{QD}}^{(\text{target})}(t)\|_{2, [t_0, t_1]}^2 \right. \\
& \quad \left. + \|I_{\text{QD}, \text{R}}[\Psi](t) - I_{\text{QD}, \text{R}}^{(\text{target})}(t)\|_{2, [t_0, t_1]}^2 \right) \\
& \text{s.t.} \quad i\partial_t \psi_q(t) = \mathbf{H}(\vec{u}_L, \vec{u}_R, t) \psi_q(t), \quad t \in [0, T], \\
& \quad \psi_q(0) = \psi_q^0, \\
& \quad U_\alpha(\vec{u}_\alpha, \tau_0) = 0, \quad \alpha \in \{L, R\}.
\end{aligned} \tag{6.18}$$

The system has now the freedom to adjust the density and currents from time 0 to t_0 such that the target patterns can be reached. There are two ways to achieve a DC current flowing through a Josephson junction:

1. Following the equations (6.14) - (6.16), only the case $U(t) = 0$ produces a DC current, namely $I(t) = I_1 \sin(\chi_0)$. This is the DC Josephson effect. In general, this relation is not true for our model, since the quantum dot always supports two Andreev bound states for $U = 0$ [SPC10]. They lead to persistent oscillations in the current and density [Ste07, KKSG08, SPC10]. The oscillations in the current can be compensated by small variations of the bias $U(t) = U_L(t) - U_R(t)$ around the origin. Figure 6.9 shows an example of such a solution. This approach is limited by I_1 and hence does not work for arbitrary large DC currents.

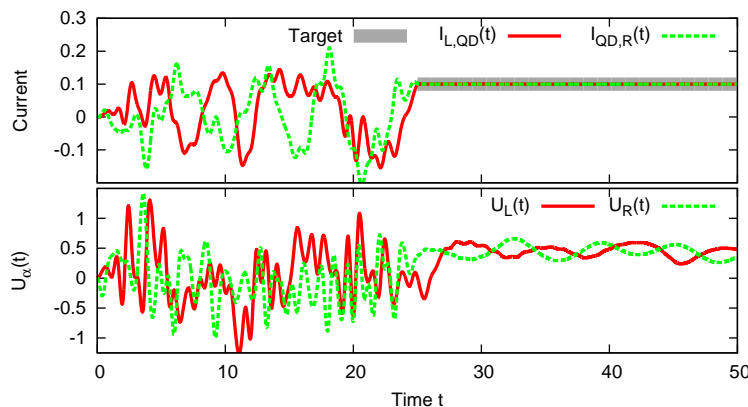


Figure 6.9: SQDS junction with optimized currents $I_{L, \text{QD}}(t)$ and $I_{\text{QD}, \text{R}}(t)$. We removed the constraint $U_L(t) = -U_R(t)$, since the target cannot be reached otherwise. The target is the same for both currents and starts at $t = 25$. The parameters are: $\Gamma_\alpha = 0.2$, $\varepsilon_{\text{QD}} = 0.5$, $\chi_\alpha = 0$, $t_0 = 25$, $t_1 = 50$.

2. An alternative approach is to apply a DC bias across the junction, leading to a linear increase in the phase difference $\chi(t)$ and thus to oscillations in

the currents. This is the AC Josephson effect. These oscillations can be compensated again by small variations in the bias, the reaction to these changes cancels the Josephson oscillations. Figure 6.10 shows an example for this type of solutions.

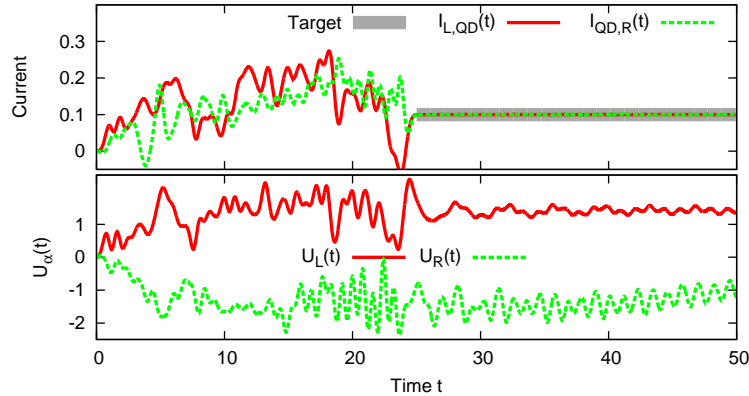


Figure 6.10: Same junction as in figure 6.9, but a different solution for the problem.

6.4 Cooper pair splitting in a Y-shaped junction

In this section, we demonstrate how to optimize the Cooper pair splitting efficiency in a two-quantum dot Y-junction. The overall idea is to create entangled electrons at two quantum dots.

The entanglement of quantum particles has fascinated the scientific community since the proposition of the Einstein-Podolsky-Rosen (EPR) Gedankenexperiment [EPR35]. Entanglement means that two particles are linked such that the measurement of one particle is sufficient to completely determine the quantum state of the other one. A prominent example is a pair of electrons with opposite spin. Suppose, you have a pair of entangled electron in a spin singlet. Then, one spin is up and the other spin is always pointing downwards. Photons are a second example which can be entangled with respect to the polarization.

The EPR Gedankenexperiment is directly linked to the question of non-locality of quantum mechanics: Can a measurement at position x have an influence on a simultaneous or later independent measurement at a different position x' ? This question can be cast into a mathematical formula known as

Bell's inequality [Bel64]. A violation of the latter would prove the non-locality of quantum mechanics.

Great progress has been achieved with entangled photons, but the final experiment ruling out all possible loopholes has not yet been accomplished [GMR⁺13]. For example, the two measurements at (x,t) and (x',t') have to be separated such that $c|t - t'| < \|x - x'\|$, i.e. no information of the first measurement can be transmitted to the second. Hence large distances are typically required to close this loophole [WJS⁺98]. Another important loophole stems from the detector efficiency, i.e. one has to take into account that undetected particles might behave completely different compared to the detected ones. Typically, one uses the fair sampling assumption stating that the detected particles are selected randomly and behave statistically in the same way as the undetected ones.

To do similar Bell test experiments with electrons is much more difficult and remains an open challenge. In recent years, a number of ingenious experiments to create entangled electrons have been performed [HCNS09, HCB⁺11, HPR⁺10, SBS12], going along with several theoretical developments [RSL01, RL02, SFM04, MBB06, GZ07, BHLY11]. The basic idea is to use a superconductor as a source of entangled electrons. In the BCS ground state, electrons form Cooper pairs due to the attractive interaction caused by phonons. These pairs consist of two electrons with opposite spin and momentum.

The idea is to create a splitted Cooper pair at the two quantum dots, i.e. one electron is on the left quantum dot and the other with opposite spin is on the right one (see sketch in figure 6.11). However, this process competes with the case of both electrons moving onto the same quantum dot. The latter can be suppressed by a large charging energy of the quantum dots caused by the Coulomb interaction. This make double occupancies less likely.

We propose a way to achieve splitting efficiencies of 99% and more, which we hope will help the eventual experimental demonstration of the violation of Bell's inequality. In comparison to traditional approaches, our method has two major differences. First, we do not rely on a large Coulomb repulsion on the quantum dots but rather use optimal control theory to tailor the bias in the normal leads in such a way that the splitting probability is maximized. Second, we look at the Cooper pair density on the quantum dots as opposed to the experimental approaches working currents of entangled electrons in the two normal conducting leads. Consequently, a direct comparison of results is not easily possible as the efficiencies measure different ratios. As a future work, it might be worth doing an extensive comparative study answering whether the here created pair eventually moves towards the leads or stays on the quantum dots. In experiments, splitting efficiencies for the current of 90% have been realized in recent experiments [SBS12] being significantly higher than previous results. Despite this progress, the experimental proof of the violation of Bell's inequality is still pending.

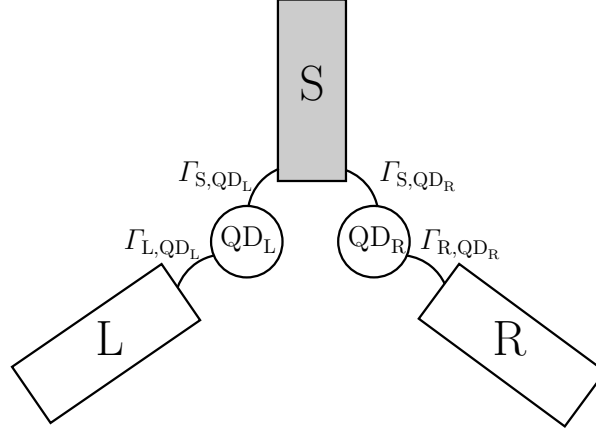


Figure 6.11: Sketch of the Y junction and explanation of all relevant parameters. Only the lead labeled with S is superconducting. The gray color is used to indicate the superconducting part. The aim is to create entangled electrons on the two quantum dots. All three leads are semi infinite.

In contrast to all systems studied in the previous sections, we now work with three leads. The system is sketched in figure 6.11. It consists of two quantum dots (QD_L and QD_R), one superconducting (S) and two normal leads (L and R).

The Hamiltonian of our modified model reads

$$\hat{H}(t) = \sum_{\alpha \in \{L,R,S\}} \hat{H}_\alpha + \sum_{\alpha \in \{L,R,S\}} \hat{H}_{T,\alpha}(t), \quad (6.19)$$

$$\begin{aligned} \hat{H}_\alpha = \sum_{k=0}^{\infty} \sum_{\sigma \in \{\uparrow, \downarrow\}} & \left(t_\alpha \hat{c}_{\alpha k, \sigma}^\dagger \hat{c}_{\alpha(k+1), \sigma} + \text{h.c.} \right) \\ & + \sum_{k=0}^{\infty} \left(\Delta_\alpha \hat{c}_{\alpha k, \uparrow}^\dagger \hat{c}_{\alpha k, \downarrow}^\dagger + \text{h.c.} \right) \text{ for } \alpha \in \{S, L, R\}, \end{aligned} \quad (6.20)$$

$$\hat{H}_{T,S} = \sum_{\alpha \in \{L,R\}} \sum_{\sigma \in \{\uparrow, \downarrow\}} \left(t_{S, \text{QD}_\alpha} \hat{c}_{S0, \sigma}^\dagger \hat{c}_{\text{QD}_\alpha, \sigma} + \text{h.c.} \right), \quad (6.21)$$

$$\hat{H}_{T,\alpha}(t) = \sum_{\sigma \in \{\uparrow, \downarrow\}} \left(t_{\alpha, \text{QD}_\alpha} e^{i\gamma_{\alpha, \text{QD}_\alpha}(t)} \hat{c}_{\alpha 0, \sigma}^\dagger \hat{c}_{\text{QD}_\alpha, \sigma} + \text{h.c.} \right) \text{ for } \alpha \in \{L, R\}. \quad (6.22)$$

Note that there is only a bias in the left and right lead. All parameters are again chosen real and positive. Furthermore, we work at temperature $T = 0$ and assume the wide band limit $t_{\alpha, \text{QD}_\beta} \ll t_\alpha$. Again, only the coupling strengths $\Gamma_{\alpha, \text{QD}_\beta} = 2t_{\alpha, \text{QD}_\beta}^2 / t_\alpha$ will be stated.

In the following, we demonstrate how to optimize the Cooper pair splitting

efficiency in the above model of a two-quantum dot Y-junction. The goal is to operate the device as a Cooper pair splitter that creates entangled electrons on the two quantum dots. The splitting of a Cooper pair can be understood as a crossed Andreev reflection. An incoming electron in one of the normal leads gets reflected into the other lead as a hole. This creates a Cooper pair in the superconductor. The process is sketched in figure 6.12 (top left). Similarly, the opposite process removes a Cooper pair from the superconductor. Besides, there are three other possible reflection processes: (a) normal reflection, (b) Andreev reflection, and (c) elastic cotunneling. The latter corresponds to a reflection of the incoming electron to the opposite lead. These three processes together with the crossed Andreev reflection are all sketched in figure 6.12.

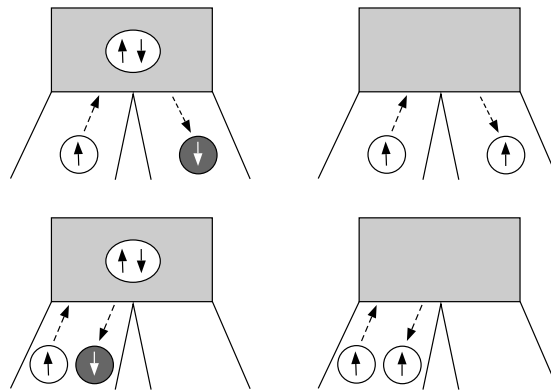


Figure 6.12: Overview of the four possible reflection processes. Black arrows indicate electrons, white arrows represent holes. The gray block is the superconducting lead S of figure 6.11. Top left: Sketch of a crossed Andreev reflection. The incoming spin up electron in the left lead gets reflected as a spin down hole to the right lead. Simultaneously, a Cooper pair is created in the superconducting lead. The opposite process, which removes a Cooper pair from the superconductor, is also possible. Bottom left: The reflected hole stays in the left lead. This corresponds to the normal Andreev reflection. Top right: Sketch of an elastic cotunneling process. Now, the incoming electron gets reflected into the right lead. Bottom right: Alternatively, the electron can also be reflected into the left lead corresponding to normal reflection.

The central ingredient for the optimization process is the proper definition of a suitable objective function which is then to be minimized. It has to quantify the Cooper pair splitting efficiency. To this end, we first define the so-called pairing density or anomalous density as

$$P_{\text{QD}_\alpha, \text{QD}_\beta}(t) = \langle \hat{c}_{\text{QD}_\alpha, \downarrow}(t) \hat{c}_{\text{QD}_\beta, \uparrow}(t) \rangle. \quad (6.23)$$

We use its absolute value squared $|P_{\text{QD}_\alpha, \text{QD}_\beta}(t)|^2$ as a measure for the Cooper

pair density with one electron at QD_α and the other at QD_β . We propose to minimize the following objective function:

$$-\frac{1}{t_1 - t_0} \int_{t_0}^{t_1} dt \frac{\sum_{\alpha \neq \alpha' \in \{L, R\}} |P_{\text{QD}_\alpha, \text{QD}_{\alpha'}}(t)|^2}{\sum_{\alpha, \alpha' \in \{L, R\}} |P_{\text{QD}_\alpha, \text{QD}_{\alpha'}}(t)|^2}. \quad (6.24)$$

The fraction represents the Cooper pair splitting efficiency at time t , which is expressed as the amount of Cooper pairs being split up divided by the total amount of Cooper pairs on the quantum dots. We calculate its average over the time span from t_0 to t_1 . The pairing densities $P_{\text{QD}_\alpha, \text{QD}_\beta}(t)$ are obtained from the single particle wave functions $\psi_q(t)$, i.e., the solutions of the time-dependent Bogoliubov-de Gennes equation (2.44).

We want to tailor the bias such that we maximize the time averaged Cooper pair splitting efficiency. The corresponding optimization problem then reads

$$\begin{aligned} \min_{\vec{u}_L, \vec{u}_R \in \mathbb{R}^{N+1}} & -\frac{1}{t_1 - t_0} \int_{t_0}^{t_1} dt \frac{|P_{\text{QD}_L, \text{QD}_R}(t)|^2 + |P_{\text{QD}_R, \text{QD}_L}(t)|^2}{\sum_{\alpha, \alpha' \in \{L, R\}} |P_{\text{QD}_\alpha, \text{QD}_{\alpha'}}(t)|^2} \\ \text{s.t.} \quad & P_{\text{QD}_\alpha, \text{QD}_\beta} = \int dq f(\varepsilon_q) u_q(\text{QD}_\alpha, t) [v_q(\text{QD}_\beta, t)]^*, \\ & i\partial_t \psi_q(t) = \mathbf{H}(\vec{u}_L, \vec{u}_R, t) \psi_q(t), \quad t \in [0, T], \\ & \psi_q(0) = \psi_q^0, \\ & U_\alpha(\vec{u}_\alpha, \tau_0) = 0, \quad \alpha \in \{L, R\}. \end{aligned} \quad (6.25)$$

The problem can be solved using again standard derivative-free algorithms for non-linear optimization problems, for example the ones provided by the library NLOpt.

To achieve high splitting efficiencies it is essential that the junction is asymmetric, i.e. the couplings to the left and to the right quantum dot must not be equal. This is necessary since we observe an upper bound of 50% for the Cooper pair splitting efficiency in symmetric junctions, which is already achieved in the ground state by the usual Cooper pair tunneling leading to the proximity effect. Hence any optimization starting in the ground state will not improve the results. The underlying cause for this limitation is still unknown and under investigation. In order to bypass this issue, we choose an asymmetric coupling of the quantum dots to the normal leads.

The results of such an optimization are depicted in figure 6.13. The bias is tailored such that the Cooper pair splitting efficiency is maximized. It suppresses the non-splitting processes. The efficiency is optimized in the time interval from $t_0 = 10$ to $t_1 = 40$. This interval is indicated by the underlying thick gray line in the plot of the efficiency (second from top). In this interval, we achieve an average efficiency of more than 99%. The values of $|P_{\text{QD}_L, \text{QD}_R}(t)|^2$ and $|P_{\text{QD}_R, \text{QD}_L}(t)|^2$ are on top of each other. The resulting currents flowing

through the junction indicate, that in the time average, there is a net current flowing from the right normal conducting lead (R) via the superconductor (S) to the left one (L). This is deduced from the observation that $I_{\text{QD}_L, \text{S}}(t)$ and $I_{\text{S}, \text{QD}_R}(t)$ are both negative in the time average. We point out, that this does not say anything about the movement of the entangled Cooper pairs.

This result clearly demonstrates that the Coulomb interaction at the quantum dots is not necessary in order to obtain high efficiencies. One can also succeed with optimized biases.

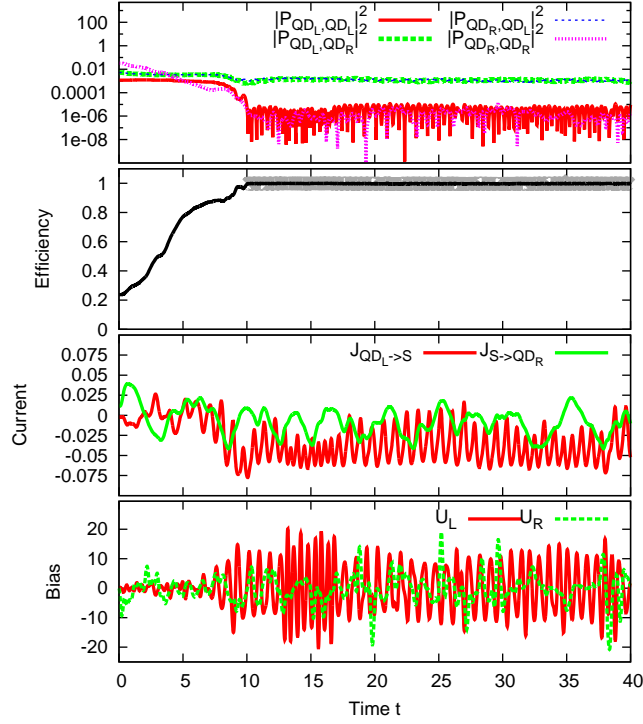


Figure 6.13: Simulation with an optimized bias. (a) Top: $|P_{\text{QD}_\alpha, \text{QD}_\beta}(t)|^2$ as a function of time. (b) Second from top: Resulting efficiency, gray line indicates time interval of optimization. (c) Second from bottom: Resulting currents $I_{\text{QD}_L, \text{S}}(t)$ and $I_{\text{S}, \text{QD}_R}(t)$. (d) Bottom: Tailored bias $U_L(t)$ and $U_R(t)$ of the optimization. The parameters are: $\Gamma_{\text{S}, \text{QD}_L} = \Gamma_{\text{S}, \text{QD}_R} = \Gamma_{\text{N}, \text{QD}_L} = 0.2$, $\Gamma_{\text{N}, \text{QD}_R} = 1$, $N = 200$.

6.5 Conclusion

Usually, in the field of molecular electronics, the goal is to calculate the steady-state or time-dependent current that is generated by a given bias and gate voltage. Sometimes, however, one may be interested in taking a step beyond this point and control the current or other observables of the junction. To this end we have presented an algorithm that allows us to calculate the time-dependent bias that achieves a prescribed goal. In the examples presented, we determine numerically the time-dependent bias that forces the current, the density or the molecular vibration to follow a given temporal pattern. The method is general and not restricted to the observables listed above. In the final section we apply our approach to optimize the Cooper pair splitting efficiency in a Y-junction with two quantum dots. We successfully create spatially separated entangled electron pairs with an efficiency of nearly 100%. We expect our approach to be useful in the control of other - essentially arbitrary - observables in molecular junctions.

Chapter 7

Summary and Outlook

In this thesis we have investigated properties of quantum dots coupled to normal and superconducting leads using two different methods. The first one calculates the large time behaviour of the nonequilibrium Green's functions and is a further development of an existing scheme for the time averaged current in junctions with normal leads [SKRG08]. Our approach yields the asymptotics of the current and the density for junctions with superconducting leads at low computational cost. The other method provides access to the observables at all times by propagating single particle wave functions [SPC10]. For the latter, we have designed an efficient numerical implementation. The speed improvement originates from an optimized data storage and data access as well as from a reduction of the algorithm's time complexity from $\mathcal{O}(n^2)$ to $\mathcal{O}(n(\log n)^2)$, where n is the number of time steps.

Our actual study starts with the analysis of the Josephson effects and the current-voltage characteristics. This provides first insights into the charge transfer mechanisms of Josephson junctions. These are direct transmission, single and multiple Andreev reflection. We report deviations from the original current-phase relation derived by Josephson, which go back to a first order approximation in the coupling to the leads. Furthermore, we observe a resonance condition for particles crossing the dot resulting in the suppression of off-resonance charge transfer processes.

The latter findings are confirmed by the calculation of the spectral function $\mathbf{A}(\omega, T)$, which yields a time-resolved picture of the density of states. The spectral function turns out to have negative value and thus does not allow a simple probability interpretation. It can be viewed as the time-energy analogue of the Wigner function, for which the occurrence of negative values is well known. The problem is resolved by taking the time-energy uncertainty into account and convoluting the spectral function with two Gaussians in the time-energy space. This represents a process of measuring. The resulting distribution is positive-semidefinite, provided that the Gaussians obey the time-energy un-

certainty relation. Having this interpretation at hand, we can visualise and interpret internal changes in the dot when switching the bias. In particular, we illustrate the disappearance and reformation of the Andreev bound states under the influence of a bias pulse.

All results are obtained by neglecting the Coulomb interaction and by treating the pairing potential as an input parameter. This leaves space for further studies extending our work and modelling the electron-electron interaction using an on-site Hubbard interaction as it has already been done for junctions with normal leads [KSK⁺10]. Furthermore, it would be interesting to analyse the proximity effect in the central region by calculating the pairing potential self-consistently.

Next, we generalize our model to allow for a vibrational mode in the dot using the Ehrenfest approximation. We rigorously discuss the stability of the system against small perturbations in the vibrational coordinate for normal and hybrid junctions. Although we work in the limit where the vibrational motion is slow compared to the electronic timescale, we need to go beyond the adiabatic approximation in order to explain all occurring instabilities in the vibrational coordinate. They originate either from a maximum in the effective potential or from a negative effective damping coefficient. We extend the analysis to Josephson junctions in the limit of a large bias and obtain similar criteria for stability. These results can be used to drive the vibration using the bias, working only in certain parameter regimes. Furthermore, we investigate resonances of the different frequencies of the system, in particular the case where the Josephson frequency and the vibrational mode come close. We show that the resonance produces a sharp peak in the amplitude of the current oscillation. We predict that a measurement of the latter can be used to determine the vibrational frequency of the molecule with high accuracy. The vibrational signatures in the current-voltage characteristics are much sharper than those produced by photon assisted tunneling which could alternatively be used to determine the vibrational frequency.

Since the vibration is treated classically, we are not able to observe phenomena like the Franck-Condon blockade. As a future work, we propose to study the behaviour of the vibration in the neighbourhood of an avoided crossing of two potential energy surfaces and incorporate surface hoppings.

Finally, we have explored how to control observables of the system using a tailored bias. The basic idea is to minimize the objective function with the help of derivative-free optimization algorithms. Despite the simplicity of our control scheme, we are able to demonstrate how to force the current, the density or the vibration to follow a predefined pattern. In particular, we are able to obtain a direct current flowing through a Josephson junction. We expect the approach to be useful, for example when the target is a specific state in the presence of multistability or a dynamically unstable steady state.

The approach can be used for essentially arbitrary objective functions and not only to control a given observable. We successfully demonstrated how to employ

the method to maximize the Cooper pair splitting efficiency in a Y-shaped junction. The goal is to create entangled electrons which are spatially separated. In this way, we are able to create entangled electrons with an efficiency of nearly 100%.

As a concluding remark, we remind the reader that this thesis is based on a simple non-interacting tight-binding model. The ultimate prospective goal is to study the time dynamics of superconducting materials with the help of *ab initio* calculations. First progress for normal-conducting junctions using time-dependent density functional theory has already been achieved [KNHG14]. This work employs a modified version of the time propagation algorithm. Since the calculation of superconducting materials with time-dependent density functional theory for superconductors [WKG94] is much more complex, a lot of work remains to be done in this direction.

Appendix A

Time propagation method

A.1 Diagonal elements of the inverse of a tridiagonal matrix

In this section, we explain how to calculate the diagonal elements of the inverse of a tridiagonal matrix. The procedure is adapted from the work [KSA⁺05]. It will be used in the sections A.2 and B.3. Consider an infinite-dimensional tridiagonal matrix

$$\mathbf{A} = \left(\begin{array}{c|ccc} \mathbf{b}_0 & \mathbf{c}_0 & 0 & \\ \hline \mathbf{a}_0 & \mathbf{b}_1 & \mathbf{c}_1 & \\ 0 & \mathbf{a}_1 & \mathbf{b}_2 & \ddots \\ & & \ddots & \ddots \end{array} \right) = \begin{pmatrix} \mathbf{A}_{00} & \widetilde{\mathbf{A}}_{01} \\ \widetilde{\mathbf{A}}_{10} & \widetilde{\mathbf{A}}_{11} \end{pmatrix}. \quad (\text{A.1})$$

with $\mathbf{a}_k, \mathbf{b}_k, \mathbf{c}_k \in \mathbb{C}^{n \times n}, k \in \mathbb{N}_0$ and

$$\begin{aligned} \mathbf{A}_{00} &= \mathbf{b}_0, & \widetilde{\mathbf{A}}_{01} &= \begin{pmatrix} \mathbf{c}_0 & 0 & \dots \end{pmatrix}, \\ \widetilde{\mathbf{A}}_{10} &= \begin{pmatrix} \mathbf{a}_0 \\ 0 \\ \vdots \end{pmatrix}, & \widetilde{\mathbf{A}}_{11} &= \begin{pmatrix} \mathbf{b}_1 & \mathbf{c}_1 & \\ \mathbf{a}_1 & \mathbf{b}_2 & \ddots \\ & \ddots & \ddots \end{pmatrix}. \end{aligned} \quad (\text{A.2})$$

We want to calculate the diagonal elements of the matrix $\mathbf{A}^{-1} \equiv \widetilde{\mathbf{B}}_{00}$. The matrix $\widetilde{\mathbf{B}}_{00}$ can be partitioned in the same way as \mathbf{A} :

$$\mathbf{A}^{-1} = \widetilde{\mathbf{B}}_{00} = \begin{pmatrix} \mathbf{B}_{00} & \widetilde{\mathbf{B}}_{01} \\ \widetilde{\mathbf{B}}_{10} & \widetilde{\mathbf{B}}_{11} \end{pmatrix} \quad (\text{A.3})$$

with $\mathbf{B}_{00} \in \mathbb{C}^{n \times n}$. We iterate the partitioning and obtain

$$\tilde{\mathbf{B}}_{11} = \begin{pmatrix} \mathbf{B}_{11} & \tilde{\mathbf{B}}_{12} \\ \tilde{\mathbf{B}}_{21} & \tilde{\mathbf{B}}_{22} \end{pmatrix}, \quad \tilde{\mathbf{B}}_{22} = \begin{pmatrix} \mathbf{B}_{22} & \tilde{\mathbf{B}}_{23} \\ \tilde{\mathbf{B}}_{32} & \tilde{\mathbf{B}}_{33} \end{pmatrix}, \quad \tilde{\mathbf{B}}_{33} = \begin{pmatrix} \mathbf{B}_{33} & \tilde{\mathbf{B}}_{34} \\ \tilde{\mathbf{B}}_{43} & \tilde{\mathbf{B}}_{44} \end{pmatrix}, \quad \dots \quad (\text{A.4})$$

with $\mathbf{B}_{kk} \in \mathbb{C}^{n \times n}$, $k \in \mathbb{N}$. We write

$$\begin{pmatrix} \mathbf{A}_{00} & \tilde{\mathbf{A}}_{01} \\ \tilde{\mathbf{A}}_{10} & \tilde{\mathbf{A}}_{11} \end{pmatrix} = \begin{pmatrix} 0 & \tilde{\mathbf{A}}_{01} \\ \tilde{\mathbf{A}}_{10} & 0 \end{pmatrix} + \begin{pmatrix} \mathbf{A}_{00} & 0 \\ 0 & \tilde{\mathbf{A}}_{11} \end{pmatrix}, \quad (\text{A.5})$$

and obtain for the inverse of \mathbf{A}

$$\begin{pmatrix} \mathbf{B}_{00} & \tilde{\mathbf{B}}_{01} \\ \tilde{\mathbf{B}}_{10} & \tilde{\mathbf{B}}_{11} \end{pmatrix} = \begin{pmatrix} \mathbf{A}_{00} & 0 \\ 0 & \tilde{\mathbf{A}}_{11} \end{pmatrix}^{-1} - \begin{pmatrix} \mathbf{A}_{00} & 0 \\ 0 & \tilde{\mathbf{A}}_{11} \end{pmatrix}^{-1} \begin{pmatrix} 0 & \tilde{\mathbf{A}}_{01} \\ \tilde{\mathbf{A}}_{10} & 0 \end{pmatrix} \begin{pmatrix} \mathbf{B}_{00} & \tilde{\mathbf{B}}_{01} \\ \tilde{\mathbf{B}}_{10} & \tilde{\mathbf{B}}_{11} \end{pmatrix}. \quad (\text{A.6})$$

This yields

$$\mathbf{B}_{00} = \mathbf{A}_{00}^{-1} - \mathbf{A}_{00}^{-1} \tilde{\mathbf{A}}_{01} \tilde{\mathbf{B}}_{10} \quad (\text{A.7})$$

$$\tilde{\mathbf{B}}_{10} = \tilde{\mathbf{A}}_{11}^{-1} \tilde{\mathbf{A}}_{10} \mathbf{B}_{00} \quad (\text{A.8})$$

and thus

$$\mathbf{B}_{00} = \left[\mathbf{A}_{00} - \tilde{\mathbf{A}}_{01} \tilde{\mathbf{A}}_{11}^{-1} \tilde{\mathbf{A}}_{10} \right]^{-1}. \quad (\text{A.9})$$

Iterating the procedure finally results in

$$\mathbf{B}_{00} = \frac{\mathbb{1}}{\mathbf{b}_0 - \mathbf{c}_0 \frac{\mathbb{1}}{\mathbf{b}_1 - \mathbf{c}_1 \frac{\mathbb{1}}{\dots \mathbf{a}_1}} \mathbf{a}_0} \quad (\text{A.10})$$

and

$$\mathbf{B}_{mm} = \frac{\mathbb{1}}{\mathbf{b}_m - \mathbf{c}_m \frac{\mathbb{1}}{\mathbf{b}_{m+1} - \mathbf{c}_{m+1} \frac{\mathbb{1}}{\dots \mathbf{a}_{m+1}}} \mathbf{a}_m}. \quad (\text{A.11})$$

In the case of $\mathbf{a}_0 = \mathbf{a}_1 = \mathbf{a}_2 = \dots$, $\mathbf{b}_0 = \mathbf{b}_1 = \mathbf{b}_2 = \dots$ and $\mathbf{c}_0 = \mathbf{c}_1 = \mathbf{c}_2 = \dots$, we obtain the implicit equation

$$\mathbf{B}_{00} = \frac{\mathbb{1}}{\mathbf{b}_0 - \mathbf{c}_0 \mathbf{B}_{00} \mathbf{a}_0}. \quad (\text{A.12})$$

A.2 Calculation of the embedding matrices

In order to calculate the source and memory term, we need the embedding matrices $\mathbf{Q}_\alpha^{(m)}$. We recall their definition from equation (3.39):

$$\mathbf{Q}_\alpha^{(m)} = \mathbf{H}_{C\alpha} \frac{(\mathbf{1} - i\delta\mathbf{H}_{\alpha\alpha})^m}{(\mathbf{1} + i\delta\mathbf{H}_{\alpha\alpha})^{m+1}} \mathbf{H}_{\alpha C}. \quad (\text{A.13})$$

Since they include the inversion of an infinite dimensional matrix, this cannot be done directly. The scheme is taken from the works [KSA⁺05, SPC10]. The entries of the matrices $\mathbf{Q}_\alpha^{(m)}$ are mostly zero, except for the ends of the diagonal. This is due to the fact that the hopping matrices only act on the sites in the direct neighbourhood of the interfaces. Thus we can write them as

$$\mathbf{Q}_L^{(m)} = \begin{pmatrix} \mathbf{q}_L^{(m)} & 0 & \dots & 0 \\ 0 & 0 & \dots & 0 \\ \vdots & \vdots & \ddots & \vdots \\ 0 & 0 & \dots & 0 \end{pmatrix}, \quad \mathbf{Q}_R^{(m)} = \begin{pmatrix} 0 & \dots & 0 & 0 \\ \vdots & \ddots & \vdots & \vdots \\ 0 & \dots & 0 & 0 \\ 0 & \dots & 0 & \mathbf{q}_R^{(m)} \end{pmatrix}. \quad (\text{A.14})$$

Similarly, the entries of the matrices $\mathbf{H}_{\alpha C} = \mathbf{H}_{C\alpha}^\dagger$ and $\mathbf{H}_{\alpha\alpha}$ are mostly zero and are written as

$$\mathbf{H}_{CR} = \begin{pmatrix} 0 & 0 & 0 & \dots \\ \vdots & \vdots & \vdots & \\ 0 & 0 & 0 & \dots \\ \mathbf{t}_{CR} & 0 & 0 & \dots \end{pmatrix}, \quad \mathbf{H}_{CL} = \begin{pmatrix} \dots & 0 & 0 & \mathbf{t}_{CL} \\ \dots & 0 & 0 & 0 \\ \vdots & \vdots & \vdots & \\ \dots & 0 & 0 & 0 \end{pmatrix}, \quad (\text{A.15})$$

$$\mathbf{H}_{LL} = \begin{pmatrix} \dots & \ddots & \ddots & \ddots & & \\ \dots & 0 & \mathbf{t}_L & \mathbf{h}_L & \mathbf{t}_L^\dagger & 0 \\ \dots & 0 & 0 & \mathbf{t}_L & \mathbf{h}_L & \mathbf{t}_L^\dagger \\ \dots & \dots & 0 & 0 & \mathbf{t}_L & \mathbf{h}_L \end{pmatrix}, \quad (\text{A.16})$$

$$\mathbf{H}_{RR} = \begin{pmatrix} \mathbf{h}_R & \mathbf{t}_R & 0 & 0 & \dots & \\ \mathbf{t}_R^\dagger & \mathbf{h}_R & \mathbf{t}_R & 0 & 0 & \dots \\ 0 & \mathbf{t}_R^\dagger & \mathbf{h}_R & \mathbf{t}_R & 0 & \dots \\ & & \ddots & \ddots & \ddots & \end{pmatrix}. \quad (\text{A.17})$$

Using the technique of a generating function, we get

$$\mathbf{q}_\alpha^{(m)} = \mathbf{t}_{C\alpha} \left(\frac{(\mathbb{1} - i\delta\mathbf{H}_{\alpha\alpha})^m}{(\mathbb{1} + i\delta\mathbf{H}_{\alpha\alpha})^{m+1}} \right)_{(\alpha 0, \alpha 0)} \mathbf{t}_{\alpha C} \quad (\text{A.18})$$

$$= \mathbf{t}_{C\alpha} \frac{1}{m!} \left(-\frac{\partial}{\partial x} + \frac{\partial}{\partial y} \right)^m \left(\frac{\mathbb{1}}{x\mathbb{1} + i\delta y \mathbf{H}_{\alpha\alpha}} \right)_{(\alpha 0, \alpha 0)} \Big|_{x=y=1} \mathbf{t}_{\alpha C}, \quad (\text{A.19})$$

where the subindex $(\alpha 0, \alpha 0)$ denotes the projection onto the site $\alpha 0$. We define

$$\mathbf{p}_\alpha^{(0)}(x, y) = \left(\frac{\mathbb{1}}{x\mathbb{1} + i\delta y \mathbf{H}_{\alpha\alpha}} \right)_{(\alpha 0, \alpha 0)}, \quad (\text{A.20})$$

$$\mathbf{p}_\alpha^{(m)}(x, y) = \frac{1}{m!} \left(-\frac{\partial}{\partial x} + \frac{\partial}{\partial y} \right)^m \mathbf{p}_\alpha^{(0)}(x, y), \quad m \in \mathbb{N}. \quad (\text{A.21})$$

The matrices $\mathbf{q}_\alpha^{(m)}$ are then calculated via $\mathbf{q}_\alpha^{(m)} = \mathbf{t}_{C\alpha} \mathbf{p}_\alpha^{(m)}(1, 1) \mathbf{t}_{\alpha C}$. The matrix $\mathbf{p}_\alpha^{(0)}(x, y)$ can be calculated using the result of equation (A.12):

$$\mathbf{p}_\alpha^{(0)}(x, y) = \frac{\mathbb{1}}{x\mathbb{1} + i\delta y \mathbf{h}_\alpha + \delta^2 y^2 \mathbf{t}_\alpha \mathbf{p}_\alpha^{(0)}(x, y) \mathbf{t}_\alpha^\dagger}. \quad (\text{A.22})$$

This equation is a fixed-point equation for the matrix $\mathbf{p}_\alpha^{(0)}(x, y)$. Performing a fixed-point iteration with $x = y = 1$ eventually gives $\mathbf{q}_\alpha^{(0)} = \mathbf{t}_{C\alpha} \mathbf{p}_\alpha^{(0)}(1, 1) \mathbf{t}_{\alpha C}$. The calculation of $\mathbf{p}_\alpha^{(m)}(x, y)$, $m \in \mathbb{N}$ is based on the identity

$$0 = \frac{1}{m!} \left(-\frac{\partial}{\partial x} + \frac{\partial}{\partial y} \right)^m \frac{\mathbb{1}}{\mathbf{p}_\alpha^{(0)}(x, y)} \mathbf{p}_\alpha^{(0)}(x, y), \quad m \in \mathbb{N}. \quad (\text{A.23})$$

We combine the equation (A.23) with the equations (A.21) and (A.22) and eventually obtain for $x = y = 1$

$$\begin{aligned} (\mathbb{1} + i\delta \mathbf{h}_\alpha) \mathbf{p}_\alpha^{(m)}(1, 1) &= (\mathbb{1} - i\delta \mathbf{h}_\alpha) \mathbf{p}_\alpha^{(m-1)}(1, 1) \\ &\quad - \delta^2 \sum_{k=0}^m \mathbf{t}_\alpha \mathbf{p}_\alpha^{(k)}(1, 1) \mathbf{t}_\alpha^\dagger \mathbf{p}_\alpha^{(m-k)}(1, 1) \\ &\quad - 2\delta^2 \sum_{k=1}^m \mathbf{t}_\alpha \mathbf{p}_\alpha^{(k-1)}(1, 1) \mathbf{t}_\alpha^\dagger \mathbf{p}_\alpha^{(m-k)}(1, 1) \\ &\quad - \delta^2 \sum_{k=2}^m \mathbf{t}_\alpha \mathbf{p}_\alpha^{(k-2)}(1, 1) \mathbf{t}_\alpha^\dagger \mathbf{p}_\alpha^{(m-k)}(1, 1). \end{aligned} \quad (\text{A.24})$$

This equation can be transformed into a Sylvester equation for $\mathbf{p}_\alpha^{(m)}(1,1)$ of the type

$$\mathbf{A}\mathbf{X} + \mathbf{X}\mathbf{B} = \mathbf{C} \quad (\text{A.25})$$

with the unknown matrix \mathbf{X} . One possibility to solve for \mathbf{X} is to cast this equation into the normal linear equation

$$\left(\mathbb{1}_{n \times n} \otimes \mathbf{A} + \mathbf{B}^T \otimes \mathbb{1}_{n \times n}\right) \text{vec}\{\mathbf{X}\} = \text{vec}\{\mathbf{C}\}, \quad (\text{A.26})$$

with the Kronecker product \otimes and the matrix-to-vector operator $\text{vec} : \mathbb{C}^{n \times m} \rightarrow \mathbb{C}^{n \cdot m}$ [SS97]. An alternative approach is to use Schur decompositions as it implemented in LAPACK [And99].

This procedure allows a fast and easy calculation of $\mathbf{p}_\alpha^{(m)}(1,1)$, provided all other $\mathbf{p}_\alpha^{(j)}(1,1)$ with $j < m$ are known. The matrix $\mathbf{p}_\alpha^{(0)}(1,1)$ is calculated using the continuous fraction from above. The matrices $\mathbf{Q}_\alpha^{(m)}$ can then be constructed using

$$\mathbf{q}_\alpha^{(m)} = \mathbf{t}_{C\alpha} \mathbf{p}_\alpha^{(m)} \mathbf{t}_{\alpha C}. \quad (\text{A.27})$$

A.3 Calculation of the source term

The source term $S_\alpha^{(m)}$ was defined in section 3.2 and reads

$$S_\alpha^{(m)} = -2i\delta\mathbf{z}_\alpha^{(m)} \mathbf{H}_{C\alpha} \frac{(\mathbb{1} - i\delta\mathbf{H}_{\alpha\alpha})^m}{(\mathbb{1} + i\delta\mathbf{H}_{\alpha\alpha})^{m+1}} \psi_\alpha^{(0)}. \quad (\text{A.28})$$

For a practical implementation, the source term has to be reformulated since it cannot be computed directly in the above way. We denote the ground state energy of the wave function ψ with E . At time $t = 0$, we have

$$E\psi_\alpha^{(0)} = \mathbf{H}_{\alpha\alpha}\psi_\alpha^{(0)} + \mathbf{H}_{\alpha C}\psi_C^{(0)}, \quad (\text{A.29})$$

$$(x + i\delta y E)\psi_\alpha^{(0)} = (x\mathbb{1} + i\delta y \mathbf{H}_{\alpha\alpha})\psi_\alpha^{(0)} + i\delta y \mathbf{H}_{\alpha C}\psi_C^{(0)}. \quad (\text{A.30})$$

Using the identity

$$\frac{(1 - i\delta\xi)^m}{(x + i\delta y\xi)^{m+1}} = \frac{1}{m!} \left(-\frac{\partial}{\partial x} + \frac{\partial}{\partial y}\right)^m \frac{1}{x + i\delta y\xi}, \quad (\text{A.31})$$

we finally arrive at

$$\frac{(\mathbb{1} - i\delta\mathbf{H}_{\alpha\alpha})^m}{(\mathbb{1} + i\delta\mathbf{H}_{\alpha\alpha})^{m+1}}\psi_\alpha^{(0)} = \frac{1}{m!} \left(-\frac{\partial}{\partial x} + \frac{\partial}{\partial y} \right)^m \frac{\mathbb{1}}{x\mathbb{1} + iy\delta\mathbf{H}_{\alpha\alpha}} \Big|_{x=y=1} \psi_\alpha^{(0)} \quad (\text{A.32})$$

$$= \frac{1}{m!} \left(-\frac{\partial}{\partial x} + \frac{\partial}{\partial y} \right)^m \left(\frac{1}{x + i\delta y E} \psi_\alpha^{(0)} + \frac{\mathbb{1}}{x\mathbb{1} + i\delta y \mathbf{H}_{\alpha\alpha}} \frac{i\delta y}{x + i\delta y E} \mathbf{H}_{\alpha C} \psi_C^{(0)} \right) \Big|_{x=y=1} \quad (\text{A.33})$$

$$= \frac{(1 - i\delta E)^m}{(1 + i\delta E)^{m+1}} \psi_\alpha^{(0)} \quad (\text{A.34})$$

$$+ i\delta \sum_{j=0}^m \frac{(1 - i\delta E)^{m-j}}{(1 + i\delta E)^{m-j+1}} \frac{(\mathbb{1} - i\delta\mathbf{H}_{\alpha\alpha})^j}{(\mathbb{1} + i\delta\mathbf{H}_{\alpha\alpha})^{j+1}} \mathbf{H}_{\alpha C} \psi_C^{(0)}$$

$$+ i\delta \sum_{j=1}^m \frac{(1 - i\delta E)^{m-j}}{(1 + i\delta E)^{m-j+1}} \frac{(\mathbb{1} - i\delta\mathbf{H}_{\alpha\alpha})^{j-1}}{(\mathbb{1} + i\delta\mathbf{H}_{\alpha\alpha})^j} \mathbf{H}_{\alpha C} \psi_C^{(0)}.$$

Thus

$$S_\alpha^{(m)} = -2i\delta\mathbf{z}_\alpha^{(m)} \left(f^{(m)} \mathbf{H}_{C\alpha} \psi_\alpha^{(0)} + i\delta \sum_{j=0}^m f^{(m-j)} \mathbf{Q}_\alpha^{(j)} \psi_C^{(0)} + i\delta \sum_{j=1}^m f^{(m-j)} \mathbf{Q}_\alpha^{(j-1)} \psi_C^{(0)} \right) \quad (\text{A.35})$$

with

$$f^{(j)} = \frac{(1 - i\delta E)^j}{(1 + i\delta E)^{j+1}}. \quad (\text{A.36})$$

The source term $S_\alpha^{(m)}$, $m > 0$ can be further reformulated for a more efficient numerical implementation, as it was already done in [Nit08, Kho12] for systems

with normal leads:

$$\begin{aligned}
S_\alpha^{(m)} &= \frac{1 - i\delta E}{1 + i\delta E} \frac{\mathbf{z}_\alpha^{(m)}}{\mathbf{z}_\alpha^{(m-1)}} \left[-2i\delta \mathbf{z}_\alpha^{(m-1)} \left(f^{(m-1)} \mathbf{H}_{C\alpha} \psi_\alpha^{(0)} \right. \right. \\
&\quad \left. \left. + i\delta \sum_{j=0}^{m-1} f^{(m-1-j)} \mathbf{Q}_\alpha^{(j)} \psi_C^{(0)} + i\delta \sum_{j=1}^{m-1} f^{(m-1-j)} \mathbf{Q}_\alpha^{(j-1)} \psi_C^{(0)} \right) \right] \\
&\quad + 2\delta^2 f^{(0)} \mathbf{z}_\alpha^{(m)} \left(\mathbf{Q}_\alpha^{(m)} + \mathbf{Q}_\alpha^{(m-1)} \right) \psi_C^{(0)} \\
&= \frac{1 - i\delta E}{1 + i\delta E} \frac{\mathbf{z}_\alpha^{(m)}}{\mathbf{z}_\alpha^{(m-1)}} S_\alpha^{(m-1)} + \frac{2\delta^2}{1 + i\delta E} \mathbf{z}_\alpha^{(m)} \left(\mathbf{Q}_\alpha^{(m)} + \mathbf{Q}_\alpha^{(m-1)} \right) \psi_C^{(0)}.
\end{aligned} \tag{A.37}$$

(A.38)

Appendix B

Derivation of the NEGF method

B.1 Large time behaviour of the current and density

The goal of this section is to derive formulas for the density and the current after the transient. As already explained in section 3.3, the Hamiltonians $\mathbf{H}_{\alpha C}(t)$ will be time-independent in this section. The observables read in terms of the nonequilibrium Green's functions as

$$n_k(t) = -i[\mathbf{G}_{kk}^<(t,t)]_{(\uparrow,\uparrow)} + i[\mathbf{G}_{kk}^>(t,t)]_{(\downarrow,\downarrow)}, \quad (\text{B.1})$$

$$= -i[\mathbf{G}_{CC}^<(t,t)]_{(k\uparrow,k\uparrow)} + i[\mathbf{G}_{CC}^>(t,t)]_{(k\downarrow,k\downarrow)}, \quad (\text{B.2})$$

$$I_{k,l}(t) = 2\text{Re Tr} \{ \mathbf{G}_{lk}^<(t,t) \mathbf{H}_{kl}(t) \boldsymbol{\sigma}_z \} \quad (\text{B.3})$$

$$= 2\text{Re Tr} \{ [\mathbf{G}_{CC}^<(t,t)]_{(l,k)} [\mathbf{H}_{CC}(t)]_{(k,l)} \boldsymbol{\sigma}_z \}. \quad (\text{B.4})$$

The main idea is to derive equations for the long time behaviour of $\mathbf{G}_{CC}^{\gtrless}(t,t)$. Our derivation presented here adapts the ideas of the work [SKGR07] which calculates the currents $I_{\alpha C}(t)$ for junctions with normal leads by analyzing the large time behaviour of $\mathbf{G}_{C\alpha}^<(t,t) \mathbf{H}_{\alpha C}$.

We recall the definition of the Keldysh contour γ from section 2.2.1 which is shown again in figure B.1. The contour starts at t_0 which will be set to $-\infty$ after the derivation, corresponding to the usual approach which applies perturbations in the past at $t_0 = -\infty$.

We further make heavy use of convolutions and products of two and more functions defined on the Keldysh contour. Derivations of various useful identities can be found in [vLDS+06, SvL13].

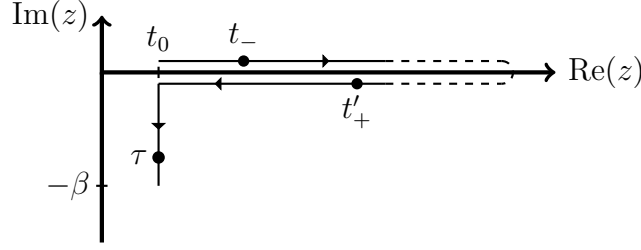


Figure B.1: Sketch of the Keldysh contour γ in the complex time plane. Variables t_{\pm} denote times on the upper (-) or lower (+) branch of the horizontal part. The variable τ is used for times on the vertical part.

We define the symbols \cdot and \star as

$$[\mathbf{A} \cdot \mathbf{B}](t, t') = \int_{t_0}^{\infty} d\bar{t} \mathbf{A}(t, \bar{t}) \mathbf{B}(\bar{t}, t'), \quad (\text{B.5})$$

$$[\mathbf{A} \star \mathbf{B}](t, t') = \int_{t_0}^{t_0 - i\beta} d\tau \mathbf{A}(t, \tau) \mathbf{B}(\tau, t'). \quad (\text{B.6})$$

Multiple products are defined analogously, i.e. $[\mathbf{A} \cdot \mathbf{B} \cdot \mathbf{C}](t, t') = [\mathbf{A} \cdot [\mathbf{B} \cdot \mathbf{C}]](t, t')$. Let $\mathbf{g}(z, z')$ be the Green's function of the uncontacted System with $\mathbf{H}_{\alpha C} = \mathbf{H}_{C\alpha} = 0$ which is linked to the full Green's function via [SKGR07]

$$\mathbf{G}(z, z') = \mathbf{g}(z, z') + \int_{\gamma} d\tilde{z} \mathbf{g}(z, \tilde{z}) \begin{pmatrix} 0 & \mathbf{H}_{LC} & 0 \\ \mathbf{H}_{CL} & 0 & \mathbf{H}_{CR} \\ 0 & \mathbf{H}_{RC} & 0 \end{pmatrix} \mathbf{G}(\tilde{z}, z') \quad (\text{B.7})$$

$$= \mathbf{g}(z, z') + \int_{\gamma} d\tilde{z} \mathbf{G}(z, \tilde{z}) \begin{pmatrix} 0 & \mathbf{H}_{LC} & 0 \\ \mathbf{H}_{CL} & 0 & \mathbf{H}_{CR} \\ 0 & \mathbf{H}_{RC} & 0 \end{pmatrix} \mathbf{g}(\tilde{z}, z'). \quad (\text{B.8})$$

Carrying out the matrix multiplication and using identities for the retarded and advanced Green's functions yields [vLDS+06]

$$\mathbf{G}_{C\alpha}^{\text{R,A}}(t, t') = [\mathbf{G}_{CC}^{\text{R,A}} \cdot \mathbf{H}_{C\alpha} \mathbf{g}_{\alpha\alpha}^{\text{R,A}}](t, t'), \quad (\text{B.9})$$

$$\mathbf{G}_{\alpha C}^{\text{R,A}}(t, t') = [\mathbf{g}_{\alpha\alpha}^{\text{R,A}} \mathbf{H}_{\alpha C} \cdot \mathbf{G}_{CC}^{\text{R,A}}](t, t'). \quad (\text{B.10})$$

We will further make use of the several relations which are taken from [SKGR07],

but adapted to our definition of the Keldysh contour:

$$\mathbf{G}^{\geq}(t,t') = \mathbf{G}^{\text{R}}(t,t_0)\mathbf{G}^{\geq}(t_0,t_0)\mathbf{G}^{\text{A}}(t_0,t'), \quad (\text{B.11})$$

$$\mathbf{g}^{\lceil}(t,\tau) = i\mathbf{g}^{\text{R}}(t,t_0)\mathbf{g}^{\lceil}(t_0,\tau), \quad (\text{B.12})$$

$$\mathbf{g}^{\lceil}(\tau,t) = -i\mathbf{g}^{\lceil}(\tau,t_0)\mathbf{g}^{\text{A}}(t_0,t), \quad (\text{B.13})$$

$$\mathbf{G}_{\alpha\text{C}}^{\geq}(t_0,t_0) = [\mathbf{g}_{\alpha\alpha}^{\lceil}\mathbf{H}_{\alpha\text{C}} \star \mathbf{G}_{\text{CC}}^{\lceil}](t_0,t_0), \quad (\text{B.14})$$

$$\mathbf{G}_{\alpha\alpha'}^{\geq}(t_0,t_0) = \delta_{\alpha\alpha'}\mathbf{g}_{\alpha\alpha}^{\geq}(t_0,t_0) + [\mathbf{g}_{\alpha\alpha}^{\lceil}\mathbf{H}_{\alpha\text{C}} \star \mathbf{G}_{\text{CC}}^{\text{M}} \star \mathbf{H}_{\text{C}\alpha'}\mathbf{g}_{\alpha'\alpha'}^{\lceil}](t_0,t_0). \quad (\text{B.15})$$

The superscript \lceil (\lceil) denotes that the first (second) time argument is on the vertical part of the Keldysh contour. Similarly, the superscript M indicates that both time arguments are complex. The variables t and t' always represent real time arguments and τ is reserved for complex ones, which are on the vertical part of the Keldysh contour.

We further recall the definition of the embedding self-energy:

$$\Sigma_{\alpha}^{\text{R,A},\geq}(t,t') = \mathbf{H}_{\text{C}\alpha}\mathbf{g}_{\alpha\alpha}^{\text{R,A},\geq}(t,t')\mathbf{H}_{\alpha\text{C}}, \quad (\text{B.16})$$

$$\Sigma_{\alpha}^{\lceil}(t,\tau) = \mathbf{H}_{\text{C}\alpha}\mathbf{g}_{\alpha\alpha}^{\lceil}(t,\tau)\mathbf{H}_{\alpha\text{C}}, \quad (\text{B.17})$$

$$\Sigma_{\alpha}^{\lceil}(\tau,t') = \mathbf{H}_{\text{C}\alpha}\mathbf{g}_{\alpha\alpha}^{\lceil}(\tau,t')\mathbf{H}_{\alpha\text{C}}. \quad (\text{B.18})$$

We now express $\mathbf{G}_{\text{CC}}^{\leq}(t,t)$ in terms of quantities of the central region, that are $\mathbf{G}_{\text{CC}}^{\text{R,A},\geq,\lceil,\lceil,\text{M}}$ and $\Sigma_{\alpha}^{\text{A},\geq,\lceil,\lceil}$.

At this point, we are a bit more general than necessary and express $\mathbf{G}_{\text{CC}}^{\geq}(t,t')$ in term of matrices of the central region. At the end of the derivation, we set $t' = t$. This allows us to reuse the intermediate results in a later part of the appendix.

$$\mathbf{G}_{\text{CC}}^{\geq}(t,t') \stackrel{(\text{B.11})}{=} [\mathbf{G}^{\text{R}}(t,t_0)\mathbf{G}^{\geq}(t_0,t_0)\mathbf{G}^{\text{A}}(t_0,t')]_{\text{CC}} \quad (\text{B.19})$$

$$= \mathbf{G}_{\text{CC}}^{\text{R}}(t,t_0)\mathbf{G}_{\text{CC}}^{\geq}(t_0,t_0)\mathbf{G}_{\text{CC}}^{\text{A}}(t_0,t') \quad (\text{B.20})$$

$$+ \sum_{\alpha \in \{\text{L,R}\}} \mathbf{G}_{\text{C}\alpha}^{\text{R}}(t,t_0)\mathbf{G}_{\alpha\text{C}}^{\geq}(t_0,t_0)\mathbf{G}_{\text{CC}}^{\text{A}}(t_0,t')$$

$$+ \sum_{\alpha \in \{\text{L,R}\}} \mathbf{G}_{\text{CC}}^{\text{R}}(t,t_0)\mathbf{G}_{\text{C}\alpha}^{\geq}(t_0,t_0)\mathbf{G}_{\alpha\text{C}}^{\text{A}}(t_0,t')$$

$$+ \sum_{\alpha,\alpha' \in \{\text{L,R}\}} \mathbf{G}_{\text{C}\alpha}^{\text{R}}(t,t_0)\mathbf{G}_{\alpha\alpha'}^{\geq}(t_0,t_0)\mathbf{G}_{\alpha'\text{C}}^{\text{A}}(t_0,t')$$

$$= \sum_{m=1}^4 \mathbf{R}^{(m)}(t,t'). \quad (\text{B.21})$$

We now can evaluate the four terms $\mathbf{R}^{(m)}(t,t')$:

$$\mathbf{R}^{(1)}(t,t') = \mathbf{G}_{\text{CC}}^{\text{R}}(t,t_0)\mathbf{G}_{\text{CC}}^{\geq}(t_0,t_0)\mathbf{G}_{\text{CC}}^{\text{A}}(t_0,t'), \quad (\text{B.22})$$

$$\mathbf{R}^{(2)}(t,t') = \sum_{\alpha \in \{L,R\}} \mathbf{G}_{C\alpha}^R(t,t_0) \mathbf{G}_{\alpha C}^{\geq}(t_0,t_0) \mathbf{G}_{CC}^A(t_0,t') \quad (\text{B.23})$$

$$\stackrel{(\text{B.9})}{=} \sum_{\alpha \in \{L,R\}} [\mathbf{G}_{CC}^R \cdot \mathbf{H}_{C\alpha} \mathbf{g}_{\alpha\alpha}^R](t,t_0) \quad (\text{B.24})$$

$$\stackrel{(\text{B.12})}{=} -i \sum_{\alpha \in \{L,R\}} [\mathbf{G}_{CC}^R \cdot \Sigma_{\alpha}^{\lceil} \star \mathbf{G}_{CC}^{\lceil}](t,t_0) \mathbf{G}_{CC}^A(t_0,t'), \quad (\text{B.25})$$

$$\mathbf{R}^{(3)}(t,t') = \sum_{\alpha \in \{L,R\}} \mathbf{G}_{CC}^R(t,t_0) \mathbf{G}_{C\alpha}^{\geq}(t_0,t_0) \mathbf{G}_{\alpha C}^A(t_0,t') \quad (\text{B.26})$$

$$\stackrel{(\text{B.9})}{=} \sum_{\alpha \in \{L,R\}} \mathbf{G}_{CC}^R(t,t_0) [\mathbf{G}_{CC}^{\lceil} \star \mathbf{H}_{C\alpha} \mathbf{g}_{\alpha\alpha}^{\lceil}](t_0,t_0) \quad (\text{B.27})$$

$$\stackrel{(\text{B.13})}{=} \sum_{\alpha \in \{L,R\}} \mathbf{G}_{CC}^R(t,t_0) [\mathbf{G}_{CC}^{\lceil} \star \Sigma_{\alpha}^{\lceil} \cdot \mathbf{G}_{CC}^A](t_0,t'), \quad (\text{B.28})$$

$$\mathbf{R}^{(4)}(t,t') = \sum_{\alpha, \alpha' \in \{L,R\}} \mathbf{G}_{C\alpha}^R(t,t_0) \mathbf{G}_{\alpha\alpha'}^{\geq}(t_0,t_0) \mathbf{G}_{\alpha'C}^A(t_0,t') \quad (\text{B.29})$$

$$\stackrel{(\text{B.9}), (\text{B.10})}{=} \sum_{\alpha, \alpha' \in \{L,R\}} [\mathbf{G}_{CC}^R \cdot \mathbf{H}_{C\alpha} \mathbf{g}_{\alpha\alpha}^R](t,t_0) \quad (\text{B.30})$$

$$\stackrel{(\text{B.16})-(\text{B.18})}{=} \sum_{\alpha \in \{L,R\}} [\mathbf{G}_{CC}^R \cdot \Sigma_{\alpha}^{\geq} \cdot \mathbf{G}_{CC}^A](t,t') \quad (\text{B.31})$$

$$+ \sum_{\alpha, \alpha' \in \{L,R\}} [\mathbf{G}_{CC}^R \cdot \Sigma_{\alpha}^{\lceil} \star \mathbf{G}_{CC}^M \star \Sigma_{\alpha'}^{\lceil} \cdot \mathbf{G}_{CC}^A](t,t').$$

Combining equations (B.22), (B.25), (B.28), and (B.31) with (B.21) leads to

$$\begin{aligned}
\mathbf{G}_{\text{CC}}^{\geq}(t, t') &= \mathbf{G}_{\text{CC}}^{\text{R}}(t, t_0) \mathbf{G}_{\text{CC}}^{\geq}(t_0, t_0) \mathbf{G}_{\text{CC}}^{\text{A}}(t_0, t') & (\text{B.32}) \\
&\quad - i \sum_{\alpha \in \{\text{L}, \text{R}\}} [\mathbf{G}_{\text{CC}}^{\text{R}} \cdot \Sigma_{\alpha}^{\downarrow} \star \mathbf{G}_{\text{CC}}^{\uparrow}](t, t_0) \mathbf{G}_{\text{CC}}^{\text{A}}(t_0, t') \\
&\quad + \sum_{\alpha \in \{\text{L}, \text{R}\}} \mathbf{G}_{\text{CC}}^{\text{R}}(t, t_0) [\mathbf{G}_{\text{CC}}^{\downarrow} \star \Sigma_{\alpha}^{\uparrow} \cdot \mathbf{G}_{\text{CC}}^{\text{A}}](t_0, t') \\
&\quad + \sum_{\alpha \in \{\text{L}, \text{R}\}} [\mathbf{G}_{\text{CC}}^{\text{R}} \cdot \Sigma_{\alpha}^{\geq} \cdot \mathbf{G}_{\text{CC}}^{\text{A}}](t, t') \\
&\quad + \sum_{\alpha, \alpha' \in \{\text{L}, \text{R}\}} [\mathbf{G}_{\text{CC}}^{\text{R}} \cdot \Sigma_{\alpha}^{\downarrow} \star \mathbf{G}_{\text{CC}}^{\text{M}} \star \Sigma_{\alpha'}^{\uparrow} \cdot \mathbf{G}_{\text{CC}}^{\text{A}}](t, t').
\end{aligned}$$

The final step of this section is to look at the long time behaviour and to set $t' = t$. We assume

$$\lim_{t \rightarrow \infty} \mathbf{G}_{\text{CC}}(t_{\pm}, z') = \lim_{t' \rightarrow \infty} \mathbf{G}_{\text{CC}}(z, t'_{\pm}) = 0 \quad (\text{B.33})$$

$$\lim_{t \rightarrow \infty} \Sigma_{\alpha}(t_{\pm}, z') = \lim_{t' \rightarrow \infty} \Sigma_{\alpha}(z, t'_{\pm}) = 0 \quad (\text{B.34})$$

for fixed z, z' on the Keldysh contour. It is for example sufficient to demand the L^1 integrability with respect to ω of

$$\left[\mathbf{g}_{\alpha\alpha}^{\geq}(\omega, T) \right]_{(\alpha 0, \alpha 0)} \stackrel{\tau = t - t'}{=} \int_{T = \frac{t+t'}{2}}^{\infty} d\tau e^{i\omega\tau} \left[\mathbf{g}_{\alpha\alpha}^{\geq} \left(T + \frac{\tau}{2}, T - \frac{\tau}{2} \right) \right]_{(\alpha 0, \alpha 0)}, \quad (\text{B.35})$$

$$\mathbf{G}_{\text{CC}}^{\geq}(\omega, T) \stackrel{\tau = t - t'}{=} \int_{T = \frac{t+t'}{2}}^{\infty} d\tau e^{i\omega\tau} \mathbf{G}_{\text{CC}}^{\geq} \left(T + \frac{\tau}{2}, T - \frac{\tau}{2} \right). \quad (\text{B.36})$$

Note that this condition does not allow any bound states, hence one has to choose the system at t_0 carefully, for example with a superconducting central region preventing Andreev bound states to be formed. As soon as a bias is applied, these are not problematic any more. The Riemann-Lebesgue lemma then guarantees to the desired limits.

We finally can drop all terms which tend to zero as $t \rightarrow \infty$. The remainder is the first part of $\mathbf{R}^{(4)}$:

$$\mathbf{G}_{\text{CC}}^{\geq}(t, t) \stackrel{t \rightarrow \infty}{\sim} \left[\mathbf{G}_{\text{CC}}^{\text{R}} \cdot \Sigma^{\geq} \cdot \mathbf{G}_{\text{CC}}^{\text{A}} \right](t, t) \quad (\text{B.37})$$

with $\Sigma^{\geq} = \Sigma_{\text{L}}^{\geq} + \Sigma_{\text{R}}^{\geq}$. It is convenient to set the initial time t_0 of the Keldysh contour to $t_0 = -\infty$, which will be assumed in the following.

B.2 Evaluation for a monochromatic central Hamiltonian

In this section, we adopt the procedure of [SKRG08] and reformulate the equation (B.37) with the help of a Fourier expansion. We specify the central Hamiltonian to be monochromatic, i.e.

$$\mathbf{H}_{\text{CC}}(t) = \mathbf{H}_{\text{CC}}^0 + \mathbf{U}_+ e^{i\omega_0 t} + \mathbf{U}_- e^{-i\omega_0 t}. \quad (\text{B.38})$$

The other projections of the total Hamiltonian are considered to be time-independent. If we assume, that the system with the applied bias does not have any bound states and has no history dependence, then we can expand the advanced and retarded Green's function of the central region as

$$\mathbf{G}_{\text{CC}}^{\text{R,A}}(t, t') = \sum_{m \in \mathbb{Z}} \int_{-\infty}^{\infty} \frac{d\omega}{2\pi} \mathbf{G}_m^{\text{R,A}}(\omega) e^{-i\omega(t-t') + im\omega_0 t'}. \quad (\text{B.39})$$

The self-energies $\Sigma_{\alpha}^{\text{R,A},\gtrless}(t, t')$ depend only on the time difference $t - t'$, thus we can write $\Sigma_{\alpha}^{\text{R,A},\gtrless}(t - t')$ instead of $\Sigma_{\alpha}^{\text{R,A},\gtrless}(t, t')$. The self-energies can be expressed in the frequency space as

$$\Sigma_{\alpha}^{\text{R,A},\gtrless}(t, t') = \int_{-\infty}^{\infty} \frac{d\omega}{2\pi} e^{-i\omega(t-t')} \Sigma_{\alpha}^{\text{R,A},\gtrless}(\omega). \quad (\text{B.40})$$

Recall, that the initial time t_0 of the Keldysh contour was set to $t_0 = -\infty$, which allows us to make use of the following property of the Fourier transform:

$$\int_{-\infty}^{\infty} dt e^{i\omega t} = 2\pi \delta(\omega). \quad (\text{B.41})$$

For a simpler notation, we define $\mathbb{Z}^2 = \mathbb{Z} \times \mathbb{Z}$ and $\mathbf{m} = (m_1, m_2) \in \mathbb{Z}^2$. We now insert the expansions of equations (B.39) and (B.40) into the equation (B.37).

We then evaluate the integrals by using equation (B.41) and finally arrive at:

$$[\mathbf{G}_{\text{CC}}^{\text{R}} \cdot \Sigma^{\geq} \cdot \mathbf{G}_{\text{CC}}^{\text{A}}](t, t) \quad (\text{B.42})$$

$$= \iint_{-\infty}^{\infty} dt_1 dt_2 \mathbf{G}_{\text{CC}}^{\text{R}}(t, t_1) \Sigma^{\geq}(t_1, t_2) \mathbf{G}_{\text{CC}}^{\text{A}}(t_2, t) \quad (\text{B.43})$$

$$= \iint_{-\infty}^{\infty} dt_1 dt_2 \iint_{-\infty}^{\infty} \frac{d\omega_1 d\omega_2}{4\pi^2} \sum_{\mathbf{m} \in \mathbb{Z}^2} \mathbf{G}_{m_1}^{\text{R}}(\omega_1) \Sigma^{\geq}(t_1 - t_2) \mathbf{G}_{m_2}^{\text{A}}(\omega_2) \quad (\text{B.44})$$

$$e^{-i\omega_1(t-t_1)+im_1\omega_0 t_1} e^{-i\omega_2(t_2-t)+im_2\omega_0 t}$$

$$= \iint_{-\infty}^{\infty} d\tau_1 dt_2 \iint_{-\infty}^{\infty} \frac{d\omega_1 d\omega_2}{4\pi^2} \sum_{\mathbf{m} \in \mathbb{Z}^2} \mathbf{G}_{m_1}^{\text{R}}(\omega_1) \Sigma^{\geq}(\tau_1) \mathbf{G}_{m_2}^{\text{A}}(\omega_2) \quad (\text{B.45})$$

$$e^{-i\omega_1(t-\tau_1+t_2)+im_1\omega_0(\tau_1+t_2)} e^{-i\omega_2(t_2-t)+im_2\omega_0 t}$$

$$= \int_{-\infty}^{\infty} dt_2 \iint_{-\infty}^{\infty} \frac{d\omega_1 d\omega_2}{4\pi^2} \sum_{\mathbf{m} \in \mathbb{Z}^2} \mathbf{G}_{m_1}^{\text{R}}(\omega_1) \Sigma^{\geq}(\omega_1 + m_1\omega_0) \mathbf{G}_{m_2}^{\text{A}}(\omega_2) \quad (\text{B.46})$$

$$e^{-i\omega_1(t-t_2)+im_1\omega_0 t_2} e^{-i\omega_2(t_2-t)+im_2\omega_0 t}$$

$$= \int_{-\infty}^{\infty} \frac{d\omega}{2\pi} \sum_{\mathbf{m} \in \mathbb{Z}^2} \mathbf{G}_{m_1}^{\text{R}}(\omega) \Sigma^{\geq}(\omega + m_1\omega_0) \mathbf{G}_{m_2}^{\text{A}}(\omega + m_1\omega_0) e^{i(m_1+m_2)\omega_0 t} \quad (\text{B.47})$$

$$= \int_{-\infty}^{\infty} \frac{d\omega}{2\pi} \sum_{\mathbf{m} \in \mathbb{Z}^2} \mathbf{G}_{m_1}^{\text{R}}(\omega - m_1\omega_0) \Sigma^{\geq}(\omega) \mathbf{G}_{m_2}^{\text{A}}(\omega) e^{i(m_1+m_2)\omega_0 t}. \quad (\text{B.48})$$

The fluctuation-dissipation theorem [HJ96, SvL13] reads

$$\mathbf{g}_{\alpha}^{<}(\omega) = -f^{<}(\omega) \left(\mathbf{g}_{\alpha}^{\text{R}}(\omega) - \mathbf{g}_{\alpha}^{\text{A}}(\omega) \right), \quad (\text{B.49})$$

$$\mathbf{g}_{\alpha}^{>}(\omega) = -f^{>}(\omega) \left(\mathbf{g}_{\alpha}^{\text{R}}(\omega) - \mathbf{g}_{\alpha}^{\text{A}}(\omega) \right) \quad (\text{B.50})$$

with the Fermi functions $f^{<}(\omega) = [1 + \exp(\beta\omega)]^{-1}$, $f^{>}(\omega) = f^{<}(\omega) - 1$. This yields

$$\Sigma_{\alpha}^{<}(\omega) = i f^{<}(\omega) \Gamma_{\alpha}(\omega), \quad (\text{B.51})$$

$$\Sigma_{\alpha}^{>}(\omega) = i f^{>}(\omega) \Gamma_{\alpha}(\omega) \quad (\text{B.52})$$

with $\Gamma_\alpha(\omega) = i [\Sigma_\alpha^R(\omega) - \Sigma_\alpha^A(\omega)]$. We define $\mathbf{G}_m(\omega) \equiv \mathbf{G}_m^R(\omega - m\omega_0) = [\mathbf{G}_{-m}^A(\omega)]^\dagger$, $\Gamma = \Gamma_L + \Gamma_R$ and obtain the final results:

$$n_k(t) \stackrel{t \rightarrow \infty}{\sim} \int_{-\infty}^{\infty} \frac{d\omega}{2\pi} \sum_{\mathbf{m} \in \mathbb{Z}^2} e^{i(m_1 - m_2)\omega_0 t} \left[f^<(\omega) [\mathbf{G}_{m_1}(\omega) \Gamma(\omega) \mathbf{G}_{m_2}^\dagger(\omega)]_{(k\uparrow, k\uparrow)} - f^>(\omega) [\mathbf{G}_{m_1}(\omega) \Gamma(\omega) \mathbf{G}_{m_2}^\dagger(\omega)]_{(k\downarrow, k\downarrow)} \right] \quad (\text{B.53})$$

and

$$I_{k,l}(t) \stackrel{t \rightarrow \infty}{\sim} 2\text{Re} \text{Tr} \left\{ \int_{-\infty}^{\infty} \frac{d\omega}{2\pi} \sum_{\mathbf{m} \in \mathbb{Z}^2} e^{i(m_1 - m_2)\omega_0 t} f^<(\omega) \left[\mathbf{G}_{m_1}(\omega) \Gamma(\omega) \mathbf{G}_{m_2}^\dagger(\omega) \right]_{(l,k)} [\mathbf{H}_{CC}(t)]_{(l,k)} \boldsymbol{\sigma}_z \right\}. \quad (\text{B.54})$$

We are often only interested in the time averaged density and current. Since they are periodic with frequency $\omega_0 = \frac{2\pi}{T_0}$, we define

$$n_{k,\text{DC}} = \lim_{t \rightarrow \infty} \frac{1}{T_0} \int_t^{t+T_0} dt' n_k(t'), \quad (\text{B.55})$$

$$I_{k,l,\text{DC}} = \lim_{t \rightarrow \infty} \frac{1}{T_0} \int_t^{t+T_0} dt' I_{kl}(t'). \quad (\text{B.56})$$

This yields

$$n_{k,\text{DC}} = \int_{-\infty}^{\infty} \frac{d\omega}{2\pi} \sum_{\mathbf{m} \in \mathbb{Z}} \left[f^<(\omega) [\mathbf{G}_m(\omega) \Gamma(\omega) \mathbf{G}_m^\dagger(\omega)]_{(k\uparrow, k\uparrow)} - f^>(\omega) [\mathbf{G}_m(\omega) \Gamma(\omega) \mathbf{G}_m^\dagger(\omega)]_{(k\downarrow, k\downarrow)} \right] \quad (\text{B.57})$$

and

$$I_{k,l,\text{DC}} = 2\text{Re} \text{Tr} \left\{ \int_{-\infty}^{\infty} \frac{d\omega}{2\pi} \sum_{\mathbf{m} \in \mathbb{Z}^2} f^<(\omega) \left[\mathbf{G}_{m_1}(\omega) \Gamma(\omega) \mathbf{G}_{m_2}^\dagger(\omega) \right]_{(l,k)} \left[\mathbf{H}_{CC}^0 \delta_{m_1, m_2} + \mathbf{U}_+ \delta_{m_1+1, m_2} + \mathbf{U}_- \delta_{m_1-1, m_2} \right]_{(l,k)} \boldsymbol{\sigma}_z \right\}. \quad (\text{B.58})$$

The next task is to derive an algorithm for the matrices $\mathbf{G}_m(\omega)$. The matrices $\Gamma_\alpha(\omega)$ and $\Sigma_\alpha^A(\omega)$ can be calculated analytically using equation (3.15).

B.3 Calculation of the matrices $\mathbf{G}_m(\omega)$

This section is based on the work [SKRG08], which uses the recursive scheme of [Mar03]. The central Hamiltonian $\mathbf{H}_{\text{CC}}(t)$ is considered to be monochromatic, i.e.

$$\mathbf{H}_{\text{CC}}(t) = \mathbf{H}_{\text{CC}}^0 + \mathbf{U}_+ e^{i\omega_0 t} + \mathbf{U}_- e^{-i\omega_0 t}. \quad (\text{B.59})$$

We define $\mathbf{g}_{\text{CC}}^{\text{R}}$ as the retarded Green's function for the system with $\mathbf{U}_{\pm} = 0$:

$$\mathbf{g}_{\text{CC}}^{\text{R}}(t, t') = \int_{-\infty}^{\infty} \frac{d\omega}{2\pi} \mathbf{g}_{\text{CC}}^{\text{R}}(\omega) e^{-i\omega(t-t')}, \quad (\text{B.60})$$

$$\mathbf{g}_{\text{CC}}^{\text{R}}(\omega) = \lim_{\eta \searrow 0} [(\omega + i\eta)\mathbf{1} - \mathbf{H}_{\text{CC}}^0 - \Sigma_{\text{L}}^{\text{R}}(\omega) - \Sigma_{\text{R}}^{\text{R}}(\omega)]^{-1}, \quad (\text{B.61})$$

$$\mathbf{G}_{\text{CC}}^{\text{R}}(t, t') = \sum_{m \in \mathbb{Z}} \int_{-\infty}^{\infty} \frac{d\omega}{2\pi} \mathbf{G}_m^{\text{R}}(\omega) e^{-i\omega(t-t') + im\omega_0 t'}. \quad (\text{B.62})$$

The retarded embedding self-energy $\Sigma_{\alpha}^{\text{R}}(\omega)$ was defined in equation (3.15). We insert these expressions into the Dyson equation

$$\mathbf{G}_{\text{CC}}^{\text{R}}(t, t') = \mathbf{g}_{\text{CC}}^{\text{R}}(t, t') + \int_{-\infty}^{\infty} d\bar{t} \mathbf{g}_{\text{CC}}^{\text{R}}(t, \bar{t}) (\mathbf{U}_+ e^{i\omega_0 \bar{t}} + \mathbf{U}_- e^{-i\omega_0 \bar{t}}) \mathbf{G}_{\text{CC}}^{\text{R}}(\bar{t}, t') \quad (\text{B.63})$$

and obtain for $m \in \mathbb{Z}$

$$\mathbf{G}_m^{\text{R}}(\omega) = \mathbf{g}_{\text{CC}}^{\text{R}}(\omega) (\delta_{m,0} + \mathbf{U}_+ \mathbf{G}_{m-1}^{\text{R}}(\omega + \omega_0) + \mathbf{U}_- \mathbf{G}_{m+1}^{\text{R}}(\omega - \omega_0)). \quad (\text{B.64})$$

We introduce the notation $\mathbf{G}_m(\omega) = \mathbf{G}_m^{\text{R}}(\omega - m\omega_0)$ and $\mathbf{g}_m(\omega) = \mathbf{g}_{\text{CC}}^{\text{R}}(\omega - m\omega_0)$ which leads to the more compact equation:

$$\mathbf{G}_m(\omega) = \mathbf{g}_m(\omega) (\delta_{m,0} + \mathbf{U}_+ \mathbf{G}_{m-1}(\omega) + \mathbf{U}_- \mathbf{G}_{m+1}(\omega)). \quad (\text{B.65})$$

We write it as a system of linear equations:

$$\left(\begin{array}{ccc|ccc} & & & \vdots & & \\ & & & 0 & \vdots & \\ & & & 0 & 0 & \\ \hline & & & -\mathbf{g}_{-1}\mathbf{U}_- & 0 & 0 \dots \\ \hline \dots & 0 & -\mathbf{g}_0\mathbf{U}_+ & \mathbb{1} & -\mathbf{g}_0\mathbf{U}_- & 0 \dots \\ \hline \dots & 0 & 0 & -\mathbf{g}_1\mathbf{U}_+ & & \\ & & 0 & 0 & & \\ & & \vdots & 0 & & \\ & & & \vdots & & \end{array} \right) \begin{pmatrix} \vdots \\ \mathbf{G}_{-3} \\ \mathbf{G}_{-2} \\ \mathbf{G}_{-1} \\ \mathbf{G}_0 \\ \mathbf{G}_1 \\ \mathbf{G}_2 \\ \mathbf{G}_2 \\ \vdots \end{pmatrix} = \begin{pmatrix} \vdots \\ 0 \\ 0 \\ 0 \\ \mathbf{g}_0 \\ 0 \\ 0 \\ 0 \\ \vdots \end{pmatrix} \quad (\text{B.66})$$

with

$$\mathbf{W}^{(-)} = \begin{pmatrix} \ddots & \ddots & \ddots & 0 & \vdots \\ & -\mathbf{g}_{-3}\mathbf{U}_+ & \mathbb{1} & -\mathbf{g}_{-3}\mathbf{U}_- & 0 \\ \dots & 0 & -\mathbf{g}_{-2}\mathbf{U}_+ & \mathbb{1} & -\mathbf{g}_{-2}\mathbf{U}_- \\ & \dots & 0 & -\mathbf{g}_{-1}\mathbf{U}_+ & \mathbb{1} \end{pmatrix}, \quad (\text{B.67})$$

$$\mathbf{W}^{(+)} = \begin{pmatrix} \mathbb{1} & -\mathbf{g}_1\mathbf{U}_- & 0 & \dots & \\ -\mathbf{g}_2\mathbf{U}_+ & \mathbb{1} & -\mathbf{g}_2\mathbf{U}_- & 0 & \dots \\ 0 & -\mathbf{g}_3\mathbf{U}_+ & \mathbb{1} & -\mathbf{g}_3\mathbf{U}_- & \\ \vdots & 0 & \ddots & \ddots & \ddots \end{pmatrix}. \quad (\text{B.68})$$

We define $\mathbf{W}_{\pm,m}^{-1}$, $m \in \mathbb{N}$ as the m -th block on the diagonal of the inverse matrix $[\mathbf{W}^{(\pm)}]^{-1}$. The counting starts at the top left (bottom right) corner of the matrix. Combining this definition with the above linear equation gives the following relation for $m > 0$:

$$\mathbf{G}_{\pm m}(\omega) = \mathbf{W}_{\pm,m}^{-1}(\omega) \mathbf{g}_{\pm m}(\omega) \mathbf{U}_{\pm} \mathbf{G}_{\pm(m-1)}(\omega). \quad (\text{B.69})$$

The entries $\mathbf{W}_{\pm,m}^{-1}(\omega)$ can be calculated using the continuous fraction of equation (A.11):

$$\mathbf{W}_{\pm,m}^{-1}(\omega) = \frac{\mathbb{1}}{\mathbb{1} - \mathbf{g}_{\pm m}(\omega) \mathbf{U}_{\mp} \frac{\mathbb{1}}{\mathbb{1} - \mathbf{g}_{\pm(m+1)}(\omega) \mathbf{U}_{\mp} \frac{\mathbb{1}}{\dots \mathbf{g}_{\pm(m+2)}(\omega) \mathbf{U}_{\pm}} \mathbf{g}_{\pm(m+1)}(\omega) \mathbf{U}_{\pm}}}, \quad (\text{B.70})$$

$$= \frac{\mathbb{1}}{\mathbf{g}_{\pm m}^{-1}(\omega) - \mathbf{U}_{\mp} \frac{\mathbb{1}}{\mathbf{g}_{\pm(m+1)}^{-1}(\omega) - \mathbf{U}_{\mp} \frac{\mathbb{1}}{\dots \mathbf{U}_{\pm}} \mathbf{U}_{\pm}} \mathbf{g}_{\pm m}^{-1}(\omega)}. \quad (\text{B.71})$$

In the above equation, we made use of the identity $[\mathbf{1} + \mathbf{AB}]^{-1} = [\mathbf{A}^{-1} + \mathbf{B}]^{-1}\mathbf{A}^{-1}$. We define

$$\mathbf{W}_{\pm,m}^{-1}(\omega) = \widetilde{\mathbf{W}}_{\pm,m}^{-1}(\omega)\mathbf{g}_{\pm m}^{-1}(\omega), \quad (\text{B.72})$$

$$\widetilde{\mathbf{W}}_{\pm,m}^{-1}(\omega) = \frac{\mathbf{1}}{\mathbf{g}_{\pm m}^{-1}(\omega) - \mathbf{U}_{\mp}\widetilde{\mathbf{W}}_{\pm,m+1}^{-1}(\omega)\mathbf{U}_{\pm}}, \quad (\text{B.73})$$

$$\mathbf{g}_{\pm m}(\omega) = \lim_{\eta \searrow 0} [(\omega \mp m\omega_0 + i\eta)\mathbf{1} - \mathbf{H}_{\text{CC}}^0 - \Sigma^{\text{R}}(\omega \mp m\omega_0)]^{-1}, \quad (\text{B.74})$$

and obtain

$$\mathbf{G}_0(\omega) = \mathbf{g}_0(\omega) (\delta_{m,0} + \mathbf{U}_+\mathbf{G}_{-1}(\omega) + \mathbf{U}_-\mathbf{G}_1(\omega)) \quad (\text{B.75})$$

$$\begin{aligned} &= \mathbf{g}_0(\omega) (\delta_{m,0} + \mathbf{U}_+\mathbf{W}_{-1}^{-1}(\omega)\mathbf{g}_{-1}(\omega)\mathbf{U}_-\mathbf{G}_0(\omega) \\ &\quad + \mathbf{U}_-\mathbf{W}_{+1}^{-1}(\omega)\mathbf{g}_{-1}(\omega)\mathbf{U}_+\mathbf{G}_0(\omega)). \end{aligned} \quad (\text{B.76})$$

This equation can be solved for $\mathbf{G}_0(\omega)$:

$$\mathbf{G}_0(\omega) = [\mathbf{g}_0^{-1}(\omega) - \mathbf{U}_-\widetilde{\mathbf{W}}_{+1}^{-1}(\omega)\mathbf{U}_+ - \mathbf{U}_+\widetilde{\mathbf{W}}_{-1}^{-1}(\omega)\mathbf{U}_-]^{-1}. \quad (\text{B.77})$$

Using $\mathbf{G}_0(\omega)$ as a starting point, all other matrices $\mathbf{G}_{\pm m}(\omega)$ with $m > 0$ can be calculated as:

$$\mathbf{G}_{\pm m}(\omega) = \mathbf{W}_{\pm,m}^{-1}(\omega)\mathbf{g}_{\pm m}(\omega)\mathbf{U}_{\pm}\mathbf{G}_{\pm(m-1)}(\omega) \quad (\text{B.78})$$

$$= \widetilde{\mathbf{W}}_{\pm,m}^{-1}(\omega)\mathbf{U}_{\pm}\mathbf{G}_{\pm(m-1)}(\omega), \quad m > 0. \quad (\text{B.79})$$

The remaining problem is the numerical calculation of $\widetilde{\mathbf{W}}_{\pm,m}^{-1}(\omega)$. Therefore, one simply truncates the recursion depth of the continuous fraction in equation (B.73) by setting $\widetilde{\mathbf{W}}_{\pm,m_{\text{max}}}^{-1}(\omega) = 0$ for some value m_{max} . This allows us to calculate the matrices $\mathbf{G}_{\pm m}(\omega)$ for $m < m_{\text{max}}$. Of course, one has to check the convergence of the final results with respect to m_{max} , the choice $m_{\text{max}} = 10$ turned out to be a reasonable initial guess.

Appendix C

Calculation of the spectral function using NEGFs

C.1 Large time behaviour of the spectral function

In this section we want to calculate the spectral function $\mathbf{A}_{\text{CC}}(\omega, T)$. We recall the definitions from equations (4.14) and (4.16):

$$\mathbf{A}_{\text{CC}}(t, t') = i [\mathbf{G}_{\text{CC}}^>(t, t') - \mathbf{G}_{\text{CC}}^<(t, t')], \quad (\text{C.1})$$

$$\mathbf{A}_{\text{CC}}(\omega, T) = \frac{1}{2\pi} \int_{-\infty}^{\infty} d\tau e^{i\omega\tau} \mathbf{A}_{\text{CC}}\left(T + \frac{\tau}{2}, T - \frac{\tau}{2}\right), \quad (\text{C.2})$$

with the relative time $\tau = t - t'$ and the average time $T = \frac{t+t'}{2}$.

The goal is to calculate the large time behaviour of $\mathbf{A}_{\text{CC}}(\omega, T)$ with respect to T . We assume, that $\mathbf{A}_{\text{CC}}(t, t') \rightarrow 0$ as $|t - t'| \rightarrow \infty$, which is a reasonable assumption and is already part of the derivation in section B.1. This implies, that we can look at $\mathbf{G}_{\text{CC}}^{\cong}(t, t')$ and drop all contributions which go to zero as $t, t' > b$ and $b \rightarrow \infty$. This corresponds to looking at the large time behaviour in both time arguments simultaneously.

We start with the reformulation of equation (B.32) for $\mathbf{G}_{\text{CC}}^{\geq}(t, t')$:

$$\begin{aligned}
\mathbf{G}_{\text{CC}}^{\geq}(t, t') &= \mathbf{G}_{\text{CC}}^{\text{R}}(t, t_0) \mathbf{G}_{\text{CC}}^{\geq}(t_0, t_0) \mathbf{G}_{\text{CC}}^{\text{A}}(t_0, t') & (\text{C.3}) \\
&\quad - i \sum_{\alpha \in \{\text{L}, \text{R}\}} [\mathbf{G}_{\text{CC}}^{\text{R}} \cdot \Sigma_{\alpha}^{\downarrow}] \star \mathbf{G}_{\text{CC}}^{\uparrow}(t, t_0) \mathbf{G}_{\text{CC}}^{\text{A}}(t_0, t') \\
&\quad + \sum_{\alpha \in \{\text{L}, \text{R}\}} \mathbf{G}_{\text{CC}}^{\text{R}}(t, t_0) [\mathbf{G}_{\text{CC}}^{\downarrow} \star \Sigma_{\alpha}^{\uparrow} \cdot \mathbf{G}_{\text{CC}}^{\text{A}}](t_0, t') \\
&\quad + \sum_{\alpha \in \{\text{L}, \text{R}\}} [\mathbf{G}_{\text{CC}}^{\text{R}} \cdot \Sigma_{\alpha}^{\geq} \cdot \mathbf{G}_{\text{CC}}^{\text{A}}](t, t') \\
&\quad + \sum_{\alpha, \alpha' \in \{\text{L}, \text{R}\}} [\mathbf{G}_{\text{CC}}^{\text{R}} \cdot \Sigma_{\alpha}^{\downarrow}] \star \mathbf{G}_{\text{CC}}^{\text{M}} \star \Sigma_{\alpha'}^{\uparrow} \cdot \mathbf{G}_{\text{CC}}^{\text{A}}(t, t').
\end{aligned}$$

We are interested in the large time behaviour of $\mathbf{G}_{\text{CC}}^{\geq}(t, t')$ with both time arguments being large, i.e. $t, t' > b$. We then drop all terms which tend to zero as $b \rightarrow \infty$ and obtain

$$\mathbf{G}_{\text{CC}}^{\geq}(t, t') \stackrel{t, t' \rightarrow \infty}{\sim} [\mathbf{G}_{\text{CC}}^{\text{R}} \cdot \Sigma^{\geq} \cdot \mathbf{G}_{\text{CC}}^{\text{A}}](t, t'). \quad (\text{C.4})$$

It is again useful to set the initial time t_0 of the Keldysh contour to $-\infty$. We now insert again the Fourier expansion for $\mathbf{G}_{\text{CC}}^{\text{R/A}}(t, t')$ of equation (B.39) and use relation (B.41):

$$[\mathbf{G}_{\text{CC}}^{\text{R}} \cdot \Sigma^{\geq} \cdot \mathbf{G}_{\text{CC}}^{\text{A}}](t, t') \quad (\text{C.5})$$

$$= \iint_{-\infty}^{\infty} dt_1 dt_2 \mathbf{G}_{\text{CC}}^{\text{R}}(t, t_1) \Sigma^{\geq}(t_1, t_2) \mathbf{G}_{\text{CC}}^{\text{A}}(t_2, t') \quad (\text{C.6})$$

$$= \iint_{-\infty}^{\infty} dt_1 dt_2 \iiint_{-\infty}^{\infty} \frac{d\omega_1 d\omega_2 d\omega_3}{(2\pi)^3} \sum_{\mathbf{m} \in \mathbb{Z}^2} \mathbf{G}_{m_1}^{\text{R}}(\omega_1) \Sigma^{\geq}(\omega_2) \mathbf{G}_{m_2}^{\text{A}}(\omega_3) \quad (\text{C.7})$$

$$e^{-i\omega_1(t-t_1)+im_1\omega_0 t_1} e^{-i\omega_2(t_1-t_2)} e^{-i\omega_3(t_2-t')+i\omega_3(t_2-t')+im_2\omega_0 t}$$

$$= \int_{-\infty}^{\infty} \frac{d\omega_1}{2\pi} \sum_{\mathbf{m} \in \mathbb{Z}^2} \mathbf{G}_{m_1}^{\text{R}}(\omega_1 - m_1\omega_0) \Sigma^{\geq}(\omega_1) \mathbf{G}_{m_2}^{\text{A}}(\omega_1) \quad (\text{C.8})$$

$$e^{-i\omega_1(t-t')+i\omega_0(m_1 t + m_2 t')}.$$

Using the relative time $\tau = t - t'$ and average time $T = \frac{t+t'}{2}$, we can calculate

the Fourier transform with respect to τ :

$$\left[\mathbf{G}_{\text{CC}}^{\text{R}} \cdot \Sigma^{\geq} \cdot \mathbf{G}_{\text{CC}}^{\text{A}} \right] (\omega, T) \quad (\text{C.9})$$

$$= \frac{1}{2\pi} \int_{-\infty}^{\infty} d\tau e^{i\omega\tau} \int_{-\infty}^{\infty} \frac{d\omega_1}{2\pi} \mathbf{G}_{m_1}^{\text{R}}(\omega_1 - m_1\omega_0) \Sigma^{\geq}(\omega_1) \mathbf{G}_{m_2}^{\text{A}}(\omega_1) \quad (\text{C.10})$$

$$e^{-i\omega_1\tau + i\omega_0 m_1(T + \frac{\tau}{2}) + i\omega_0 m_2(T - \frac{\tau}{2})}$$

$$= \frac{1}{2\pi} \sum_{\mathbf{m} \in \mathbb{Z}^2} \mathbf{G}_{m_1}^{\text{R}} \left(\omega - m_1\omega_0 + \frac{\omega_0}{2}(m_1 - m_2) \right) \Sigma^{\geq} \left(\omega + \frac{\omega_0}{2}(m_1 - m_2) \right)$$

$$\mathbf{G}_{m_2}^{\text{A}} \left(\omega + \frac{\omega_0}{2}(m_1 - m_2) \right) e^{i(m_1+m_2)\omega_0 T}. \quad (\text{C.11})$$

We use again the fluctuation-dissipation theorem of equations (B.49) and (B.50) as well as the definitions $\mathbf{G}_m(\omega) \equiv \mathbf{G}_m^{\text{R}}(\omega - m\omega_0) = [\mathbf{G}_{-m}^{\text{A}}(\omega)]^\dagger$, $\Sigma_\alpha^{\geq}(\omega) = i f^{\geq}(\omega) \Gamma_\alpha(\omega)$. This eventually yields

$$\left[\mathbf{G}_{\text{CC}}^{\text{R}} \cdot \Sigma^{\geq} \cdot \mathbf{G}_{\text{CC}}^{\text{A}} \right] (\omega, T) \quad (\text{C.12})$$

$$= \frac{i}{2\pi} \sum_{\mathbf{m} \in \mathbb{Z}^2} f^{\geq} \left(\omega + \frac{\omega_0}{2}(m_1 - m_2) \right) \mathbf{G}_{m_1} \left(\omega + \frac{\omega_0}{2}(m_1 - m_2) \right) \quad (\text{C.13})$$

$$\Gamma \left(\omega + \frac{\omega_0}{2}(m_1 - m_2) \right) \mathbf{G}_{-m_2}^\dagger \left(\omega + \frac{\omega_0}{2}(m_1 - m_2) \right) e^{i(m_1+m_2)\omega_0 T}.$$

We assumed that $\mathbf{G}_{\text{CC}}^{\geq}(t, t') \rightarrow 0$ if $|t - t'| \rightarrow \infty$, which allows us to look at the large time behaviour with respect to $\frac{t+t'}{2}$. This gives us the final expression for

$\mathbf{G}_{\text{CC}}^{\lessgtr}(\omega, T)$ and $\mathbf{A}_{\text{CC}}(\omega, T)$:

$$\mathbf{G}_{\text{CC}}^{\lessgtr}(\omega, T) \stackrel{T \rightarrow \infty}{\sim} \frac{i}{2\pi} \sum_{\mathbf{m} \in \mathbb{Z}^2} e^{i(m_1+m_2)\omega_0 T} f^{\lessgtr} \left(\omega + \frac{\omega_0}{2}(m_1 - m_2) \right) \quad (\text{C.14})$$

$$\begin{aligned} & \mathbf{G}_{m_1} \left(\omega + \frac{\omega_0}{2}(m_1 - m_2) \right) \Gamma \left(\omega + \frac{\omega_0}{2}(m_1 - m_2) \right) \\ & \mathbf{G}_{-m_2}^\dagger \left(\omega + \frac{\omega_0}{2}(m_1 - m_2) \right), \end{aligned}$$

$$\mathbf{G}_{\text{CC}}^{\lessgtr}(\omega, T) \stackrel{T \rightarrow \infty}{\sim} \frac{i}{2\pi} \sum_{\mathbf{m} \in \mathbb{Z}^2} e^{i(m_1+m_2)\omega_0 T} f^{\lessgtr} \left(\omega + \frac{\omega_0}{2}(m_1 - m_2) \right) \quad (\text{C.15})$$

$$\begin{aligned} & \mathbf{G}_{m_1} \left(\omega + \frac{\omega_0}{2}(m_1 - m_2) \right) \Gamma \left(\omega + \frac{\omega_0}{2}(m_1 - m_2) \right) \\ & \mathbf{G}_{-m_2}^\dagger \left(\omega + \frac{\omega_0}{2}(m_1 - m_2) \right), \end{aligned}$$

$$\mathbf{A}_{\text{CC}}(\omega, T) \stackrel{T \rightarrow \infty}{\sim} \frac{1}{2\pi} \sum_{\mathbf{m} \in \mathbb{Z}^2} e^{i(m_1+m_2)\omega_0 T} \mathbf{G}_{m_1} \left(\omega + \frac{\omega_0}{2}(m_1 - m_2) \right) \quad (\text{C.16})$$

$$\Gamma \left(\omega + \frac{\omega_0}{2}(m_1 - m_2) \right) \mathbf{G}_{-m_2}^\dagger \left(\omega + \frac{\omega_0}{2}(m_1 - m_2) \right).$$

This result is consistent with the expression for the density $n_k(t)$ of equation (B.53) after some variable shifts:

$$n_k(t) = -i[\mathbf{G}_{kk}^{\lessgtr}(t, t)]_{\uparrow\uparrow} + i[\mathbf{G}_{kk}^{\lessgtr}(t, t)]_{\downarrow\downarrow} \quad (\text{C.17})$$

$$= -i \int_{-\infty}^{\infty} d\omega \left[\mathbf{G}_{kk}^{\lessgtr} \left(\omega, \frac{t+t}{2} \right) \right]_{\uparrow\uparrow} + i \int_{-\infty}^{\infty} d\omega \left[\mathbf{G}_{kk}^{\lessgtr} \left(\omega, \frac{t+t}{2} \right) \right]_{\downarrow\downarrow}, \quad (\text{C.18})$$

$$\begin{aligned} & \stackrel{t \rightarrow \infty}{\sim} \int_{-\infty}^{\infty} \frac{d\omega}{2\pi} \sum_{\mathbf{m} \in \mathbb{Z}^2} e^{i(m_1-m_2)\omega_0 t} \left[f^{\lessgtr}(\omega) [\mathbf{G}_{m_1}(\omega) \Gamma(\omega) \mathbf{G}_{m_2}^\dagger(\omega)]_{(k\uparrow, k\uparrow)} \right. \\ & \quad \left. - f^{\lessgtr}(\omega) [\mathbf{G}_{m_1}(\omega) \Gamma(\omega) \mathbf{G}_{m_2}^\dagger(\omega)]_{(k\downarrow, k\downarrow)} \right]. \end{aligned} \quad (\text{C.19})$$

In some cases, we are only interested in the time-averaged quantities:

$$\mathbf{G}_{\text{CC,DC}}^{\geq}(\omega) = \lim_{t \rightarrow \infty} \frac{1}{T_0} \int_t^{t+T_0} dT \mathbf{G}_{\text{CC}}^{\geq}(\omega, T) \quad (\text{C.20})$$

$$= \frac{i}{2\pi} \sum_{m \in \mathbb{Z}} f^{\geq}(\omega + m\omega_0) \mathbf{G}_m(\omega + m\omega_0) \quad (\text{C.21})$$

$$\mathbf{\Gamma}(\omega + m\omega_0) \mathbf{G}_m^{\dagger}(\omega + m\omega_0),$$

$$\mathbf{A}_{\text{CC,DC}}(\omega) = \lim_{t \rightarrow \infty} \frac{1}{T_0} \int_t^{t+T_0} dT \mathbf{A}_{\text{CC}}(\omega, T) \quad (\text{C.22})$$

$$= \frac{1}{2\pi} \sum_{m \in \mathbb{Z}} \mathbf{G}_m(\omega + m\omega_0) \mathbf{\Gamma}(\omega + m\omega_0) \mathbf{G}_m^{\dagger}(\omega + m\omega_0) \quad (\text{C.23})$$

with $T_0 = \frac{2\pi}{\omega_0}$.

C.2 Convolved spectral function

The goal of this section is to proof

$$0 \leq [\widetilde{\mathbf{A}}_{\text{QD}}(\omega, T)]_{\sigma\sigma} \quad (\text{C.24})$$

$$\equiv \iint_{-\infty}^{\infty} d\omega' dT' [\mathbf{A}_{\text{QD}}(\omega', T')]_{\sigma\sigma} M_{\sigma\omega, \sigma T}(\omega - \omega', T - T') \quad (\text{C.25})$$

for $\sigma\omega, \sigma T > 0$, $\sigma\omega\sigma T \geq \frac{1}{2}$ and the Gaussian kernel $M_{\sigma\omega, \sigma T}(\omega, T)$ defined as

$$M_{\sigma\omega, \sigma T}(\omega, T) = \frac{1}{2\pi\sigma\omega\sigma T} e^{-\frac{T^2}{2\sigma_T^2} - \frac{\omega^2}{2\sigma_\omega^2}}. \quad (\text{C.26})$$

The proof follows the work [Car75]. We will make use of the following relations:

$$\frac{1}{\sigma\sqrt{2\pi}} \int_{-\infty}^{\infty} dx e^{-\frac{1}{2}\left(\frac{x-\mu}{\sigma}\right)^2} = 1, \quad (\text{C.27})$$

$$\frac{1}{\sigma\sqrt{2\pi}} \int_{-\infty}^{\infty} dx e^{i\omega x} e^{-\frac{1}{2}\left(\frac{x-\mu}{\sigma}\right)^2} = e^{-\frac{\sigma^2\omega^2}{2} + i\mu\omega}. \quad (\text{C.28})$$

$$[\widetilde{\mathbf{A}}_{\text{QD}}(\omega, T)]_{\sigma\sigma} \quad (\text{C.29})$$

$$= \int_{-\infty}^{\infty} d\omega' dT' [\mathbf{A}_{\text{QD}}(\omega', T')]_{\sigma\sigma} M_{\sigma\omega, \sigma T}(\omega - \omega', T - T')$$

$$= \frac{1}{4\pi^2 \sigma_\omega \sigma_T} \iiint_{-\infty}^{\infty} d\omega' dT' d\tau' \left[\mathbf{A}_{\text{QD}} \left(T' + \frac{\tau'}{2}, T' - \frac{\tau'}{2} \right) \right]_{\sigma\sigma} \quad (\text{C.30})$$

$$e^{i\omega'\tau'} e^{-\frac{(T-T')^2}{2\sigma_T^2} - \frac{(\omega-\omega')^2}{2\sigma_\omega^2}}$$

$$= \frac{1}{2\pi\sqrt{2\pi}\sigma_T} \iint_{-\infty}^{\infty} dT' d\tau' \left[\mathbf{A}_{\text{QD}} \left(T' + \frac{\tau'}{2}, T' - \frac{\tau'}{2} \right) \right]_{\sigma\sigma} \quad (\text{C.31})$$

$$e^{-\frac{\sigma_\omega^2 \tau'^2}{2} + i\tau'\omega} e^{-\frac{(T-T')^2}{2\sigma_T^2}}$$

$$\stackrel{x=T'+\frac{\tau'}{2}}{=} \frac{2}{2\pi\sqrt{2\pi}\sigma_T} \iint_{-\infty}^{\infty} dx dy [\mathbf{A}_{\text{QD}}(x, y)]_{\sigma\sigma} \quad (\text{C.32})$$

$$e^{-\frac{\sigma_\omega^2 (x-y)^2}{2} + i(x-y)\omega} e^{-\frac{(T-\frac{x+y}{2})^2}{2\sigma_T^2}}.$$

We split the exponential function as follows:

$$e^{-\frac{\sigma_\omega^2 (x-y)^2}{2} + i(x-y)\omega} e^{-\frac{(T-\frac{x+y}{2})^2}{2\sigma_T^2}} \quad (\text{C.33})$$

$$= e^{\frac{\sigma_\omega^2 xy - \frac{T^2}{2} - \frac{xy}{4\sigma_T^2}}{}} e^{i\omega x - \frac{\sigma_\omega^2 x^2}{2} - \frac{\frac{x^2}{4} - Tx}{2\sigma_T^2}} e^{-i\omega y - \frac{\sigma_\omega^2 y^2}{2} - \frac{\frac{y^2}{4} - Ty}{2\sigma_T^2}}$$

and define

$$f(x, \omega, T) = \frac{1}{\sqrt{2\pi}} e^{i\omega x - \frac{\sigma_\omega^2 x^2}{2} - \frac{\frac{x^2}{4} - Tx}{2\sigma_T^2}}. \quad (\text{C.34})$$

We specify $\sigma = \uparrow$, the case $\sigma = \downarrow$ follows in a similar way. We insert the expansion of $[\mathbf{A}_{\text{QD}}(t, t')]_{\uparrow\uparrow}$ from equation (4.18) and use above definition:

$$[\widetilde{\mathbf{A}}_{\text{QD}}(\omega, T)]_{\uparrow\uparrow} \quad (\text{C.35})$$

$$= \frac{2e^{-\frac{T^2}{2\sigma_T^2}}}{\sqrt{2\pi}\sigma_T} \iint_{-\infty}^{\infty} dx dy [\mathbf{A}_{\text{QD}}(x, y)]_{\uparrow\uparrow} f(x, \omega, T) [f(y, \omega, T)]^* e^{\sigma_\omega^2 xy - \frac{xy}{4\sigma_T^2}}$$

$$= \frac{2e^{-\frac{T^2}{2\sigma_T^2}}}{\sqrt{2\pi}\sigma_T} \iint_{-\infty}^{\infty} dx dy \sum_q u_{\text{QD},q}(x) [u_{\text{QD},q}(x)]^* \quad (\text{C.36})$$

$$f(x, \omega, T) [f(y, \omega, T)]^* e^{\sigma_\omega^2 xy - \frac{xy}{4\sigma_T^2}}$$

$$= \frac{2e^{-\frac{T^2}{2\sigma_T^2}}}{\sqrt{2\pi}\sigma_T} \sum_q \sum_{k=0}^{\infty} \frac{(\sigma_\omega^2 - \frac{1}{4\sigma_T^2})^k}{k!} \quad (\text{C.37})$$

> 0 , since $\sigma_T > 0$ ≥ 0 , since $\sigma_\omega \sigma_T \geq \frac{1}{2}$

$$\underbrace{\left[\int_{-\infty}^{\infty} dx u_{\text{QD},q}(x) f(x, \omega, T) x^k \right] \left[\int_{-\infty}^{\infty} dy u_{\text{QD},q}(y) f(y, \omega, T) y^k \right]^*}_{=CC^* \geq 0}$$

$$\geq 0. \quad (\text{C.38})$$

The proof for $[\widetilde{\mathbf{A}}_{\text{QD}}(\omega, T)]_{\downarrow\downarrow}$ follows straight forward by substituting $u_{\text{QD},q}(x)$ by $v_{\text{QD},q}(x)$.

Bibliography

- [AB63a] V. Ambegaokar and A. Baratoff. Tunneling Between Superconductors. *Physical Review Letters*, 10(11):486–489, 1963, <http://dx.doi.org/10.1103/physrevlett.10.486>.
- [AB63b] V. Ambegaokar and A. Baratoff. Tunneling Between Superconductors. *Physical Review Letters*, 11(2):104, 1963, <http://dx.doi.org/10.1103/physrevlett.11.104>.
- [AB06] A. S. Alexandrov and A. M. Bratkovsky. Comment on 'Hysteresis, Switching, and Negative Differential Resistance in Molecular Junctions: a Polaron Model', by M. Galperin, M.A. Ratner, and A. Nitzan, *Nano Lett.* 5, 125 (2005). 2006, <http://arxiv.org/abs/cond-mat/0603467>.
- [AB07] A. S. Alexandrov and A. M. Bratkovsky. Fast polaron switching in degenerate molecular quantum dots. *Journal of Physics: Condensed Matter*, 19(25):255203+, 2007, <http://dx.doi.org/10.1088/0953-8984/19/25/255203>.
- [AB09] A. S. Alexandrov and A. M. Bratkovsky. Polaronic memory resistors strongly coupled to electrodes. *Physical Review B*, 80:115321+, 2009, <http://dx.doi.org/10.1103/physrevb.80.115321>.
- [ABB+98] A. Assion, T. Baumert, M. Bergt, T. Brixner, B. Kiefer, V. Seyfried, M. Strehle, and G. Gerber. Control of Chemical Reactions by Feedback-Optimized Phase-Shaped Femtosecond Laser Pulses. *Science*, 282(5390):919–922, 1998, <http://dx.doi.org/10.1126/science.282.5390.919>.
- [Abr57] A. A. Abrikosov. On the Magnetic Properties of Superconductors of the Second Group. *Sov. Phys. JETP*, 5:1174+, 1957.

- [ALPK09] A. F. Amin, G. Q. Li, A. H. Phillips, and U. Kleinekathöfer. Coherent control of the spin current through a quantum dot. *The European Physical Journal B*, 68(1):103–109, 2009, <http://dx.doi.org/10.1140/epjb/e2009-00075-9>.
- [And64] A. F. Andreev. Thermal conductivity of the intermediate state of superconductors. *Sov. Phys. JETP*, 19:1228–1231, 1964.
- [And99] E. Anderson. *LAPACK users' guide*. Software, environments, tools. Society for Industrial and Applied Mathematics, 1999, <http://www.worldcat.org/isbn/9780898714470>.
- [AR63] P. W. Anderson and J. M. Rowell. Probable Observation of the Josephson Superconducting Tunneling Effect. *Physical Review Letters*, 10(6):230–232, 1963, <http://dx.doi.org/10.1103/physrevlett.10.230>.
- [AR74] A. Aviram and M. A. Ratner. Molecular rectifiers. *Chemical Physics Letters*, 29(2):277–283, 1974, [http://dx.doi.org/10.1016/0009-2614\(74\)85031-1](http://dx.doi.org/10.1016/0009-2614(74)85031-1).
- [Arr02] L. Arrachea. Current oscillations in a metallic ring threaded by a time-dependent magnetic flux. *Physical Review B*, 66(4):045315+, 2002, <http://dx.doi.org/10.1103/physrevb.66.045315>.
- [AWM⁺12] K. F. Albrecht, H. Wang, L. Mühlbacher, M. Thoss, and A. Komnik. Bistability signatures in nonequilibrium charge transport through molecular quantum dots. *Physical Review B*, 86:081412+, 2012, <http://dx.doi.org/10.1103/physrevb.86.081412>.
- [BCS57] J. Bardeen, L. N. Cooper, and J. R. Schrieffer. Theory of Superconductivity. *Physical Review*, 108(5):1175–1204, 1957, <http://dx.doi.org/10.1103/physrev.108.1175>.
- [Bel57] R. Bellman. *Dynamic programming*. Princeton University Press, 1957, <http://www.worldcat.org/isbn/0486428095>.
- [Bel64] J. S. Bell. On the Einstein Podolsky Rosen Paradox. *Physics*, 1:195–200, 1964.
- [BES07] T. Böhler, A. Edtbauer, and E. Scheer. Conductance of individual C60 molecules measured with controllable gold electrodes. *Physical Review B*, 76:125432+, 2007, <http://dx.doi.org/10.1103/physrevb.76.125432>.

- [BHLY11] P. Buset, W. J. Herrera, and A. Levy Yeyati. Microscopic theory of Cooper pair beam splitters based on carbon nanotubes. *Physical Review B*, 84(11):115448+, 2011, <http://dx.doi.org/10.1103/physrevb.84.115448>.
- [BHS⁺10] S. Ballmann, W. Hieringer, D. Secker, Q. Zheng, J. A. Gladysz, A. Görling, and H. B. Weber. Molecular Wires in Single-Molecule Junctions: Charge Transport and Vibrational Excitations. *ChemPhysChem*, 11(10):2256–2260, 2010, <http://dx.doi.org/10.1002/cphc.200900974>.
- [BM11] M. Bohr and K. Mistry. Intel’s Revolutionary 22 nm Transistor Technology. 2011.
- [Bre73] R. P. Brent. *Algorithms for Minimization Without Derivatives*. Prentice-Hall, 1973, <http://www.worldcat.org/isbn/0486419983>.
- [BTK82] G. E. Blonder, M. Tinkham, and T. M. Klapwijk. Transition from metallic to tunneling regimes in superconducting microconstrictions: Excess current, charge imbalance, and supercurrent conversion. *Physical Review B*, 25(7):4515–4532, 1982, <http://dx.doi.org/10.1103/physrevb.25.4515>.
- [Büt86] M. Büttiker. Four-Terminal Phase-Coherent Conductance. *Physical Review Letters*, 57(14):1761–1764, 1986, <http://dx.doi.org/10.1103/physrevlett.57.1761>.
- [Car75] N. D. Cartwright. A non-negative Wigner-type distribution. *Physica A: Statistical Mechanics and its Applications*, 83(1):210–212, 1975, [http://dx.doi.org/10.1016/0378-4371\(76\)90145-x](http://dx.doi.org/10.1016/0378-4371(76)90145-x).
- [CFP62] M. H. Cohen, L. M. Falicov, and J. C. Phillips. Superconductive Tunneling. *Physical Review Letters*, 8(8):316–318, 1962, <http://dx.doi.org/10.1103/physrevlett.8.316>.
- [CFR05] G. Cuniberti, G. Fagas, and K. Richter. *Introducing Molecular Electronics*. Springer, 2005, <http://www.worldcat.org/isbn/3540279946>.
- [CG14] A. Castro and E. K. U. Gross. Optimal control theory for quantum-classical systems: Ehrenfest molecular dynamics based on time-dependent density-functional theory. *Journal of Physics A: Mathematical and Theoretical*, 47(2):025204+, 2014, <http://dx.doi.org/10.1088/1751-8113/47/2/025204>.

- [CK98] D. Colton and R. Kress. *Inverse Acoustic and Electromagnetic Scattering Theory (Applied Mathematical Sciences)*. Springer, 2nd edition, 1998, <http://www.worldcat.org/isbn/354062838X>.
- [CLRS09] T. H. Cormen, C. E. Leiserson, R. L. Rivest, and C. Stein. *Introduction to algorithms*. The MIT Press, 2009, <http://www.worldcat.org/isbn/0262533057>.
- [CMRY96] J. C. Cuevas, A. Martín-Rodero, and A. Levy Yeyati. Hamiltonian approach to the transport properties of superconducting quantum point contacts. *Physical Review B*, 54(10):7366–7379, 1996, <http://dx.doi.org/10.1103/physrevb.54.7366>.
- [Coo56] L. N. Cooper. Bound Electron Pairs in a Degenerate Fermi Gas. *Physical Review*, 104(4):1189–1190, 1956, <http://dx.doi.org/10.1103/physrev.104.1189>.
- [CPG80] T. D. Clark, R. J. Prance, and A. D. C. Grassie. Feasibility of hybrid Josephson field effect transistors. *Journal of Applied Physics*, 51(5):2736–2743, 1980, <http://dx.doi.org/10.1063/1.327935>.
- [CRRG09] A. Castro, E. Räsänen, A. Rubio, and E. K. U. Gross. Femtosecond laser pulse shaping for enhanced ionization. *EPL (Europhysics Letters)*, pages 53001+, 2009, <http://dx.doi.org/10.1209/0295-5075/87/53001>.
- [CS10] J. C. Cuevas and E. Scheer. *Molecular Electronics*. World Scientific Publishing Company, 2010, <http://www.worldcat.org/isbn/9814282588>.
- [Cue99] J. C. Cuevas. *Electronic Transport in Normal and Superconducting Nanocontacts*. PhD thesis, Universidad Autónoma de Madrid, 1999.
- [DK11] A. A. Dzhioev and D. S. Kosov. Stability analysis of multiple nonequilibrium fixed points in self-consistent electron transport calculations. *The Journal of Chemical Physics*, 135(17):174111+, 2011, <http://dx.doi.org/10.1063/1.3658736>.
- [dLLGP08] N. P. de Leon, W. Liang, Q. Gu, and H. Park. Vibrational Excitation in Single-Molecule Transistors: Deviation from the Simple Franck-Condon Prediction. *Nano Lett.*, 8(9):2963–2967, 2008, <http://dx.doi.org/10.1021/nl801882a>.

- [DRCR08] R. D'Amico, D. A. Ryndyk, G. Cuniberti, and K. Richter. Charge-memory effect in a polaron model: equation-of-motion method for Green functions. *New Journal of Physics*, 10(8):085002+, 2008, <http://dx.doi.org/10.1088/1367-2630/10/8/085002>.
- [DWM04] M. H. Devoret, A. Wallraff, and J. M. Martinis. Superconducting Qubits: A Short Review, 2004, <http://arxiv.org/abs/arXiv:cond-mat/0411174>.
- [EG04] N. Elghobashi and L. Gonzalez. Breaking the strong and weak bonds of OHF- using few-cycle IR + UV laser pulses. *Physical Chemistry Chemical Physics*, 6(16):4071+, 2004, <http://dx.doi.org/10.1039/b409446h>.
- [EKMO03] N. Elghobashi, P. Krause, J. Manz, and M. Oppel. IR+UV laser pulse control of momenta directed to specific products: Quantum model simulations for HOD* \rightarrow H+OD versus HO+D. *Physical Chemistry Chemical Physics*, 5(21):4806–4813, 2003, <http://dx.doi.org/10.1039/b305305a>.
- [Eli60] G. M. Eliashberg. Interactions between electrons and lattice vibrations in a superconductor. *Sov. Phys. JETP*, 11:696+, 1960.
- [EPR35] A. Einstein, B. Podolsky, and N. Rosen. Can Quantum-Mechanical Description of Physical Reality Be Considered Complete? *Physical Review*, 47(10):777–780, 1935, <http://dx.doi.org/10.1103/physrev.47.777>.
- [Fag06] R. L. Fagaly. Superconducting quantum interference device instruments and applications. *Review of Scientific Instruments*, 77(10):101101+, 2006, <http://dx.doi.org/10.1063/1.2354545>.
- [FJ05] M. Frigo and S. G. Johnson. The Design and Implementation of FFTW3. *Proceedings of the IEEE*, 93(2):216–231, 2005, <http://dx.doi.org/10.1109/jproc.2004.840301>.
- [FP12] K. J. Franke and J. I. Pascual. Effects of electron-vibration coupling in transport through single molecules. *Journal of Physics: Condensed Matter*, 24(39):394002+, 2012, <http://dx.doi.org/10.1088/0953-8984/24/39/394002>.
- [Frö54] H. Fröhlich. On the Theory of Superconductivity: The One-Dimensional Case. *Proceedings of the Royal Society of London*.

- Series A. Mathematical and Physical Sciences*, 223(1154):296–305, 1954, <http://dx.doi.org/10.1098/rspa.1954.0116>.
- [FZB08] J. Fransson, J. X. Zhu, and A. V. Balatsky. Vibrating Superconducting Island in a Josephson Junction. *Physical Review Letters*, 101(6):067202+, 2008, <http://dx.doi.org/10.1103/physrevlett.101.067202>.
- [GK02] A. O. Gogolin and A. Komnik. Multistable transport regimes and conformational changes in molecular quantum dots. 2002, <http://arxiv.org/abs/cond-mat/0207513>.
- [GL50] V. L. Ginzburg and L. D. Landau. To the theory of superconductivity. *Zh. Eksp. Teor. Fiz.*, 20:1064+, 1950.
- [GMR⁺13] M. Giustina, A. Mech, S. Ramelow, B. Wittmann, J. Kofler, J. Beyer, A. Lita, B. Calkins, T. Gerrits, S. W. Nam, R. Ursin, and A. Zeilinger. Bell violation using entangled photons without the fair-sampling assumption. *Nature*, 497(7448):227–230, 2013, <http://dx.doi.org/10.1038/nature12012>.
- [GNR06] M. Galperin, A. Nitzan, and M. A. Ratner. Reply to Comment by Alexandrov and Bratkovsky [cond-mat/0603467, cond-mat/0606366]. 2006, <http://arxiv.org/abs/cond-mat/0604112>.
- [GNR08] M. Galperin, A. Nitzan, and M. A. Ratner. The non-linear response of molecular junctions: the polaron model revisited. *Journal of Physics: Condensed Matter*, 20(37):374107+, 2008, <http://dx.doi.org/10.1088/0953-8984/20/37/374107>.
- [Gor59] L. P. Gor'kov. Microscopic derivation of the Ginzburg-Landau equations in the theory of superconductivity. *Sov. Phys. JETP*, 9:1364–1367, 1959.
- [GRN04] M. Galperin, M. A. Ratner, and A. Nitzan. Hysteresis, Switching, and Negative Differential Resistance in Molecular Junctions: A Polaron Model. *Nano Lett.*, 5(1):125–130, 2004, <http://dx.doi.org/10.1021/nl048216c>.
- [GRN07] M. Galperin, M. A. Ratner, and A. Nitzan. Molecular transport junctions: vibrational effects. *Journal of Physics: Condensed Matter*, 19(10):103201+, 2007, <http://dx.doi.org/10.1088/0953-8984/19/10/103201>.

- [Gun94] U. W. Günsenheimer. *Josephsonströme und dissipativer Ladungstransport in mesoskopischen Supraleiter-Normalleiter-Supraleiter-Kontakten*. PhD thesis, Universität Würzburg, 1994, <http://d-nb.info/94570173X>.
- [GvdG08a] K. Goto and R. A. van de Geijn. Anatomy of high-performance matrix multiplication. *ACM Trans. Math. Softw.*, 34(3):1–25, 2008, <http://dx.doi.org/10.1145/1356052.1356053>.
- [GvdG08b] K. Goto and R. A. van de Geijn. High-performance implementation of the level-3 BLAS. *ACM Trans. Math. Softw.*, 35(1):1–14, 2008, <http://dx.doi.org/10.1145/1377603.1377607>.
- [GZ07] D. S. Golubev and A. D. Zaikin. Non-local Andreev reflection in superconducting quantum dots. *Physical Review B*, 76:184510+, 2007, <http://dx.doi.org/10.1103/physrevb.76.184510>.
- [HBT09] R. Härtle, C. Benesch, and M. Thoss. Vibrational Nonequilibrium Effects in the Conductance of Single Molecules with Multiple Electronic States. *Physical Review Letters*, 102:146801+, 2009, <http://dx.doi.org/10.1103/physrevlett.102.146801>.
- [HCB⁺11] L. Hofstetter, S. Csonka, A. Baumgartner, G. Fülöp, S. d’Hollosy, J. Nygård, and C. Schönberger. Finite-Bias Cooper Pair Splitting. *Physical Review Letters*, 107(13):136801+, 2011, <http://dx.doi.org/10.1103/physrevlett.107.136801>.
- [HCNS09] L. Hofstetter, S. Csonka, J. Nygard, and C. Schönberger. Cooper pair splitter realized in a two-quantum-dot Y-junction. *Nature*, 461(7266):960–963, 2009, <http://dx.doi.org/10.1038/nature08432>.
- [HJ96] H. Haug and A. P. Jauho. *Quantum Kinetics in Transport and Optics of Semiconductors*. Springer, 1996, <http://www.worldcat.org/isbn/3540616020>.
- [HLS85] E. Hairer, C. Lubich, and M. Schlötte. Fast Numerical Solution of Nonlinear Volterra Convolution Equations. *SIAM Journal on Scientific and Statistical Computing*, 6(3):532–541, 1985, <http://dx.doi.org/10.1137/0906037>.
- [HMM89] B. Hartke, J. Manz, and J. Mathis. Mode selective control of unimolecular dissociations: Survey, and model simulations for

- HDO \rightarrow H+DO, D+HO. *Chemical Physics*, 139(1):123–146, 1989, [http://dx.doi.org/10.1016/0301-0104\(89\)90007-4](http://dx.doi.org/10.1016/0301-0104(89)90007-4).
- [HPR⁺10] L. G. Herrmann, F. Portier, P. Roche, A. Levy Yeyati, T. Kontos, and C. Strunk. Carbon Nanotubes as Cooper-Pair Beam Splitters. *Physical Review Letters*, 104(2):026801+, 2010, <http://dx.doi.org/10.1103/physrevlett.104.026801>.
- [HRG13] M. Hellgren, E. Räsänen, and E. K. U. Gross. Optimal control of strong-field ionization with time-dependent density-functional theory. *Physical Review A*, 88(1):013414+, 2013, <http://dx.doi.org/10.1103/physreva.88.013414>.
- [HT11a] R. Härtle and M. Thoss. Resonant electron transport in single-molecule junctions: Vibrational excitation, rectification, negative differential resistance, and local cooling. *Physical Review B*, 83:115414+, 2011, <http://dx.doi.org/10.1103/physrevb.83.115414>.
- [HT11b] R. Härtle and M. Thoss. Vibrational instabilities in resonant electron transport through single-molecule junctions. *Physical Review B*, 83:125419+, 2011, <http://dx.doi.org/10.1103/physrevb.83.125419>.
- [HWL⁺09] A. K. Hüttel, B. Witkamp, M. Leijnse, M. R. Wegewijs, and H. S. J. van der Zant. Pumping of Vibrational Excitations in the Coulomb-Blockade Regime in a Suspended Carbon Nanotube. *Physical Review Letters*, 102(22):225501+, 2009, <http://dx.doi.org/10.1103/physrevlett.102.225501>.
- [JA13] A. Jovchev and F. Anders. Influence of vibrational modes on the quantum transport through a nano-device, 2013, <http://arxiv.org/abs/1302.0184>.
- [JBSW99] G. Johansson, E. N. Bratus, V. S. Shumeiko, and G. Wendin. Resonant multiple Andreev reflections in mesoscopic superconducting junctions. *Physical Review B*, 60(2):1382–1393, 1999, <http://dx.doi.org/10.1103/physrevb.60.1382>.
- [JLMS65] R. C. Jaklevic, J. Lambe, J. E. Mercereau, and A. H. Silver. Macroscopic Quantum Interference in Superconductors. *Physical Review Online Archive (Prola)*, 140:A1628–A1637, 1965, <http://dx.doi.org/10.1103/physrev.140.a1628>.

- [JLSM64] R. C. Jaklevic, J. Lambe, A. H. Silver, and J. E. Mercereau. Quantum Interference Effects in Josephson Tunneling. *Physical Review Letters*, 12(7):159–160, 1964, <http://dx.doi.org/10.1103/physrevlett.12.159>.
- [JMS90] W. Jakubetz, J. Manz, and H. J. Schreier. Theory of optimal laser pulses for selective transitions between molecular eigenstates. *Chemical Physics Letters*, 165(1):100–106, 1990, [http://dx.doi.org/10.1016/0009-2614\(90\)87018-m](http://dx.doi.org/10.1016/0009-2614(90)87018-m).
- [Jos62] B. D. Josephson. Possible new effects in superconductive tunnelling. *Physics Letters*, 1(7):251–253, 1962, [http://dx.doi.org/10.1016/0031-9163\(62\)91369-0](http://dx.doi.org/10.1016/0031-9163(62)91369-0).
- [JR92] R. S. Judson and H. Rabitz. Teaching lasers to control molecules. *Physical Review Letters*, 68(10):1500–1503, 1992, <http://dx.doi.org/10.1103/physrevlett.68.1500>.
- [KB89] L. P. Kadanoff and G. Baym. *Quantum Statistical Mechanics: Green's Function Methods in Equilibrium and Non-Equilibrium Problems (Advanced Book Classics)*. Perseus Books (Sd), 1989, <http://www.worldcat.org/isbn/0201094223>.
- [KCG11] K. Krieger, A. Castro, and E. K. U. Gross. Optimization schemes for selective molecular cleavage with tailored ultrashort laser pulses. *Chemical Physics*, 391(1):50–61, 2011, <http://dx.doi.org/10.1016/j.chemphys.2011.04.014>.
- [Kho12] E. Khosravi. *Time-Dependent Phenomena in Quantum Transport*. PhD thesis, Free University Berlin, 2012, <http://d-nb.info/1034300261>.
- [KKSG08] E. Khosravi, S. Kurth, G. Stefanucci, and E. K. U. Gross. The Role of Bound States in Time-Dependent Quantum Transport. *Applied Physics A*, 93(2):355+, 2008, <http://dx.doi.org/10.1007/s00339-008-4864-9>.
- [KNHG14] W. Y. Kim, D. Nitsche, K. Hong, and E. K. U. Gross. Time-Dependent Density Functional Method with Exact Open Boundary Condition for Electron Dynamics at Metal-Molecule Interfaces. *in preparation*, 2014.
- [KRG⁺89] R. Kosloff, S. A. Rice, P. Gaspard, S. Tersigni, and D. J. Tanner. Wavepacket dancing: Achieving chemical selectivity by shaping light pulses. *Chemical Physics*, 139(1):201–220, 1989, [http://dx.doi.org/10.1016/0301-0104\(89\)90012-8](http://dx.doi.org/10.1016/0301-0104(89)90012-8).

- [Kro64] A. S. Kronrod. Integration with control of accuracy (Russian). *Dokl. Akad. Nauk SSSR*, 154:283–286, 1964.
- [Kro65] A. S. Kronrod. *Nodes and weights of quadrature formulas: sixteen-place tables*. Consultants Bureau, 1965, <http://www.worldcat.org/oclc/70380167>.
- [KSA⁺05] S. Kurth, G. Stefanucci, C. O. Almbladh, A. Rubio, and E. K. U. Gross. Time-dependent quantum transport: A practical scheme using density functional theory. *Physical Review B*, 72(3):035308+, 2005, <http://dx.doi.org/10.1103/physrevb.72.035308>.
- [KSK⁺10] S. Kurth, G. Stefanucci, E. Khosravi, C. Verdozzi, and E. K. U. Gross. Dynamical Coulomb Blockade and the Derivative Discontinuity of Time-Dependent Density Functional Theory. *Physical Review Letters*, 104(23):236801+, 2010, <http://dx.doi.org/10.1103/physrevlett.104.236801>.
- [KSKG09] E. Khosravi, G. Stefanucci, S. Kurth, and E. K. U. Gross. Bound states in time-dependent quantum transport: oscillations and memory effects in current and density. *Phys. Chem. Chem. Phys.*, 11(22):4535–4538, 2009, <http://dx.doi.org/10.1039/b906528h>.
- [KSvON06] J. Koch, M. Semmelhack, F. von Oppen, and A. Nitzan. Current-induced nonequilibrium vibrations in single-molecule devices. *Physical Review B*, 73:155306+, 2006, <http://dx.doi.org/10.1103/physrevb.73.155306>.
- [KUS⁺12] E. Khosravi, A. M. Uimonen, A. Stan, G. Stefanucci, S. Kurth, R. van Leeuwen, and E. K. U. Gross. Correlation effects in bistability at the nanoscale: Steady state and beyond. *Physical Review B*, 85:075103+, 2012, <http://dx.doi.org/10.1103/physrevb.85.075103>.
- [KvO05] J. Koch and F. von Oppen. Franck-Condon Blockade and Giant Fano Factors in Transport through Single Molecules. *Physical Review Letters*, 94(20):206804+, 2005, <http://dx.doi.org/10.1103/physrevlett.94.206804>.
- [KvOA06] J. Koch, F. von Oppen, and A. V. Andreev. Theory of the Franck-Condon blockade regime. *Physical Review B*, 74(20):205438+, 2006, <http://dx.doi.org/10.1103/physrevb.74.205438>.

- [KVS14] A. Kartsev, C. Verdozzi, and G. Stefanucci. Nonadiabatic Van der Pol oscillations in molecular transport. *The European Physical Journal B*, 87(1):1–12, 2014, <http://dx.doi.org/10.1140/epjb/e2013-40905-5>.
- [Lan57] R. Landauer. Spatial variation of currents and fields due to localized scatterers in metallic conduction. *IBM J. Res. Dev.*, 1(3):223–231, 1957, <http://dx.doi.org/10.1147/rd.13.0223>.
- [LBH10] J. T. Lü, M. Brandbyge, and P. Hedegård. Blowing the Fuse: Berry’s Phase and Runaway Vibrations in Molecular Conductors. *Nano Lett.*, 10(5):1657–1663, 2010, <http://dx.doi.org/10.1021/nl904233u>.
- [Leh08] M. C. Lehn. *FLENS - A Flexible Library for Efficient Numerical Solutions*. PhD thesis, University of Ulm, 2008, <http://d-nb.info/997797606>.
- [LK10] G. Q. Li and U. Kleinekathöfer. Optimal control of shot noise and Fano factor by external fields. *The European Physical Journal B*, 76(2):309–319, 2010, <http://dx.doi.org/10.1140/epjb/e2010-00206-3>.
- [LL35] F. London and H. London. The Electromagnetic Equations of the Supraconductor. *Proceedings of the Royal Society of London. Series A - Mathematical and Physical Sciences*, 149(866):71–88, 1935, <http://dx.doi.org/10.1098/rspa.1935.0048>.
- [LLKD04] B. J. LeRoy, S. G. Lemay, J. Kong, and C. Dekker. Electrical generation and absorption of phonons in carbon nanotubes. *Nature*, 432(7015):371–374, 2004, <http://dx.doi.org/10.1038/nature03046>.
- [LMD07] A. La Magna and I. Deretzis. Phonon Driven Nonlinear Electrical Behavior in Molecular Devices. *Physical Review Letters*, 99:136404+, 2007, <http://dx.doi.org/10.1103/physrevlett.99.136404>.
- [LMNR13] G. Li, B. Movaghar, A. Nitzan, and M. A. Ratner. Polaron formation: Ehrenfest dynamics vs. exact results. *The Journal of Chemical Physics*, 138(4):044112+, 2013, <http://dx.doi.org/10.1063/1.4776230>.

- [LMR01] R. J. Levis, G. M. Menkir, and H. Rabitz. Selective Bond Dissociation and Rearrangement with Optimally Tailored, Strong-Field Laser Pulses. *Science*, 292(5517):709–713, 2001, <http://dx.doi.org/10.1126/science.1059133>.
- [LSK07] G. Q. Li, M. Schreiber, and U. Kleinekathöfer. Coherent laser control of the current through molecular junctions. *EPL (Europhysics Letters)*, pages 27006+, 2007, <http://dx.doi.org/10.1209/0295-5075/79/27006>.
- [LYCLDMR97] A. Levy Yeyati, J. C. Cuevas, A. López-Dávalos, and A. Martín-Rodero. Resonant tunneling through a small quantum dot coupled to superconducting leads. *Physical Review B*, 55(10):R6137–R6140, 1997, <http://dx.doi.org/10.1103/physrevb.55.r6137>.
- [Mar03] D. F. Martinez. Floquet-Green function formalism for harmonically driven Hamiltonians. *Journal of Physics A: Mathematical and General*, 36(38):9827+, 2003, <http://dx.doi.org/10.1088/0305-4470/36/38/302>.
- [Mar09] R. J. Marks. *Handbook of Fourier Analysis & Its Applications*. Oxford University Press, USA, 2009, <http://www.worldcat.org/isbn/0195335929>.
- [Max50] E. Maxwell. Isotope Effect in the Superconductivity of Mercury. *Physical Review Online Archive (Prola)*, 78(4):477, 1950, <http://dx.doi.org/10.1103/physrev.78.477>.
- [MBB06] J. P. Morten, A. Brataas, and W. Belzig. Circuit theory of crossed Andreev reflection. *Physical Review B*, 74:214510+, 2006, <http://dx.doi.org/10.1103/physrevb.74.214510>.
- [MCH⁺97] R. M. Metzger, B. Chen, U. Höpfner, M. V. Lakshmikantham, D. Vuillaume, T. Kawai, X. Wu, H. Tachibana, T. V. Hughes, H. Sakurai, J. W. Baldwin, C. Hosch, M. P. Cava, L. Brehmer, and G. J. Ashwell. Unimolecular Electrical Rectification in Hexadecylquinolinium Tricyanoquinodimethanide. *J. Am. Chem. Soc.*, 119(43):10455–10466, 1997, <http://dx.doi.org/10.1021/ja971811e>.
- [MDD⁺07] A. Marchenkov, Z. Dai, B. Donehoo, R. N. Barnett, and U. Landman. Alternating current Josephson effect and resonant superconducting transport through vibrating Nb nanowires. *Nat Nano*, 2(8):481–485, 2007, <http://dx.doi.org/10.1038/nnano.2007.218>.

- [MO33] W. Meissner and R. Ochsenfeld. Ein neuer Effekt bei Eintritt der Supraleitfähigkeit. *Naturwissenschaften*, 21(44):787–788, 1933, <http://dx.doi.org/10.1007/bf01504252>.
- [Moo65] G. E. Moore. Cramming More Components onto Integrated Circuits. *Electronics*, 38(8):114–117, 1965, <http://dx.doi.org/10.1109/jproc.1998.658762>.
- [MRLY11] A. Martín-Rodero and A. Levy Yeyati. Josephson and Andreev transport through quantum dots. *Advances in Physics*, 60(6):899–958, 2011, <http://dx.doi.org/10.1080/00018732.2011.624266>.
- [MSS01] Y. Makhlin, G. Schön, and A. Shnirman. Quantum-state engineering with Josephson-junction devices. *Reviews of Modern Physics*, 73(2):357–400, 2001, <http://dx.doi.org/10.1103/revmodphys.73.357>.
- [MSSvL09] P. Myöhänen, A. Stan, G. Stefanucci, and R. van Leeuwen. Kadanoff-Baym approach to quantum transport through interacting nanoscale systems: From the transient to the steady-state regime. *Physical Review B*, 80:115107+, 2009, <http://dx.doi.org/10.1103/physrevb.80.115107>.
- [MSSvL10] P. Myöhänen, A. Stan, G. Stefanucci, and R. van Leeuwen. Kadanoff-Baym approach to time-dependent quantum transport in AC and DC fields. *Journal of Physics: Conference Series*, 220(1):012017+, 2010, <http://dx.doi.org/10.1088/1742-6596/220/1/012017>.
- [MTN12] P. J. Mohr, B. N. Taylor, and D. B. Newell. CODATA recommended values of the fundamental physical constants: 2010. *Reviews of Modern Physics*, 84:1527–1605, 2012, <http://dx.doi.org/10.1103/revmodphys.84.1527>.
- [MW92] Y. Meir and N. S. Wingreen. Landauer formula for the current through an interacting electron region. *Physical Review Letters*, 68(16):2512–2515, 1992, <http://dx.doi.org/10.1103/physrevlett.68.2512>.
- [Nam60] Y. Nambu. Quasi-Particles and Gauge Invariance in the Theory of Superconductivity. *Physical Review Online Archive (Prola)*, 117(3):648–663, 1960, <http://dx.doi.org/10.1103/physrev.117.648>.

- [Nit08] D. Nitsche. Simulation of Time-Dependent Electronic Transport. Master's thesis, Free University Berlin, 2008.
- [NM65] J. A. Nelder and R. Mead. A Simplex Method for Function Minimization. *The Computer Journal*, 7(4):308–313, 1965, <http://dx.doi.org/10.1093/comjnl/7.4.308>.
- [NNM⁺01] J. Nagamatsu, N. Nakagawa, T. Muranaka, Y. Zenitani, and J. Akimitsu. Superconductivity at 39 K in magnesium diboride. *Nature*, 410(6824):63–64, 2001, <http://dx.doi.org/10.1038/35065039>.
- [Nob14] Nobelstiftelsen. *Les prix Nobel en 1913*. Imprimerie Royale, P.-A. Norstedt & Söne, Stockholm, 1914.
- [OGK88] L. Oliveira, E. Gross, and W. Kohn. Density-Functional Theory for Superconductors. *Physical Review Letters*, 60(23):2430–2433, 1988, <http://dx.doi.org/10.1103/physrevlett.60.2430>.
- [Onn11a] H. K. Onnes. Further experiments with liquid helium. C. On the change of electric resistance of pure metals at very low temperatures, etc. IV. The resistance of pure mercury at helium temperatures. *Comm. Phys. Lab. Univ. Leiden*, 120b, 1911, http://dx.doi.org/10.1007/978-94-009-2079-8_15.
- [Onn11b] H. K. Onnes. Further experiments with liquid helium. D. On the change of electric resistance of pure metals at very low temperatures, etc. V. The disappearance of the resistance of mercury. *Comm. Phys. Lab. Univ. Leiden*, 122b, 1911, http://dx.doi.org/10.1007/978-94-009-2079-8_16.
- [Onn11c] H. K. Onnes. Further experiments with liquid helium. G. On the electrical resistance of pure metals, etc. VI. On the sudden change in the rate at which the resistance of mercury disappears. *Comm. Phys. Lab. Univ. Leiden*, 124c, 1911, http://dx.doi.org/10.1007/978-94-009-2079-8_17.
- [PBG62] L. S. Pontryagin, V. G. Boltyanskii, R. V. Gamkrelidze, and E. F. Mishchenko. *Mathematical Theory of Optimal Processes*. John Wiley & Sons, New York/London, 1962.
- [PDR88] A. P. Peirce, M. A. Dahleh, and H. Rabitz. Optimal control of quantum-mechanical systems: Existence, numerical approximation, and applications. *Physical Review A*, 37(12):4950–4964, 1988, <http://dx.doi.org/10.1103/physreva.37.4950>.

- [Pei33] R. Peierls. Zur Theorie des Diamagnetismus von Leitungselektronen. *Zeitschrift für Physik A Hadrons and Nuclei*, 80(11-12):763–791, 1933, <http://dx.doi.org/10.1007/bf01342591>.
- [PK03] J. P. Palao and R. Kosloff. Optimal control theory for unitary transformations. *Physical Review A*, 68(6):062308+, 2003, <http://dx.doi.org/10.1103/physreva.68.062308>.
- [Pow94] M. J. D. Powell. A direct search optimization method that models the objective and constraint functions by linear interpolation. In Susana Gomez and Jean-Pierre Hennart, editors, *Advances in Optimization and Numerical Analysis*, volume 275, pages 51–67. 1994, http://dx.doi.org/10.1007/978-94-015-8330-5_4.
- [Pow98] M. J. D. Powell. Direct search algorithms for optimization calculations. *Acta Numerica*, 7(-1):287–336, 1998, <http://dx.doi.org/10.1017/s0962492900002841>.
- [Pow06] M. J. D. Powell. The NEWUOA software for unconstrained optimization without derivatives. In G. Pillo and M. Roma, editors, *Large-Scale Nonlinear Optimization*, volume 83 of *Nonconvex Optimization and Its Applications*, chapter 16, pages 255–297. Springer US, Boston, 2006, http://dx.doi.org/10.1007/0-387-30065-1_16.
- [Pow09] M. J. D. Powell. The BOBYQA algorithm for bound constrained optimization without derivatives. *Department of Applied Mathematics and Theoretical Physics, Cambridge England, technical report NA2009/06*, 2009.
- [PPC⁺05] A. N. Pasupathy, J. Park, C. Chang, A. V. Soldatov, S. Lebedkin, R. C. Bialczak, J. E. Grose, L. A. K. Donev, J. P. Sethna, D. C. Ralph, and P. L. McEuen. Vibration-Assisted Electron Tunneling in C140 Transistors. *Nano Lett.*, 5(2):203–207, 2005, <http://dx.doi.org/10.1021/nl048619c>.
- [PSC09] E. Perfetto, G. Stefanucci, and M. Cini. Equilibrium and time-dependent Josephson current in one-dimensional superconducting junctions. *Physical Review B*, 80(20):205408+, 2009, <http://dx.doi.org/10.1103/physrevb.80.205408>.
- [RBBH12] E. Räsänen, T. Blasi, M. F. Borunda, and E. J. Heller. Optical control of entangled states in semiconductor quan-

- tum wells. *Physical Review B*, 86(20):205308+, 2012, <http://dx.doi.org/10.1103/physrevb.86.205308>.
- [RC07] D. A. Ryndyk and G. Cuniberti. Nonequilibrium resonant spectroscopy of molecular vibrons. *Physical Review B*, 76:155430+, 2007, <http://dx.doi.org/10.1103/physrevb.76.155430>.
- [RCW⁺07] E. Räsänen, A. Castro, J. Werschnik, A. Rubio, and E. K. U. Gross. Optimal Control of Quantum Rings by Terahertz Laser Pulses. *Physical Review Letters*, 98(15):157404+, 2007, <http://dx.doi.org/10.1103/physrevlett.98.157404>.
- [RDCR08] D. A. Ryndyk, P. D'Amico, G. Cuniberti, and K. Richter. Charge-memory polaron effect in molecular junctions. *Physical Review B*, 78:085409+, 2008, <http://dx.doi.org/10.1103/physrevb.78.085409>.
- [RH13] E. Räsänen and E. J. Heller. Optimal control of quantum revival. *The European Physical Journal B*, 86(1):1–5, 2013, <http://dx.doi.org/10.1140/epjb%252fe2012-30921-4>.
- [RHC06] D. A. Ryndyk, M. Hartung, and G. Cuniberti. Nonequilibrium molecular vibrons: An approach based on the nonequilibrium Green function technique and the self-consistent Born approximation. *Physical Review B*, 73:045420+, 2006, <http://dx.doi.org/10.1103/physrevb.73.045420>.
- [RK13] D. M. Reich and C. P. Koch. Cooling molecular vibrations with shaped laser pulses: optimal control theory exploiting the timescale separation between coherent excitation and spontaneous emission. *New Journal of Physics*, 15(12):125028+, 2013, <http://dx.doi.org/10.1088/1367-2630/15/12/125028>.
- [RL02] P. Recher and D. Loss. Creation of Nonlocal Spin-Entangled Electrons via Andreev Tunneling, Coulomb Blockade, and Resonant Transport. *Journal of Superconductivity*, 15(1):49–65, 2002, <http://dx.doi.org/10.1023/A:1014027227087>.
- [RM12] E. Räsänen and L. B. Madsen. Strong-field-ionization suppression by light-field control. *Physical Review A*, 86(3):033426+, 2012, <http://dx.doi.org/10.1103/physreva.86.033426>.
- [Row90] T. Rowan. *Functional Stability Analysis of Numerical Algorithms*. PhD thesis, Department of Computer Sciences, University of Texas at Austin, 1990.

- [RPM13] E. Räsänen, A. Putaja, and Y. Mardoukhi. Optimal control strategies for coupled quantum dots. *Central European Journal of Physics*, 11(9):1066–1073, 2013, <http://dx.doi.org/10.2478/s11534-013-0277-2>.
- [RS09] R. P. Riwar and T. L. Schmidt. Transient dynamics of a molecular quantum dot with a vibrational degree of freedom. *Physical Review B*, 80(12):125109+, 2009, <http://dx.doi.org/10.1103/physrevb.80.125109>.
- [RSL01] P. Recher, E. V. Sukhorukov, and D. Loss. Andreev tunneling, Coulomb blockade, and resonant transport of nonlocal spin-entangled electrons. *Physical Review B*, 63:165314+, 2001, <http://dx.doi.org/10.1103/physrevb.63.165314>.
- [RSWN50] C. A. Reynolds, B. Serin, W. H. Wright, and L. B. Nesbitt. Superconductivity of Isotopes of Mercury. *Physical Review Online Archive (Prola)*, 78(4):487, 1950, <http://dx.doi.org/10.1103/physrev.78.487>.
- [SBS12] J. Schindele, A. Baumgartner, and C. Schönberger. Near-Unity Cooper Pair Splitting Efficiency. *Physical Review Letters*, 109:157002+, 2012, <http://dx.doi.org/10.1103/physrevlett.109.157002>.
- [Sch01] W. Schleich. *Quantum optics in phase space*. Wiley-VCH, 2001, <http://www.worldcat.org/isbn/9783527294350>.
- [SFM04] O. Sauret, D. Feinberg, and T. Martin. Quantum master equations for the superconductor-quantum dot entangler. *Physical Review B*, 70(24):245313+, 2004, <http://dx.doi.org/10.1103/physrevb.70.245313>.
- [Sha63] S. Shapiro. Josephson Currents in Superconducting Tunneling: The Effect of Microwaves and Other Observations. *Physical Review Letters*, 11:80–82, 1963, <http://dx.doi.org/10.1103/physrevlett.11.80>.
- [SKGR07] G. Stefanucci, S. Kurth, E. K. U. Gross, and A. Rubio. *Time-dependent transport phenomena*, volume 17, chapter 10, pages 247–284. Elsevier, 2007, [http://dx.doi.org/10.1016/s1380-7323\(07\)80028-8](http://dx.doi.org/10.1016/s1380-7323(07)80028-8).
- [SKRG08] G. Stefanucci, S. Kurth, A. Rubio, and E. K. U. Gross. Time-dependent approach to electron pumping in open quantum systems. *Physical Review B*, 77(7):075339+, 2008, <http://dx.doi.org/10.1103/physrevb.77.075339>.

- [SPAS⁺10] G. Sonne, M. E. Peña-Aza, R. I. Shekhter, L. Y. Gorelik, and M. Jonson. Voltage-driven superconducting weak link as a refrigerator for cooling of nanomechanical vibrations. *Low Temperature Physics*, 36(10):902–910, 2010, <http://dx.doi.org/10.1063/1.3515521>.
- [SPC10] G. Stefanucci, E. Perfetto, and M. Cini. Time-dependent quantum transport with superconducting leads: A discrete-basis Kohn-Sham formulation and propagation scheme. *Physical Review B*, 81(11):115446+, 2010, <http://dx.doi.org/10.1103/physrevb.81.115446>.
- [SS97] W. H. Steeb and T. K. Shi. *Matrix Calculus and Kronecker Product With Applications and C++ Programs*. World Scientific Pub Co Inc, 1997, <http://www.worldcat.org/isbn/9810232411>.
- [ST02] S. E. Sklarz and D. J. Tannor. Loading a Bose-Einstein condensate onto an optical lattice: An application of optimal control theory to the nonlinear Schrödinger equation. *Physical Review A*, 66(5):053619+, 2002, <http://dx.doi.org/10.1103/physreva.66.053619>.
- [Ste80] S. Stenholm. The Wigner function. I. The physical interpretation. *European Journal of Physics*, 1(4):244+, 1980, <http://dx.doi.org/10.1088/0143-0807/1/4/012>.
- [Ste07] G. Stefanucci. Bound states in *ab initio* approaches to quantum transport: A time-dependent formulation. *Physical Review B*, 75(19):195115+, 2007, <http://dx.doi.org/10.1103/physrevb.75.195115>.
- [SvL13] G. Stefanucci and R. van Leeuwen. *Nonequilibrium Many-Body Theory of Quantum Systems: A Modern Introduction*. Cambridge University Press, 2013, <http://www.worldcat.org/isbn/0521766176>.
- [SWR88] S. Shenghua, A. Woody, and H. Rabitz. Optimal control of selective vibrational excitation in harmonic linear chain molecules. *The Journal of Chemical Physics*, 88(11):6870–6883, 1988, <http://dx.doi.org/10.1063/1.454384>.
- [TKLvR08] O. Tal, M. Krieger, B. Leerink, and J. M. van Ruitenbeek. Electron-Vibration Interaction in Single-Molecule Junctions: From Contact to Tunneling

- Regimes. *Physical Review Letters*, 100(19):196804+, 2008, <http://dx.doi.org/10.1103/physrevlett.100.196804>.
- [TM10] M. Tahir and A. MacKinnon. Time-dependent quantum transport in a resonant tunnel junction coupled to a nanomechanical oscillator. *Physical Review B*, 81(19):195444+, 2010, <http://dx.doi.org/10.1103/physrevb.81.195444>.
- [TvLPS13] R. Tuovinen, R. van Leeuwen, E. Perfetto, and G. Stefanucci. Time-dependent Landauer-Büttiker formula for transient dynamics. *Journal of Physics: Conference Series*, 427(1):012014+, 2013, <http://dx.doi.org/10.1088/1742-6596/427/1/012014>.
- [UKS⁺10] A. M. Uimonen, E. Khosravi, G. Stefanucci, S. Kurth, R. van Leeuwen, and E. K. U. Gross. Real-time switching between multiple steady-states in quantum transport. *Journal of Physics: Conference Series*, 220(1):012018+, 2010, <http://dx.doi.org/10.1088/1742-6596/220/1/012018>.
- [UKS⁺11] A. M. Uimonen, E. Khosravi, A. Stan, G. Stefanucci, S. Kurth, R. van Leeuwen, and E. K. U. Gross. Comparative study of many-body perturbation theory and time-dependent density functional theory in the out-of-equilibrium Anderson model. *Physical Review B*, 84:115103+, 2011, <http://dx.doi.org/10.1103/physrevb.84.115103>.
- [Ull12] C. Ullrich. *Time-Dependent Density-Functional Theory: Concepts and Applications (Oxford Graduate Texts)*. Oxford University Press, USA, 2012, <http://www.worldcat.org/isbn/0199563020>.
- [vLDS⁺06] R. van Leeuwen, N. E. Dahlen, G. Stefanucci, C. O. Almbladh, and U. von Barth. Introduction to the Keldysh Formalism. In M. A. L. Marques, C. A. Ullrich, F. Nogueira, A. Rubio, K. Burke, and E. K. I. Gross, editors, *Time-Dependent Density Functional Theory*, volume 706 of *Lecture Notes in Physics*, pages 33–59. Springer Berlin Heidelberg, 2006, http://dx.doi.org/10.1007/3-540-35426-3_3.
- [VSA06] C. Verdozzi, G. Stefanucci, and C. O. Almbladh. Classical Nuclear Motion in Quantum Transport. *Physical Review Letters*, 97(4):046603+, 2006, <http://dx.doi.org/10.1103/physrevlett.97.046603>.

- [Wal76] J. R. Waldram. The Josephson effects in weakly coupled superconductors. *Reports on Progress in Physics*, 39(8):751+, 1976, <http://dx.doi.org/10.1088/0034-4885/39/8/002>.
- [WAT⁺87] M. K. Wu, J. R. Ashburn, C. J. Torng, P. H. Hor, R. L. Meng, L. Gao, Z. J. Huang, Y. Q. Wang, and C. W. Chu. Superconductivity at 93 K in a new mixed-phase Y-Ba-Cu-O compound system at ambient pressure. *Physical Review Letters*, 58(9):908–910, 1987, <http://dx.doi.org/10.1103/physrevlett.58.908>.
- [Wig32] E. Wigner. On the Quantum Correction For Thermodynamic Equilibrium. *Physical Review*, 40(5):749–759, 1932, <http://dx.doi.org/10.1103/physrev.40.749>.
- [WJS⁺98] G. Weihs, T. Jennewein, Ch Simon, H. Weinfurter, and A. Zeilinger. Violation of Bell’s Inequality under Strict Einstein Locality Conditions. *Physical Review Letters*, 81(23):5039–5043, 1998, <http://dx.doi.org/10.1103/physrevlett.81.5039>.
- [WKG94] O. J. Wacker, R. Kümmel, and E. K. U. Gross. Time-Dependent Density-Functional Theory for Superconductors. *Physical Review Letters*, 73(21):2915–2918, 1994, <http://dx.doi.org/10.1103/physrevlett.73.2915>.
- [WNC⁺04] S. W. Wu, G. V. Nazin, X. Chen, X. H. Qiu, and W. Ho. Control of Relative Tunneling Rates in Single Molecule Bipolar Electron Transport. *Physical Review Letters*, 93(23):236802+, 2004, <http://dx.doi.org/10.1103/physrevlett.93.236802>.
- [WP05] R. C. Whaley and A. Petitet. Minimizing development and maintenance costs in supporting persistently optimized BLAS. *Softw. Pract. Exper.*, 35(2):101–121, 2005, <http://dx.doi.org/10.1002/spe.v35:2>.
- [WPD01] R. C. Whaley, A. Petitet, and J. J. Dongarra. Automated empirical optimizations of software and the ATLAS project. *Parallel Computing*, 27(1-2):3–35, 2001, [http://dx.doi.org/10.1016/s0167-8191\(00\)00087-9](http://dx.doi.org/10.1016/s0167-8191(00)00087-9).
- [WPHT11] H. Wang, I. Pshenichnyuk, R. Härtle, and M. Thoss. Numerically exact, time-dependent treatment of vibrationally coupled electron transport in single-molecule junctions.

- The Journal of Chemical Physics*, 135(24):244506+, 2011, <http://dx.doi.org/10.1063/1.3660206>.
- [ZBR98] W. Zhu, J. Botina, and H. Rabitz. Rapidly convergent iteration methods for quantum optimal control of population. *The Journal of Chemical Physics*, 108(5):1953–1963, 1998, <http://dx.doi.org/10.1063/1.475576>.
- [ZE10] A. Zazunov and R. Egger. Adiabatic polaron dynamics and Josephson effect in a superconducting molecular quantum dot. *Physical Review B*, 81(10):104508+, 2010, <http://dx.doi.org/10.1103/physrevb.81.104508>.
- [ZEMM06] A. Zazunov, R. Egger, C. Mora, and T. Martin. Superconducting transport through a vibrating molecule. *Physical Review B*, 73:214501+, 2006, <http://dx.doi.org/10.1103/physrevb.73.214501>.
- [ZFM06] A. Zazunov, D. Feinberg, and T. Martin. Phonon-mediated negative differential conductance in molecular quantum dots. *Physical Review B*, 73:115405+, 2006, <http://dx.doi.org/10.1103/physrevb.73.115405>.
- [ZG10] A. Zacarias and E. K. U. Gross. Transport properties of chrysazine-type molecules. *Theoretical Chemistry Accounts: Theory, Computation, and Modeling (Theoretica Chimica Acta)*, 2010, <http://dx.doi.org/10.1007/s00214-009-0683-0>.
- [ZWZ12] X. Zhang, Q. Wang, and Y. Zhang. Model-driven Level 3 BLAS Performance Optimization on Loongson 3A Processor. In *2012 IEEE 18th International Conference on Parallel and Distributed Systems*, pages 684–691. IEEE, 2012, <http://dx.doi.org/10.1109/icpads.2012.97>.
- [ZXW12] L. Zhang, Y. Xing, and J. Wang. First-principles investigation of transient dynamics of molecular devices. *Physical Review B*, 86:155438+, 2012, <http://dx.doi.org/10.1103/physrevb.86.155438>.

Acknowledgements

First of all, I wish to express my sincere thank to Prof. E.K.U. Gross for giving me the opportunity to write my PhD thesis at the Max Planck Institute of Microstructure Physics in Halle (Saale). Thank you for the freedom you gave me to pursue my own ideas and for the financial support during my time at the institute.

I would like to thank Andreas Linscheid, Danilo Nitsche, Dr. Elham Khosravi, Frank Essenberger and Dr. Gianluca Stefanucci for all kinds of scientific discussions and explanations. In particular, I would like to thank my office colleague Dr. Mariana Odashima for the perfect working atmosphere in the office. Furthermore, I am very grateful to all the people proofreading the drafts of my thesis. I wish to express my gratitude to Dr. Michael Lehn for developing, maintaining and especially for providing support for the library FLENS. It was the basis for all codes written in the course of my research for this work and simplified the code development enormously.

Finally I want to thanks my parents for the unceasing support during my studies. My deepest gratitude goes to Beatrice for her understanding, encouragement and everything else in the last years.

Curriculum vitae

Personal details

First Name Klaus
Middle Name Jochen
Last Name Pototzky
Date of Birth 14.02.1986
Place of Birth Nürnberg, Germany

Education

6/2005 Abitur at the Gymnasium Roth, Roth, Germany

9/2005 Study of Physics at the Friedrich-Alexander
- 6/2010 University of Erlangen-Nürnberg, Germany
Diploma thesis: “Beschreibung ungerader deformierter
Atomkerne mit der Skyrme-Hartree-Fock Methode”

9/2005 Study of Mathematics at the Friedrich-Alexander
- 9/2010 University of Erlangen-Nürnberg, Germany
Bachelor thesis: “Ein algorithmischer Kopositivitäts-
nachweis basierend auf Zerlegungen des Standardsimplex”

8/2007 Exchange student at the University of Lund, Sweden
- 1/2008

since 9/2010 PhD student at the Max Planck Institute of
Microstructure Physics, Halle (Saale), Germany

Publications

- K. J. Pototzky and E.K.U. Gross. Driving vibrations in hybrid and Josephson junctions. *Submitted to Nano Letters*, 2014.
- K. J. Pototzky and E.K.U. Gross. Controlling observables in time-dependent quantum transport. *Submitted*, 2014, <http://arxiv.org/abs/1407.2554>.
- K. J. Pototzky and E.K.U. Gross. How to interpret the spectral density of the Keldysh nonequilibrium Green's function. *Submitted*, 2014, <http://arxiv.org/abs/1405.5984>.
- K. J. Pototzky, J. Erler, P.-G. Reinhard, V. O. Nesterenko. Properties of odd nuclei and the impact of time-odd mean fields: A systematic Skyrme-Hartree-Fock analysis. *The European Physical Journal A*, 46(2):299-310, 2010, <http://dx.doi.org/10.1140/epja/i2010-11045-6>.

Eidesstattliche Erklärung

Hiermit erkläre ich gemäß §5 Abs. 4 der Promotionsordnung der Naturwissenschaftlichen Fakultät II - Chemie, Physik und Mathematik der Martin-Luther Universität Halle-Wittenberg vom August 2012, dass ich die vorliegende Arbeit selbständig und ohne fremde Hilfe verfasst habe. Es wurden keine, außer die angegebenen Quellen und Hilfsmittel benutzt und die den benutzten Werken wörtlich oder inhaltlich entnommenen Stellen wurden als solche kenntlich gemacht.

Desweiteren erkläre ich gemäß §5 Abs. 5 der Promotionsordnung, dass ich bisher keine vergeblichen Promotionsversuche an dieser oder einer anderen Fakultät unternommen habe.

Halle (Saale), den 14.7.2014

Klaus Jochen Pototzky